University of Tartu
Institute of Physics

Tallinn Technical University
Institute of Mechanical Engineering

Frantsevich Institute for Problems of Materials Science
of National Academy of Sciences of Ukraine

Vladimir Pokropivny
Rynno Lohmus
Irina Hussainova
Alex Pokropivny
Sergey Vlassov

INTRODUCTION TO NANOMATERIALS AND NANOTECHNOLOGY

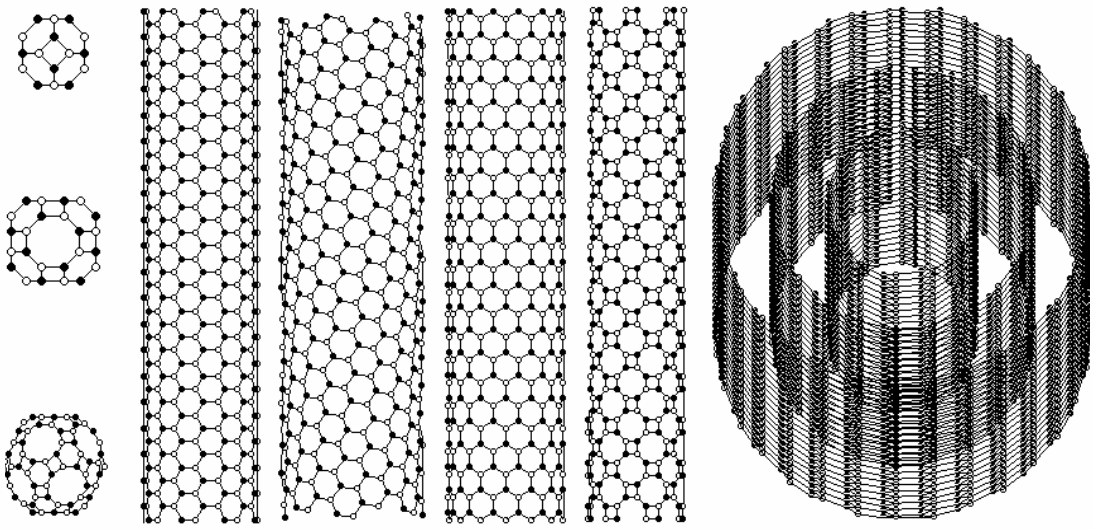

Tartu 2007

V. Pokropivny, R. Lohmus, I. Hussainova, A. Pokropivny, S. Vlassov. Introduction in nanomaterials and nanotechnology. – University of Tartu. – 2007, 225p.
(Special lecture course for bachelors, MSc, post-graduates and specialists in nanotechnology)

Physics and chemistry of nanostructures or nanophysics and nanochemistry are relatively new areas of science arisen in last decade of past century after discovery of fullerenes and nanotubes. It is introduction into more extent interdisciplinary integrated modern science known now as nanotechnology rapidly developing. At this stage of growing knowledge authors have shortly outlined the subject and classifications of nanostructures, interesting milestones, main principles, methods, techniques, as well as general directions of future perspective research to be a guideline in a see of modern research. Main mechanisms of physico-chemical processes affected formation of nanostructured materials and their properties are clearly expressed, in particular, a dielectric permittivity as a principal characteristic of electric, magnetic, acoustic, optic transparency, superconducting, and other properties of nanoceramics and nanometals. The peculiar properties of nanostructures are emphasized to be result of size effects, external and internal, classical and quantum ones, that arise in zero-dimensional quantum dots, one-dimensional wires, and two-dimensional layers. Numerous applications are considered including microlasers, photonic crystals, probe microscopy, left-handed materials with negative refraction index, etc. Novel idea is advanced that new discovery of novel fundamental laws, phenomena and applied effects are possible only in artificially fabricated nanostructures with new effect theoretically predicted and designed in advance. Content of the course covers the types, classification and peculiarities of nanostructures, size effects, synthesis and growth, fullerenes, nanotubes, microlasers, photonics, scanning probe microscopy, nanomanipulation, etc. The course is based on the lectures given during several years for students of Kiev National University (Ukraine), Tartu University and Tallinn Technical University (Estonia).

RAK/NSF Meede 1.1 Project has supported this work. Also Estonian Science foundation grants no. 6658,6537, 6660 and Ukraine Nanotechnology Science Foundation. Estonian Nanotechnology Competence Center projects were also engaged to this work

Copyright:
Vladimir Pokropivny (Tartu University, Tallinn University, Frantsevich Institute for Problems of Materials Science of NASU),
Rynno Lohmus (Tartu University),
Irina Hussainova (Tallinn University of Technology),
Alex Pokropivny (Frantsevich Institute for Problems of Materials Science of NASU),
Sergey Vlassov (Tartu University).

ISBN: 978–9949–11–741–3

Tartu University Press
www.tyk.ee

CONTENTS

1. INTRODUCTION

Nanoscience primarily deals with synthesis, characterization, exploration, and exploitation of nanostructured materials. These materials are characterized by at least one dimension in the nanometer range. A nanometer (nm) is one billionth of a meter, or 10^{-9} m. One nanometer is approximately the length equivalent to 10 hydrogen or 5 silicon atoms aligned in a line.

The processing, structure and properties of materials with grain size in the tens to several hundreds of nanometer range are research areas of considerable interest over the past years. A revolution in materials science and engineering is taking place as researchers find ways to pattern and characterize materials at the nanometer length scale. New materials with outstanding electrical, optical, magnetic and mechanical properties are rapidly being developed for use in information technology, bio-engineering, and energy and environmental applications.

On nanoscale, some physical and chemical material properties can differ significantly from those of the bulk structured materials of the same composition; for example, the theoretical strength of nanomaterials can be reached or *quantum effects* may appear; crystals in the nanometer scale have a low melting point (the difference can be as large as 1000°C) and reduced lattice constants, since the number of surface atoms or ions becomes a significant fraction of the total number of atoms or ions and *the surface energy* plays a significant role in the thermal stability. Therefore, many material properties must now be revisited in light of the fact that a considerable increase in surface-to-volume ratio is associated with the reduction in material size to the nanoscale, often having a prominent effect on material performance. Historically, fundamental material properties such as elastic modulus have been characterized in bulk specimens using macroscopic, and more recently microscopic, techniques. However, as nanofabrication advances continue, these bulk properties are no longer sufficient to predict performance when devices are fabricated with small critical dimensions.

Although nanotechnology is a new area of research, nanomaterials are known to be used for centeries. For example, the Chinese used gold nanoparticles as an inorganic dye to introduce red color into their ceramic porcelains more than thousand years ago. Roman glass artifacts contained metal nanoparticles, which provided beautiful colours. In medivial times, nanoparticles were used for decoration of cathedral windows.

What really new about nanoscience is the combination of our ability to see and *manipulate matter* on the nanoscale and our understanding of atomic scale interactions. Advances in the materials processing along with the precipitous rise in the sophistication of routine, commonly available tools capable for characterization of materials with force, displacement and spatial resolutions as small as picoNewtons (pN = 10^{-12} N), nanometer (nm = 10^{-9} m) and Angstrom (A = 10^{-10} m), respectively, have provided unprecedented opportunities to probe the structure and mechanical response of materials on nanoscale. In addition, major improvements in computer support have allowed *the simulations of material structures* and behavior with a degree of accuracy unimaginable as recently as a decade ago.

Although study on materials in the nanometer scale can be traced back for centuries, the current fever of nanotechnology is at least partly driven by the ever *shrinking of devices* in the semiconductor industry. The continued decrease in device dimensions has followed the well-known *Moore's law* predicted in 1965 and illustrated in Fig. 1. The trend line illustrates the fact that the transistor size has decreased by a factor of 2 every 18 months since 1950.

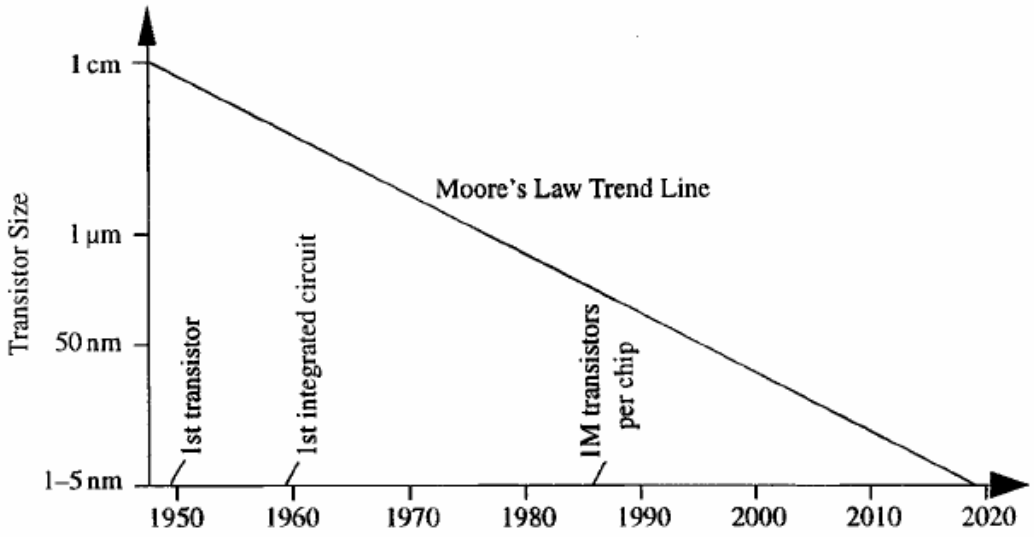

Fig. 1. "Moore's Law" plot of transistor size versus year.

There are many *nanoscale electronic devices* available now: tunneling junctions; devices with negative differential electrically configurable switches; carbon nanotube transistor; and single molecular transistor; ultrahigh density nanowires lattices and circuits with metal and semiconductor nanowires; etc. Devices have also been connected together to form circuits capable of performing single functions such as basic memory and logic function. Computer architecture based on nanoelectronics (also known as nanocomputers) has also been intensively studied. Various processing techniques have been applied in the fabrication of nanoelectronics such as focused ion beam (FIB), electron beam lithography, and imprint lithography. Major obstacles preventing the development of such devices include addressing nanometer-sized objects such as nanoparticles and molecules, molecular vibrations, robustness and the poor electrical conductivity. Certainly, nanomaterials play an important role not only in semiconductor – based electronics.

Nano-sized materials currently are used in numerous industries, e.g., carbon black particles make rubber tires wear resistant; nanofibers are used for insulation and reinforcement of composites; iron oxide creates the magnetic material used in disk drives and audio-video tapes; nano-zinc oxides and titania are used as sunblocks for UV rays; etc. Nanoscale particles and nanothin layers of materials are being used, among other things, to make products lighter, stronger or more conductive. Some of the products on the market using nanotechnology are: magnetic recording tapes; computer hard drivers; bumpers on cars; solid – state compasses; protective and glare – reducing coatings for eyeglasses and windows; automobile catalyc converters; metal – cutting tools; dental bonding agents; longer – lasting tennis ball; burn and wound dressing; ink; etc. Promising applications of nanotechnology in medicine and/or biology have attracted a lot of attention and have become a fast growing field. One of the attractive applications in nanomedicine is the creation of nanoscale devices for improved therapy and diagnostics. Such nanoscale devices or nanorobots serve as vehicles for delivery of therapeutic agents, detectors or guardians against early disease and perhaps repair of metabolic or genetic defects. For applications in medicine, the major challenge is "miniaturization": new instruments to analyze tissues literally down to the molecular level, sensors smaller than a cell allowing to look at ongoing functions, and small

machines that literally circulate within a human body pursuing pathogens and neutralizing chemical toxins.

Researchers expect to develop *new commercial applications for nanotechnology* for the next several years. They include: advanced drug – delivering systems, including implantable devices that automatically administer drugs and sense drug levels; medical diagnostic tools, such as cancer – tagger mechanisms and "lab-on-a-chip" diagnostics for physicians; cooling chips or wafer to replace compressors in cars, refrigerators, air conditioners and other devices, using no chemicals or moving parts; sensors for airborne chemicals or other toxins; solar fuel cells and portable power to provide inexpensive, clean energy; etc.

Nanotechnology (NT) is proposed presently to define as the complex of fundamental and engineering sciences that integrates a chemistry, physics and biology of nanostructures with a materials science, electronics, and processes technologies focused on a comprehensive research of nanostructures, on a development of atomistic physical-chemical processes, self- and automatic-assembling of nanomaterials and workpieces using complex probe microscopes combined with other tools, resulted in a fabrication and manufacturing of nanodevices, nanomachines, ultra-low integrated circuits, micro-opto-electro-mechanical systems, nanobiorobots, etc.

In reality the NT have been arisen in early 80-th, when the scanning tunneling microscopy, the atomic force and other probe microscopes were invented. These have given the opportunity to realize *the main concept of NT* formulated by Richard Feynman, namely, to assemble artificially the nanoworkpieces and nanodevices from single atoms and molecules.

Huge advantage of Pentium-4 over IBM-360 have been achieved by a miniaturizing of integrated circuits and fabricating of microchips containing ca. $\sim 10^9$ units/cm^2 of ~200nm in size. And this is not a limit; the size of individual units may be decreased at least on the orders of magnitudes.

With regard to nanoworld, a natural question has arisen "*where are its boundaries*?"

Formally it is restricted by size of nanoparticles, $d < 100$nm. Physically it is determined by a variety of size effects. Decrease in size results in the particles physical-chemical properties changing and, consequently, the properties of nano-materials are changed dramatically and sometime cordially. The size effects may be divided into two types, the internal and external ones, as well as the classical and quantum effects. Internal or *intrinsic size effects* are determined as a change of the properties peculiar to particles (the lattice parameters, melting temperature, hardness, band gap, luminescence, diffusion coefficients, chemical activity, sorption, etc.) irrespective of external disturbances. *External size effects* arise inevitably and always in the processes of interaction between different physical fields and matters under decreasing of their building units (the particles, grains, domains) down to a crucial value, when this size becomes to be comparable with a length of physical phenomena (the free length of electrons, phonons, coherent length, screening length, irradiative wave length, etc.). In turn *the classical size effects* appear to become apparent in variation of lattice parameters, hardness, plasticity, thermal conductivity, diffusion, etc. *The quantum size effects* manifest themselves in a blue shift of luminescence, in the rise of peculiar low-dimensional quantum states, in the quantization of electroconductivity in magnetic field, in the oscillation of the superconductivity critical temperature, magnetoresistance and other physical characteristics, in the generation of hypersound, etc. Hence, studying the size effects in novel nanostructured materials activated by different external fields one can hope for the discovery of novel effects and phenomena and for the development of novel nanotechnology on this base.

Nanotechnology therefore is *the complex interdisciplinary science* including:

1. *Nanochemistry* (nanocolloid, sol-gel and quantum chemistry) destined for self-assembling and synthesis of nanoparticles as well as for research of their intrinsic size effects.
2. *Nanophysics* (quantum physics, spintronics, photonics) destined for artificial assempling and fabrication of nanostructures as well as for research of their external size effects.
3. *Nanomaterials science* (nanopowder technology, nanoceramics compounds, nano-tribology, nanosintering and other nanoprocesses) destined for research, development and production of novel nanostructured architectures, functional nanomaterials and smart nanocomponents with unique properties.
4. *Nanoelectronics, optoelectronics and nanoengineering* destined for development of novel technological processes, nanomotors, nanoactuators, nanodevices, micro-opto-electro-mechanical systems (MEMS, MOEMS), ultra-large integrated circuits (ULCI), nanorobots, etc.
5. *Nanobionics* destined for development of novel biomachine complexes, such as nanobiochips, nanobiorobots, etc.
6. *Nanometrology, nanodevice-building and nano-hand-craft* destined for development of special nanotools, instrumentations, information and computational systems for support of NT itself.

The association of these sciences in nanotechnology reflects both their inherent inter-connection around the nanoobjects and *the change in technology paradigm*, namely, the nanomaterial, nanodevice or nanosystem seems to be fabricated by the automatic artificial assembling or self-assembling from molecules or clusters *in whole*, *in situ*, *in place*, in the single technological process incorporating them then in microdevices, rather then by aggregating of different components as now. In place of the traditional processes of thermo mechanical treatment (the rolling, cutting, welding, soldering, molding, etc.) and of microelectronics processes (the chemical and physical vapor depositions, lithography, etc.) the novel atomistic nanotechnology processes (the nanomanipulation, artificial- and self-assembling, nanolithography, membrane-templating synthesis, sol-gel synthesis, molecular-beam epitaxy, etc.) are expected to will come.

Living in macroworld human come into controllable tunable contact with nanoworld mainly by means of a tip of probe microscope, so the contact “tip-surface” is the contact of macroworld with nanoworld. Therefore the key problem of novadays nanotechnology is a comprehensive research of atomistic mechanisms of *the nanocontact phenomena* (adhesion, indentation, friction, wear, etc.) in dependence on a type of interatomic intermolecular bonds, type and structure of contact materials, size of tip and nanostructure, value of load, width of gap, environment, temperature, external electric and magnetic fields, frequency and intensity of electromagnetic waves, and so on. These researches have to be expressed in development of *the techniques for tunable manipulation, characterization, control, and position assembling of nanostructures*, particulary, seizure, gripping, restraining, turning, moving, breaking, reset and adhesion of a molecular building block onto prescribed place. Such operations at atomic and molecular level are just the ones which become to be principal for nanotechnology.

It should be emphasized that NT has not intended to replace the existence micro-technologies, but to stay in close connection with them to complement them in the deeper study and advanced control of nanoworld.

Atoms, molecules, clusters, fullerenes, supramolecular structures, their crystals, nanotubes, nanowires, nanorodes, their arrays and photonic crystals serve as *NT objectives.*

Fullerenes and atomic clusters are the smallest zero-dimensional (0D) nanostructures called quantum dots possessing the properties inherent for nanomaterial rather than for single atom. Note that for fullerenes it should mean not only the buckyball C_{60}, but the multitude of another carbon C_n and noncarbon clusters and metcarbes $Me@C_n$. Presently a number of experimental nanodevices was developed on this base, e.g. the switchers, diodes, transistors, amplifiers, sensors, optical filters, solar cells, magneto-optical recorders, etc.

Nanotubes, nanorodes, nanowires, nanofibers manifest more advanced and promising properties as being the 1D quantum wires nanoscopic in diameter but microscopic in length. Their unique properties stem from capability of the ring and cylindrical types of acoustic and electromagnetic waves to propagate that makes them a unique nanolaboratory for research of quantum resonance phenomena. All stated above also concern to noncarbon 1D nanowires and nanotubes based on boron-nitride, oxides, chalcogenides, dichalcogenides, chalogenides, and some other III–V and II–VI compounds possessing of the most manifold physical-chemical characteristics.

Reduced two-dimensional *2D heterostructures,* nanolayers and nanodisks as being the well known 2D quantum wells are believed to migrate from micro- to nano-electronics. In addition the 2D arrays of nanowires and nanotubes ordered in 2D forest arrays or 2D crystals seem to be novel and very perspective core of NT. Their unique properties have to be determined by new principles of electromagnetic waves propagation based on the Bragg diffraction law rather than on the total internal reflection. They are the quantum and, in the same time, the macroscopic 2D crystals in which the various quantum states and resonance effects are expected. Actually such resonance states can be recognized as the novel state of matter, research of which appears to become the advanced direction in nanophysics. On this base the waveguides, laser emitting diodes, infrared sensors and other nanodevices have already been developed.

Design and assembling of such artificial media, search for new unusual effects and phenomena, as well as development of the up-to-date nanodevices on their base seems to be the most promising way in the nearest NT development. The example is the discovery of “left” matter or metamaterials, in which unconventional inverse refraction law, inverse Doppler and inverse Cherenkov effects were observed. In nanomaterials science the structure-form engineering will put in the forefront in addition to the impurity engineering. Material becomes not a raw or a pig but it is forming at once as a nano-workpiece. Note that advantage of nanomaterials is hoped to proclaim itself just at developing of nanodevices, the electronic gnat for example, rather than in the large scale industry.

By *peculiarity of the nanoworld* is the cancellation of distinctions between the living and inorganic matter. The exchange of substance being the indication of life manifests itself on the supramolecular level rather than a molecular one. Proteins, membranes, and nuclein acids refer to giant natural nanostructures built in result of self-assembling. The analogy opens a fantastic opportunity for nanomaterials and nanodevices fabrication by such biomimicry. Artificial growth of pearls inside mussels, as well as ordering of non-equilibrium defects into 2D nanostructures on a surface of semiconductors under the ion bombardment and implantation are the examples.

Principal question is “what are the peculiar features inherent to nowadays nano-technology taking into consideration that atomic and molecular physics, chemical synthesis technologies, microelectronics, etc., were existed before NT era?” *The novelty* includes:

– the artificial manipulating by nanoobjects and manual or automatic assembling of the nanodevices designed beforehand using a “bottom-up” approach;

– the deliberate meddling in processes mechanisms with the comprehensive control of a chemical self-assembling at molecular level;
– the invention, design and production of nanodevices of submictometer size followed by their integration into micro-, mezo-, -and macro-systems.

Entering into NT it should be warn of some *illusions and problems*.

Firstly, decrease in particles size *is restricted from below* because it does not always result into improvement of the properties. For instance, the optimal size of disperse inclusions in oxide ceramics ca. ~10–20 μk was shown to exist at which the optimal combination of hardness and durability is achieved.

Secondly, with particles size decrease the processes of *thermal instability* and phase transitions were shown to take place resulting in nondurability of nanosystems. For instance, the well-known words IBM, NANO, and corals drown on substrate by atomic-force microscopy were turn out to be unstable due to fast surface diffusion of building atoms. Since the covalent bonded semiconductors and ceramics preferably appear to be stable and durable, the nanomaterials for NT are thought to be nonmetallic.

Thirdly, a cosmic irradiation and radiation background are capable atoms to knock-out from nanostructures leading in *degradation* of their properties and in worsening of nanodevice operation.

Fourthly, *a thermal noise* and vibrations will be significant circumstances influenced the properties and characteristics of nanodevices. In particular, it limits certainty of probe microscope position, which must never be less then a half-amplitude of thermal vibrations.

Fifthly, even negligible concentration of inherent impurities and *irremovable contamination* enable to destroy the assembling processes, so a super-high-purity feed reagents and clean-room processes are required.

Concluding, all physical discoveries in vacuum have been already made except further discovery of the vacuum itself. Novel discoveries, laws, phenomena, technical decisions, solutions, and inventions will be possibly made only in special designed and assembled artificial nanostructures to be fabricated by future materials science.

Materials science concept is shown in fig. 2 illustrating the inherent interconnection between the composition, structure, properties, technology and applications.

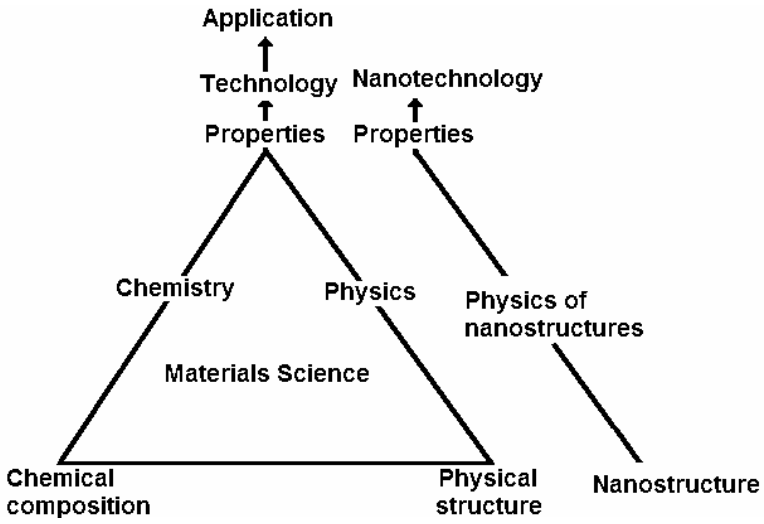

Fig. 2. Fundamental triad of materials science.

Material is not a dull bar, blank, block, pig, but it is the immense word, the Universe, the media in which new physical laws may be discovered. Actually, there are 100 pure natural elements in the Periodical Table on base of which 10,000 XY binary, 1,000,000 XYZ ternary, 100,000,000 quaternary, etc, compounds may theoretically exist accounting the chemical composition. This abundance in many times increases with account of physical structure including nanostructures. However only 500,000 compounds are known presently to exist in modern crystallography database. Hence the abundance of novel undiscovered compounds with new unique properties is very huge forming the challenging frontier of research for future nanotechnology.

At present time we meet NT in child age. The announcement of grand projects, such as biochips and nanobiorobots for medicine, smart dust for space research, etc., have become as motivation for it's intense development, that may influence upon a civilization development. In USA, EC, Japan, Russia and other leading countries the great funds were released for NT projects. The perspectives of NT at the beginning of 21 century looks very optimistic, since a severe reality is capable to darken these somewhat naive prospects. However, in any case the development of NT is unavoidable and it is doomed to success.

The aim of this book is to summarize the fundamentals and technical approaches in processing and behaviour of nanomaterials to provide the readers systematic, comprehensive and brief information in the challenging field of nanomaterials and nano technology. Therefore, this part is a general introduction for students of the physical science and technology, especially students of mechanical engineering and materials science, and for people just entering the field.

2. CLASSIFICATION OF NANOSTRUCTURES

2.1. Gleiter's classification of nanostructured materials

The materials and/or devices sintered by means of the controlled manipulation of their microstructure on the atomic level may be divided into three categories.

The first category comprises materials and/or devices with reduced dimensions and/or dimensionality in the form of isolated, substrate-supported or embedded nanometer-sized particles, thin wires or thin films. The techniques that are most frequently used to produce this type of microstructure are chemical vapor deposition (CVD), physical vapor deposition (PVD), various aerosol techniques, and precipitation from the vapor, supersaturated liquids or solids. Well-known examples of technological applications of materials the properties of which depend on this type of microstructure are catalysts and semiconductor devices utilizing single or multilayer quantum well structures.

The second category comprises materials and/or devices in which the nanometer-sized microstructure is limited to a thin (nanometer-sized) surface region of a bulk material. PVD, CVD, ion implantation and laser beam treatments are the most widely applied procedures to modify the chemical composition and/or atomic structure of solid surfaces on a nanometer scale. Surfaces with enhanced corrosion resistance, hardness, wear resistance or protective coatings are examples taken from today's technology in which the properties of a thin surface layer are improved by means of creating a nanometer-sized microstructure in a thin surface region. For example, patterns in the form of an array of nanometer-sized islands (e.g. quantum dots) connected by thin (nanometer scale) wires. Patterns of this type may be synthesized by lithography, by means of local probes (e.g. the tip of a tunneling microscope, near-field methods, focused electron or ion beams) and/or surface precipitation processes. Such kind of processes and/or devices are expected to play a key role in the production of the next generation of electronic devices such as highly integrated circuits, terabit memories, single electron transistors, quantum computers, etc.

The third category comprises bulk solids with a nanometer-scale microstructure. Those are solids in which the chemical composition, the atomic arrangement and/or the size of the building blocks (e.g. crystallites or atomic/molecular groups) forming the solid varies on a length scale of a few nanometers throughout the bulk.

One of the basic results of the materials science is the insight that most properties of solids depend on the microstructure. A reduction in the spatial dimension, or confinement of particles or quasi-particles in a particular crystallographic direction within a structure generally leads to changes in physical properties of the system in that direction. Hence the another classification of nanostructured materials and systems essentially depends on the number of dimensions which lie within the nanometer range: (a) 3D-systems confined in three dimensions, e.g. structures typically composed of consolidated equiaxed crystallites; (b) 2D-systems confined in two dimensions, e.g. filamentary structures where the length is substantially greater than the cross-sectional dimensions; (c) 1D-systems confined in one dimension, e.g. layered or laminate structures; (d) 0D-zero-dimensional structures, e.g. nano-pores and nano-particles, Fig. 3.

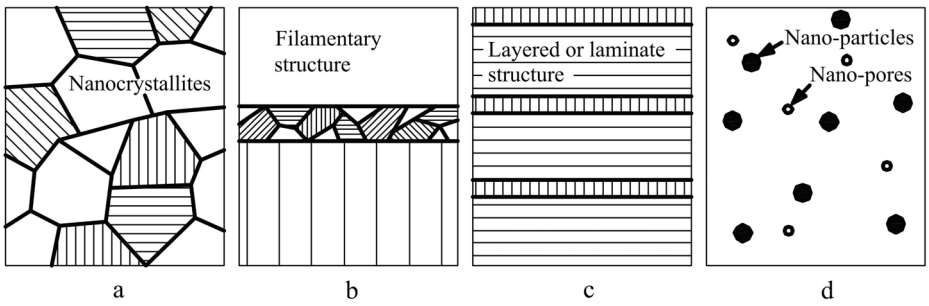

Fig. 3. Schematic classification of nano – materials: (a) three – dimensional structures; (b) two – dimensional; (c) one – dimensional; and (d) zero – dimensional structures.

The most well-known example of the correlation between the atomic structure and the properties of a bulk material is probably the spectacular variation in the hardness of carbon when it transforms from diamond to graphite. Comparable variations have been noted if the atomic structure of a solid deviates far from equilibrium or if its size is reduced to a few interatomic spacing. An example of the latter case is the change in color of CdS crystals if their size is reduced to a few nano-meters.

Three-dimensional structures or bulk materials with a nanometer-sized microstructure are assembled of nanometer-sized building blocks or grains that are mostly crystallites. The schematic model of the nanostructured material is shown in Fig. 4.

These building blocks may differ in their atomic structure, their crystallographic orientation and/or their chemical composition. If the building blocks are crystallites, incoherent or coherent interfaces may be formed between them, depending on the atomic structure, the crystallographic orientation and/or the chemical composition of adjacent crystallites. In other words, materials assembled of nanometer-sized building blocks are microstructurally heterogeneous consisting of the building blocks (e.g. crystallites) and the regions between adjacent building blocks (e.g. grain boundaries). It is this inherently heterogeneous structure on a nanometer scale that is crucial for many of their properties and distinguishes them from glasses, gels, etc. that are microstructurally homogeneous.

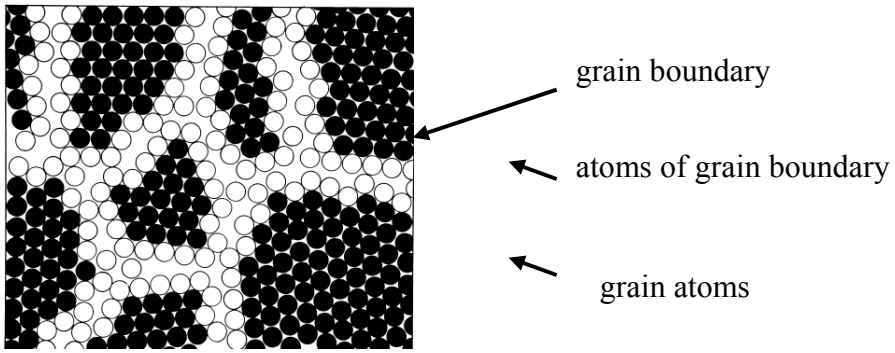

Fig. 4. Schematic model of a nanostructured material (adapted from Gleiter H., Acta Mater., 2000, vol. 48).

Nanostructured materials (NSMs) as a subject of nanotechnology are low-dimensional materials comprising building units of a submicron or nanoscale size at least in one direction and exhibiting size effects. Development of any science needs in classification. First classification scheme of NSMs was proposed by H. Gleiter in 1995 and further was extended by V.Pokropivny and V. Skorokhod in 2005. In recent years the

hundreds of new NSMs and abundance of novel nanostructures (NSs) have been obtained so the need in their classification is ripen.

Crystalline forms and chemical composition was assumed by Gleiter as a basis of a classification scheme of NSMs where both intercrystalline grain boundaries and crystallites were regarded as building blocks (fig. 5). However this scheme seems to be incomplete because of zero- and one-dimensional (0D, 1D) structures such as fullerenes and nanotubes were not considered. Therefore in this scheme there are actually 3 classes and 4 types in each of them rather than 12 classes.

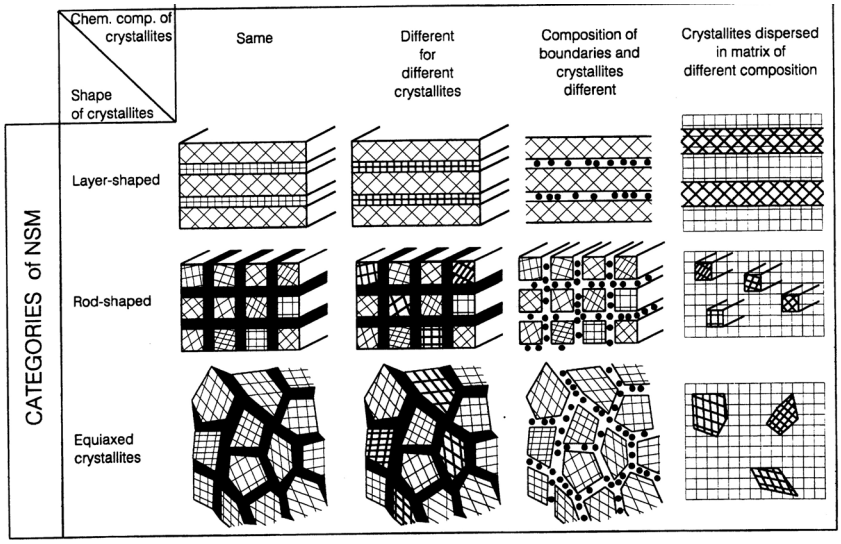

Fig. 5. Gleiter's classification schema for NSM according to their chemical composition and the dimensionality (shape) of the crystallites (structural elements) forming the NSM.

2.2. Classification of nanostructures by dimensionality

Nanostructures (NSs) should be separated from NSMs because the former (NSs) are characterized by a form and dimensionality while the last (NSMs) by a composition in addition. Hence NSs should be classified accurately upon one of these sign, namely, dimensionality, as being the general natural attribute, integrated a size and shape or form. Abundance of forms for bulk 3D materials is infinite. Under transition into nanoworld an atomic difference between some shapes can be neglected regarding these forms as the same due to their low dimension. Hence one can conclude that a number of NS-classes becomes to be finite. This brings up the problem of modern NSs classification.

Under a nanostructure we understand the structure the one size of which d at least is less or equal to a critical one d^*, $d \le d^* \approx 10^2$ nm. The value of d^* have not certain meanings because it is dictated by a critical characteristic of some physical phenomena (free path length of electrons, phonons, length of de Broglie wave, length of external electromagnetic and acoustical waves, correlation length, penetration length, diffusion length, etc.) giving rise to the size effects.

We constitute our classification of NSs on their dimensionality. It may be one of the four, namely, 0D, 1D, 2D or 3D. All NSs can be build from elementary units (blocks) having low dimensionality 0D, 1D, and 2D. The 3D units are excluded because they

can't be used to build low dimensional NSs except 3D matrix. However 3D structures can be considered as NSMs if they involve the 0D, 1D, 2D NSs. This is just the case that Gleiter considered in his classification of NSMs.

Let us introduce the notation of NSs

$$k\mathrm{D}lmn... \qquad (1)$$

where k is a dimensionality of NS as a whole, while the integers l,m,n denotes the dimensionality of the NS's building units of different types. Each integer l,m,n refers to different type unit, so the number of these integers must be equal to the number of the different constituting units. From the definition of NSs the condition leads, namely, $k \geq l,m,n$, and $k,l,m,n = 0,1,2,3$.

It follows from this conditions that restricted number of NSs classes exists, namely, 3 sorts of elementary units (0D, 1D, 2D), 9 single classes of $k\mathrm{D}l$ type built of 1 sort units, 19 binary classes of $k\mathrm{D}lm$ type built of 2 sort units, and variety of ternary, quaternary, etc., classes. Restricting the classification by 5 main ternary structures of $k\mathrm{D}lmn$ type built of 3 sort units, we obtain in the result 3+9+19+5=36 classes of NSs shown in fig. 6.

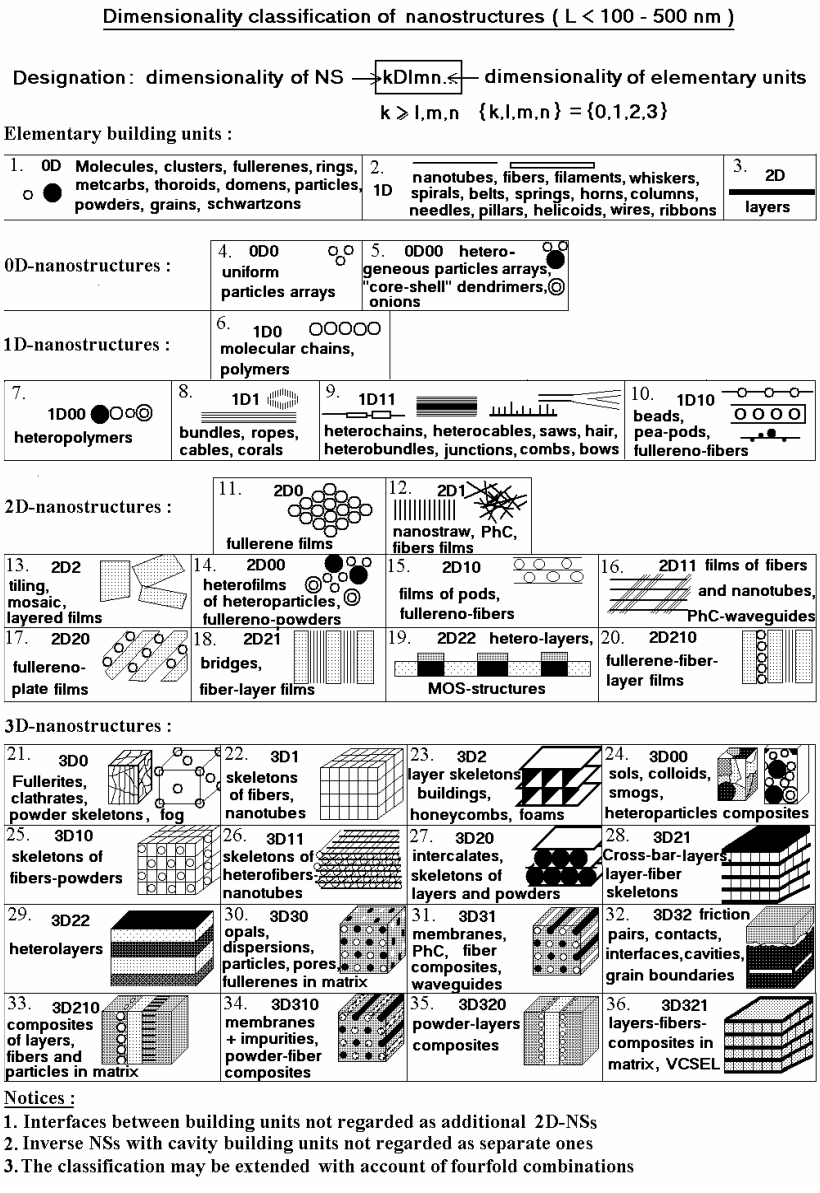

Fig. 6. Dimensionality classification of nanostructures.

All kinds of NSs known in the literature belong to one of these classes. However some of classes still remain to be poor demonstrated although there is the predictive ability of the suggested classification. On this basis the combined classification of NSMs can be further developed with account of the secondry signs, in particular, the type and composition of materials, such as polymers, metals, dielectrics, semiconductors, ceramics (carbides, nitrides, borides, oxides, etc.), cermets, etc.

2.3. Concept of "surface form engineering" in nanomaterial science

Concept of a "grain boundary engineering" is appereant from Gleiter's classification stated that the properties of NSMs strongly depend on the grain boundaries. In a similar manner the new concept of a "surface form engineering" follows from the classification proposed. In this classification the NSs properties strongly depend on free surface shape. It is based on the essential difference between intercrystalline grain boundaries and free surfaces. The boundaries give rise to the inner classical (IC) size effects, such as diffusion enhancement, decrease in melting point, lattice parameter, etc. The surfaces determine the form, shape, dimensionality, and thereby class of NSs. Sharp thin free surface can serve as a mirror for reflection of the electromagnetic, acoustic and de Broglie waves, in contrast to thickened diffusive grain boundaries, that only transmit and scatter these waves. This puts on forefront the indexes of refraction, absorption, and transmission of all the waves as main peculiar characteristics of NSs.

Value of any classification is determined by an ability to predict some general properties. With the aim for any mesh, for each NS-class in our case, the general properties should be related to representative for this NS-class. Then, determining a class of NS, we are capable to predict its general properties. However at the present time the properties of NSs are studied insufficiently with rare exception. In particular, a general dependence of density of electron states (DOS) on the NS-dimensionality is well known, namely, $\rho(E) \sim \sqrt{E}$, $\rho(E) = const$, $\rho(E) \sim \frac{1}{\sqrt{E - E_0}}$, and $\rho(E) \sim \delta(E - E_0)$ for the 3D, 2D, 1D, and 0D nanostructures, respectively. Hence we can predict the general behavior of DOS for each class of NSs combining the DOS of their building units and NS as whole. For instance, the DOS of 2D1 NS-class may predicted to be $\rho(E) \sim const + \frac{1}{\sqrt{E - E_0}}$.

In addition to dimensionality a size of NSs becomes to be the main factor determining their properties. In extreme case of nanoparticle $d << \lambda_{external}$ a size and form have not affect its interaction with external electromagnetic field. In opposite extreme case of bulk 3D material of $d >> \lambda_{internal}$ a size and form have not affect its interaction with internal waves due to their intense scattering and vigorous attenuation.

Only in case of $d \sim \lambda$ the size restriction of NSs leads to quantum confinement and causes the inner quantum (IQ) size effects manifested itself in optical spectra. Electron reflection from NS-surface when electron free path length becomes greater then NS-size, $l_{el} \geq d$, may lead to decrease in electroconductivity, etc. Phonon reflection from NS-surface when the phonon free path length stands out NS-size, $l_{ph} \geq d$, may lead to cut of a long wave phonon spectrum, and to decrease of thermal conductivity, heat

capacity, Debye temperature, hypersound generation, and other IQ size effects. Variety of external size effects, both classical (EC) and quantum (EQ) type, may arise under interaction of NSs with external field, when its wave length becomes to be compatible with NS-size, $\lambda_{em} \approx d$. In this case a condition of total internal reflection or Bragg reflection $d \cdot \sin\theta = n\lambda_{em}/2$ may be fulfilled. For instance, the NSs of 2D11 class such as photonic crystals can act as light waveguide and left-handed media, in which unusual unique phenomena were predicted, namely, negative refraction index, inverse Doppler and Cherenkov effects.

Beside size effects the variety of resonance effects was shown to be possible in NSs, in particular, Aaronov-Bohm, magneto-acoustic, photogalvanic effects, in which NS serves as resonator for acoustic, electronic, elrctromagnetic waves. In special nano-tubular crystals on special sole super-frequency an unique photo-acousto-electronic super-resonance between microwave, hypersound, and matter waves was suggested to be possible. The state can be regarded as novel nanostructured state of matter, in which a lossless repumping and converting of the electromagnetic, acoustic and electronic energies, one to each other, was suggested to be possible.

One can conclude that in accordance with suggested “surface form engineering” a geometry shape becomes to be a principal factor determining the properties of NSMs. In comparison with our 36 classes in fig. 6 there are only 4 classes in Gleiter's scheme in fig. 5 where more then 32 classes are absent, though there are just the new precise classes that belong to new excited field of nanotechnology.

Geometry always plays an exceptional role in physics. Generalizing Einstein principle of general relative theory one can say that “physics is geometry plus physical laws”. This is in Universe. Applied to nanoworld this principle can be reformulated as follows: “nanophysics is geometry of surface and size of NSs plus critical characteristics of physical phenomena in materials". Geometric forms can be designed theoretically in couple with prediction of novel size effects and resonance phenomena.

Excited idea arises of a theoretical design of novel size effects and resonance phenomena combining diversity of NSs-forms with the critical characteristics of materials. Suggesting their meaning is 36 and 10 respectively, one can obtain limited number (360) of the size effects and resonance phenomena. In the result nanoworld one can image as “multi-room (~ 360) house” of size effects and resonance phenomena. Paraphrasing the well known Feynman's aphorism we can say “There are plenty rooms of restricted classes at a bottom".

Hence, the principally new result of the proposed classification is an opportunity of *a priori* prediction and theoretical design of novel NSMs with unique properties. Attention should be focused on engineering of surface forms of NSs in addition to grain boundaries extending paradigm of nanostructured materials science and nanotechnology.

3. PECULIARITIES OF NANOSTRUCTURED MATERIALS

3.1. Introduction

Nanostructured materials (NSM) have their own peculiar characteristic distinguished them from the bulk macroscopic 3D materials.

Relative to microstructural (MSM) metals and alloys, the NSM contain a higher fraction of grain boundary volume (for example, for a grain size of 10 nm, between 14 and 27% of all atoms reside in a region within 0.5–1.0 nm of a grain boundary); therefore, grain boundaries play a significant role in the materials properties. Changes in the grain size result in a high density of incoherent interfaces or other lattice defects such as dislocations, vacancies, etc. As the grain size d of the solid decreases, the proportion of atoms located at or near grain boundaries relative to those within the interior of a crystalline grain, scales as $1/d$. This has important implications for properties in ultra-fine-grained materials which will be principally controlled by interfacial properties rather than those of the bulk.

The misfit between adjacent crystallites in the grain boundaries changes the atomic structure (e.g. the average atomic density, the nearest-neighbor coordination, etc.) of materials. At high defect densities the volume fraction of defects becomes comparable with the volume fraction of the crystalline regions. In fact, this is the case if the crystal diameter becomes comparable with the thickness of the interfaces.

From the courses of physics and mechanics, the role of structural defects in material properties is well established. Vacancies are point defects in the crystalline structure of a solid that may control many physical properties in materials such as conductivity and reactivity. However, nanocrystals are predicted to be essentially vacancy-free; their small size precludes any significant vacancy concentration. This result has important consequences for all thermo mechanical properties and processes (such as creep and precipitation) which are based on the presence and migration of vacancies in the lattice.

Planar defects, such as dislocations, in the crystalline structure of a solid are extremely important in determining the mechanical properties of a material. It is expected that dislocations would have a less dominant role to play in the description of the properties of nanocrystals than in the description of the properties of microcrystals (mc), owing to the dominance of crystal surfaces and interfaces. The free energy of a dislocation is made up of a number of terms: (i) the core energy (within a radius of about three lattice planes from the dislocation core); (ii) the elastic strain energy outside the core and extending to the boundaries of the crystal, and (iii) the free energy arising from the entropy contributions. In mc the first and second terms increase the free energy and are by far the most dominant terms. Hence dislocations, unlike vacancies, do not exist in thermal equilibrium.

In nanocrystals, the elastic strain energy is reduced. The forces on dislocations due to externally applied stresses are reduced by a factor of about three and the inter-active forces between dislocations are reduced by a factor of about 10. Hence re-covery rates and the annealing out of dislocations to free surfaces are expected to be reduced, as well. Dislocations are positioned closer together and dislocations movement in the net is hindered by interaction between them. Together with the reduced elastic strain energy, this fact results in dislocations that are relatively immobile and the imposed stress necessary to deform a material increases with decrease in grain size. Moreover, nano-structures allow alloying of components that are commonly immiscible in the solid and/or molten state. For example, Fig. 4 schematically represents a model of the

nanostructured copper – bismuth (Cu – Bi) alloy. Bismuth atoms are incorporated in the boundaries at sites of enhanced local free volume.

In nanocrystalline alloy of silver – iron (Ag – Fe), there exist a mixture of nanometer-sized Ag and Fe crystals. In the (strained) interfacial regions between Ag and Fe crystals, solid solutions of Fe atoms in Ag crystallites and Ag atoms in the Fe crystallites are formed although both components are immiscible in the liquid as well as in the solid state. Similar effects may occur in the grain boundaries between adjacent Fe and Ag crystals.

From the point of view of physics, size effects are important if the characteristic size of the building blocks of the microstructure is reduced to the point where critical length scales of physical phenomena (e.g. the mean free paths of electrons or phonons, a coherency length, a screening length, etc.) become comparable with the characteristic size of the crystallites.

From basic courses of physics and chemistry, the wave – particle duality of electron, the architecture of atom and the Schrodinger equation, which is the basic non-relativistic wave equation used in one version of quantum mechanics to describe the behavior of a particle in a field of force, are well-known. The Schrodinger equation is used to find the allowed energy levels of quantum mechanical systems (such as atoms, or transistors). The associated wave function gives the probability of finding the particle at a certain position. The solution to this equation is a wave that describes the quantum aspects of a system. Or, in other words, the Schrodinger equation is the representation of the wave function which yields the probability of the physical variables in the terms of expectation values.

It was shown that electron band structure of solids considers the electron waves in a periodic crystalline potential. One of the approaches is to treat the free electrons in metals quantum mechanically and consider their wave-like properties. The free valence electrons are assumed to be constrained within a potential well which essentially stops them from leaving the metal (the ‘particle-in-a-box’ model). The box boundary conditions require the wave functions to vanish at the edges of the crystal (or ‘box’). The allowed wave functions given by the Schrodinger equation then correspond to certain wavelengths. For a one-dimensional box of length L, the permitted wavelengths are $\lambda_n = 2L/n$, where n =1, 2, 3 . . . is the quantum number of the state; the permitted wave vectors $k_n = 2\pi/\lambda$ are given by $k_n = n\pi/L$.

In the free electron model, the energies of the electronic states depend on $1/L^2$ where L is the dimension of the system in that particular direction; the spacing between successive energy levels also varies as $1/L^2$. This behavior is also clear from the description of a solid as a giant molecule: as the number of atoms in the molecule increases, the molecular orbitals gradually move closer together. Thus if the number of atoms in a system, hence the length scale, is substantially different to that in a normal bulk material, the energies and energy separations of the individual electronic states will be very different.

As the system size decreases, the allowed energy bands become substantially narrower than in an infinite solid. The delocalized electronic properties of a solid become severely distorted and the electrons in a reduced-dimensional system tend to behave more like the ‘particle in a box’ description; this is the phenomenon of quantum confinement. In other words, the electronic states are more like those found in localized molecular bonds rather than those in a macroscopic solid.

The main effect of these alterations to the bulk electronic structure is to change the total energy and hence, ignoring entropy considerations and the thermodynamic stability of the reduced length scale system relative to that of a normal bulk crystal. This can have a number of important implications. It may change the most energetically stable

form of a particular material; for example, small nanoparticles or nano-dimensional layers may adopt a different crystal structure from that of the normal bulk material. For example, some metals which normally adopt a hexagonal close-packed atomic arrangement have been reported to adopt a face-centered cubic structure in confined systems such as metallic multi-layers. If a different crystallographic structure is adopted below some particular critical length scale, then this arises from the corresponding change in the electronic density of states, which often results in a reduced total energy for the system.

Reduction of system size may change the chemical reactivity, which will be a function of the structure and occupation of the outermost electronic energy levels. Correspondingly, physical properties such as electrical, thermal, optical and magnetic characteristics, which also depend on the arrangement of the outermost electronic energy levels, may be changed. For example, metallic systems can undergo metal – insulator transitions as the system size decreases, resulting from the formation of a forbidden energy band gap. Other properties such as mechanical strength that, to a first approximation, depends on the change in electronic structure as a function of applied stress, and hence interatomic spacing, may also be affected. Transport properties may also change in that they may now exhibit a quantized rather than continuous behavior, owing to the changing nature and separation of the electron energy levels. Table 1 gives some evidences of materials properties change in dependence on grain size.

Table 1. The properties of MC and NC materials of the same chemical composition.

Material	Structure/Property		Critical Grain Size, nm
	Nano	Conventional	
Y_2O_3	monoclinic	cubic	≈13
ZrO_2	tetragonal	monoclinic	8–26
ZrO_2 (YSZ)	reduced thermal conductivity	regular	24–30
TiO_2	anatase	rutile	50
Cr_2O_3	superparamagnetic	antiferromagnetic	>80
$BaTiO_3$	cubic	tetragonal	120
$BaTiO_3$	variable T_{Curie}	constant T_{Curie}	120
Cu	reduced Young's modulus	regular	<100
Ni	reduced T_{Curie}	regular	<100

3.2. Extended internal surface

First of all the NSMs have very extended inner surface S_f between nanograins in polycrystallites.

Consider for instance a specific area (the area per unit of volume) of internal surface for porous 2D crystal such a membrane. Number of cylindrical pores in volume L^3 is: $n = \frac{L^3}{L \cdot a^2} = \frac{L^2}{a^2} = \left(\frac{L}{a}\right)^2$, the area of one pore is $S_p = \pi dL$, then the specific area is $S_f = \pi dL \cdot \left(\frac{L}{a}\right)^2 = \frac{\pi L^3}{d}\left(\frac{d}{a}\right)^2$. Hence, the smaller a diameter or/and the greater a

packing density of pores the greater the surface area. For instance, for porous Si (PSi) with packing density d/a~1 and $d = 10^{-8}$ m we have $S_f = 300\,\mathrm{m}^2$, that is close to area of football field.

Because of a number of atoms placed at the surface and in the volume of nanoparticle is proportional to $\sim L^2$ and $\sim L^3$ respectivaly, the relative number of the surface atoms is increased with reduction of particle size as $n \sim 1/L$.

Polycrystals, the crystals consisting of bonded nanoparticles, also have extended inner surface as being the surface of grain boundaries between nanoparticles in a sintered powder material or between nanograins in nanometal.

3.3. Increasing of surface energy and tension

Energy is a key physical characteristic because a knowledge of which give us a possibility to calculate a variety of derivative characteristic such as the elastic modula, heat capacity, etc., using thermodynamics approach.

Having the extended surface, the nanocrystals have therefore extended external free surface energy (Gibbs energy):

$$\Delta G_s = \gamma \cdot S_f \tag{2}$$

where γ is a specific surface energy (the energy per surface unit), or a specific work to create the free surface area, or a specific tension.

Let us estimate this value. Physicist is forced to estimate any physical values, i.e., not calculate it exactly (this is a special problems for specialists) but just estimate qualitatively in order of magnitude. Estimate γ by dimensionality approach. Express it in terms of known physical value, close to γ, namely, a sublimation energy as being the energy requested for evaporation of one atom from a surface ΔH_s. For all chemical elements it is varied in the range from 80 kJ/mol for cesium, to 900 kJ/mol for tungsten (1 kJ/mol=0.01036 eV/molecule/atom).

Mol is a mass of matter in grams that contains N_A atoms. It is equal to the number of this element in Periodic Table. The number N_A=6 10^{23}1/mol is Avogadro's number, dividing on which one can transform any experimental macroscopic physical value into the microscopic one and *vice-versa*.

For estimation of γ in accordance with surface dimensionality one need to divide it on any characteristic area. In the physical sense, it is surface area per one atom $S_a \sim 10^{-19}$ m^2. Taking ΔH_s ~ 100 kJ/mol we obtain:

$$\gamma \approx \frac{\Delta H_s}{N_A S_a} \approx \frac{100 kJ/mol}{6 \cdot 10^{23} 1/mol \cdot 10^{-19} m^2} \approx 2 \frac{J}{m^2}$$

For more precise a calculus of interatomic bonds called as pair potential method is requested. Here a key characteristic is the pair potential of interatomic interaction that in general describes the interaction energy between two atoms, molecules, particles in dependence of distance between them $\varphi(r)$ (fig. 7). There are four types of bonds, the metallic, ionic, covalent (chemical), and van-der-Waals (disperse) type. From one side a potential is determined by electronic subsystem so it may be calculated using *ab initio* (quantum first principle) methods or fitted to known characteristics of crystals. From another side a potential gives the possibility for calculation of cohesive bond energy of the crystal and variety of its derived thermophysical characteristic in the result.

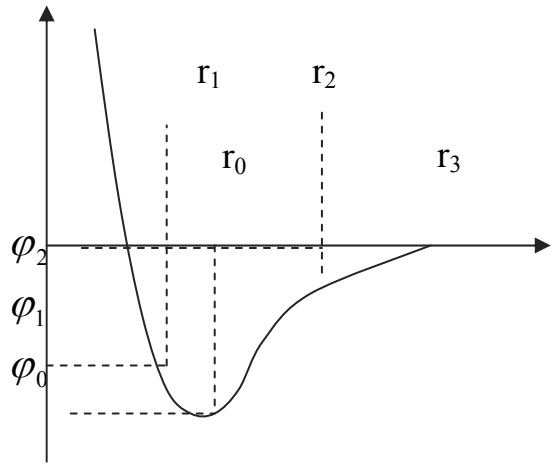

Fig. 7. Scheme of pair interatomic potential

For instance, let us calculate the surface energy of {100} body-centered-cubic (BCC) lattice.

The energy per one atom in the bulk in general case is a sum of pair bonds with neighboring atoms:

$$E_c = \frac{1}{2}\sum_{i=1}^{K} n_i \varphi_i(r) \qquad (3)$$

where n_i is a number of atoms on the K-th coordination sphere. With account of two spheres, K=2, we have

$$E_c = \frac{1}{2}\left[8\varphi(r_1) + 6\varphi(r_2)\right] = 4\varphi_1 + 3\varphi_2$$

The energy per one atom on the surface {100} of BCC lattice is

$$E_s = \frac{1}{2}\left[4\varphi(r_1) + 5\varphi(r_2)\right] = 2\varphi_1 + 2,5\varphi_2$$

Specific surface energy is the difference between the energy of the atom in the bulk and on the surface divided per surface area for one atom:

$$\gamma = \frac{E_c - E_s}{S_a} = \frac{4\varphi_1 + 3\varphi_2 - 2\varphi_1 - 2,5\varphi_2}{a^2} = \frac{2\varphi_1 + 0,5\varphi_2}{a^2}$$

Taking φ_1 = –0,3 eV, φ_2 = –0,2 eV, a = 0,35 nm, $r_2 = a$, we obtain ~ 1 J/m^2. This is typical order of magnitude of the experimentally measured surface energy for metals.

The surface energy causes the surface tension or the surface tangential force F=γa. The tension exist for any surface, including a plane surface.

For nanoparticles of curvature r an additional Laplace tension is arisen P_L=2γ/r. It is responsible for capillary phenomena and wetting of liquids. The Laplace tension for solid particles is considered often as Laplace pressure compressed a particle. For instance, for small r=10 nm liquid nanoparticle, the Laplace pressure is very high P_L=2γ/r=2 J/m2/10nm = 200 MPa, which is comparable with the pressure of gunpowder gas in gun barrel.

3.4. Grain boundaries

Grain boundary (GB) is the junction of two crystalline particles. There are two main types of GBs, namely, the rotation and torsion GBs (fig. 8), which are characterized by the angle θ of rotation or torsion of one grain relative to another. Under rotation at some special angles θ_0 the some number n of lattice sites of one grain may by coincidence with some sites at another grain, forming the coincidence site lattice, that is characterized by the reciprocal density of coincidence sites $\Sigma=1/n$. In the case of ideal matching of similar perfect lattices all the sites coincide, so $n = 1$ and $\Sigma=1$. For twin boundary every third site coincides, so $\Sigma=3$. In the respect of Σ all boundaries are divided into the special boundaries with $\Sigma < 50$, and the general high angle boundaries $\Sigma > 50$ with random disorientation. As a rule in metals the majority of boundaries is of the high angle type with disordered amorphous structure. They are characterized by the relatively large free volume, the great number of dangling or weakened bonds, and the extended GB width of ~1 nm. Therefore, the general GBs have the energy of near half of surface energy and greater than of special one:

$$\gamma_{specialGB} < \gamma_{generalGB} = \frac{1}{2}\gamma_{surface} \approx 0.5\frac{J}{m^2}$$

Special GBs have the smaller energy due to its ordered structure, that is shown in fig. 8.

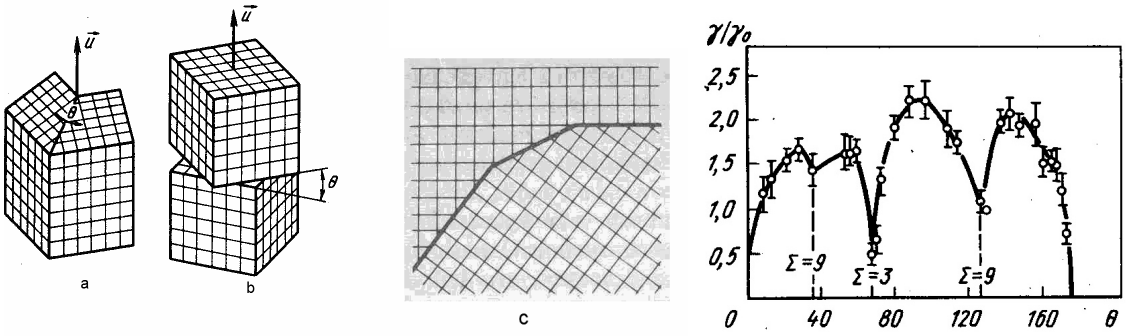

Fig. 8. Three main types of grain boundaries (incident (a), torsion (b), and curved (c) together with the typical dependence of the relative GB energy on disorientation angle for aluminum showing the drop in energies for special GBs.

In general, GBs in NSM have specific structural features, which are responsible for their specific behavior and properties. The structure of GB in NSM in many cases is in non-equilibrium state with high densities of non-periodically arranged GB defects. Non-equilibrium NSMs are inherently heterogeneous on a nano-meter scale consisting of nanometer-sized building blocks separated by boundary regions. The various types of non-equilibrium NSM differ by the characteristic features of their building blocks (e.g. crystallites with different or identical chemical composition, different or identical atomic structure, different or identical shape, size, etc.). However, the size, structure, etc. of the building blocks are not the only microstructural features distinguishing different NC materials. In fact, the boundary regions between them play a similar role. The chemical composition, atomic structure, thickness, etc. of the boundary regions are equally crucial for the properties of NC materials. In other words, even if the building blocks, e.g. the crystallites of two NC materials, have comparable size, chemical

composition, etc., the properties of both materials may deviate significantly if their interfacial structures differ.

One of the technologically attractive features of non-equilibrium NC materials is the fact that their microstructure (and properties) can be manipulated by the mode of fabrication. This allows a wide variety of microstructures to be generated. Method of preparation strongly affects the structure and boundaries behavior of GBs. For example, nanocrystalline nickel (crystal size about 10 nm, density about 94%) prepared by consolidation of Ni powder exhibited little (<3%) ductility whereas nanocrystalline Ni (similar grain size and chemical composition) obtained by means of an electro-deposition process could be deformed extensively (>100%). The major difference noticed between both materials is the energy stored in the interfacial regions suggesting different interfacial structures. The enthalpy stored in nc Pt may be reduced during annealing up to 50% without grain growth (i.e. at constant crystal size and chemical composition). The reduction is presumably caused by atomic rearrangements in the boundary regions. Measurements of other properties of NSMs (e.g. thermal expansion, specifc heat, compressibility) and spectroscopic studies (e.g. by Mossbauer or positron lifetime spectroscopy) indicate structural differences between chemically identical nc materials with comparable crystallite sizes if these materials were prepared by different methods and/or if their previous time – temperature history was different. The non-equilibrium character of nc materials implies that any comparison of experimental observations is meaningful only if the specimens used have comparable crystal size, chemical composition, preparation mode and time – temperature history. Moreover, the non-equilibrium character of nc materials renders them susceptible to structural modifcations by the methods applied to study their structure.

3.5. Instability of 3D0 NSM due to grain growth

Schematically, the structure of NSM can be represented as it is shown in Figure 9. GB consists of several types of extrinsic defects, namely, stationary dislocations with Burgers vectors normal to a boundary plane, gliding or tangential dislocations with Burgers vectors tangential to the boundary plane, and disclinations in triple junctions. Disclinations and grain boundary dislocations form elastically distorted layers (zones) near grain boundaries.

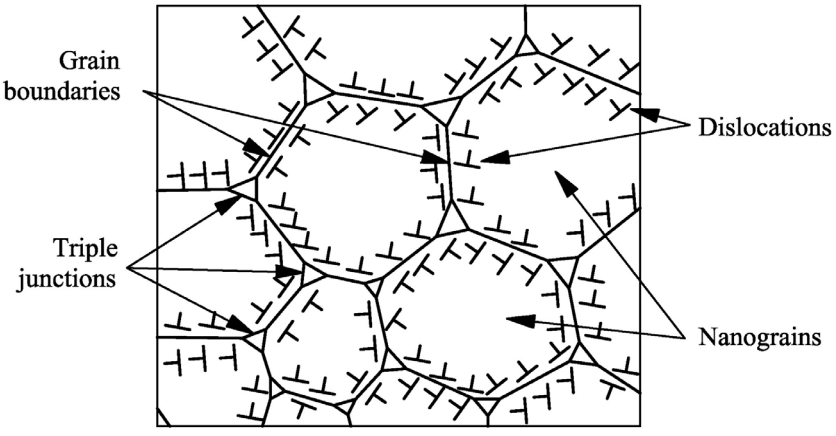

Fig. 9. Schematic representation of a nano–grained structure of 3D0 NSM.

The structural misfit between grains in bulk material locally modifies the atomic structure by reducing the atomic density and by altering the coordination between nearest neighbor atoms relative to perfect crystal. Moreover, the low-temperature atomic structure of the boundaries of NC materials differs from the boundaries structure of polycrystals by a rigid body translation. The deviating rigid body relaxation of boundaries results from the different constraints in both materials: in polycrystalline materials adjacent grains are free to minimize the boundary energy by a translational motion relative to one another (called rigid body relaxation). In nano materials the constraints exerted by the neighboring nanometer – sized crystallites limit the rigid body relaxation and there are many restrictions on the GB arrangement. GBs in NC materials are very short and their length is often does not exceed 100 nm. Nano – sized GBs easily undergo structural transformations related to changes in their length and shape. In particular, the enhanced local migration facilitates grain growth and GB sliding processes.

Grain growth occurs in materials to reduce the overall energy of the system by reducing the total grain boundary energy. Therefore, grain growth in NC materials is primarily driven by the excess energy stored in the grain or interphase boundaries. The boundaries move toward their centers of curvature and the rate of movement varies with the amount of curvature. The earliest theoretical considerations of the kinetics of normal grain growth assume a linear relationship between the rate of grain growth and the inverse grain size, which in turn is proportional to the radius of curvature of the grain boundaries. This assumption yields, under ideal conditions, the following equation for grain growth:

$$d^2 - d_0^2 = kt$$

where d and d_0 are the grain sizes at the beginning of the process and at time, t, respectively. K is a constant that depends on temperature and can be expressed by Arrhenius – type equation:

$$k = k_0 \exp(-Q/RT),$$

where Q is the activation enthalpy for isothermal grain growth, R the molar gas constant and k_0 a constant that is independent of the absolute temperature T. The activation enthalpy, Q, is often used to determine the microscopic mechanism which dominates the grain growth.

In practice the ideal situation is met very rarely. The general form of the expression for grain growth is therefore taken to be as lollowing:

$$r^n - r_0^n = kt$$

Here, r is the average grain radius and n is empirical exponent that strongly depends on temperature.

To prevent grain growth, the grain boundaries mobility should be impeded. This can be readily achieved via the pinning effect of fine pores or second phase inclusions. The total free energy of a segment of boundary intersecting an inclusion is reduced by the product of the cross-section of the inclusion and the specific boundary free energy. Zener relation between the stable grain radius r and the radius r_p and volume fraction f_p of the inclusions shows a critical ratio of f and r above which no grain growgh may occur:

$$r/r_p \approx 3/4f_p$$

This relationship implies that when a fine dispersion of small inclusions can be generated, then small volume fractions of inclusions can stabilize a microstructure with a very fine grain size. In the stable microstructure the location of each boundary corresponds to a local energy minimum, and the material is therefore in a metastable state. When the temperature is increased, grain growth will remain suppressed until the inclusions dissolve in the matrix or until they become mobile.

On the other hand, there is a strong elastic interaction between neighboring nano – sized GBs because the extremely short distances between them are close to the characteristic scales of their stress fields. Interacting dislocations of the GB tends to minimize the elastic energy of GB ensembles in NC materials. The low energy ensembles exhibit a certain structural stability because there is an energy barrier needed to destroy low energy structures. This a bit hampers grain growth and other processes associated with structural transformations of GBs. High density ensembles of triple junctions also contribute to the structural stability of nano materials because they serve as effective drag centers for GB migration and grain growth process.

A second commonly used retarding effect is that of solute drag. In many solid solutions, solute atoms are known to segregate to the boundaries forming a solute cloud in the vicinity of the boundary. Three modes of motion may occur depending on the relative rates of boundary and solute-cloud mobility: (1) if the boundary migrates slowly, it drags a solute cloud along with it, thus reducing the boundary mobility and, hence, grain growth; (2) if the boundary migrates very fast, it breaks away from the solute atoms and moves freely; (3) at intermediate migration rates, the boundary breaks loose locally from its cloud and this impurity-free segment bulges out. In nc materials the first two cases are more likely to occur. As the boundaries of nano structures exhibit higher atom solubility than those of cg materials, solute drag effects may be expected to be even more pronounced. For example, pinning of the GB in nc Ni solid by the Ni_3P precipitates in a crystallized Ni – P amorphous alloy and segregation of Si to grain boundaries in a Ni – Si solid solution have been found to be responsible for preventing grain growth in nc phases. In addition to the kinetic factors discussed so far, energetic effects may also affect the growth rate of the crystallites in nano materials. For instance, it was found that samples with smaller grain sizes have enhanced thermal stabilities, therefore the grain growth temperatures and the activation energy for growth in a nc solids are higher in comparison with coarser grains. This is attributed to the configuration and the energetic state of the interfaces in the nanocrystalline materials.

In general, the solute solubility in the core of grain boundaries differs considerably from the solubility in the interior of the crystals. Therefore, in thermodynamic equilibrium, the grain boundaries are enriched or depleted in solute. This can have two beneficial effects on the stability of the microstructure. The first effect is solute drag. The second one is a reduction of the driving force for grain growth. According to the Gibbs adsorption equation, the grain boundary free energy decreases when solute segregates to the boundary. Experimental evidence shows that the decrease can be substantial, and the theory indicates that in alloy systems with a large atomic size mismatch, the grain boundary free energy may even be reduced to zero.

4. SIZE EFFECTS IN NSM

4.1. Definition and types

When size of particles is reduced from macro to nano-scale a dramatic change in all its properties is observed. Such phenomena are called as *size effects.*

Polycrystal in general one can image as composite material consisting of two phases, namely, the bulk grains and the grain boundary phases. If grain size in polycrystal is reduced a relative part of grain boundary phase is increased that leads to a change in all properties of polycrystal. Such size effects are named as *intrinsic (I) or inherent size effects.* They occurs by oneself under reduction of particle size.

Extrinsic (E) or induced size effects are determined as the phenomena which occur under interaction of reduced particles with the external electric, magnetic, electro-magnetic, acoustic, radiation, thermal, or chemical fields.

In general all size effects may have both a classic and quantum nature so in that accordance they may be classified as *classic (C) and quantum (Q) size effects*.

Hence a variety of all size effects may be divided on four types, namely, IC, IQ, EC, EQ.

By *Gleiter's definition the size effects* arise in microstructures if its size d is reduced up to a critical value d~d* when scale length of physical phenomenon (free path length of electrons, phonons, etc, coherent length, screening length, etc.) becomes to be equal to or compatible with characteristic size (length, thickness, diameter) of building blocks of microstructures. The summary table of different size effects is presented in table 2.

Table 2. Summary table of size effects. Designation of type of size effect: I – inner, E – external, C – classical, Q – quantum.

Property	**Influence of size reduction on properties of nanoparticle**	**Type**
Structural	Decrease or increase of lattice parameter	IC
	Structure transformations	IC
Mechanical	Enhancement of hardness, strength, fracture ductility	IC
	Arise of superplasticity	IC
	Raising of wear resistance	IC
Thermal	Decrease of melting point	IC
	Decrease of phase transition temperatures	IC
	Decrease of melting entropy	IC
	Softening of phonon spectra	IC
Thermo-dynamical	Increase of heat capacity	IC
	Increase of thermal expansion	IC
	Decrease of Debye temperature	IQ
	Stabilization of high temperature phases	IC
Kinetic	Increase of diffusion coefficient	IC
	Sharp drop of thermal conductance under some critical size d*	IQ
	Oscillation of kinetic coefficients	IQ
Electrical	Increase of conductivity for nanometals	IQ
	Arise of conductivity for nanodielectrics	IQ
	Increase of dielectric inductivity for ferroelectrics at d*	EC
Electronic	Increase of band gap	IQ
	Arise of phonon generation	IQ
	Raising of conductivity under low temperatures in semimetallic Bi	IQ

Property	Influence of size reduction on properties of nanoparticle	Type
Magnetic	Increase or decrease of coercive force at d*	IQ
	Decrease of Curie temperature	IQ
	Rice of paramegnetism in ferromagnetics at some d*	EQ
	Rice of gaint magnetoresistance	EQ
	Rise of maximal temperature of magnetoresistance	EQ
	Increase of magnetic permeability in ferromagnetics at d*	EC
Optical	Diffraction and interference	EC
	Increase of absorption in ultraviolet range (blue shift)	IQ
	Oscillation of optical absorption	EQ
	Arise of nonlinear optical properties	EQ
Chemical	Increase of catalytic activity	IC
	Increase of velocity of physico-chemical interactions	IC
	Swap of solubility	IC

4.2. Internal classic (IC) size effects

4.2.1. Reduction of lattice parameter

Laplace tension P_L for nanoparticle is so big that can cause a bulk compression that in turn reduces a lattice parameter on the Δa value shown in fig. 10a. It may be estimated from the rule of proportionality:

$$\frac{\Delta a}{a} = \frac{P_L}{K_T},$$

where $K_T \approx 10^{11}$ Pa is a compressibility modulus, therefore $\frac{\Delta a}{a} = \frac{200 \cdot 10^6 Pa}{10^{11} Pa} = 2 \cdot 10^{-3}$.

The value is small but it is able to cause phase transitions under some conditions. For example, the inclusions of Y_2O_3 in oxide ZrO_2 change its structure from monoclinic into triclinic.

For some alloys the reversible effect is arisen, e.g. the increasing of lattice parameter in nanoparticles. That means that sign of the effect depends not only Laplace pressure but on a change of interatomic potential and forces under transition from a bulk to surface.

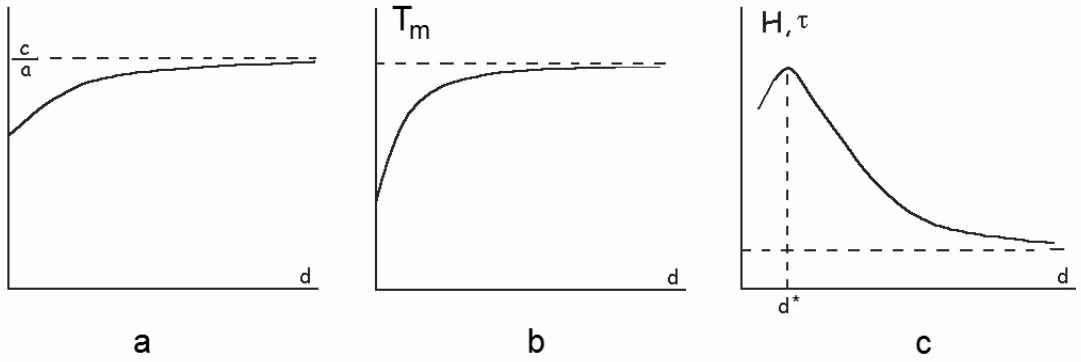

Fig. 10. Dependence of lattice parameter (a), melting temperature (b) and hardness (c) on size of crystalline particle.

4.2.2. Decrease in melting point

Fig. 10b illustrates the general experimental dependence of a melting point T_m on the nanoparticle size d showing a decrease in T_m with d reduction. Its physical origin is the increase of surface energy, the increase of amplitude of atomic vibrations, and the additional surface growth of thermal vibration energy in the result. This effect may be estimated from the dimensionality of related physical values using the simple Thompson's relation:

$$T_m(d) = T_m \exp\left(-\frac{P_L \cdot V_a}{Q}\right) = T_m\left(1 - \frac{2\gamma V_a}{dQ}\right) \qquad (4)$$

where Q is the fusion heat.

For instance, for the bulk silver T_m= 960^{0}C, $\gamma = 0{,}9$ J/m^2, $V_a = 4\pi r_a^3/3 = 13{,}5\cdot 10^{-30}$ m^3, Q = 11,3 kJ/mol, then for nanoparticle of d= 10nm in size from (4) one can obtain T_m = 835^{0}C, i.e. the drop on 87%.

4.2.3. Decreasing of thermal conductivity

In the gas kinetic theory, the relation for thermal conductivity is known:

$$K = \frac{1}{3} Cvl \qquad (5)$$

where v is a particle velocity, l is a free path length, $C = cn$ is a heat capacity of unit volume, c is a heat capacity of single particle, n is a number of particles.

One can apply this simple model for thermal phonons gas in metal regarding the free path length is the free phonon path, l=l_{phonon}. For bulk solid of big size $d > l_{phonon}$, the size effect do not arise. However under reducing of the size d it can become smaller than free path length $d < l_{phonon}$, resulting to a cut of phonon spectra and decreasing of K. In particular for a quarts particle of 10 nm in size at zero temperature T=0^{0}C the size effect is not pronounced. However at T=-190^{0}C, the l_{phonon} is increased from 4 nm to 54 nm, therefore K is decreased in $\frac{K}{K_0} = \frac{Cl}{C_0 l_0} = \frac{50nm}{54nm} = 0{,}2$ time, in spite of decrease of heat capacity from 2 to 0.55 J/cm^3 K.

This phenomenon is used in industry of heat resistance materials, in particular, for fabrication of the heat resistance coating of turbine blades. Refractory corrosion resisted zirconium dioxide ZrO_2 is used as a base material due to its natural very low heat conductivity, K = 2 W/cm K. By doping and heat treating at high temperatures the particular phase transition from monoclinic to triclinic structure is forced. The mixed two phase structure with the triclinic nanoparticles of d = 20 – 30 nm in size is created and stabilized. In the result, because of $d < l_{phonon}$, the heat conductivity is increased in several times in couple with the increasing of the strength, heat resistance, fracture ductility, and coating adhesion for refractory Ni-based alloy of turbine blade.

4.2.4. Diffusion enhancement

In polycrystalline nanometal a significant part of atoms is placed at the internal grain boundaries, intercrystalline, interphase interfaces. Many experiments demonstrates the enhancement of GB diffusion in comparison with the bulk diffusion. Really, in atomic diffusion theory a diffusion coefficient is equal to:

$$D \approx k\Delta^2 z \nu_i e^{-\frac{Q}{kT}} = D_0 e^{-\frac{Q}{kT}},$$

where κ is a geometrical coefficient, Δ is a jump length in nearest-neighbor site, (for BCC lattice $\Delta = \frac{a\sqrt{3}}{2}$), $\nu_i = \frac{1}{2\pi}\sqrt{\frac{\alpha}{m}}$ is an oscillation frequency, z is a number of neighboring atoms, Q is an activation energy.

Hence a relative increasing of GB diffusion coefficient is in general

$$\frac{D_{GB}}{D_0} = \frac{K_{ГЗ}\Delta_{ГЗ}{}^2 Z_{ГЗ}\Gamma_i e^{-Q_{ГЗ}/kT}}{K_0\Delta_0{}^2 Z_0\Gamma_i e^{-Q_0/kT}} \approx \frac{1}{3} e^{-\frac{(Q_{ГЗ}-Q_0)}{kT}}$$

In case of bulk copper $D_0 = 10^{-5}$ m^2/c, Q = 104 kJ/mol, $D_0 = 1{,}7\cdot10^{-19}$ m^2/c. Increased free volume of GB enhances the jump amplitude Δ and decreases activation energy Q. Therefore, for nanostructured copper the diffusion is enhanced in $\frac{D_{GB}}{D_0} \approx 10^2$ times.

4.2.5. Increasing of plastic yield strength and hardness of polycrystal

In physics of strength the Hall-Petch relation is well known of which accordance a hardness and yield strength are increased under the reduction of the grain size d of polycrystal:

$$\tau_{П} = \tau_0 + \frac{K_1}{\sqrt{d}} \qquad (6),$$

where τ_0 deformation strength of monocrystal is, τ_P is a strength of polycrystal, K_1 is a coefficient of fracture ductility. The dependence is shown in fig. 10c and successfully used in the industry.

However in extreme case $d \to 0$ this relation do not works. The critical size $d = d*$ exists when τ approaches its maximal value $\tau = \tau*$ and then drops again. The reason is disappearance of dislocation, the carriers of plastic deformation, due to nanoparticle size becomes to be smaller than a dislocation length, $d < l_{dislocation}$, because of which all dislocations come to a surface.

4.3. External classic (EC) size effects at interaction of light with matter

In electrodynamics of continuous media, a matter is characterized by two fundamental values, namely, the dielectric permittivity ε and the magnetic permeability μ.

Reminder the general relations of the theory (in SI units).

The vector of the dielectric polarization is $\vec{P} = \alpha\vec{E}$, where α is a polarizability of matter, or the dielectric susceptibility.

The vector of the electric induction or dielectric displacement is

$$\vec{D} = \varepsilon\vec{E} = \vec{E} + 4\pi\vec{P} = \vec{E}(1 + 4\pi\alpha);\ \varepsilon = 1 + 4\pi\alpha;\ \alpha = \frac{\varepsilon - 1}{4\pi} \qquad (7)$$

The vector of the magnetic induction is $\vec{B} = \mu\vec{H}$.

With account of magnetization vector $\vec{M} = \chi\vec{H}$, where χ is the magnetic susceptibility, one can obtain

$$\vec{B} = \vec{H} + 4\pi\vec{M} = (1 + 4\pi\chi)\vec{H};\ \mu = 1 + 4\pi\chi;\ \chi = \frac{\mu - 1}{4\pi} \qquad (8)$$

In general case $\varepsilon > 1, \alpha > 0$, $\mu > 0$, while χ is arbitrary.

Difference between the dielectric and magnetic permittivity and susceptibility originates from the fundamental distinction of sources of the magnetic and electric fields. By source of electric field is a Coulomb charge, while of magnetic field is a moving of charges, because of a magnetic charge known as “Dirac monopol” is absent in nature. Huge but unsuccessful efforts were expended to find Dirac monopol in nature and in cosmic rays. However the existence of Dirac monopol do not contradicts to Maxwell equations so they may be reformulated with its account, regarding a spin as Dirac monopol. This intrigue challenge of modern physics is opened for very keen students.

In anisotropic media the constants transform in tensors

$$D_i = D_{oi} + \varepsilon_{ik}E_k,\ \ B_i = \mu_{ik}H_k$$

where ε_{ik} is a dielectric symmetric tensor $\varepsilon_{ik} = \varepsilon_{ki}$, and $\mu_{ik} = \mu_{ki}$ is a magnetic symmetric tensor of permeability.

Absolute majority of substances is nonmagnetic so $\chi << \alpha$, and $\mu = 1$. The reason is that magnetization is solely a quantum phenomenon, the relativistic effect of second order of electron velocity in atom υ / c.

The size effects arise in nanostructures interacting with the external electro-magnetic field when their characteristic size is comparable with wave lehgth $d \sim \lambda$.

For extremely small nanoparticles the case arise of the quasi-stationary field, or the case of great wavelength $d << \lambda$, or the case of small frequencies $\omega << \frac{c}{d}$, accounting $\lambda = \frac{c}{\omega}$. In this case the Maxwell equations are simplified. Magnetic field induces a Fuco current and penetrates in a conductor at *the depth of the skin layer*,

$$\lambda_F << \delta \approx \frac{c}{\sqrt{\omega\sigma}}, \tag{9}$$

where λ_F is a free path length of electron at Fermi level.
To study size effects a comparison is requested of δ with d, and δ with λ.

If $\lambda_F << d$ the internal (I) size effects arises.

If $\delta << d$ the external (E) size effects arises, where parameters ε and μ, or α and χ, are assumed to be constants independent on volume. They depend on the particle shape and orientation in external field.

Consider for instance a magnetic polarization of an isotropic conductive cylinder of radius *a* in a uniform periodic field normal to cylinder axis. General solution is

$$\chi = -\frac{1}{2\pi}\left[1 - \frac{2}{ak}\frac{J_1(ka)}{J_o(ka)}\right]$$

where J_0, J_1 are the Bessel functions,

In the case of thin nanocylinder, $a << \delta$, the solution takes a form:

$$\chi' = -\frac{1}{24a}\left(\frac{a}{\delta}\right)^4 = -\frac{\pi a^4\sigma^2\omega^2}{6c^4}, \quad \chi'' = \frac{1}{8\pi}\left(\frac{a}{\delta}\right)^2 = \frac{a^2\sigma\omega}{4c^2}$$

while in the case of thick $a >> \delta$ cylinder:

$$\chi' = -\frac{1}{2\pi}\left(1 - \frac{\delta}{a}\right) = -\frac{1}{2\pi}\left(1 - \frac{c}{a\sqrt{2\pi\sigma\omega}}\right), \quad \chi'' = \frac{\delta}{2\pi a} = \frac{c}{2\pi a\sqrt{2\pi\sigma\omega}}$$

where χ' and χ'' are the real and imagine parts of magnetic susceptibility respectivaly describing a $\chi(d)$ dependence. It is one of the examples of the EC size effects in electrodynamics.

Intrinsic size effects have been studied very rarely because of young age of nanoscience. This is a challenge of our time, a challenge of nanophysics. There are a lot of research topics and objectives to investigate for students, postgraduates, and researches.

4.4. Intrinsic quantum (IQ) size effects

4.4.1. Transformation of absorption spectra of sodium from atom to solid

Variety of processes induced by light occurs during interaction of matter with electromagnetic field, in particular, the excitation of electrons, ionization and defragmentation of atoms, dissociation of molecules, disintegration of clusters, luminescence of solids, etc. In fig. 11, a transformation of sodium absorption spectra under transition from atom to cluster and further to solid is shown.

Physicist should understand how read spectra as the mathematic formula. Absorption (fluorescence) spectrum of Na atom (fig. 10,a) relates to the transition $^2S_{1/2} - {}^2P_{3/2}$, it is a

double pick l={589.0 nm, 589.6 nm}. The spectrum of Na_3 cluster (fig. 11,b) expands into the discrete molecular spectrum reflecting electron excitations and atom oscillations. Continuous spectrum of Na_8 cluster (fig. 11,c) reflects the processes of dissociations and defragmentation of cluster on atoms. Spectrum of nanoparticle (fig. 11d) reflects resonance absorption of cluster atoms. Spectrum of massive film (fig. 11,e) reflects the interband transitions of electrons in metal.

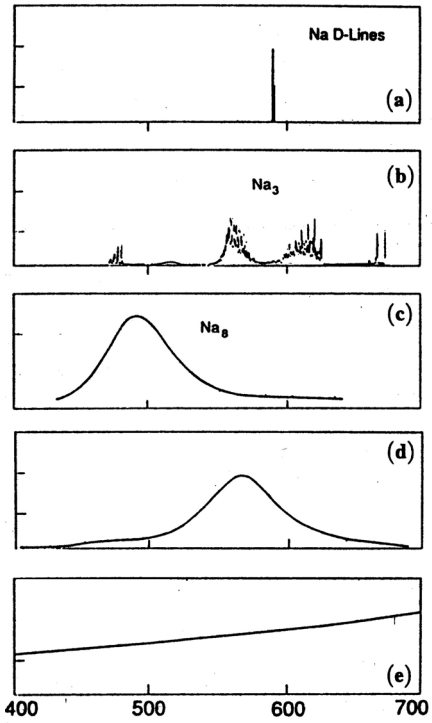

Fig. 11. Optical absorption spectra of sodium (in arbitrary units): a) for atom, b) for cluster Na_3, c) for cluster Na_8, d) for nanoparticle of d<10 nm size (~10^6 atoms) in NaCl crystal, e) for thin film of d=10 nm width.

4.4.2. Blue shift – the increasing of band gap and luminescence frequency

Fig. 12 shows the transformation of a luminescence spectrum of ZnO under conversion to nanostructured state. A blue shift of luminescence spectrum under a reduction of the particle (grain) size is seen.

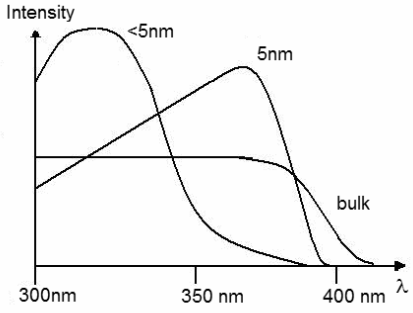

Fig. 12. Luminescence spectrum of ZnO for different particles size.

4.4.3. Broadening of energetic bands

What is responsible for the blue shift? Gleiter explains it as follows. Blue shift phenomenon is a quantum size effect. If grain size is comparable with electron de-Broighle wave generated by absorbed phonons, a quantum confinement increases absorption energy and frequency of luminescence in result. However, it is unclear in what a manner.

We explain this phenomenon simpler and physically clear. All genial is simple. Noble price fellow Peter Kapitsa at King Physical Society said: "...Ukrainian philosopher Gregory Skovoroda wrote: We should be thankful to God who created a nature in such a manner that all the simple is true, but all the intricate is false".

Optical properties are connected with electronic structure, a change in zone structure leads to a change in absorption and luminescence spectra.

Nanoparticles are intermediate in size between atom and solid. Their electronic spectra follow in the same manner. Consider the change of a zone structure of solid under decreasing of its size to nanoparticle and atom (fig. 13).

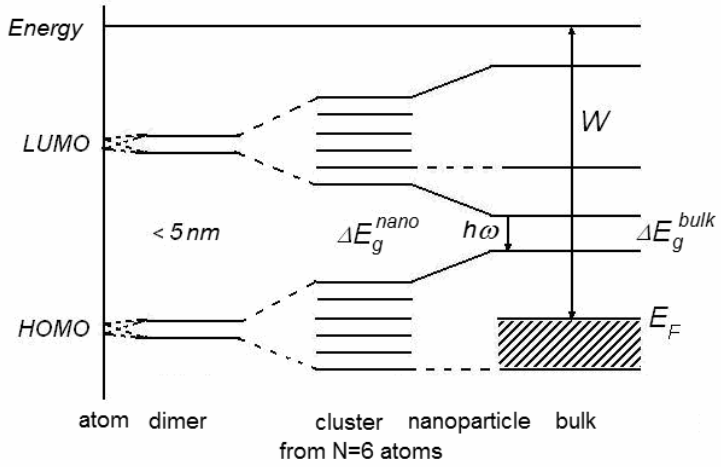

Fig. 13. Transformation of zone structure of a solid under reduction of its size from macro- to nano-scale down to a single atom, showing the increase of the band gap ΔE_g and the blue shift $\hbar\omega = \Delta E_g$ for nanoparticles and nanostructured state of matter. Here W is a work function, E_F is a Fermi energy, HOMO is the highest occupied molecular orbital, LUMO is the lowest unoccupied molecular orbital.

Electronic spectra of atoms are known to be the discrete spectrum of energy levels E_n. In accordance with Pauli principle two or more electrons cannot occupy the same place or take the same energy. Therefore the energy levels are splitten to some small value Δ_n, forming an energetic band, a width of which is proportional to a number of the levels or atoms N, $\Delta E_g^0 = \Sigma\Delta_n = N\Delta_n$. It means that the band gap increases simultaneously when reducing the size of particle, hence $\Delta E_g^{nano} > \Delta E_g^{bulk}$. From fig. 13 is seen that the luminescence frequency is proportional to ΔE_g due to $\Delta E_g = \hbar\omega$. Hence for nanoparticles the luminescence frequency is increased $\omega^n > \omega^0$, that in physical sense is just the blue shift.

Consider the example of porous silicon (PSi). In 1990 Lay Canham from DERA, UK, has discovered photoluminiscence in PSi under ultraviolet excitation, and then in

1992 electroluminescence in PSi has been discovered. As in the case of ZnO under increase of pore diameter, the blue shift was found to occur in PSi.

4.4.4. Phase transitions in ferromagnetic and ferroelectrics

Ferromagnetic is a permanent magnet, a magnetic moment of which is caused by a sum of magnetic moments of atoms or magnetized domains of d* size. Ferromagnetism is solely a quantum phenomenon. A size of the domain is determined by a number of magnetic ordered atoms, depending on both an exchange-correlation interaction of localized or free itinerant electrons and the interaction of atomic magnetic moments. Hysteresis loop between magnetization and magnetic field is the key peculiarity of ferromagnetic.

Ferroelectrics are their electric analogs, a polarization vector of which is determined by a sum of polarization vectors of single atoms and electric domains. Ferroelectricity is defined as physical phenomena in which a spontaneous electric dipole moment can be reoriented from one crystallographic direction to another by an applied electric field. Hysteresis loop between polarization and electric field is the key peculiarity of ferroelectrics. Most useful ferroelectric possess high dielectric constants and follow Curie-Weiss behavior near the Curie point where the materials transforms from the ferroelectric state to a high-temperature paraelectric state. *All ferroelectrics are also piezoelectric, pyroelectric, and electrooptic*. It is these five phenomena, *dielectric hysteresis, electric permittivity, piezoelectricity, pyroelectricity, and electro-optic behavior*, that makes ferroelectric materials useful for applications. High permittivity is used in capacitors, piezoelectricity in electromechanical transducers, pyroelectricity in infrared imaging system, electro-optics in photonic communications, and dielectric hysteresis in nonvolatile memories.

Barium titanate $BaTiO_3$ is the most practically important ferroelectrics. In fig. 14 its perovskite structure and vibration modes responsible for light absorption are shown. Uncompensated vibrations of TiO_6 octahedrons with respect to Ba sublattice leads to a tetragonal distortion, a loss of inverse point symmetry, and the appearance of the polarization vector in the result.

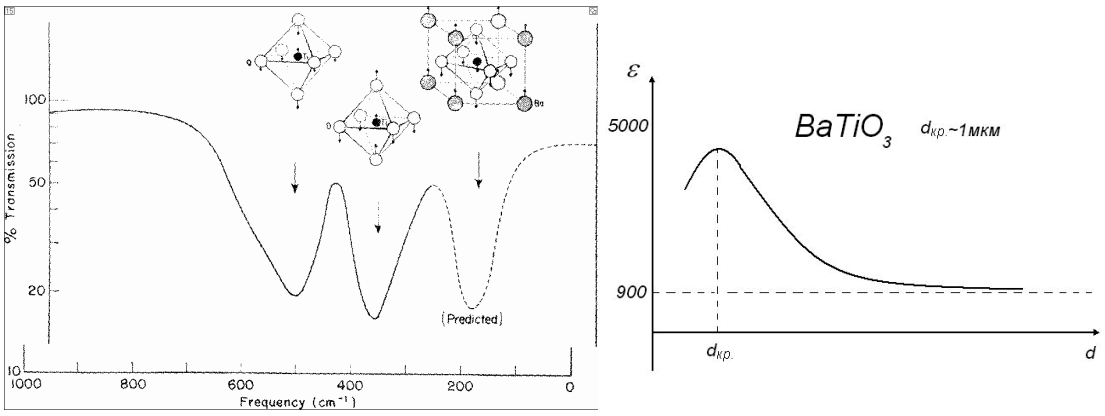

Fig. 14. Transmission spectrum and vibration modes in the perovskite structure of the ferroelectric, responsible for the light absorption.

Fig. 15. Dependence of dielectric permittivity of barium-titanate ceramics $BaTiO_3$ on size of nanoparticles.

Phase transformations under transition from solid to nanostructured state is illustrated in fig. 16.

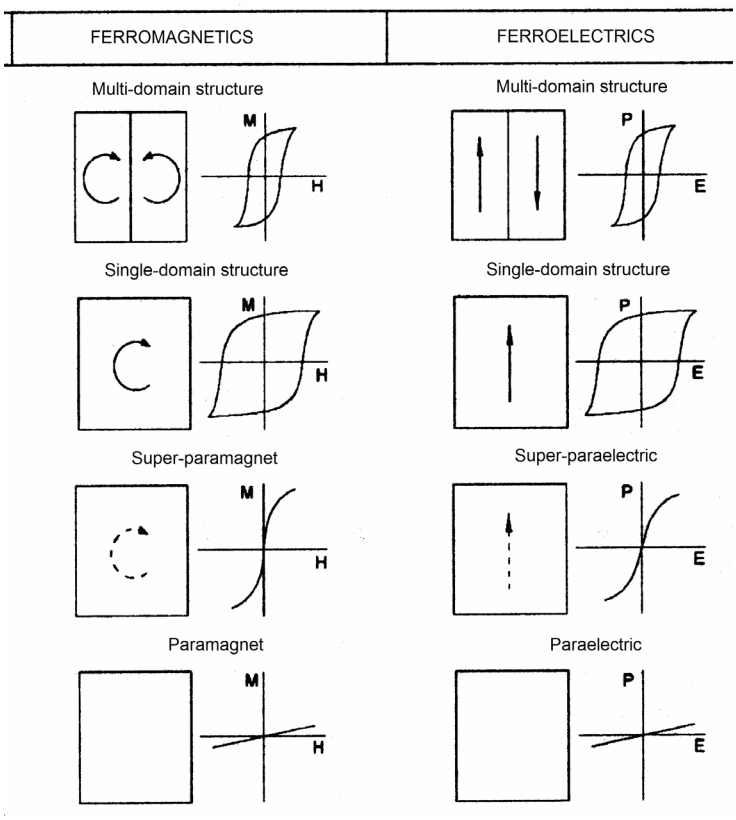

Fig. 16. Change of magnetization energy with decreasing of particle size and related phase transitions from ferromagnetic to paramagnetic state.

Under decreasing of size of polycrystal the size of single domain is constant or weakly changes, so the number of domains is decreased at first stage of the size decreasing, that result in decrease of total magnetic moment. At d=d* (~100 nm), the total moment of polycrystal decreases to a moment of single domain. The hysteresis approaches maximum due to strong interaction of spins within the single domain. Further decreasing of domain size, when a nanoparticle size becomes smaller than a spin wave length $d < \lambda_{spin}$, causes a decrease of the number of atomic magnetic moments, their correlation energy is decreased and at some critical value (d*~10 nm) it becomes to be smaller than induced magnetic moment of single atom. From this size all magnetic properties of nanoparticle with $d < d*$ depends on the induced magnetic moment of single atom, meaning a phase transition in a paramagnetic state, or on magnetic moments of unlocalized itinerant electrons, meaning a phase transition in diamagnetic state.

Such increasing of dielectric permittivity of ferroelectric barium titanate $BaTiO_3$ under transition into nanocrystalline state is shown in the fig. 15. This effect is widely used in ceramic industry for increase of electric capacity of electrocapacitors.

4.5. Extrinsic quantum (EQ) size effects in semimetallic bismuth Bi

Consider another class of materials, the semimetals, characterized by very small band gap, close to thermal energy ~0.01 eV, that is a reason of its temperature dependent properties.

Bismuth is semimetal with unique properties due to its inherent classic and quantum size effects. It serves as a typical model material for investigation of semimetals. Electronic properties of Bi are very distinguished from typical metals. Fermi surface of Bi is very complicated and anisotropic, having extended electronic and hole pockets. Hence the effective electron mass is very small and the Fermi wave length (de-Broighle wave length of electron at Fermi level) is very big

$$\lambda_F = h/m^* v_F \sim 40 \text{ nm} \qquad (10)$$

that overcomes this value for metals on two orders of magnitude.

Free electron path length l_{el} in Bi is extremely large, $l_{el} > 1$ mm at T=4.2 K, that is two order of magnitude greater than for metals due to small electron concentration in semimetal and a resultant small electron scattering.

This great l_{el} leads to the classical size effects while a great λ_F leads to the quantum size effects.

Bulk bismuth has nonlinear current-voltage dependence. Under some critical voltage U_c, the energy of electrons overcomes the band gap, hence the electron concentration in conductive band is sharply raised in couple with current. (fig. 17a)

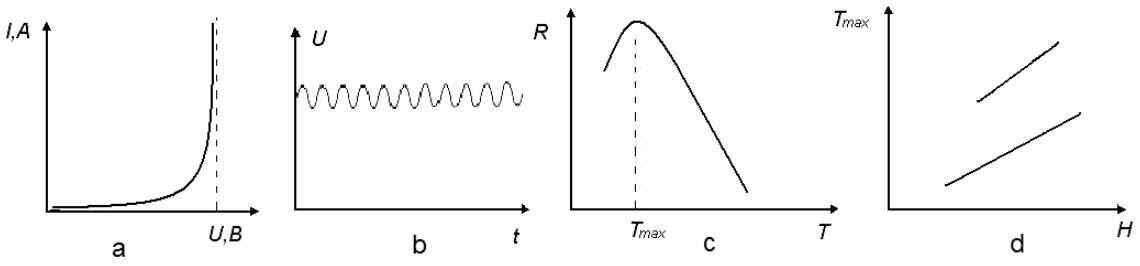

Fig. 17 a) Current-voltage curve for semimetal bismuth; b) EQ size effect in Bi – the generation of phonons caused by interaction with electrons, accelerated in external electric field; c) EQ size effect in Bi nanowire – drop of resistance R at $T=T_{max}$; d) EQ size effect in the nanocrystalline bismuth Bi – growth of T_{max} of magnetoresistance.

Intrinsic classic (IC) size effect manifest itself in change of this U(I) dependence when reducing of a particle size.

Intrinsic quantum (IQ) size effect arises when a size of particle becomes to be compatible with a phonon free path length

$$l_{ph} > d$$

In the case, phonons are reflected from walls of nanoparticle leading to *cut of the phonon spectra* and *the drop of thermal conductance*.

Consider *the extrinsic quantum* (EQ) size effect in Bi, namely, *the phonon generation in a strong electric field*, (fig. 17b), that is explained as follows. Velocity of

current carries is known to increase with electric field voltage U, namely, $v_F \sim U$. Under some critical value of the voltage U_c the velocity approaches its maximum and then overcomes the sound velocity of phonons

$$v_F > v_s$$

In this case a strong electron-phonon interaction is raised as well as strong scattering of electrons on phonons. The surplus electron energy expends on the generation of phonons creating a phonon flow in a direction of electron drift. This phonon effect known as *Esaki effect* reminder the Cherenkov effect for photons.

The wave length of this natural acoustic vibrations is determined by a crystal length, when in accordance with the Fabry-Perrout resonator theory, this length is equal to the integer number of half-waves, $n\lambda_{ph}/2=d$. For nanoparticle of 10 nm in size the frequency of main oscillation mode is $\nu = v_s/\lambda_{ph}$ = 3 km/sec / 2 10 μk = 1.5 GHz. Decreasing of the film thickness or wire diameter one can increase the frequency of ultrasonic and hypersonic waves.

Consider another quantum size effects that manifest itself in *the anomalous temperature dependence of resistance* of the Bi nanowires (fig. 17c). For the conventional metals the electroresistance growths with growth of temperature, $\rho=\rho_0+\alpha\Delta T$, where α is positive coefficient of thermoresistance. The reason is a decrease of velocity of electrons due to its scattering on ion lattice.

In the bulk bismuth this coefficient is known to be negative because of the temperature growth and small band gap. Then the condition arise $\kappa T > \Delta_g$, resulting in the growth of both the concentration of electrons in a conductive band and the electron current, as well as in a drop of a total resistance, leading to the nonlinear current-voltage curve in bulk Bi shown in fig. 17a.

In the nanocrystalline Bi, in nanowires, nanolayers, the de-Broighl wavelength of electrons is restricted by small size of these nanostructures

$$d \sim \lambda_F \sim 40 \text{ nm}$$

In the result the quantum confinement is arisen. Electrons occupy narrow bands and do not scatter on phonons because of its low thermal energy is smaller than interlevel energy, $kT < \Delta E_i$, the electron mobility growths, the current growths, the resistance drops at some temperature $T=T_{max}$ (fig. 17c). This is another extrinsic quantum (EQ) effect.

Extrinsic quantum (EQ) size effect arises in a magnetic field B because of the electrons move at cyclotron orbits of $R_c=m^*v_F/|e|B$ in radius. In a bulk solid, where $d > R_c$, this leads to additional decrease of electron-phonon scattering and magnetoresistance in the result. In nanostructures (nanowires, nanofilms), where $R_c > d$, electrons are scattered on walls resulted to increase of magnetoresistance. This leads to increasing of T_{max} (fig. 17d).

5. TECHNIQUES FOR SYNTHESIS AND CONSOLIDATION OF NSM

There are two general approaches to the synthesis of nanomaterials and the fabrication of nanostructures: one is *the bottom-up approach*, that is the miniaturization of the components, as articulated by Feynman in his famous lecture in 1959 stated that "there is plenty of room at the bottom"; and *the top-down approach* of *the self-assembly* of molecular components, where each nanostructured component becomes part of a superstructure. Attrition or milling is a typical top-down method in making nanoparticles, whereas the colloidal dispersion is a good example of bottom-up approach in the synthesis of nanoparticles. Bottom-up, or self-assembly, approaches to nanofabrication use chemical or physical forces operating at the nanoscale to assemble basic units into larger structures. Bottom-up approaches seek to have smaller components arrange themselves into more complex assemblies, while top-down approaches seek to create nanoscale devices by using larger, externally-controlled ones to direct their assembly. Lithography may be considered as a hybrid approach, since the growth of thin films is bottom-up whereas etching is top-down, while nanolithography and nanomanipulation are commonly a bottom-up approach.

The purpose of this chapter is to introduce the methods of the production of ultra-fine particles, which form the building blocks of nanostructured materials. Most of the time, nanoparticles are embedded into a matrix to obtain desirable properties of material, or nanoparticles themselves are processed into a film or a coating.

Nanoparticles can be synthesized in many different ways, both in chemical reactions and physical processes. Most common methods used for the commercial or industrial manufacture of nanoparticles may be divided into four main groups:

- Gas phase processes including vapor deposition, flame pyrolysis, high temperature evaporation and plasma synthesis.
- Liquid phase methods in which chemical reactions in solvents lead to the formation of colloids, aerosols.
- Sol-gel technique.
- Solid phase mechanical processes including grinding, milling and alloying.

Even for the same material different methods are often used in order to optimize specific properties of nanoparticles such as size, size distribution, symmetry, purity and others.

5.1. Vapor – phase synthesis

Vapor phase deposition can be used to fabricate thin films, multilayers, nanotubes, nanofilaments or nanometer-sized particles. The general techniques can be classified broadly as either physical vapor deposition (PVD) or chemical vapor deposition (CVD). PVD involves the conversion of solid material into a gaseous phase by physical processes; this material is then cooled and re-deposited on a substrate with perhaps some modification, such as reaction with a gas. Examples of PVD conversion processes include thermal evaporation (such as resistive or electron beam heating or even flame synthesis), laser ablation or pulsed laser deposition (where a short nanosecond pulse from a laser is focused onto the surface of a bulk target), spark erosion and sputtering (the removal of a target material by bombardment with atoms or ions).

Most nanoparticle synthesis methods in the gas phase are based on homogeneous nucleation of a supersaturated vapor and subsequent particle growth by condensation, coagulation and capture.

In general, vapor forms within an aerosol reactor at elevated temperatures. The precursor material in the form of as solid, liquid or gas is introduced into the reactor where it is heated and mixed with a carrier gas. The supersaturated vapor is produced by cooling or by chemical decomposition reaction or by some combination of these. The most straightforward method of achieving super saturation is to evaporate a solid into a background gas. By including a reactive gas such as oxygen, oxides or other compounds of the evaporated material can be produced.

The nucleation process is initiated by the formation of very small nucleus from the molecular phase. These nuclei subsequently grow by surface growth mechanisms (heterogeneous condensation, surface reaction) and by collision and coagulation. Further collisions can result in the formation of loosely bound agglomerates or chain like, dendritic forms.

The most common heating or evaporation process are: the flame pyrolysis, furnace flow reactors, laser induced pyrolysis, laser vaporization, thermal plasma, microwave plasma, sputtering, laser ablation.

5.1.1. Gas-Vapor deposition

Chemical Vapor Deposition (CVD) methods are well known in a semiconductors industry. In CVD process, vapor is formed in a reaction chamber by pyrolysis, reduction, oxidation or nitridation, and then deposited on the surface. Areas of growth are controlled by patterning processes like photolithography or photomasking (deposition patterns are etched on to the surface layers of the wafers).

The most important application of CVD methods is the synthesis of carbon nanotubes where CVD is considered to offer one of the most effective routes for scaling up to industrial production. Many other nanoparticles are synthesized by CVD as well.

5.1.2. Plasma – based synthesis

Plasma spraying of materials onto substrates to form protective coatings is widely used industrial practice. The use of plasma (i.e., ionized gas) during vapor deposition allows accessing to different chemical and physical processes and obtaining final materials of high-purity. There are several different types of *plasma deposition* reactor for plasma-assisted PVD and CVD.

In plasma reactors temperatures of the order of 10,000°C can be achieved, causing evaporation or initiating chemical reactions. The main types of plasma used are Direct Current (DC) plasma jet, DC art plasma and Radio-Frequency (RF) induction plasma.

DC glow discharge involves the ionization of gas atoms by electrons emitted from a heated filament. The gas ions in the plasma are then accelerated to produce a directed ion beam. If the gas is a reactive precursor gas, this ion beams used to deposit directly onto a substrate. If an inert gas is used, the ion beam strikes a target material which sputters neutral atoms onto a neighboring substrate.

Another modification is a *magnetron sputtering*. In sputtering methods material is vaporized from a solid surface by bombardment with ions of inert gas from sputter sources like an ion gun or hollow cathode plasma sputter. Plasma is created by the application of a large DC potential between two parallel plates. A static magnetic field

is applied near a sputtering target and confines the plasma to the vicinity of the target. Ions from the high-density plasma sputter material, predominantly in the form of neutral atoms, from the target onto a substrate. One of the greatest benefits of the magnetrons is high deposition rate (about 1 μm/min) that makes the method to be industrially viable. Moreover, multiple targets can be rotated so as to produce a multilayered coating on the substrate.

Nowadays, *vacuum arc deposition* is well-established process for producing of thin films and nanoparticles. This technique involves the initiation of an arc by contacting a cathode made of a target material. An igniter is attached to an anode in order to generate a low-voltage, high-current self-sustaining arc. The arc ejects ions and material droplets from a small area on the cathode. Further, the ions are accelerated towards a substrate while any large droplets are filtered out before deposition (Figure 18).

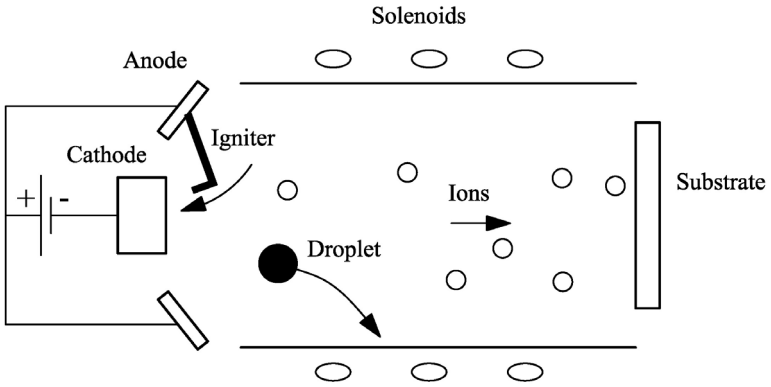

Fig. 18. Schematic diagram of a vacuum arc deposition technique.

One of the outstanding strides in plasma processing for nanoparticles synthesis is the developed process of the vapor condensation. The principle of this method is illustrated in Figure 19. The precursor material is put into the working chamber with a stable arc. The chamber is filled by reactive gas that becomes ionized; then molecular clusters are formed and cooled to produce nanoparticles.

In the plasma-assisted PVD processes the vapor phases originate from a solid target. Instead, plasma-enhanced CVD employs gas phase precursors that are dissociated to form molecular fragments which condense to form thin films or nanoparticles. The dissociation temperatures required for CVD tend to be much lower than for conventional CVD processes due to the high energy of the plasma, and this may be of importance for deposition on sensitive substrates such as semiconductors and polymers.

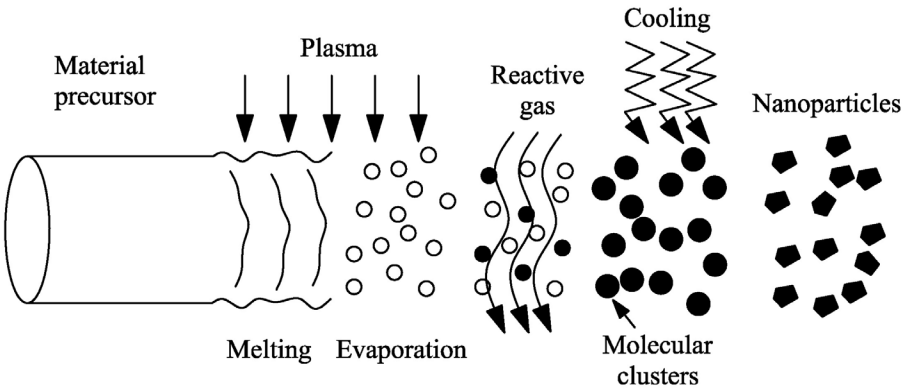

Fig. 19. Principle of the vapor condensation process.

5.1.3. Molecular beam epitaxy

A molecular beam epitaxy (MBE) machine is essentially an ultra-high-precision, ultra clean evaporator, combined with a set of in-situ tools, such as Auger electron spectroscopy (AES) and/or reflection high-energy electron diffraction (RHEED), for characterization of the deposited layers during growth. The reactor consists of an ultra-high-vacuum chamber (typically better than 5 x 10^{-14} atm pressure) of approximately 1.5 m diameter (Figure 20). The most important aspect of MBE is the slow deposition rate (1 to 300 nm per minute), which allows the films to grow epitaxialy on a heated substrate under UHV conditions.

The sources can be either solid or gaseous and an MBE machine will typically have an array of multiple sources, which can be shuttered to allow layered, alternating heterostructures to be produced. Semiconductor quantum wells, superlattices and quantum wires and metallic or magnetic multilayers for spin valve structures are deposited using this technique.

In solid-source MBE, ultra-pure elements such as gallium and arsenic are heated in separate quasi-Knudsen effusion cells until they begin to slowly evaporate. The evaporated elements then condense on the wafer, where they may react with each other. In the example of gallium and arsenic, single-crystal gallium arsenide is formed. The term "beam" simply means that evaporated atoms do not interact with each other or any other vacuum chamber gases until they reach the wafer, due to the long mean free paths of the beams. The substrate is rotated to ensure even growth over its surface. By operating mechanical shutters in front of the cells, it is possible to control which semiconductor or metal is deposited. For example, opening the Ga and As cell shutters results in the growth of GaAs. Shutting the Ga cell and opening the Al cell switches the growth to AlAs. As the shutters can be switched rapidly, in comparison to the rate at which material is deposited, it is possible to grow very thin layers exhibiting very sharp interfaces. Other effusion cells contain elements required for doping, and it is possible to monitor the growth by observing the electron diffraction pattern produced by the surface.

MBE can also be performed using gaseous sources, and this is often termed chemical beam epitaxy (CBE). When the sources are metal-organic compounds, the process is known as *metallorganic MBE (MOMBE)*.

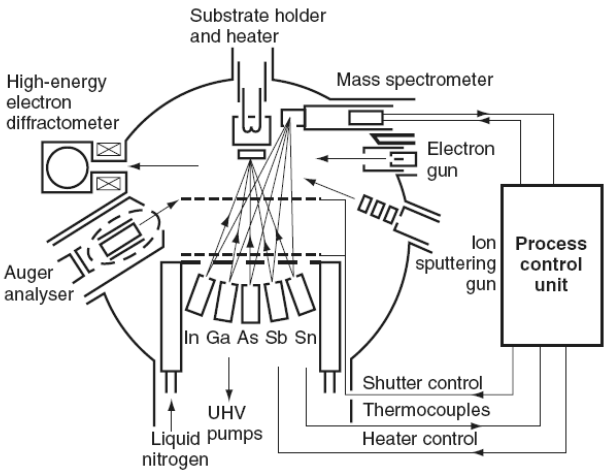

Fig. 20. Schematic diagram of a molecular beam epitaxy thin film deposition system (adapted from *Nanoscale Science and Technology*, Eds. R.W. Kelsall, I.W. Hamley, M. Geoghegan, John Wiley&Sons Ltd, 2005).

5.1.4. Inert gas condensation

Gas condensation, as a technique for producing nanoparticles, refers to the formation of nanoparticles in the gas phase, i. e., condensing atoms and molecules in the vapor phase. *The inert gas condensation (IGC)* process is one of the most known and well established procedures for the production of nanopowders. These powders are widely used for electrically conductive adhesives and polymers, which find application, among other things, for the surface mounting technique in electronics. Figure 21 gives a schematic overview of the IGC procedure. Here a material, often a metal, is evaporated from a heated metallic source into a chamber which has been previously evacuated to about 10^{-7} torr and backfilled with inert gas to a low-pressure. The metal vapor cools through collisions with the inert gas atoms, becomes supersaturated and then nucleates homogeneously; the particle size is usually in the range 1–100 nm and can be controlled by varying the inert gas pressure. Ultimately, the particles are collected and may be compacted to produce a dense nanomaterial.

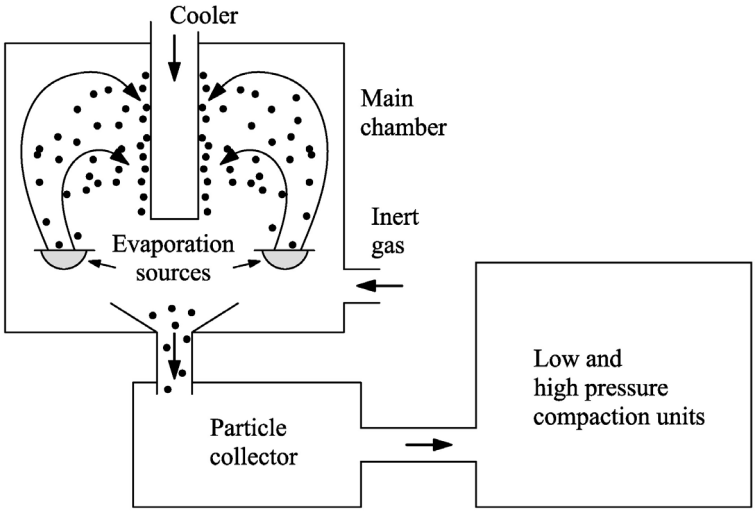

Fig. 21. Schematic diagram of an inert gas condensation apparatus

5.1.5. Flame pyrolysis

Flame pyrolysis is widely used in production of carbon black, fumed silica (SiO_2), ultrafine TiO_2 and many other materials. In this process flame heat is used to initiate the chemical reactions. The disadvantage of this method is that it usually yields agglomerated particles.

Furnace flow reactors (fig. 22) are the simplest systems used to produce saturated vapor for substances having a large vapor pressure at intermediate temperatures. In these systems a crucible containing the source material is placed in a heated flow of inert carrier gas. Materials with low vapor pressure can be fed in as suitable precursors.

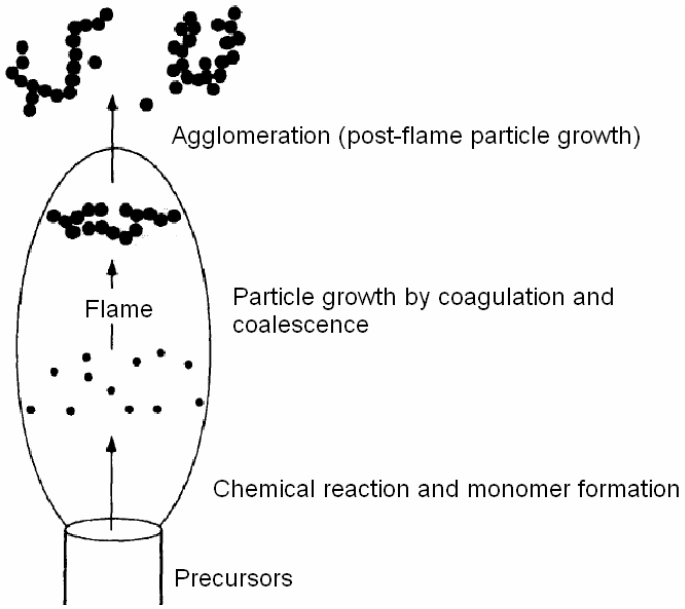

Fig. 22. Schematic diagram of a flame pyrolysis

In the *laser pyrolysis* technique IR laser is used to rapidly heat a flowing reacting gas. The source molecules are heated selectively by absorption of the laser energy whereas the carrier gas is not. Heating leads to decomposition of the precursors and super saturation is created resulting in nanoparticle formation.

5.2. Liquid phase synthesis

Precipitating nanoparticles from a solution of chemical compounds can be classified into five major categories: (1) colloidal methods; (2) sol – gel processing; (3) water – oil microemulsions method; (4) hydrothermal synthesis; and (5) polyol method. Some of these techniques of nanoparticles producing are discussed below.

5.2.1. Colloidal methods

Colloidal methods are simple and well established wet chemistry precipitation processes in which solutions of the different ions are mixed under controlled temperature and pressure to form insoluble precipitates. For metal nanoparticles the basic principles of colloidal preparation were known since antiquity. E.g. gold colloids used for high quality red and purple stained glass from medieval times to date. However proper scientific investigations of colloidal preparation methods started only in 1857 when Faraday has published results of his experiments with gold. He prepared gold colloids by reduction of $HAuCl_4$ with phosphorus. Today, colloidal processes are widely used to produce such nanomaterials like metals, metal oxides, organics, and pharmaceuticals.

An important sub-set of colloidal methods are *sonochemistry methods*, in which acoustic cavitation is used to control the process. By applying the ultrasonic radiation to the precursor solution the chemical reactions is initiated. The ultrasound leads to creation, growth and rapid collapse of small bubbles, which act like nucleation centers. The growth of nucleus ends after bubble collapse.

Nanoparticles produced by wet chemical methods can remain in liquid suspension for further use or may be collected by filtering or by spray drying to produce a dry powder.

5.2.2. Solution precipitation

This method relies on the precipitation of nanometer-sized particles within a continuous fluid solvent. An inorganic metal salt, such as chloride, nitride and so on, is dissolved in water. Metal cations exist in the form of metal hydrate species, for example, $Al(H_2O)^{3+}$ or $Fe(H_2O_6)^{3+}$. These hydrates are added with basic solutions, such as NaOH or Na_4OH. The hydrolyzed species condense and then washed, filtered, dried and calcined in order to obtain the final product.

Described method is relatively simple and widely used for production of single and multi – components oxide nanopowders using optimized reactions and reaction conditions. Moreover, subsequent processing of colloids can include additional colloidal precipitation on particle surfaces to produce a core–shell nanoparticle structure, deposition on substrates to produce quantum dots, self-assembly on substrates as ordered 2D and even 3D arrays, and finally embedding in other media to form nanocomposites. One problem inherent in many colloidal methods is aging of colloid solutions, e.g. the particles can increase their size as a function of time.

5.2.3. Electrodeposition

The principle of electrodeposition is inducing chemical reactions in an aqueous electrolyte solution with the help of applied voltage, e.g. this is the process of using electrical current to coat an electrically conductive object with a relatively thin layer of metal. This method is relevant to deposition of nanostructured materials include metal oxides and chalcogenides.

The process of electrodepositing may be either anodic or cathodic. In an anodic process, a metal anode is electrochemically oxidized in the presence of other ions in solution, which then react together and deposit on the anode. Meanwhile in a cathodic process, components are deposited onto the cathode from solution precursors.

Electrodeposition is relatively cheap and can be performed at low temperatures which will minimize interdiffusion of materials in the case of a multilayered thin film preparation. The film thickness can be controlled by monitoring the amount of charge delivered, whereas the deposition rate can be followed by the variation of the current with time. The composition and defect chemistry can be controlled by the magnitude of the applied potential, which can be used to deposit non-equilibrium phases. Pulsing or cycling the applied current or potential in a solution containing a mixture of precursors allows the production of a multilayered material. The potential during the pulse will determine the species deposited whilst the thickness of individual layers is determined by the charge passed. Alternatively, the substrate can be transferred periodically from one electrolytic cell to another. The final films can range in thickness from a few nanometers to tens of microns and can be deposited onto large specimen areas of complex shape, making the process highly suitable for industrial use.

Electrodeposition can also be performed within a nanoporous membrane which serves to act as a template for growth; for example, anodized alumina has cylindrical nanopores of uniform dimensions and electrodeposition within this membrane can produce nanocylinders. Deposition on planar substrates can also limit nanocrystal growth and

produce ordered arrays; if the growth is epitaxial then any strain due to lattice mismatch between the nanocrystal and the substrate can be growth-limiting. Furthermore, it is possible to modify the surface of substrates (e.g., by STM or AFM) to produce arrays of defects which can act as nucleation sites for the electrodeposition of nanocrystals.

Electrodeposition has three main attributes that make it so well suited for nano-, bio- and microtechnologies: (1) – It can be used to grow functional material through complex 3D masks; (2) – It can be performed near room temperature from water-based electrolytes; (3) – It can be scaled down to the deposition of a few atoms or up to large dimensions.

5.3. Sol-gel technique

5.3.1. Introduction

Sol-gel technology is a well-established colloidal chemistry technology, which offers possibility to produce various materials with novel, predefined properties in a simple process and at relatively low process cost. *The sol* is a name of a colloidal solution made of solid particles few hundred nm in diameter, suspended in a liquid phase. *The gel* can be considered as a solid macromolecule immersed in a solvent. So, in general terms, the sol-gel process consists in the chemical transformation of a liquid (the sol) into a gel state and with subsequent post-treatment and transition into solid oxide material.

Sol-gel process has been used for glass coating since the 1939 and today it is a common technology for fabrication of ultra-fine powders, monolithic ceramics and glasses, ceramic fibers, inorganic membranes, aerogels and other types of materials.

Sol-gel technique is one of the most popular solutions processing for nanoparticles (mostly oxides) production. This methods involve a set of chemical reactions which irreversibly convert a homogeneous solution of molecular reactant precursors (a sol) into a three-dimensional polymer (a gel) forming an elastic solid filling the same volume as the solution.

5.3.2. Sol-gel process

Figure 23 gives an insight to the process.

The hydrolysis of metal alkoxides involves nucelophilic reaction with water:

$$M(OR)_y + x\ H_2O \rightarrow M(OR)_{y-x}(OH) + x\ ROH$$

Condensation occurs when either hydrolyzed species react with each other and release a water molecule, or a hydrolyzed species react with an unhydrolyzed species and release an alcohol molecule.

Processing involves forming the gel followed by drying to remove the solvent. Gels can be cast and molded to form a microporous pre-form and dried to produce a monolithic bulk material (e.g., a xerogel or an aerogel) that can be used to form filters and membranes. They can also be spin coated or dipped to produce thin (typically 50–500 nm) films on substrates. These films are used for electronic thin film devices, for wear, chemical or oxidation protection, as well as for their optical properties (e.g., anti-reflection). Alternately, fibers can be drawn from the gel; e.g., silica fibers for light transmission. The interconnected nanoscale porosity in the dried gel can be filled via incorporation of a second material using techniques such as liquid infiltration or chemical reaction in order to obtain the nanocomposites.

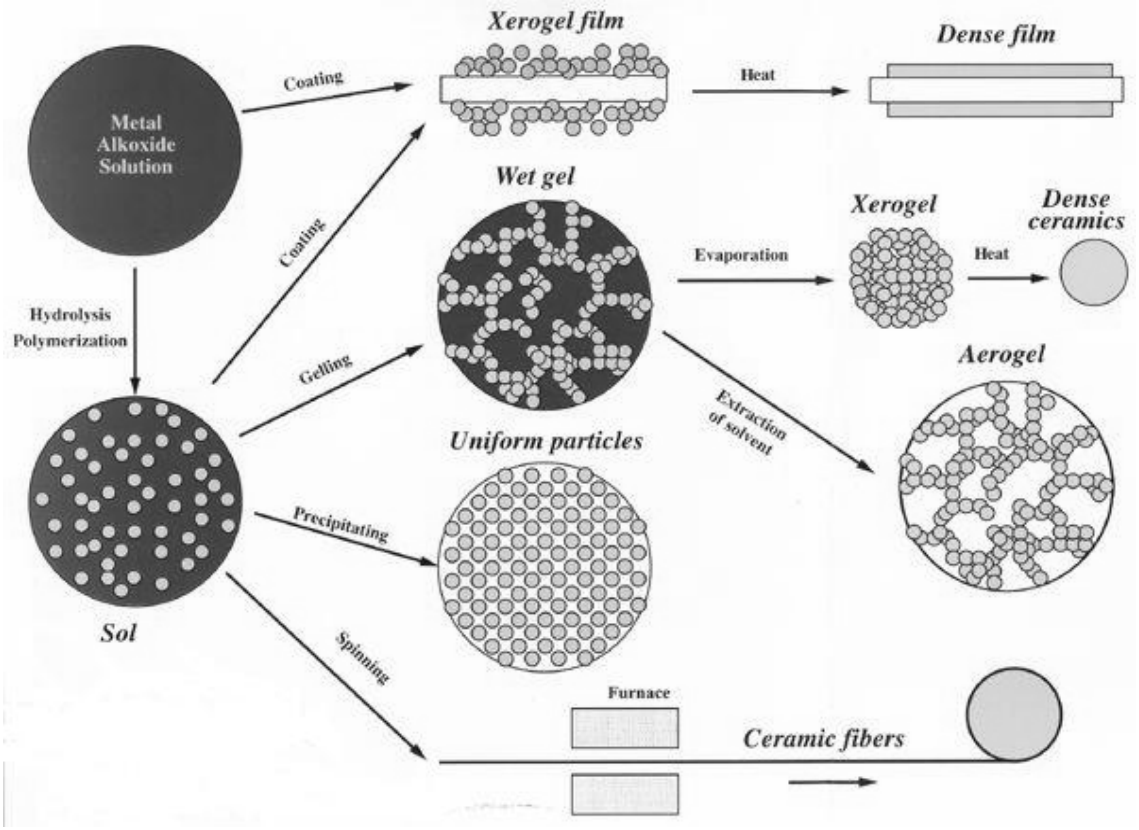

Fig. 23. Sol-gel technology and its final products.

Diphase gels use the initial gel host for the precipitation of a second phase by sol-gel routes. In another variant, organic material can be incorporated as a monomer within an inorganic gel host; the monomers can be subsequently polymerized to form a hybrid material. If a dense rather than a nanoporous material is desired, drying is followed by sintering at higher temperatures. The high surface area leads to rapid densification, which can be accompanied by significant grain growth if temperatures are too high.

The main benefits of sol–gel processing are the high purity and uniform nano-structure achievable at low temperatures.

First stage of the sol-gel process is a preparation of precursor solution. Precursors play a key role in sol-gel technology directly affecting the porosity, refractive index, hardness and other performance characteristics of the resultant material. Precursor can be inorganic, but more often metal organic precursors are used. Common metal organic precursors for the sol-gel process are metal alkoxides ($M(OR)_z$), where R stands for an alkyl group (C_xH_{2x+1}). In a typical sol-gel process, the precursor is subjected to a series of hydrolysis and polymerization reactions to form a colloidal suspension (the sol). For example, in the case of metal alkoxide, it is dissolved in alcohol and then the water is added under acidic, neutral or basic conditions. Addition of the water leads to hydrolysis in which alkoxide ligand is replaced with a hydroxyl liquid:

$$M(OR)_z + H_2O \rightarrow M(OR)_{z-1}(OH) + ROH$$

The chemical reactivity of metal alkoxides is related to the R – the larger the R, the slower the hydrolysis of metal alkoxides. Metal alkoxides are very moisture-sensitive (except silicon alkoxides) and require special handling environments. There are also more stable precursors developed like e.g. metal carboxylate, metal dialkylamides,

amorphous and crystalline colloidal sol solutions, and organic/inorganic hybrids. They are not moisture-sensitive, easy to use, and produce good coatings.

Next stage of the sol-gel process after preparation of precursor solution is a condensation reaction in which particles condense in the gel phase. For metal alkoxides, in condensation reaction the hydroxyl ligands produce polymers composed of M-O-M bonds.

In the last stage of the sol-gel process the resulting porous gel is usually chemically purified and treated by elevated temperatures, or by UV or IR radiation, to form high purity oxide materials. The gel can be modified with a number of dopants to produce unique properties in the resultant glass unattainable by other means.

Materials produced by sol-gel method can be either totally inorganic in nature or both inorganic and organic.

Sol-gel technology offers many advantages, including excellent stoichiometry control of precursor solutions, ease of compositional modifications, customizable microstructure, ease of introducing various functional groups or encapsulating sensing elements, relatively low annealing temperatures, the possibility of coating deposition on large-area substrates, and simple and inexpensive equipment.

5.3.3. Sol-gel coating processes

The most common application of sol-gel process is fabrication of various coatings and films, and it is reasonable to consider common wet coating technologies.

Dip Coating is illustrated in fig. 24. In the dip coating process the substrate is immersed into a sol and then withdrawn with a well-defined speed under controlled temperature and atmospheric conditions. The sol left on substrate forms a film with thickness mainly defined by the withdrawal speed, the solid content and the viscosity of the liquid. Next stage is a gelation (densification) of the layer by solvent evaporation and finally annealing to obtain the oxide coating.

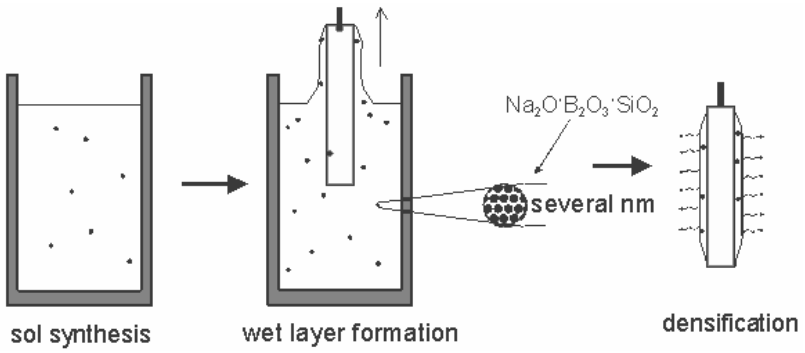

Fig. 24. Example of formation of sodium borosilicate coating on glass by dip coating (H. Schmidt, M. Mennig, Wet Coating Technologies for Glass, Tutorial, November 2000)

More recently, an *angle-dependent dip coating* process has been developed (fig. 25). In this case, the coating thickness is dependant also on the angle between the substrate and the liquid surface, so different layer thickness can be obtained on the top and bottom side of the substrate.

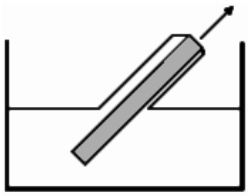

Fig. 25. Schematic of angle dependent dip coating

Spin Coating is illustrated in fig. 26. Spin coating is used for making a thin coating on relatively flat substrates or objects. The material to be made into coating is dissolved or dispersed into a solvent, and then deposited onto the surface and spun off to leave a uniform layer for subsequent processing stages and ultimate use.

General stages in spin coating include deposition of the coating fluid onto the substrate, aggressive fluid expulsion from the substrate surface by the rotational motion, gradual fluid thinning, and coating thinning by solvent evaporation.

Fig. 26. Stages of the spin coating process: deposition of the sol, spin up, spin off and gelation by solvent evaporation.

The coating thickness is inversely proportional to the square root of the rotation speed and also depends on the coating solution properties like viscosity and composition.

Flow coating processes is illustrated in fig. 27. In the flow coating process the liquid coating system is poured over the substrate to be coated as shown schematically on the figure below.

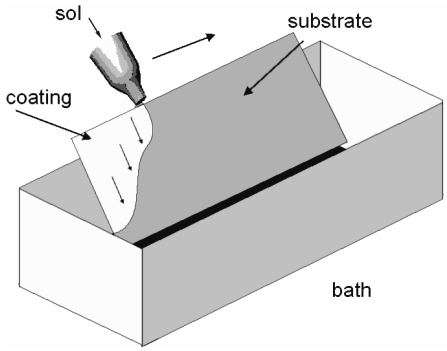

Fig. 27. Scheme of the flow-coating process

The coating thickness depends on the angle of inclination of the substrate, the coating liquid viscosity and the solvent evaporation rate. The advantage of the flow-coating process is that non-planar large substrates can be coated rather easily. As a variation of this process, the spinning of the substrate after coating may be helpful in order to obtain

more homogenous coatings. If no spinning process is employed, the coating thickness increases from the top to the bottom of the substrate.

Capillary coating is illustrated in fig. 29. Capillary or laminar flow coating process combines the high optical quality of the dip coating process with the advantage that all the coating liquid can be exploited. In this process the tubular dispense unit is moved under the substrate surface without physical contact. A spontaneous meniscus is created between the top of the slot tube (or porous cylinder) and the substrate surface, and achieving laminar deposition conditions a coating is deposited with high uniformity. Multilayer coatings can be fabricated by using two dispense lines one after the other.

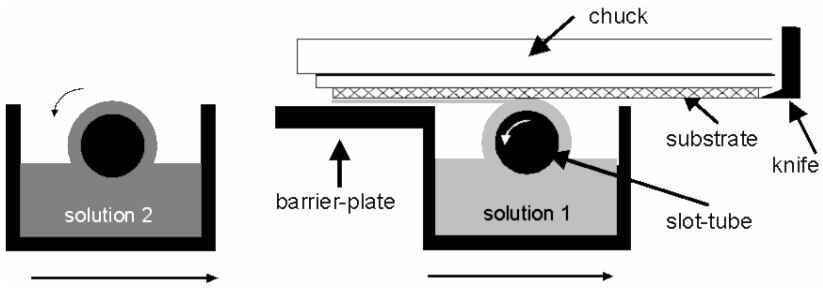

Fig. 29. Schematics of the capillary coating process (B. T. Chen, Polymer Engineering and Science 23 (1983) 399–403)

Roll coating. Roll coating is a process by which a thin liquid film is formed on a continuously moving web or substrate by using one or more rotating rolls. It is of importance that in order to avoid structures in the surface cutted roles have to be used, and coating thickness and viscosity of the liquid have to be adapted very thoroughly. Using cutted roles, the amount of liquid transported onto the glass surface is defined by the voids cutted out of the role. After the deposition, the parts have to coagulate and to form a homogeneous film. For this reason, the wetting behavior of the glass against the liquid has to be perfect and the drying speed has to be adapted to the film forming velocity. Therefore, temperature and atmosphere have to be controlled perfectly.

Spray coating techniques. Spray coating is used e.g. for coating irregularly shaped glass forms like pressed glass parts, lamps or container glass (cold end coating). Using special automatic flat spraying equipment it is possible to prepare glass like coatings (coloured coatings and electrochromic WO_3 coatings) with thickness in the range between 100 nm and 220 nm. The preparation of optical coatings by spraying offers several advantages compared to the dip coating technique, since it is several times faster, the waste of coating sols is much smaller, coating sols with rather short pot lives can be used and the coating step is suitable for establishing an in-line process.

There are also processes like the pyrosol-process, where very fine droplets are produced and sprayed onto the surface. The coating material does not hit the surface in form of liquid droplets but more or less in form of dried small particles in the nanometer range. Due to the high reactivity of these particles when reaching the hot surface, a continuous and very homogeneous glass film can be formed.

Post-treatment. In wet coating techniques, molecular structures developed by chemical synthesis can be used to develop new properties either when preserving these structures on the surface, or to develop new desired molecular structures by heat-treatment and subsequent chemical reaction on the surface. So, there are two basic routes: the first route comprises a high temperature treatment after the coating step in order to get “glass-like” or “ceramic-like” materials on the glass surface and the second type of technique would include a low-temperature UV- or infrared type of curing,

where the functional chemical structures developed in the liquid coating material, more or less are maintained during this post-treatment.

5.3.4. Sol-gel applications

The applications for sol gel-derived products are numerous. Sol-gel technologies are used in various applications including optics, electronics, energy, space, sensors and separation technology.

Sol-gel coatings are extensively used for such diverse applications as protective and optical coatings, anti-reflection coatings, passivation and planarization layers, sensors, high or low dielectric constant films, inorganic membranes, electro-optic and nonlinear optical films, electrochromics, semiconducting anti-static coatings, superconducting films, strengthening layers and ferroelectrics.

Cast into a mold, and with further drying and heat-treatment, dense ceramic or glass particles with novel properties can be obtained in the forms that cannot be created by any other method.

With the viscosity of a sol adjusted into a proper range, different fibers and needles can be drawn which can be used e.g. for fiber optic sensors or thermal insulation.

Ultra-fine and uniform ceramic powders can be formed by precipitation. These powders of single- and multicomponent compositions can be made in submicron particle size for dental and biomedical applications. Composite powders have been patented for use as agrochemicals and herbicides. Also powder abrasives, used in a variety of finishing operations, are made using a sol-gel type process.

Another important application of sol-gel processing is to carry out zeolite synthesis. Other elements (metals, metal oxides) can be easily incorporated into the final product and the silicalite sol formed by this method is very stable.

If the liquid in a wet gel is removed under a supercritical condition, a highly porous and extremely low-density material called aerogel is obtained. Drying the gel by means of low temperature treatments (25–100 C), it is possible to obtain porous solid matrices called xerogels.

Other products fabricated with this process include various ceramic membranes for microfiltration, ultrafiltration, nanofiltration, pervaporation and reverse osmosis.

5.4. Solid – state phase synthesis

One of the nanofabrication processes of major industrial importance is the high-energy ball milling, also known as mechanical attrition or mechanical alloying.

In contrast to previous three groups, where particles were produced in down up processes, mechanical methods based on top down (size reduction) processes like attrition and disintegration of larger particles. When particle size lies in nanometer range, terms ultrafine grinding or nanosizing are often used for the process.

Mechanical attrition methods give very high production rates (up to tones per hour) and are widely used for industrial production of clay, coal and metal powders.

The production process often involves wet milling in milling chamber with rotating perforated plates. Wet milling results in suspension that needs to be stabilized by adjustment of the pH to prevent particle recombination due to increasing particle–particle interactions.

5.4.1. Mechanical milling, attriction and alloying

In the 1970s, the method of *mechanical attrition (MA)* of powder particles followed by high temperature sintering was developed as an industrial process to successfully produce new alloys and phase mixtures. For example, this powder metallurgical process allows the preparation of alloys and composites which cannot be synthesized via conventional casting routes.

In the 1980s, the method of *high-energy milling* gained a lot of attention as a non-equilibrium solid-state process resulting in materials with nanoscale microstructures.

Typical objectives of the milling include particle size reduction, solid-state alloying, mixing or blending, and particle shape changes. A variety of ball mills have been developed for different purposes, among them there are tumbler-, attrition-, shaker-, vibratory -, and planetary mills, etc. However, the basic principal of mechanical attrition is similar for all processes and can be illustrated as shown in fig. 30. Coarse-grained materials in the form of powders are crushed mechanically in rotating drums by hard steel or tungsten carbide balls, usually under controlled atmospheric conditions to prevent unwanted reactions such as oxidation. This repeated deformation can cause large reductions in grain size via the formation and organization of grain boundaries within the powder particles.

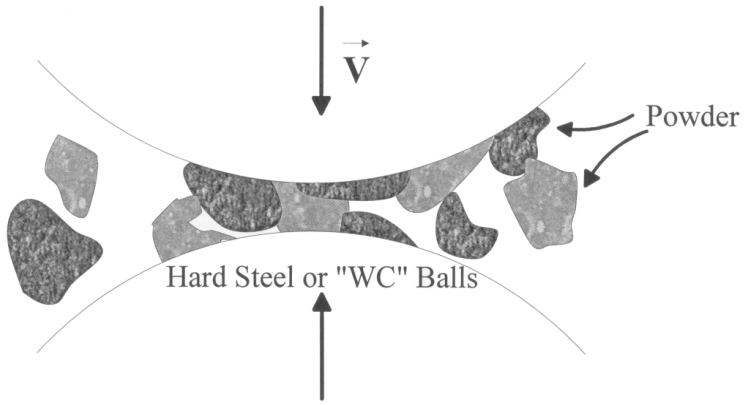

Fig. 30. Schematic representation of the process of mechanical attrition.

High-energy milling forces can be obtained by using high frequencies and small amplitudes of vibration. Ball mills are highly energetic, and reactions can take place by one order of magnitude faster compared with other types of mills. Since the kinetic energy of the balls is a function of their mass and velocity, dense materials (steel or tungsten carbide) are preferable to ceramic balls.

A conventional planetary ball mill consists of a rotating horizontal drum half-filled with small steel balls. As the drum rotates the balls drop on the powders that are being ground; the rate of grinding increases with the speed of rotation. When speeds are too high, however, the centrifugal force acting on the flying balls exceeds the force of gravity, and the balls are pinned to the wall of the drum. As a result, the grinding action stops. An attritor consists of a vertical drum with a series of impellers inside it. Set progressively at right angles to each other, the impellers energize the ball charge, causing powder size reduction because of impact between balls, between balls and container wall, and between balls, agitator shaft, and impellers. Some size reduction appears to take place by interparticle collisions and by ball sliding. A powerful motor rotates the impellers, which in turn agitate the balls in the drum.

Due to the continuous severe plastic deformation, a continuous refinement of the internal structure of the powder particles to nanometer scale occurs during high-energy mechanical attrition. The increase in temperature during this process is modest and is generally estimated to be in between 100 and 200°C. The collision time roughly corresponds to about 2 μs. The rate of structural refinement is dependent on the mechanical energy input and the work hardening of the material.

The process of grain refinement starts from the localizing of shear bands that indicates an increase in dislocations density. Hall-Petch relationship gives the value of the yield stress, σ, required to deform a polycrystalline material by dislocation movement:

$$\sigma = \sigma_o + kd^{-1/2},$$

where d is the average grain size; σ_o and k are material constants. σ_o may be treated as a friction stress below which dislocations are immobile if there are no grain boundaries in material.

At a certain level of stress, the dislocations create small angle boundaries that separate newly developed sub-grains of nano- or/and micro-meter size. Continuing mill leads to high angle boundaries formation and separation of nano-grains.

An extrapolation to nanocrystalline dimensions shows that very high stresses are required to maintain plastic deformation. Experimental values for k and σ_o are typically of about 0.5 M Nm $^{-3/2}$ and 50 MPa, respectively. For a grain size of 10 nm, the minimum yield stress is of the order of 5 GPa corresponding to 15% of the theoretical shear stress, which sets a limit to the grain size reduction achieved by plastic deformation during ball milling. Therefore, the reduction of grain size to a few nanometers is limited by the stresses applied during ball milling as long as no dramatic elastic softening of the crystal lattice occurs.

Further energy storage by mechanical deformation is only possible by an alternative mechanism. Grain boundary sliding has been observed in many cases at high temperatures leading to *superplastic behavior*. Alternatively, grain boundary sliding can also be achieved at a very small grain size and low temperature by diffusional flow of atoms along the intercrystalline interfaces which allows the synthesis of ductile ceramics. This provides a mechanism for the self-organization and rotation of the grains, thus increasing the energy of the grain boundaries proportional to their misorientation angle and excess volume.

This energetic microstructure-property relationship is schematically represented in Figure 31. Here the stored enthalpy, ΔH, in attrited Fe powder is shown as a function of average reciprocal grain size, $1/d$, since $1/d$ scales also with the volume density of grain boundaries in the nanocrystalline material. Two different regimes can be clearly distinguished: (a) – the stored enthalpy shows only a weak grain size dependence typical for dislocation controlled deformation processes for small grain size decrease at the early stages of mechanical attrition; and (b) – an energy storage becomes more efficient when the average domain size is reduced below $d^* = 30–40$ nm. The critical grain size, d^*, corresponds to the size of nanograins which are formed within the shear bands. Therefore, for domain with size $d < d^*$ deformation is controlled by the properties of the low and, later, high angle grain boundaries which are developing in stages (b).

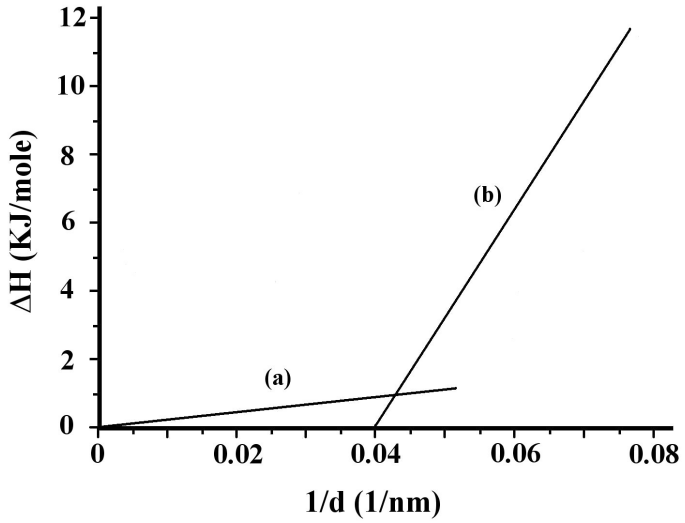

Fig. 31. The stored enthalpy *H* as function of reciprocal grain size 1/*d* of Fe at different levels of mechanical attrition.

Milling can be used to induce chemical reactions through ball – powder colliding interactions.

Mechanical alloying is a high-energy ball-milling process in which elemental blended powders are continuously welded and fractured to achieve alloying at the atomic level. Different components can be mechanically alloyed together by cold welding to produce nanostructured alloys. A nanometer dispersion of one phase in another can also be achieved. Microstructures and phases produced in this way can often be thermodynamically metastable. For example, recently the synthesis of ferrite compounds with a spinel structure (such as Fe_3O_4, $CoFeO_4$) by ball-milling aqueous solutions of metal chlorides and NaOH was reported.

Existing factors influencing the mechanical alloying/milling processes include milling time, charge ratio, milling environment, and the internal mechanics specific to each mill. Cryomilling reduces oxygen contamination from the atmosphere and minimizes the heat generated during milling; therefore, fracturing is favored over welding, especially in milling of ductile materials. For example, the grain size of nickel has been sufficiently refined when milling is conducted in liquid nitrogen instead of methanol.

Despite of its advances, mechanical attrition process for nanoparticles synthesis has some shortcomings that limit the application of this technique. One of the greatest problems of milling is high level of impurities or surface contaminations. Another problem is lack of control of the particle size distribution, and inability to tailor precisely shape and size of particles in the nanometers range.

5.4.2. Severe plastic deformation

Generally any form of mechanical deformation under shear conditions and high strain rates can lead to the formation of nanostructures, since energy pumped into crystalline structures results in lattice defects creation. The severe plastic deformation that occurs during machining, cold rolling, drawing, cyclic deformation or sliding wear has also been reported to form nanostructured material.

Severe plastic deformation (SPD) processing, in which materials are subjected to the imposition of very large strains without the introduction of concomitant changes in cross-sectional dimensions of the samples, is one of the most successful top-down approaches. Materials produced by SPD techniques have grain sizes in the range of 50–1000 nm. However, they have sub-grain structures, which are often much smaller than 100 nm. Now there are several SPD processing available: *equal-channel angular pressing (ECAP)*, *high-pressure torsion*, *accumulative roll-bonding, repetitive corrugation and friction stir processing*.

Torsion straining under high pressure and equal channel angular pressing are the most well-known methods of providing large plastic deformations and formation of nanostructures. Figure 32 schematically shows the principles of SPD techniques.

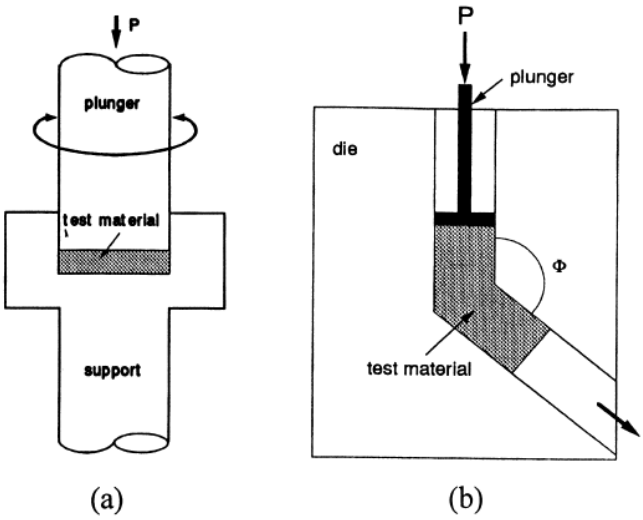

Fig. 32. Schematics of SPD methods: (a) – torsion straining; (b) – equal-channel angular (ECA) pressing.

A method of torsion straining under high pressure can be used for fabrication of disk type samples (fig. 32a). An ingot is held between anvils and strained in torsion under the applied pressure (P) of several GPa. A lower holder rotates and surface friction forces deform the ingot by shear. Due to the specific geometric shape of the sample, the main volume of the material is strained in conditions of quasi-hydrostatic compression under the applied pressure and the pressure of sample outer layers. As a result, in spite of large strain values, the deformed sample is not destroyed.

Severe torsion straining can be successfully used not only for the refinement of a microstructure but also for the consolidation of powders. During torsion straining at room temperature, high pressure can provide a rather high density that may be close to 100% in the processed disk sample.

During ECA pressing a billet of material is multiple pressed through a special die (fig. 32b). The angle of two channels intersection is usually 90^0, however, in the case of a hard-to-deform material, the angle may be changed. Moreover, for processing of hardly deformed materials, ECA pressing can be conducted at elevated temperatures. During ECAP the direction and number of billet passes through the channels are very important parameter for microstructure development.

Up to now, there is no common view on mechanisms of grains refinement. One of the proposed mechanisms is concentration of dislocations in cell walls and their absent inside cells in materials with high stacking fault energy (for ex., Cu and Ni). Further

increase in the strain results in a decrease in a cell size and an increase in cell misorientations due to dislocations movement. That can lead to intensification of rotation modes of deformation within the whole sample.

In materials with relatively low stacking fault energy, as, for ex., Ni-Cr alloy, the microstructure refinement is due to shear bands formation.

On the basis of the experimental data the following model of evolution of the materials defect structure during SPD is proposed, figure 33. The main idea is transformation of a cellular structure (fig. 33a) to a granular one. This stage is outlined by decrease in dislocation density in the grain (cell) boundaries caused by partial annihilation of dislocations of different signs when the dislocation density achieves some critical value (fig. 33b). As a result, there is an excess of dislocations with similar sign (fig. 33c). Remaining dislocations further increase misorientation in the case of dislocations with Burgers vectors directed perpendicular to the boundary; at the same time long range stress fields are connected with glide dislocations which can also lead to sliding of grains along grain boundaries, i.e. reveal rotation deformation modes which are indicated earlier for large plastic straining.

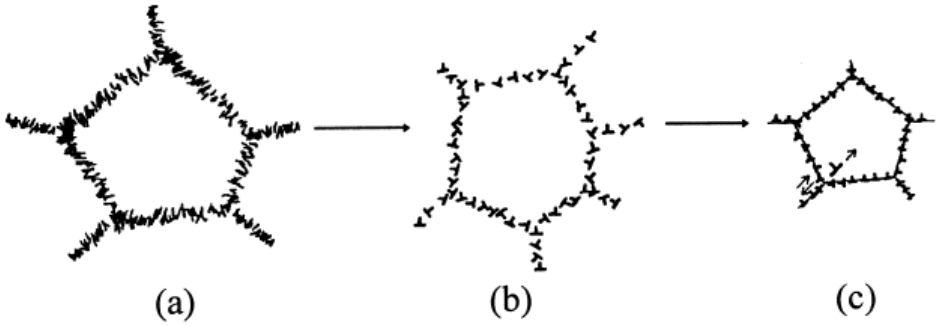

Fig. 33. Schematic model of dislocation structure evolution at different stages during severe plastic deformation (adapted from R.Z. Valiev, R.K. Islamgaliev, I. Alexandrov. *Bulk nanostructured materials from severe plastic deformation*, Progress in Mat. Sci., 2000, v. 45, 103–189)

Most of the grain boundaries in nanocrystalline materials (nc) are at non-equilibrium state. Non-equilibrium grain boundaries in NSM are characterized by excess energy and long range elastic stresses due to the presence of a high density of extrinsic defects in their structure. These stresses result in significant distortions and dilatations of the crystal lattice near grain boundaries which are revealed experimentally by TEM and X-ray methods. In turn, atomic displacements in near boundary regions change the dynamics of lattice vibrations and, as a result, change such fundamental properties as elastic modula, Debye and Curie temperatures and others, Table 3.

Table 3. Comparison of some properties for nc and coarse-grained (cg) materials.

Properties	Materials	Value	
		nc	cg
Curie temperature, K	Ni	595	631
Saturation magnetization, Am^2/kg	Ni	38.1	56.2
Debye temperature, K	Fe	240	467
Diffusion coefficient, m^2/s	Cu in Ni	1×10^{-14}	1×10^{-20}
Ultimate solubility at 293 K, %	C in α-Fe	1.2	0.06
Young's modulus, GPa	Cu	115	128

By now the nanostructures are obtained for a number of pure metals, alloys, steels and intermetallic compounds, as well as for metal – matrix composites and semiconductors. Microstructure of nano- copper produced with the help of SPD is shown in figure 34.

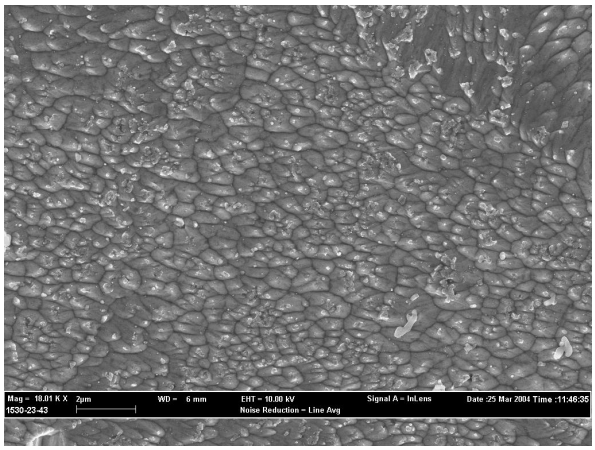

Fig. 34. Microstructure of SPD produced nc copper.

5.5. Other methods

Here are some more noteworthy methods among other existing methods.

Fujitsu Laboratories Ltd. developed a novel method for fabrication of size and alignment controlled oxide dots on a semiconductor substrate shown in fig. 35. In this method, the AFM tip is moved near the semiconductor surface and a voltage is applied. As a result, water molecules in the atmosphere decompose into Hydrogen (H^+) and Hydroxide (OH^-) ions, and OH- ions oxidize the substrate under the tip. The diameter of the oxide dots can be controlled by adjusting the durations of the voltage applications. In the next step oxide dots are removed with an etching solution or by ultrasonic cleaning in water, forming holes on the substrate. Finally, the substrate is placed into a molecular beam epitaxy (MBE) chamber, and quantum dots are fabricated using a process similar to self-assembled growth.

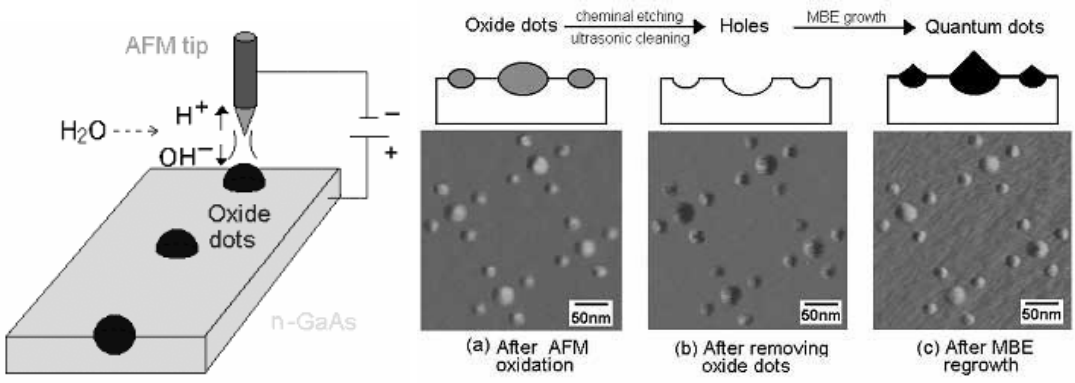

Fig. 35. Quantum dot fabrication and array of quantum dots

Another interesting method is fabrication of semiconductor tubes by rolling up (fig. 36). The release of thin semiconductor layers from a substrate surface results in the formation of a novel class of free-standing nano- and microobjects. The right hand side shows a thin strained bilayer that rolls up into a tube as soon as the sacrificial buffer layer is selectively etched away. The technique allows accurately positioning of the novel semiconductor nanostructures and therefore constitutes a powerful method to combine top-down and bottom-up approach in nanotechnology.

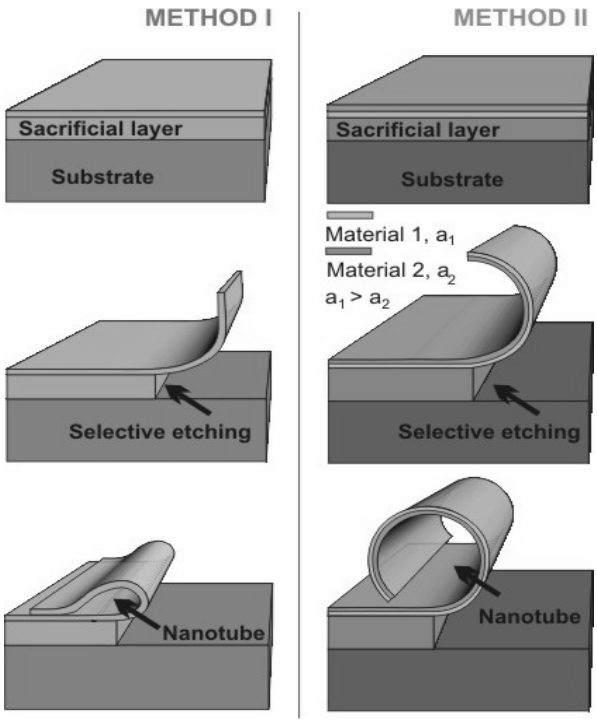

Fig. 36. Rolling up technique.

A lot of efforts are focused on development of the new and on improvement of the existing methods, to make the fabrication of nanoparticles more and more simpler, cheaper and easier to control.

5.6. Consolidation of nanopowders

To take advantage of the unique properties of bulk nanocrystalline materials, the nanometer range powders have to be densified into parts of certain properties, geometry, and size. The key to the nanopowder consolidation process is to achieve densification with minimal microstructural coarsening and/or undesirable microstructural transformations. In addition, the fully dense specimen must be of sufficient size for reliable testing of final properties or a useful final product. Attempts to produce and densify nanopowders started as early as 1968. These efforts were related to sintering MgO to achieve superplastic behavior. In the 80s, when nanopowder production was initiated on a larger scale, attention was directed to nanopowder processing. However, densification commonly resulted in either grain coarsening, or unacceptably small specimen size and insufficient bonding. Special precautions must be taken to reduce the interparticle friction and heating; as well as particles activity to minimize the danger of

explosion. The early 90s emphasized the need in development of the reproducible processing methods for manufacturing nanopowders into sizable parts that retain nanometer features. The past decade has brought significant advances in the practice and theory of nano-sintering which consequently resulted in the production of fully dense parts with nanometer grain size.

The densification process for conventional powders is well known, both theoretically and practically. However, the densification of nanopowders poses significant additional challenges. Powder agglomeration, high reactivity and, therefore, contamination, grain coarsening, and ultimate loss of the nano-features, and inability to fabricate large and dense parts are among the main problems. Outlined problems may adversely influence the overall quality of final product.

5.6.1. Sintering of nanoparticles

Thermodynamically, nanopowders are highly unstable. The sintering process is driven by the tendency to reduce the excessively large surface area per unit volume. For example, 1 kg of copper spherical particles of 5 nm in radius has a total surface area of around 75000 m^2, while the same amount of particles of radius 50 microns will have the surface area of 15 m^2. The extra energy of a surface with a radius of curvature, R, may be calculated as a stress (σ) in a Laplace equation:

$$\sigma = \gamma / R$$

where γ is the surface energy. In nanomaterials, this sintering stress may reach very high values. For instance, the sintering stress may be as large as 300 MPa in 10 nm particles compared to only 3 MPa for 1 μm particles, if γ has a typical value of 1.5 J/m^2.

Usually, the surface energy is assumed to be isotropic. For nanocrystals with significant surface area, the anisotropy problem becomes much more critical. First, sintering starts at a lower temperature. In this case, the effects of surface energy anisotropy are more pronounced. The highly anisotropic behavior of nanoparticle surfaces may be responsible for the crystallographic alignment, which has been often observed.

The first step of powder consolidation is *compaction* of nanopowders. To produce a so-called green body, process goes at relatively low or moderate temperatures. Most sintering defects may be related to the microstructure of such green body. Inhomogeneities in density, packing, and particle size in green compact will limit the final sintered density. Such an example is the crack generation in ceramics upon sintering inhomogeneous cold compacts. Generally, nanocrystalline powders are more sensible to defects in green compacts compared to conventional powders.

Due to Hall – Petch relationship between yield stress and particle size, the cold compaction of nanoparticles requires stresses in gigapascal range. That means the new non-conventional compaction routes are necessary.

On the nano-scale, mechanical friction becomes substantial due to many interparticle contacts. These forces are a result of mechanical, electrostatic, van der Waals, and surface adsorption phenomena that are much more significant when particle size decreases down to nanometers. Friction limits particles motion and rearrangement and may cause a lower density green body formation.

Rearrangement of the particles may be facilitated by the use of lubricants or water, often in combination with ultrasonic agitation or centrifuging to obtain an acceptable powder packing prior to pressing and/or sintering. Recently, osmotic compaction has

been applied to ceramic powder compaction based on the osmotic chemical potential action. Equal or greater green densities as compared to physical pressure applications have been achieved with no mechanical breakage that external forces may produce.

Sintering process starts when powder is packed together and heated to high temperatures, typically about $2T_{melt}/3$. At this stage, diffusion becomes significant. The densification process consists of solid particle bonding or neck formation followed by continuous closing of pores from a largely open porosity to essentially a pore-free body. Multiple mechanisms are involved throughout sintering process, namely, evaporation-condensation, surface diffusion, grain boundary diffusion, bulk diffusion, viscous flow, and plastic deformation. Each transport process exhibits a particular dependence on the particle/grain size and defect density. The highest sensitivity on particle size is that of surface and grain boundary diffusion. Although simultaneous mechanisms participate, the common sintering models attribute a predominant mass transport path to a specific sintering stage. For instance, surface diffusion is considered the principle mechanism during the initial stage when the main event is the neck formation. For nanoparticles with excessive surface area, highly curved surfaces, and reduced diffusion distances, surface diffusion is expected to be extremely rapid in early sintering stages. The general relationship between sintering parameters may be expressed as follows:

$$\frac{d\rho}{dt} \sim \frac{1}{d^n} exp\left(-\frac{Q}{RT}\right)$$

where n is a constant, ρ is the density, Q is the activation energy for sintering and d is the mean powder particle diameter. The n is usually about 3 and Q is considered to be equal to the activation energy for grain boundary diffusion.

Ideally, it would be desired to start sintering with producing a green body with a larger number of initial point contacts, smaller pores in a high density compact, and a uniform pore distribution. That would allow shortening the sintering time and using lower sintering temperatures may. The sintering of both metals and ceramics starts at temperatures of $0.2 - 0.4T_{melt}$ while sintering of conventional powders starts at 0.5–0.8 T_{melt}, Table 4. Full densification of nanopowders is completed at temperatures lower than that for conventional powders, Table 5.

Table 4. Sintering onset for different powders.

Material	Particle Size (nm)	T, K	T/T_m
TiO_2	40	950	0.46
TiO_2	13	823	0.4
ZrO_2	70	1370	~0.5
ZrO_2	8–9	870–920	~0.3
Fe	2000	~900	0.5
Fe	30	393	0.21

Table 5. Full densification of different powders.

Material	Particle size, nm	Temperature, K	Percentage of densification
TiC	140–170	1900	91
TiC	5000	3070	91
ZrO_2	nano sized	1745	100
ZrO_2	conventional	> 1975	100
TiO_2	12–14	1300	100
TiO_2	1300	>1630	100
TiN	nano sized	1823	100
TiN	conventional	1823	63

The lower temperatures for minimizing grain growth may hinder good intergranular bonding, thus compromising the expected high mechanical strength and ductility. Such low sintering temperatures may also interfere with the thermochemical oxide reduction on particle surfaces necessary for subsequent sinter bonding. The most recent efforts have been very fruitful in overcoming some of these problems (e.g., agglomeration and grain size control). This has been accomplished by major improvements in the nanopowder synthesis methods and understanding of the densification processes such as pore effects in nanosintering.

The most common problem is the elimination of large pores that originate from the green compact. This elimination requires high temperatures upon subsequent sintering, thereby, promoting unwanted grain growth and losing the desired nanosize features.

Similar to equation given above for sintering parameters, the pores fraction may be estimated by:

$$\frac{1}{\rho(t)(1-\rho(t))}\cdot\frac{d\rho}{dt}\sim\frac{1}{r_p(t)}\cdot\frac{1}{d^n}exp\left(-\frac{Q}{RT}\right)$$

where $\rho(t)$ and $r_p(t)$ are the instantaneous density and pore radius, respectively.

This equation predicts that the highest densification rate occurs for the finest pore size. This relationship has two implications. First, the pore size, in addition to grain size, should be controlled during sintering. Fast sintering kinetics result from fine pores' size. Second, the densification rate is dictated by the instantaneous pore size, not only the initial pore size. Therefore, to maintain a fast sintering rate, the pore should remain small even in late sintering stages. A small pore size throughout the sintering process is also critical in controlling the final grain size. For these purposes, a small and uniform pore population is desired in the green compact. Most often, such a pore distribution is associated with a high green density in non- or weakly agglomerated powders.

The success in nanopowder consolidation is intimately related to the control of the competition between densification and coarsening. The driving force for densification is largely due to the excess of surface energy. As sintering progresses and grain boundaries are created, the driving force, Δp, for mass transport may be expressed as a Gibbs-Thomson effect:

$$\Delta p=\frac{2\gamma_b}{d}+\frac{2\gamma}{r}$$

where γ_b is the grain boundary energy, d is the average grain size, γ is the surface free energy, and r is the radius of curvature of pore surfaces. The first term is the grain coarsening tendency, while the second is the sintering driving force. When pores are small, sintering predominates or the pores control grain growth. When particles bond and grain sizes are small, the driving force for coarsening becomes important. The key to nanopowder consolidation is to control this coarsening which inevitably competes with sintering.

As a surface controlled process, sintering is critically dependent on particle surface conditions, e.g. particle contamination. Particles produced by MA techniques are more contaminated than those fabricated by, for example, IGC. Oxides, nitrides, and other compounds picked-up from the milling media are often found in consolidated parts made of attrition-milled nanopowders. However, these compounds may prevent grain coarsening when present as fine dispersions. For instance, when the inherent surface SiO_2 is present on Si_3N_4 particles, sintering is enhanced, but creep strength and toughness are impaired during Si_3N_4 part service. For nano metals production, the oxygen contaminations may cause problems because metal oxides tend to form a thin film on the surface and inhibit sintering. To solve some problems in nano materials sintering, a number of non-conventional consolidation methods have been applied to nanopowder densification.

5.6.2. Non- conventional processing

To overcome the problem of grain growth, unconventional sintering and densification techniques have been proposed. These include the use of grain growth inhibitors, high-pressure densification, shock densification, magnetic pulse compaction, microwave heating and fieal assisted methods. However, while some success was attained by these methods, the results fall short of the ideal goal of having a fast, reproducible technique which can produce a large number of high density samples (e.g., >98% relative density) with a grain size below 20 nm. The ideal method should also be able to use agglomerated powders, which are the typical products of most wet chemistry methods developed in the last few years for the synthesis of pure and doped nanopowders. Therefore, the main purpose in using the non – conventional methods is to enhance densification, thus, reducing the sintering temperature or time with the ultimate benefit of preserving final fine grain sizes.

5.6.2.1. Microwave sintering

Microwave heating offers many advantages over conventional heating. *Microwave sintering* has a rapid processing time, two to fifty times faster than conventional heating. There is also an acceleration of sintering and diffusion in the material because of high electrical fields; thus densification can occur at lower temperatures. A typical microwave sintering apparatus operates at a 2.45 GHz frequency with power output in the range of 1–6 kW. The sintering chamber consists of ceramic insulation housing (batch system) or an alumina tube insulated with ceramic insulation from outside, figure 37. The primary function of the insulation is to preserve the heat generated in the work piece. The temperatures are monitored by optical pyrometers, IR sensors and/or sheathed thermocouples placed close to the surface of the sample. The system is equipped with appropriate technique to provide the desired sintering atmosphere, such as H_2, N_2, Ar, etc, and is capable of achieving temperatures up to 1600°C.

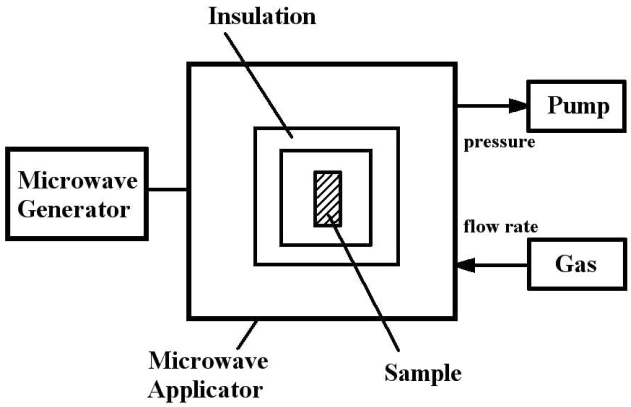

Fig. 37. Schematic diagram of microwave heating technique.

5.6.2.2. Field – assisted sintering (FAS)

One of the most interesting and promising methods of powder consolidation is *field – assisted sintering (FAS)*. Electric field assisted sintering is an emerging technology for the fabrication of metals, ceramics and their composites starting from powders. Field assisted sintering (FAS) often referred as spark plasma sintering (SPS) or pulsed electric current sintering (PECS). All these methods are essentially identical in the application of a pulsed discharge and subsequent or simultaneous resistance sintering. The technique is similar to traditional hot-pressing, but in this case the sample is heated by a high-intensity, low-voltage pulsed DC electric current flowing directly through the sample (if electrically conducting) and through a die, typically made out of graphite. This makes possible faster heating rates (up to 1000 °C/min) than in traditional hot-press systems. In addition to providing Joule heating, high intensity electric currents have also been shown to produce significant modification in the reactivity in several solid-state systems. Kinetically, activated sintering is a result of lowering the activation energies for densification. The schematic of FAS techniques is shown in figure 38.

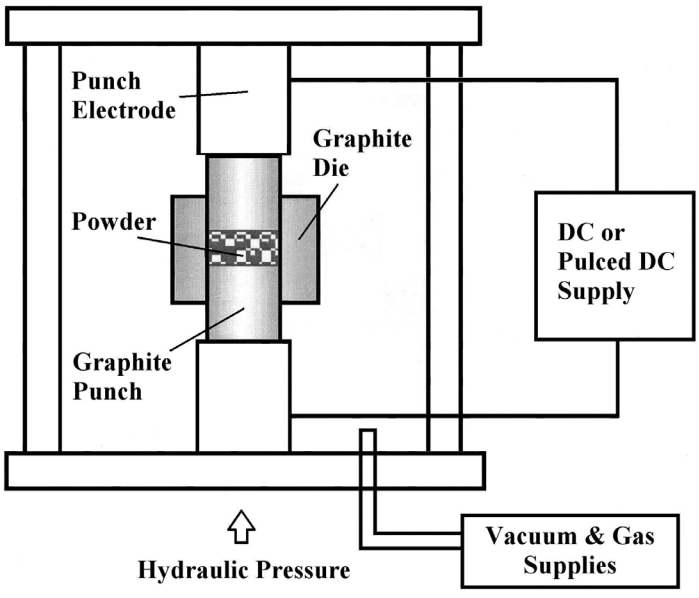

Fig. 38. Schematic diagram of a FAS technique.

The equipment consists of a mechanical device capable of uniaxial pressure application and electrical components to apply the pulsed and/or steady DC current. The loose powders are directly loaded into a punch and die unit without any additives. The machines are equipped with chambers for vacuum or controlled environment. The pressure used in the FAS method is generally limited by the compressive strength of the material used for the dies, which for typical high-density graphite is about 140 MPa. With such a pressure, combined with an appropriate thermal cycle, fully-dense ceramics with grain size between 50 and 100 nm can be obtained. The pressure may be constant throughout the sintering cycle or changed in different densification stages. The consolidation process consists of two stages: (1) an initial activation through the application of a pulsed voltage, and (2) the subsequent heating and densification by using DC current. The sintering cycles are very short. Typically less than 10 minutes for the full densification of both conductive and non-conductive materials. FAS for 3 minutes at 998^0C of mechanically synthesized Fe-85%Fe_3C achieved 99% density with a final grain size of 45 nm. This is to be compared to high isostatically pressing (HIP) of the same powders at 1298^0C for 60 minutes, with the same density value but final grain size of 87 nm. The pure $\alpha - Al_2O_3$ is consolidated to 99% density in less than 10 min at 1846^0 C. The conventional sintering of such powders reaches a similar density at 2046^0 C in 3 hours.

It was postulated that electrical current application creates favorable conditions for the removal of impurities and the activation of the powder particle surfaces. This activation explains the high densities obtained in ceramics without additives and direct grain – to – grain contact at atom scale. The pulsed current promotes electrical discharges at powder particle surfaces, thus activating them for subsequent bonding. Usually, FAS sintered materials are characterized by high densities and fine grain sizes. For instance, in TiN nanopowders, coarsening during FAS resulted in a final grain size that is at least 1 order of magnitude less than in the conventional sintering of the same powders. The limited coarsening observed in FAS sintering is attributed to a very short time at high temperatures and also reflects minimal coarsening during the initial and intermediate stages of sintering. Generally, significant densification with the little coarsening is noticed in specimens during heating phase. For example, the enhancement of the sintering behavior is observed in WC-Co powders during the heating before melting for a conventional liquid – phase sintering. The use of FAS in pre-melting state induced 98% density while only 70 % may be achieved with conventional sintering of the same powder. This enhanced low-temperature sintering is attributed to the surface activation and faster heating rate in FAS as compared to those in conventional sintering.

All FAS results indicate accelerated densification with minimum grain coarsening while achieving a good metallurgical grain-to-grain bonding. The latter may be partly explained by the ability to remove the oxides and impurities from the particle surfaces. In general the remaining oxides on powder particles are known to cause consolidation difficulties and low mechanical properties (e.g. ductility and fracture toughness) of the sintered part. These properties are critically dependent on the metallurgical bonding to take full advantage of the intrinsic strength of the material. Sintering at high temperatures in vacuum or reducing atmospheres usually provides good interparticle bonding due to oxide decomposition. In powders with more stable oxides direct grain contact may be achieved either by mechanical removal of the surface oxides or by physical activation of the particle surface prior to final densification. In field sintering oxide removal and subsequent good interparticle bonding may be attributed to phenomena ranging from resistance heating to thermal and electrical breakdown of insulating films and discharge or arcing. As in any sintering process field activated densification starts with a highly porous body. The initial pressure application proceeds

with neck formation. The neck formation is due to the geometric amplification of the pressure on the interparticle point contacts, but as the necks grow the local pressure at the necks is substantially reduced. At this stage the pulsed current is applied and a current path is established in metal or conductive ceramic powders. The goal is to achieve a uniform current path rather than local channels that may concentrate all passing current.

Another notable feature of FAS consolidation is the enhancement of either phase transformations in single phase ceramics (e.g., anatase to rutile in TiO_2) or in reactions of single components to form compounds (for example, the formetion of Al_2TiO_2 from Al_2O_3 and TiO_2 components).

5.6.2.3. Shockwave consolidation

Dynamic or shockwave consolidation proceeds with the passage of a large-amplitude compressive stress generated by plate impact or explosion without any external heating. Dynamic consolidation commonly uses explosives or high velocity impact to generate a shockwave. During the travel of the wave front, a pressure level exceeding 1 GPa is applied on a green compact confined in an enclosed container. The wave pressure imposes plastic deformation on the container, which results in an ultra-rapid consolidation of the powders into bulk materials. The high pressure is exerted for a very short duration, in the order of a microsecond, resulting in densification at extremely high strain rates (10^7–10^8 s^{-1}). Rapid processing induces particle surface heating, as compared to bulk heating for conventional processes, and allows interfacial melting while maintaining relatively low temperature inside the particles and providing densification by plastic yielding for both metals and ceramics. Localized heating due to particle interfriction enables good interparticle bonding. In nanosize powders, the heat may transfer throughout the entire particle, thus providing an advantage over coarser materials where the heating is only superficial. Best results are achieved when high temperatures are reached before the shockwave passes. If particles are heated, they may deform rather than fracture when the stress is applied. This very short, high-temperature exposure provides the best means to retain fine grain size or non-equilibrium conditions such as amorphous structures, or supersaturated solid solutions. The major drawback is the difficult coordination of these short stress and heat application events which may result in specimen cracking.

Shockwave consolidation has been applied to consolidation of both ceramic and metal nanoparticles. For instance, fully dense specimens with grain size of 20 nm were obtained in ball milled Fe-N solid solution. In the Ti-Si system, shock consolidation yielded 30–40 nm grain size of crystalline $TiSi_2$ and Ti_5Si_3 phases. Only limited grain coarsening took place upon subsequent annealing at 800°C for one hour. Full densification was also reported in mechanically alloyed TiAl specimens with final grain sizes of 15 nm. These results are compared with HIPping that provided full consolidation at 1348^0 C, 207 MPa, 2 hours, but grain sizes were about 100 nm.

6. PROPERTIES OF 3D0 NANOSTRUCTURED MATERIALS (NSM)

Nanomaterials can be metals, ceramics, polymeric materials, or composite materials. Their defining characteristic is a very small feature size in the range of 1–100 nanometers (nm). Nanomaterials are not simply another step in miniaturization, but a different arena entirely; the nanoworld lies midway between the scale of atomic and quantum phenomena, and the scale of bulk materials. At the nanomaterial level, some material properties are affected by the laws of atomic physics, rather than behaving as traditional bulk materials do.

The variety of nanomaterials is great, and range of their properties and possible applications appear to be enormous, from extraordinarily tiny electronic devices, including miniature batteries, to biomedical devices, and as packaging films, superabsorbants, components of armour, and parts of automobiles. General Motors claims to have the first vehicle to use the materials for exterior automotive applications, in running boards on its mid-size vans.

What makes these nanomaterials so different and so intriguing? Their extremely small feature size is of the same scale as the critical size for physical phenomena – for example, the radius of the tip of a crack in a material may be in the range 1–100 nm. The way a crack grows in a larger-scale, bulk material is likely to be different from crack propagation in a nanomaterial where crack and particle size are comparable. Fundamental electronic, magnetic, optical, chemical, and biological processes are also different at this level. Where proteins are 10–1000 nm in size, and cell walls 1–100 nm thick, their behaviour on encountering a nanomaterial may be quite different from that seen in relation to larger-scale materials. Nanocapsules and nanodevices may present new possibilities for drug delivery, gene therapy, and medical diagnostics.

By controlling the structures of nanomaterials at nano scale dimensions, the properties of the nanostructures can be tailored in a very predictable manner to meet the needs for a variety of applications. Examples of the engineered nanostructures include metallic and non-metallic nanoparticles, nanotubes, quantum dots and super lattices, thin films, nano composites and nanoelectronic and optoelectronic devices which utilize the superior properties of the nanomaterials to fulfil the applications.

In this chapter, the properties of nanomaterials will be shortly outlined together with the possible applications of nanomaterials.

6.1. Mechanical properties

As a primary microstructural parameter, grain size imparts significant influence on the mechanical behaviour of materials. The drive for refining grain size comes from the demand for increased strength in many applications. There is the general observation that the yield strength of metals is proportional to the inverse square root of grain size (the Hall–Petch relation):

$$\sigma = \sigma_o + kd^{-1/2},$$

where d is the average grain size; σ_o and k are constants. k may be defined as a slope of Hall-Petch plot, Fig. 17.

A number of mechanisms has been proposed to explain this phenomenon: pile-up of dislocations against the grain boundaries (GBs), GBs acting as dislocation sources and sinks, and presence of geometrically necessary dislocations in the vicinity of the GBs to account for the deformation compatibility of polycrystalline metals, etc.

Certainly, the grain size, or average grain diameter, influences the mechanical properties of a material. It is important to note in this context that the mechanisms of deformation and the properties of the NC material (NSM) not only depend on the average grain size, but are also strongly influenced by the grain size distribution and the grain boundary structure (e.g., low-angle versus high-angle grain boundaries).

Some appealing characteristics of nc metals and alloys with potential significance for engineering applications include ultra-high yield and strengths, decreased elongation and toughness, superior wear resistance, and the promise of enhanced superplastic formability at lower temperatures and faster strain rates compared to their micro structured counterparts. The need for scratch, mar and/or abrasion resistance is well established in various markets, including fingernail polishes, flooring, plastic glazing, headlamp covers and other automotive parts, transportation windows and optical lenses, where clear scratch-resistant coatings are used. Because the nanosize, many of their mechanical properties of the materials is modified, among others, hardness and elastic modulus, fracture toughness, scratch resistance, fatigue strength, and hardness. Energy dissipation, mechanical coupling within arrays of components, and mechanical nonlinearities are influenced by structuring components at the nanometer scale. This includes also the interpretation of unusual mechanical behaviour (e.g., strengths approaching the theoretical limit) and the exploration of new ways to integrate diverse classes of mechanically functional materials on the nano-size.

6.1.1. Hardness and strength

Adjacent grains normally have different crystallographic orientations and common grain boundary. In coarse grained materials, the grain boundary acts as a barrier to dislocation motion because of necessity in change of direction of motion in grain boundary regions and pile-up of dislocations at grain boundaries is envisioned as a key mechanistic process underlying an enhanced resistance to plastic flow from grain refinement. As the microstructure is refined from the micro and ultra-fine grained regime into the nc regime, this process invariably breaks down and the flow stress versus grain size relationship departs markedly from that seen at higher grain sizes, fig. 39. With further grain refinement, the yield stress peaks in many cases at an average grain size value on the order of 10 nm or so. Further decrease in grain size can cause weakening of the metal. Experimental evidence indicates that below a grain size of ~10 nm, strength decreases with further grain refinement (the so-called “inverse Hall-Petch-type” relationship).

Although there is a growing body of experimental evidence pointing to such unusual deformation responses in nc materials, the underlying mechanisms are not well understood yet.

The mechanical properties of fully-dense facial cubic centered metals (Cu, Ni and Pd) with grain size less than 100 nm have been primarily derived from uniaxial tension/ compression tests and micro- or nanoindentation. Typically, these nanocrystalline metals exhibit significantly higher yield strength, and reduced tensile elongation relative to their microcrystalline counterparts.

Furthermore, hardness and yield strength have been found to increase with decreasing grain size in this regime (<100 nm) down to at least 15 nm. The reasons for

this behaviour are still under debate as dislocation sources within grains are not expected to operate at these grain sizes. In addition, there is no documented evidence of dislocation pile-ups in deformed specimens, and any dislocation activity is primarily believed to originate and terminate at grain boundaries.

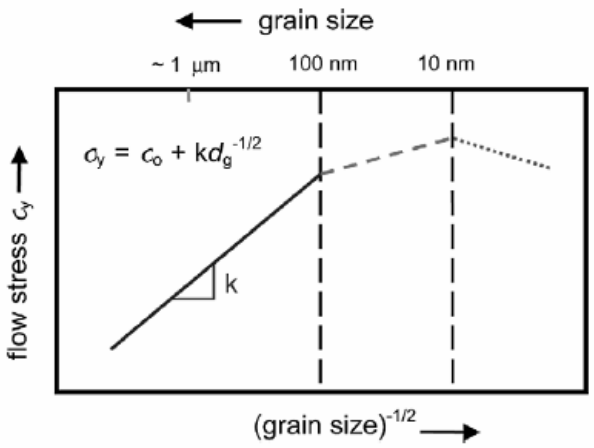

Fig. 39. Schematic representation of the variation of yield stress as a function of grain size (adapted from K. Kumar, et al., *Acta Materia*, 2003, v.51).

Among many excellent mechanical properties of nanomaterials, high hardness of nano-composites systems is one of the most intriguing. A variety of superhard nanocomposites can be made of nitrides, borides and carbides by plasma-induced chemical and physical vapor deposition. In the appropriately synthesized binary systems, the hardness of the nanocomposite exceeds significantly that given by the rule of mixtures in bulk. For example, the hardness of nc-M_nN/a– Si_3N_4 (M=Ti, W, V,…) nano-composites with the optimum content of amorphous Si_3N_4 matrix close to the percolation threshold reaches 50 GPa although that of the individual nitrides does not exceed 21 GPa. Elastic image forces are argued to require a very high stress to force dislocations to cut through the nanometer-sized nitride crystallites. This high stress may, however, not lead to fracture because any crack formed in one of the crystallites is suggested to be stopped by the ductile amorphous Si_3N_4 matrix surrounding the cracked crystallite. These superhard nanocomposites will have promising potential in hard protective coatings.

Superhardness also may come from pure nanoparticles. For example, the nearly spherical, defect-free silicon nanospheres with diameters from 20 to 50 nm possess hardness of up to 50 GPa or four times greater than that of the bulk silicon.

Since their discovery, carbon nanotubes have stimulated intensive research interests because of excellent mechanical properties. The strength of the carbon fibers increases with graphitization along the fibber axis. Carbon nanotubes, which are formed of seamless cylindrical graphene layers, represent the ideal carbon fibber and presumably have the best mechanical properties in the carbon fibbers species, showing a high Young's modulus and high tensile strength. Theoretical simulations have predicted the high modulus of carbon nanotubes. Calculated Young's module Y of single wall carbon nanotubes is found to be in the range of 0.5–5.5 TPa, that is much higher than high-strength steel (Y ~200 GPa).

The experimental measurements of Young's modulus of multiwalled carbon nanotubes with the help of thermal vibrations studying by means of transmission electron microscopy (TEM), give the value of Young's modulus of 1.8+/-0.9 TPa.

Atomic force microscope (AFM) has also been employed to measure the modulus of the carbon nanotubes. This is realized by bending the anchored carbon nanotubes with AFM tip while simultaneously recording the force by the tube as a function of the displacement from its equilibrium position. The resultant Young's modulus was 1.28+/-0.5 TPa. The values of Young's module measured from different ways were all in the range in theoretical prediction, proving the existence the high elastic modulus of the carbon nanotubes.

The tensile strength of carbon nanotubes has also been under consideration. An individual multi wall carbon nanotube was mounted between two AFM tips, one on rigid cantilever and the other on soft cantilever. By recording the whole tensile loading experiment, both the deflection of the soft cantilever from which the force applied on the nanotube and the length change of the nanotube were simultaneously obtained. The carbon nanotubes broke in the outermost layer ("sword-in-sheath" failure), and the tensile strength of this layer ranged from 11 to 63 GPa and the measured strain at failure can be as high as 12%. For comparison, the tensile strength of high-strength steel is 1–2 GPa.

Enhancement of mechanical properties of polymeric materials by nanofillers is one of the very active applications of nanomaterials. Micrometer size fillers used in traditional polymer composites show improvements in their mechanical properties such as the modulus, yield strength and glass transition temperature. However, these enhancements sacrifice the ductility and toughness of the materials. Comparably, polymer nanocomposites from nano size fillers result in unique mechanical properties at very low filler weight fractions. The dramatic improvements in the yield stress (30%) and Young's modulus (170%) in polypropylene filled with ultrafine SiO_2, as compared to micrometer-filled polypropylene, has been reported. A rubbery polyurethane elastomer filled with 40wt% of 12 nm silica particles exhibits 6 times increase in the elongation-at-break and 3 times increase in the modulus as them compared to a micrometer-sized filler reinforced polymer.

6.1.2. Ductility

Nc materials often exhibit low tensile ductility which essentially limits their practical use. The tensile elongation at fracture of nc metals is low relative to their conventional mc counterparts. There are three factors limiting the ductility: the presence of structural artefacts arising from processing, such as porosity and cracks; crack nucleation or propagation instability; plastic instability in tension. Defects obviously decrease a fracture strength as they serve as a crack initiation sites resulting in easy crack nucleation and growth, promoting brittle behavior in tension and causing failure before yielding has chance to occur. Plastic instability originates from the lack of an effective hardening mechanism and/or internal flaws; this instability manifests itself as either shear bands or through "early" necking.

During deformation, the dislocation storage and annihilation at grain boundaries are two key competing mechanisms influencing the level of the flow stress. The absence of substantial macroscopic tensile ductility in nanocrystalline fcc metals together with the observation of dimpled rupture on fracture surfaces leads to the hypothesis that deformation is localized. Localized deformation is clearly manifested through the appearance of shear bands on deformed specimen surfaces as shown in fig. 40.

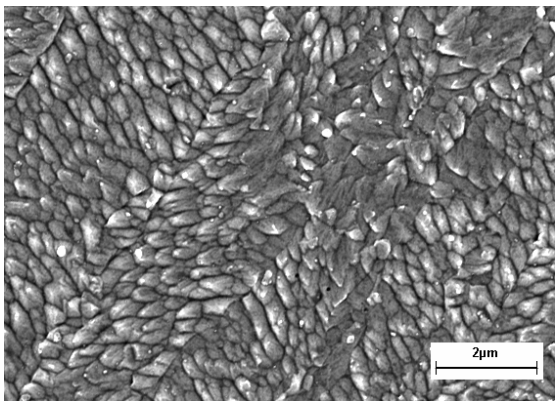

Fig. 40. Shear bands in ultra-fine grained copper produced by SPD method.

Plastic flow localization in materials in the absence of strengthening leads to the macroscopic necking, fig. 41, followed by the stress concentration in the neck region. Importance of the presence of nano-scale voids in the structure prior to deformation is now well understood. For example, the magnetron sputtered Ni, containing some grain boundary porosity, failed in a brittle manner via rapid coalescence of intergranular cracks whereas in the laser deposited film that contained no porosity the crack propagated slowly and is accompanied by continuous film thinning.

Fracture surfaces resulting from tensile tests have frequently shown dimpled rupture in nc metals, fig. 42. Further, it has been shown that the dimple size is significantly larger than the average grain size; in addition, a pair of mating fracture surfaces illustrates the presence a significant stretching of the ligaments between the dimples that indicates an appreciable local plasticity.

When the grain size is reduced down to ~10 nm or less, the resulting fracture surface still shows the dimpled rupture. Only a difference is that the dimple diameter is finer in size (but still much larger than the grain size).

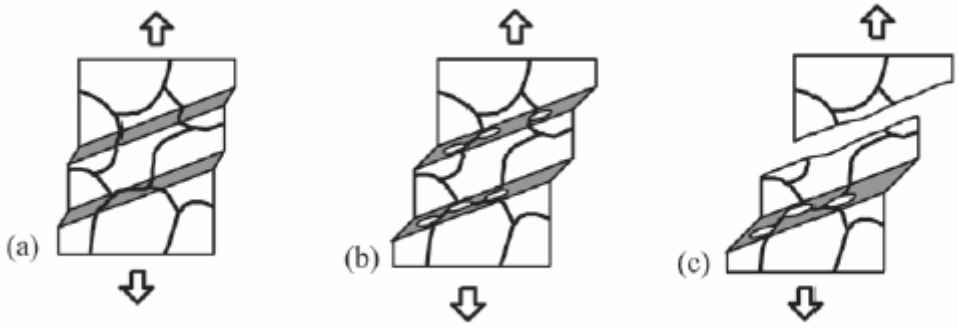

Fig. 41. Deformation and fracture of ultra-high-fine materials: (a) Plastic flow localization; (b) nanockrack nucleation; (c) final failure.

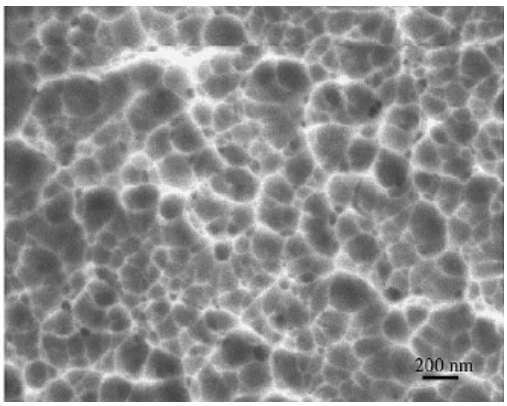

Fig. 42. Fracture surface of a 30 nm grain size electrodeposited Ni tensile specimen.

Based on the observations of dimpled rupture, dislocation activity at the crack tip, and the formation of voids at grain boundaries and triple junctions in the regions ahead of the advancing crack, a model for damage evolution and fracture was proposed and schematically depicted in fig. 43. In the early stages of deformation, dislocations are emitted from grain boundaries under the influence of an applied stress, when intragranular slip is coupled with unaccommodated grain boundary sliding to facilitate void formation at the grain boundaries. Such voids do not necessarily form at every boundary. Triple junction voids and wedge cracks can also result from grain boundary sliding if resulting displacements at the boundary are not accommodated by diffusional or power law creep. These grain boundary and triple junction voids then act as sites for nucleation of the dimples which are significantly larger than the individual grains and the rim of these dimples on the fracture surface do not necessarily coincide with grain boundaries. Thus, at a local level, the NSM demonstrates considerable plasticity and could represent localized deformation within a shear band.

The deformation and fracture processes are closely related to the coupling of dislocation-mediated plasticity and formation and growth of voids. The fundamental difference between the two approaches is that the atomistic simulations reveal intergranular crack propagation, where the GBs that are chosen by the crack path are determined by plastic deformation processes, whereas the model illustrated in fig. 43 proposes the formation of local ligaments with free surfaces as the voids evolve, stretching in concert and finally leading to transgranular fracture. Whatever the fracture mechanism, it is evident that the fracture will be heavily influenced by microstructural features such as the presence of nano-scale voids or even bubbles and the presence of grown-in twins. It is well known that bubbles filled with hydrogen (hydrogen bubbles) are often present in electrodeposited metals and these could serve as nucleation sites for the dimples. Additionally, in NSM the presence of nanovoids of 10–20 vacancies is a common feature, and voids are considered to populate grain boundaries and triple junctions. However, their location has not been experimentally verified. Presence of twins has been suggested as an inter-face control mechanism in coarse-grained metals and may represent a relevant microstructural feature that influences fracture, since many of the NS metals contain grown-in twins.

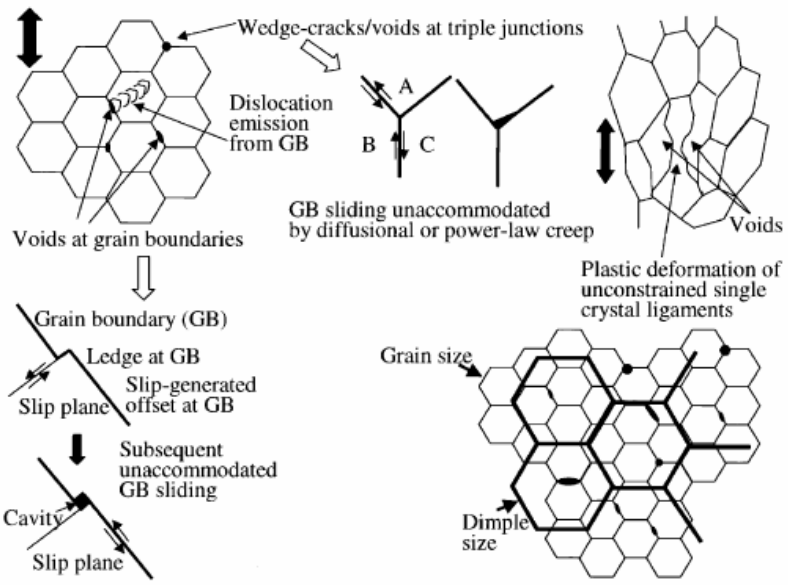

Fig. 43. A schematic illustration depicting how deformation evolves in nanocrystalline metals. Dislocation motion, void formation/growth at grain boundaries and triple junctions, the formation of partially unconstrained ligaments that deform plastically, and the interaction of these various features to produce the eventual fracture morphology are all synthesized in this figure (from Kumar et al., *Acta Materialia*, 2003, v.51, 5743 – 5774).

To improve the ductility of nanomaterials, four basic concepts are proposed. The first option is to suppress plastic flow localization through fabrication of a bimodal single-phase structure composed of nanograins and large grains, fig. 44a. The second strategy is to suppress plastic flow localization through fabrication of a composite structure consisting of ductile second – phase inclusions embedded into a nc matrix, fig. 44b. Localization of the plastic flow is effectively hampered due to the strengthening effects provided by large grains and inclusions, respectively.

The next option is to deform materials at low temperatures. In this case, recovery or dislocation annihilation, processes at grain boundaries are suppressed and do not compensate the dislocation storage at the boundaries. As a result, a nc specimen shows a good ductility due to strengthening that prevents plastic flow localization.

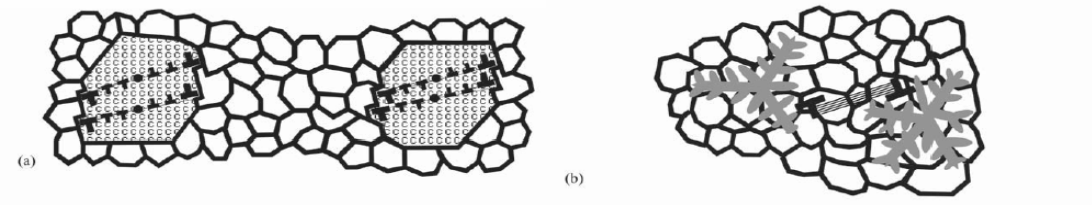

Fig. 44. NC materials with high ductility: (a) a bimodal single-phase structure composed of nanograins and large grains; and (b) nano-composite consisting of nanoscale grains and dendrite – like inclusions of the second phase (from I.A. Ovid'ko, *Rev. Adv. Mater. Sci*., 2005, v.10, 89–104).

The fourth option is using a positive strain rate sensitivity of the flow stress. The sensitivity means that a local increase of the plastic strain rate in the neck region leads to a local increase in a flow stress.

6.1.3. Applications of Mechanical Properties of NSM

Enhanced mechanical properties of the nanomaterials have many potential applications both in nano scale such as mechanical nano resonators, mass sensors, microscope probe tips and nano tweezers for nano scale object manipulation, and in macro scale applications such as structural reinforcement of polymer materials, light weight high strength materials, flexible conductive coatings, wear resistance coatings, tougher and harder cutting tools etc.

Cutting tools made of nanomaterials, such as tungsten carbide, tantalum carbide, and titanium carbide, are much harder, much more wear-resistant, erosion-resistant, and last longer than their conventional (large-grained) counterparts. Also, for the miniaturization of microelectronic circuits, the industry needs micro drills (drill bits with diameter less than the thickness of an average human hair or 100 μm) with enhanced edge retention and far better wear resistance. Since nanocrystalline carbides are much stronger, harder, and wear-resistant, they are currently being used in these micro drills.

In automobiles, nanomaterials are envisioned to be used in spark plugs. Also, automobiles waste significant amounts of energy by losing the thermal energy generated by the engine. So, the engine cylinders are envisioned to be coated with nanocrystalline ceramics, such as zirconia and alumina, which retain heat much more efficiently that result in complete and efficient combustion of the fuel.

One of the key properties required of the aircraft components is the fatigue strength, which decreases with the component's age. The fatigue strength increases with a reduction in the grain size of the material. Nanomaterials provide such a significant reduction in the grain size over conventional materials that the fatigue life is increased by an average of 200–300%. In spacecrafts, elevated-temperature strength of the material is crucial because the components (such as rocket engines, thrusters, and vectoring nozzles) operate at much higher temperatures than aircrafts and higher speeds. Nanomaterials are perfect candidates for spacecraft applications, as well.

Ceramics are very hard, brittle, and hard to machine even at high temperatures. However, with a reduction in grain size, their properties change drastically. Nanocrystalline ceramics can be pressed and sintered into various shapes at significantly lower temperatures. Zirconia, for example, is a hard, brittle ceramic, has even been rendered superplastic, i. e., it can be deformed to great lengths (up to 300% of its original length). However, these ceramics must possess nanocrystalline grains to be superplastic. Ceramics based on silicon nitride (Si_3N_4) and silicon carbide (SiC), have been used in automotive applications as high-strength springs, ball bearings, and valve lifters, and because they possess good formability and machinabilty combined with excellent physical, chemical, and mechanical properties. They are also used as components in high-temperature furnaces.

Aerogels are nanocrystalline porous and extremely lightweight materials and can withstand 100 times their weight. They are currently being used for insulation in offices, homes, etc. They are also being used as materials for "smart" windows, which darken when the sun is too bright and they lighten themselves otherwise.

6.2. Thermal properties of NSM

Many properties of the nanoscale materials have been well studied, including the optical electrical, magnetic and mechanical properties. However, the thermal properties of nanomaterials have only shown a slower progress. This is partially due to the difficulties of experimental measuring and controlling the thermal transport in nano scale dimensions. Atomic force microscope (AFM) has been introduced to measure the thermal transport of nanostructures with nanometer-scale high spatial resolution, providing a promising way to probe the thermal properties. Moreover, the theoretical simulations and analysis of thermal transport in nanostructures are still in infancy. Available approaches including numerical solutions of Fourier's law, computational calculation based on Boltzmann transport equation and molecular-dynamics (MD) simulation. More important, as the dimensions go down into nanoscale, the definition of temperature becomes questionable. In non-metallic material system, the thermal energy is mainly carried by phonons, which have a wide variation in frequency and the mean free paths (mfp). The heat carrying photons often have large wave vectors and mfp in the order of nanometer range at room temperature, so that the dimensions of the nanostructures are comparable to the mfp and wavelengths of photons. However the general definition of temperature is based on the average energy of a material system in equilibrium. For macroscopic systems, the dimension is large enough to define a local temperature in each region within the materials and this local temperature will vary from region to region, so that one can study the thermal transport properties of the materials based on certain temperature distributions in the material. But for nc systems, the dimensions may be too small to define a local temperature. Moreover, it is also problematic to use the concept of temperature which is defined in equilibrium conditions for the non-equilibrium processes of thermal transport in nanomaterials posing difficulties for theoretical analysis of thermal transport in nano scales.

In spite of all the difficulties in both experimental and theoretical characterization the thermal properties of nanomaterials, recent advances in experiments have shown that certain nanomaterials have extraordinarily thermal properties compared to their macroscopic counterparts. For example, silicon nanowires have a much smaller thermal conductivities compared to bulk silicon. Because of tubular structures of carbon nanotubes, they have extreme high thermal conductivity in axial directions and high anisotropy in the heat transport over the specimen. Interfaces are also very important factor for determine the thermal properties of nanomaterials. Generally, the internal interfaces impede the flow of heat due to photon and phonon scattering. At interface or grain boundary between similar materials, the interface disorder scatters phonons, while as the differences in elastic properties and densities of vibration states affect the transfer of vibration energy across interfaces between dissimilar materials. As a result, the nc structures with high interfaces densities reduce the thermal conductivity of the materials. These interconnected factors joined together to determine the special thermal properties of the nanomaterials.

For instance, carbon nanotubes are carbon nanostructures relating to diamond and graphite, which are well known for their high thermal conductivities. The stiff sp^3 bonds in diamond structure result in high phonon velocity and consequently high thermal conductivity. In carbon nanotubes, the carbon atoms are held together by the even stronger sp^2 bonds, so that the nanotube structures, consisting of seamlessly joined graphitic cylinders are expected to have extraordinary high thermal conductivity. The rigidity of the these nanotubes, combined with virtual absence of atomic defects or coupling to soft photon modes of the embedding medium, should make isolated nanotubes very good candidates for efficient thermal conductors. On the other hand,

one-dimensional nanowires may offer ultra low thermal conductivities, quite different from that of carbon nanotubes. In nanowires, phonons behave differently from those in the corresponding bulk materials due to the quantum confinement in the one dimension structures. The nanowires surface can introduce surface phonon modes, resulting in many different phonons polarizations other than the two transverse and one longitudinal acoustic branch found in the bulk semiconductors. Those changes in the dispersion relation can modify the group velocity and the density of states of each branch. The phonon lifetime also changes due to the strong phonon–phonon interactions and the boundary scattering within the nanostructures. Thus the phonon transports and the thermal properties of the nanowires will be significantly different from that of the bulk materials.

The phonon transport of the semiconducting nanowires has been studied experimentally and theoretically. Measurement of the thermal conductivity of silicon nanowires using a microfabricated suspended device over a temperature range of 20–320 K shows that although the nanowires had a well-defined crystalline order as in bulk materials, the observed thermal conductivity was more than two orders of magnitude smaller than that of bulk silicon, which also shows a strong dependence on the nanowires size. For a silicon nanowire with 22 nm diameter, the thermal conductivity was reduced to 10 W/m range. The appreciable change of the thermal conductivity compared to the bulk materials was ascribed to phonon–boundary scattering and the possible change in phonon dispersion due to confinement within the nanostructures.

Besides the one dimensional nanowires, multi-layers and superlattices are another type of nc structures offering low thermal conductivity. Multi-layers and superlattices are thin films consisted of alternating layers of two or more different materials stacked upon each other. In multi-layer structure, the films can be either amorphous or polycrystalline while in superlattices the films are single crystal. There are many effects in the multi-layers or superlattices structures that affect the phonon transport properties. When alternating layers of materials are stacked together, many collective mode of phonon transport may appear besides the phonon modes in each single layer. This stacking effect will be more apparent when the coherence phonon length scales are much larger than that of a single layer. It is also a coupled behaviour resulting from interference of phonon waves reflected from multiple interfaces. When the mean free path of phonons span multiple interfaces, the phonon dispersion relation is modified and zone folding occurs, even resulting in multiple phonon band gaps. Moreover, due to the modification of the phonon dispersion, the phonon group velocities will be reduced significantly and the scattering rate will also be increased. The interfaces is also an important factor in determine the phonon transport properties due to the high density of interfaces in the multi-layers or superlattices structures, as well. For example, if two materials in the superlattice have large mismatch in the phonon dispersion relations, phonons in certain frequency range cannot propagate to the neighbouring layer unless there are mode conversions at the interface. The interfaces between two different materials with different lattice constants can contain dislocations and defects, which can also scatter phonons and reduce thermal conductivity. Physical roughness and alloying may also exist at the interface depending on the processing and affect the phonon transport. The overall effect in of these factors on the phonon transport is a general decrease of thermal conductivities.

For example, atomic layer deposition and magnetron sputter deposition were used to synthesize thin-film multi-layers of W/Al_2O_3. With individual layers only of a few nanometers thick, the high interface density produced a strong impediment to heat transfer, giving an ultra low thermal conductivity of 0.6 W/mK.

Multi-layers and superlattice nanostructures have many potential applications. For example, multilayer thin films can be used as thermal barriers at high temperatures environments, such as in engines to improve their efficiencies; epitaxial superlattices of semiconductor films with low thermal conductivity can be used in thermoelectric power generation because of the ability to the control both electronic band structure and phonon transport simultaneously.

The use of nanofluid to enhance the thermal transport is another promising application of the thermal properties of nanomaterials. Nanofluids are generally referred to the solid-liquid composite materials, which consist of nanomaterials of size in the range 1–100nm suspended in a liquid. Nanofluids hold increasing attentions in both research and practical applications due to their greatly enhanced thermal properties compared to their base fluids. Many type of nanomaterials can be used in nanofluids including nanoparticles of oxides, nitrides, metals, metal carbides, and nanofibers such as single wall and multi wall carbon nanotubes, which can be dispersed in to a variety of base liquid depending on the possible applications, such as water, ethylene glycol, and oils. The most important features of nanofluids are the significant increase of thermal conductivity compared with liquids without nanomaterials, which have been proved by many experimental works.

6.3. Electrical Properties of NSM

The effects of size on electrical conductivity of nanostructures and nanomaterials are complex, since they are based on distinct mechanisms. These mechanisms can be generally grouped into four categories: surface scattering including grain boundary scattering, quantized conduction including ballistic conduction, Coulomb charging and tunneling, and widening and discrete of band gap, and change of microstructures. In addition, increased perfection, such as reduced impurity, structural defects and dislocations, would affect the electrical conductivity of nanostructures and nanomaterials.

Nanomaterials can hold considerably more energy than conventional ones because of their large grain boundary area. They are materials in which an optical absorption band can be introduced, or an existing band can be altered by the passage of current through these materials, or by the application of an electric field.

Tremendous efforts and progress have been made in the molecular electronics and nanoelectronics. In molecular electronics, single molecules are expected to be able to control electron transport, which offers the promise of exploring the vast variety of molecular functions for electronic devices, and molecules can now be crafted into a working circuit as shown schematically in fig. 45. When the molecules are biologically active, bioelectronic devices could be developed. In molecular electronics, control over the electronic energy levels at the surface of conventional semiconductors and metals is achieved by assembling on the solid surfaces, poorly organized, partial monolayers of molecules instead of the more commonly used ideal ones. Once those surfaces become interfaces, these layers exert electrostatic rather than electrodynamic control over the resulting devices, based on both electrical monopole and dipole effects of the molecules. Thus electronic transport devices, incorporating organic molecules, can be constructed without current flow through the molecules.

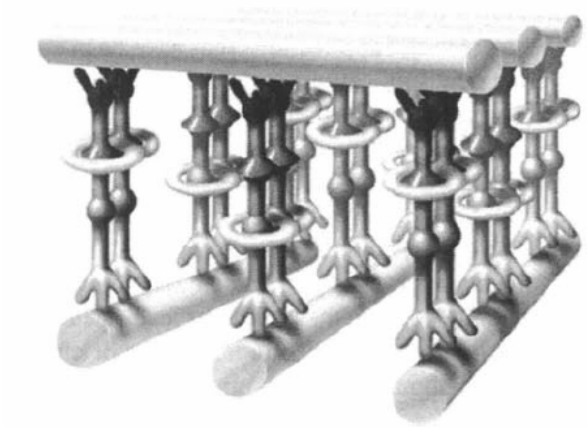

Fig. 45. Schematic of the molecules crafted into working circuit (from R.F. Service, *Science*, 2001, 293).

The simplest molecular electronics are sensors that translate unique molecular properties into electrical signals. Sensors using a field effect transistor (FET) configuration with its gate displaced into a liquid electrolyte, and an active layer of molecules for molecular recognition were reported in early 70s. A selective membrane is inserted on the insulator surface of the FET, and this permits the diffusion of specific analyte ions and construction of a surface dipole layer at the insulator surface. Such a surface dipole changes the electric potential at the insulator surface and, thus, permits the current going through the device. Such devices are also known as ion-selective FET (ISFET) or chemical FET (CHEM-FET). Thin films attached to metal nanoparticles have been shown to change their electrical conductivity rapidly and reproducibly in the presence of organic vapors, and this has been exploited for the development of novel gas sensor. The monolayer on metal nanoparticles can reversibly adsorb and desorb the organic vapor, resulting in swelling and shrinking of the thickness of the monolayer, thus changing the distance between the metal cores. Since the electron hopping conductivity through the monolayers is sensitively dependent on the distance, the adsorption of organic vapor increases the distance and leads to a sharp decrease in electrical conductivity.

Conventional and rechargeable batteries are used in almost all applications that require electric power. The energy density (storage capacity) of these batteries is quite low requiring frequent recharging. Nanocrystalline materials are good candidates for separator plates in batteries because they can hold considerably more energy than conventional ones. Nickel-metal hydride batteries made of nanocrystalline nickel and metal hydrides are envisioned to require far less frequent recharging and to last much longer.

An electrochromic device consists of materials in which an optical absorption band can be introduced, or an existing band can be altered by the passage of current through the materials or by the application of an electric field. They are similar to liquid-crystal displays (LCD) commonly used in calculators and watches and are primarily used in public billboards and ticker boards to convey information. The resolution, brightness, and contrast of these devices depend on the tungsten acid gel's grain size. Hence, nanomaterials, such as tungstic oxide gel, are being explored for this purpose.

Many nanoscale electronic devices have been demonstrated: tunneling junctions, devices with negative differential electrically configurable switches, carbon nanotube transistors, and single molecular transistors. Devices have also been connected together

to form circuits capable of performing single functions such as basic memory and logic functions. Ultrahigh density nanowires lattices and circuits with metal and semiconductor nanowires have also been demnstrated.

6.4. Optical Properties of NSM

Nanocrystalline systems have attracted much interest for their novel optical properties, which differ remarkably from bulk crystals. Key contributory factors include quantum confinement of electrical carriers within nanoparticles, efficient energy and charge transfer over nanoscale distances and in many systems a highly enhanced role of interfaces. The linear and nonlinear optical properties of such materials can be finely tailored by controlling the crystal dimensions, and the chemistry of their surfaces, fabrication technology becomes a key factor for the applications.

Surface plasmons, also known as surface plasmon polaritons, are surface electromagnetic waves that propagate parallel along a metal/dielectric (or metal/vacuum) interface. Since the wave is on the boundary of the metal and the external medium (air or water for example), these oscillations are very sensitive to any change of this boundary, such as the adsorption of molecules to the metal surface.

At an interface between two transparent media of different refractive index (glass and water), light coming from the side of higher refractive index is partly reflected and partly refracted. Above a certain critical angle of incidence, no light is refracted across the interface, and total internal reflection is observed. While incident light is totally reflected the electromagnetic field component penetrates a short (tens of nanometers) distance into a medium of a lower refractive index creating an exponentially detenuating evanescent wave. If the interface between the media is coated with a thin layer of metal (gold), and light is monochromatic and p-polarized, the intensity of the reflected light is reduced at a specific incident angle producing a sharp shadow (called surface plasmon resonance) due to the resonance energy transfer between evanescent wave and surface plasmons. Resonance conditions are influenced by the material adsorbed onto the thin metal film. Satisfactory linear relationship is found between resonance energy and mass concentration of biochemically relevant molecules such as proteins, sugars and DNA. The SPR signal which is expressed in resonance units is therefore a measure of mass concentration at the sensor chip surface. This means that the analyte and ligand association and dissociation can be observed and ultimately rate constants as well as equilibrium constants can be calculated.

Surface plasmon resonance is the coherent excitation of all the “free” electrons within the conduction band, leading to an in-phase oscillation. When the size of a metal crystal is smaller than the wave-length of incident radiation, a surface plasmon resonance is generated. Fig. 46 shows schematically generation of the surface plasmon oscillation.

For nanoparticles, localized surface plasmon oscillations can give rise to the intense colors of solutions of plasmon resonance nanoparticles and/or very intense scattering. Nanoparticles of noble metals exhibit strong ultraviolet – visible absorption bands that are not present in the bulk metal. Shifts in this resonance due to changes in the local index of refraction upon adsorption of biopolymers to the nanoparticles can also be used to detect biopolymers such as DNA or proteins. Related complimentary techniques include plasmon waveguide resonance, and Dual Polarization Interferometry.

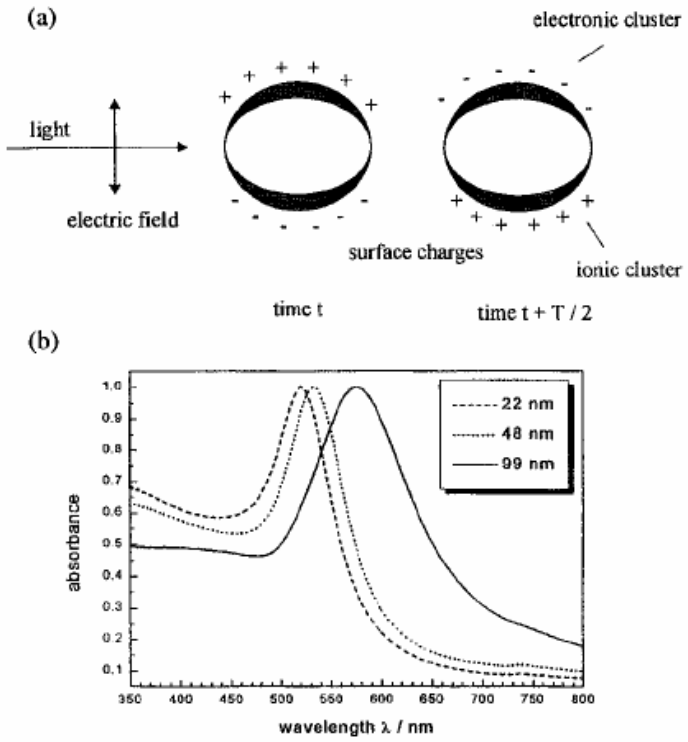

Fig. 46. Surface plasmon absorption of spherical nanoparticles and its size dependence. (a) **A** schematic illustrating the excitation of the dipole surface plasmon oscillation. The electric field of an incoming light wave induces a polarization of the (free) conduction electrons with respect to the much heavier ionic core of a spherical metal nanoparticle. **A** net charge difference is only felt at the nanoparticle surfaces, which in turn acts as a restoring force. In this way a dipolar oscillation of the electrons is created with period *T*. (b) Optical absorption spectra of 22, 48 and 99nm spherical gold nanoparticles. The broad absorption band corresponds to the surface plasmon resonance (from S. Link, **M.A.** El-Sayed *Int. Rev. Phys. Chem.* 2000, v.19, 409)

Unique optical property of nanomaterials may also arise from another quantum size effect. When the size of a nanocrystal (i.e. a single crystal nanoparticle) is smaller than the de Broglie wavelength, electrons and holes are spatially confined and electric dipoles are formed, and discrete electronic energy level would be formed in all materials. Similar to a particle in a box, the energy separation between adjacent levels increases with decreasing dimensions. The electronic configurations of nanomaterials are significantly different from that of their bulk counterpart. These changes arise through systematic transformations in the density of electronic energy levels as a function of the size, and these changes result in strong variations in the optical and electrical properties with size. Nanocrystals lie in between the atomic and molecular limit of discrete density of electronic states and the extended crystalline limit of continuous band. In any material, there will be a size below which there is substantial variation of fundamental electrical and optical properties with size, when energy level spacing exceeds the temperature. For a given temperature, this occurs at a very large size (in nanometers) in semiconductors as compared with metals and insulators. In the case of metals, where the Fermi level lies in the center of a band and the relevant energy level spacing is very small, the electronic and optical properties more closely resemble those of continuum, even in relatively small sizes (tens or hundreds of atoms). In semiconductors, the Fermi level lies between two bands, so that the edges of the bands

are dominating the low-energy optical and electrical behavior. Optical excitations across the gap depend strongly on the size, even for crystallites as large as 10,000 atoms. For insulators, the band gap between two bands is already too big in the bulk form.

The quantum size effect is most pronounced for semiconductor nanoparticles, where the band gap increases with a decreasing size, resulting in the interband transition shifting to higher frequencies. In a semiconductor, the energy separation, i.e. the energy difference between the completely filled valence band and the empty conduction band is of the order of a few electrovolts and increases rapidly with a decreasing size.

The same quantum size effect is also known for metal nanoparticles; however, in order to observe the localization of the energy levels, the size must be well below 2 nm, as the level spacing has to exceed the thermal energy (–26 meV). In a metal, the conduction band is half filled and the density of energy levels is so high that a noticeable separation in energy levels within the conduction band (intraband transition) is only observed when the nanoparticle is made up of 100 atoms. If the size of metal nanoparticle is made small enough, the continuous density of electronic states is broken up into discrete energy levels.

Glues containing nanoparticles have optical properties that give rise to uses in optoelectronics. Casings, containing nanoparticles used in electronic devices, such as computers, offer improved shielding against electromagnetic interference. Electro-chromic, devices are similar to liquid-crystal displays (LCD), are been developed with nanomaterials.

The incorporation of nanomaterials in surface coatings can provide long-term abrasion resistance without significantly effecting optical clarity, gloss, colour or physical properties.

The cosmetics industry has used nanomaterials as UV absorbers or sunscreens.

6.5. Chemical Properties of NSM

One of the important factors for the chemical applications of nanomaterials is the increment of their surface area which increases the chemical activity of the material.

Due to their enhanced chemical activity, nanostructural materials can be used as *catalysts* to react with such noxious and toxic gases as carbon monoxide and nitrogen oxide in automobile catalytic converters and power generation equipment to prevent environmental pollution arising from burning gasoline and coal.

Bulk gold is chemically inert and thus considered to be not active or useful as a catalyst. However, gold nanoparticles can have excellent catalytic properties. For example, gold nanoparticles with clean surface have demonstrated to be extremely active in the oxidation of carbon monoxide if deposited on partly reactive oxides, such as Fe_20_3, NiO and MnO, alumina and titania and are also found to be reactive. Au nanoparticles also exhibit extraordinary high activity for partial oxidation of hydrocarbons, hydrogenation of unsaturated hydrocarbons and reduction of nitrogen oxides.

Fuel cell technology is another important application of the noble metal nanoparticles relating the catalysis of the reactions. In the present, the fuel cell catalysts are based on platinum group metals (PGM). Pt and Pt-Ru alloys are some of the most frequently used catalysts from this group. In fact, the use of these metals is one major factor for cell costs, which has been one of the major drawbacks preventing it from growing into a more important technology. One possibility to produce economical catalysts is the use of bimetallic nanoparticles.

6.6. Magnetic Properties of NSM

Magnetic materials are those that exist in a state of permanent magnetization without the need to apply a field. The strength of a magnet is measured in terms of saturation magnetization and coercivity (H_c is the field required to reduce the magnetization to zero from saturation, and is applied in the opposite direction to the original saturating field) values. These values increase with a decrease in the grain size and an increase in the specific surface area (surface area per unit volume) of the grains. Therefore nanomaterials present also good properties in this field.

There are three main categories of magnetism: diamagnetism, paramagnetism and ferromagnetism. Diamagnetism is a fundamental property of all atoms and the magnetization is very small and opposed to the applied magnetic fields direction. However, many materials exhibit paramagnetism, where a magnetization develops parallel to the applied magnet field as the field is increased from zero, but the strength of the magnetization is small. Ferromagnetism is the property of those materials which are intrinsically magnetically ordered and which develop spontaneous magnetization without the need to apply a field. The ordering mechanism is the quantum mechanical exchange interaction.

Magnets made of nanocrystalline yttrium-samarium-cobalt grains possess very unusual magnetic properties due to their extremely large surface area. Typical applications for these high-power rare-earth magnets include quieter submarines, automobile alternators, land-based power generators, and motors for ships, ultra-sensitive analytical instruments, and magnetic resonance imaging (MRI) in medical diagnostics.

7. MEZO-NANO-POROUS MATERIALS

According to IUPAC, all porous materials can be subdivided into 3 categories – micro-porous materials with pore diameters of less than 2 nm, mesoporous materials with pore diameter that lies between 2 and 50 nm, and macroporous materials with pore diameters greater than 50 nm. The term nanoporous materials is usually used for those porous materials with pore diameters of less than 100 nm, but in certain cases materials with little greater pore size can be considered as nanoporous as well.

Pores itself are classified into two types: open pores which connect to the surface of the material, and closed pores which are isolated from the outside. In separation, catalysis, filtration or membranes, often penetrating open pores are required. Materials with closed pores are useful in sonic and thermal insulation, or lightweight structural applications. Pores have various shapes and morphology such as cylindrical, spherical, slit types and also more complex shapes such a hexagonal shape. Pores can be straight or curved or with many turns and twists thus having a high tortuosity. Generally porous materials have porosity (volume ratio of pore space to the total volume of the material) between 0.2–0.95.

7.1. Nanoporous materials

Like many other nanostructured materials, nanoporous materials are widely distributed in nature, both in natural minerals and in biological systems, and have been used industrially for a long time. But with development of nanotechnologies the need of synthesizing materials with precisely controlled pore size and geometry has arisen.

The most important properties of nanoporous materials, distinguishing them from other materials and determining most of their applications, are the large internal surface area and highly ordered, uniform pore structure.

Despite the fact that some amorphous microporous materials also have important industrial applications, most of microporous materials are the crystalline solids with micropores of strictly regular dimensions.

Syntheses of nanoporous materials are usually based on template-assisted bottom-up processes, including soft and hard templating methods.

One of the most common methods is a liquid crystal templating. It is based on the use of surfactant micelles as structure directing agents in a sol-gel process. Amphiphillic surfactants self assemble into cylindrical micelles, which are encapsulated by an inorganic material, which balances the charge on the micellular surfaces. Calcination, a thermal processing technique in which surfactant is burnt out, is then used to remove the organic surfactant, leaving a hexagonal arrangement of mesopores.

Sol-gel methods are also used for making aerogels, in which a gas is dispersed in a gel, producing a very light-weight solid (sometimes only few times denser than air). The example is shown in fig. 47.

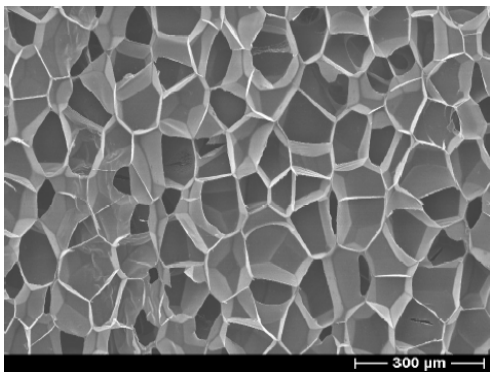

Fig. 47. Conventional polymeric foams (W. Paul, H. Weiss, *Nanoporous foams*, BASF, The Chemical Company, 2004).

Other methods include focused ion beam “drilling", microwave synthesis, selective electrochemical dissolution (dealloying), photopattering and others.

7.2. Zeolites and zeolite-like materials

Zeolites are the most common and the largest group of microporous materials. More than 150 zeolite types have been synthesized and 48 naturally occurring zeolites are known. They are basically hydrated alumino-silicate minerals with general chemical formula:

$$M^{n}_{x/n}Si_{1-x}Al_xO_2 \cdot yH_2O$$

where M = e.g. Na^+, K^+, Ag^+, $NH4^+$, H^+ …

Zeolites have three dimensional open framework structure built from tetrahedra (arrangement of SiO_4 and AlO_4 tetrahedra connected through their oxygen atoms), containing pores and voids (fig. 48). The structure and porosity is regular and periodic (fig. 48).

Due to its geometry, zeolites belong to the family of microporous solids known as “*molecular sieves*”. This term refers to the ability of these materials to selectively sort molecules based primarily on a size exclusion process.

In the voids and pores there are usually also water molecules (*zeolitic water*). One measure of the porosity is the amount of adsorbed water. The water molecules may (in many cases) be removed by heating and readsorbed at lower temperatures.

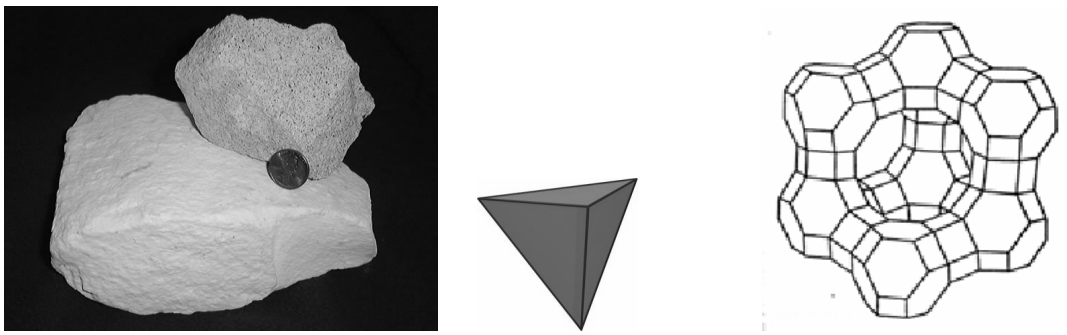

Fig. 48. General image of zeolite, the tetrahedron – one of the primary building units of alumosilicate zeolites, and diamond-like structure of faujasite.

Zeolites are widely used in domestic and commercial water purification, softening, and other applications. In chemistry, zeolites are frequently used to separate molecules. Zeolites have the potential of providing precise and specific separation of gases including the removal of H_2O, CO_2 and SO_2 from low-grade natural gas streams.

Synthetic zeolites are widely used as catalysts in the petrochemical industry. Zeolites confine molecules in small spaces, which cause changes in their structure and reactivity. The hydrogen forms of zeolites are powerful solid-state acids, and can facilitate a host of acid-catalyzed reaction, such as isomerisation, alkylation, and cracking. But the largest outlet for synthetic zeolite is the global laundry detergent market (1.44 million tons per year of anhydrous zeolite A in 1992).

High heat of adsorption and ability to hydrate and dehydrate while maintaining structural stability make possible to use zeolites as solar thermal collectors and for adsorption refrigeration. Their hygroscopic properties coupled with an inherent exothermic reaction when transitioning from a dehydrated to a hydrated form (heat adsorption), make natural zeolites effective in the storage of solar and waste heat energy. Synthetic zeolite is also being used as an additive in the production process of warm mix asphalt concrete. It helps decreasing the temperature level during manufacture and lying of asphalt concrete, resulting in lower consumption of fossil fuels, thus releasing less carbon dioxide, aerosols and vapours. In agriculture, clinoptilolite (a naturally occurring zeolite) is used as a soil treatment. It provides a source of slowly released potassium. If previously loaded with ammonium, the zeolite can serve a similar function in the slow release of nitrogen. Zeolite-based oxygen generation systems are widely used to produce medical grade oxygen. The zeolite is used as a molecular sieve, which extracts oxygen from air, in a process involving the absorbing of atmospheric nitrogen.

The second largest known group of microporous materials is the aluminophosphate family. The aluminophosphate $AlPO_4$ frameworks are formed from vertex-sharing AlO_4 and PO_4 tetrahedra. Other common microporous materials include silicoaluminophosphates, gallophosphates, or recently discovered inorganic-organic hybrids.

7.3. Mesoporous materials

Materials similar to zeolites in their properties but with greater pore size are always seemed to be very attractive, since the feasibility to obtain pores of different size and geometries offers a wide range of possibilities for hosting molecules larger than the ones exhibited for classic microporous materials. But such materials are hard to be synthesized since material with greater pores becomes instable – the nature abhors an empty space. Only in 1992 this problem was overcomed when Mobil Oil scientists discovered MS41 family of silicate amorphous mesoporous materials with narrow pore size distribution. Their most known and studied material is *MCM-41 (Mobile Crystalline Material*) – mesoporous silicate with one-dimensional hexagonal arrangement of the pores (fig. 49).

In contrast to MCM-41, the other well-known mesoporous material, *MCM-48*, (fig. 49) exhibits three-dimensional pore system (two independent and intricately interwoven networks of mesoporous channels) that is more resistant to pore blocking and allow faster diffusion of reactants than a 1D array of pores. The long-range ordering of the pores and the potential for isomorphous substitution with transition metals, enabling formation of catalytically-active centers, have incited applications in areas such as adsorption, separation and catalysis, especially in processes where bulkier molecules are used.

There is a lot of other mesoporous materials were synthesized since then. In general, these materials include some kinds of silica and alumina that have similarly-sized fine mesopores. Mesoporous oxides of niobium, tantalum, titanium, zirconium, and tin have also been reported. It is important to note, that a material that contains mesopores in part but is not regular, like silica gel, is not considered a mesoporous material.

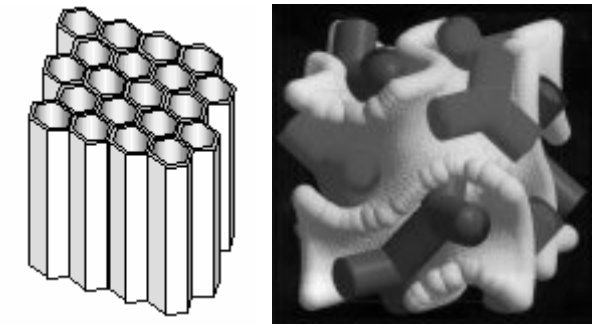

Fig. 49. Structure of zeolites MCM-41 (Mobile Crystalline Material) (C. T. Kresge, M. E. Leonowicz, W. J. Roth, et al. Nature 1992, 359, 710–712), and MCM-48 (Ji M. Kim, S.K. Kim, R.Ryoo, *Synthesis of MCM-48 single crystals*, Chem. Commun., 1998).

One of the most promising applications for mesoporous materials is hydrogen storage. Due to huge surface areas (up to 5900 m^2/g), mesoporous materials provide a vast number of sites where sorption processes can occur – potential to store a lot of hydrogen – each pore is a potential home for several hydrogen molecules.

Catalytical applications of mesoporous materials are very common in chemistry.

Mesostructured and mesoporous materials are also emerging as a new class of optical materials. The corresponding regularly arranged pores found in mesoporous materials (inorganic only) provide a high surface area to better disperse optically active components and allow for rapid diffusion for optical sensor applications.

Since 2001 the behaviour of mesoporous materials as drug delivery systems has been developed. It is based on the ability of mesoporous matrixes to absorb molecules, of pharmacological interest, followed by a potentially controlled release.

8. PHYSICAL BACKGROUND OF NANOSTRUCTURES (QUANTUM DOTS, WHISKERS, AND WELLS)

8.1. Quantization and Heisenberg's indeterminacy principle

Quantum size effects should be considered from quantum theory point of view. They follow from fundamental laws of quantum mechanics.

Heisenberg's indeterminacy principle imposes the principal restrictions on a moving of electrons and other particles

$$\Delta p_x \Delta x < h \qquad (11)$$

where p_x and x are the impulse and coordinate, $h=6.626 \cdot 10^{-34}$ J sec,
$\hbar = h/2\pi = 0.658 \cdot 10^{-15}$ eV sec is Planck constant.

From natural philosophy point of view it means a restriction of our know-ledges concerning micro-world: **we can not measure both the impulse and coordinate of electron together exactly and simultaneously.**

From physical point of view it means a quantization of physical quantities, in particular the energy.

Let us find the allowed quantum states of electron in one dimensional potential well of L thickness. Exact quantitative solution one can obtain from Schrodinger equation while here we estimate a qualitative solution using *Bohr's postulates for impulse*

$$p_n a = nh \qquad (12)$$

where n=1,2,3...is a number of quantum state, $p_n = nh/L$ is an impulse.

Then energies of quantum levels in potential well is equal to

$$E_n = p_n^2/2m = n^2h^2/2mL^2 \qquad (13)$$

where m is an electron mass.

The origin of such levels in nanoparticles is quantum effect called as *size confinement*. The values of quantum levels depends on well size. The first energy level in narrow well of $L=5a_0$ thickness is proximally equal to $E_1 = h^2/2m\ 25a_0^2 = 0.02 \cdot 27.21 \sim$ 0.5 eV,while for real quantum well of $L=100a_0$ thickness the energy is $E_1 = 0.014$ eV, while with account of effective electron mass $m^* \sim 0.1m$, $E_1 = 0.1$ eV. Essentially that minimal energy is no vanishing, this is the energy of *zero-point oscillations*.

Note that for estimation in the micro world *the atomic units* are very suitable, where h=m=e=1, while a length is measured in Bohr's radius $a_0 = h/me^2 = 0.529$ Angstrom, and energy in atomic units, 1 a.u. =27.21 eV.

8.2. Energy states and wave functions in quantum well

8.2.1. Rectangular infinite potential

Let us consider the electron moving in rectangular infinite potential well of L_z thickness shown in fig. 50a. It is a model of real *1D quantum dot* that can be applied also to *2D quantum well*, where the axes z is directed normal to layer.

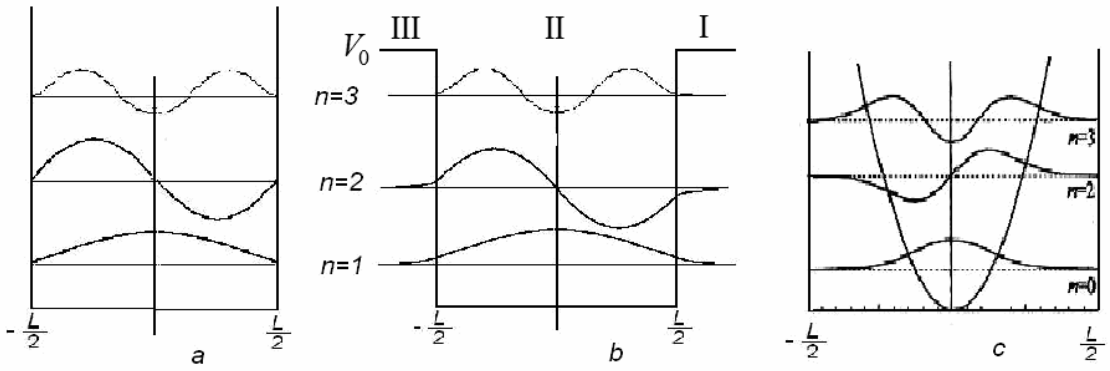

Fig. 50. Energy levels in units of $\frac{h^2}{8m^*L_z^2}$ and wave eigenfunctions $\xi_z(z)$ of electron in the 1D well of L_z thickness in form of a) the rectangular infinite potential; b) the rectangular finite potential of V_0 depth; c) the parabolic finite potential.

Schrodinger equation for this case is:

$$\left[-\frac{\hbar^2}{2m^*}\Delta + V(z)\right]\Psi(x,y,z) = E\Psi(x,y,z) \tag{14}$$

where $V(z) = \begin{cases} 0, -\frac{L_z}{2} < z < \frac{L_z}{2} \\ \infty, |z| > \frac{L_z}{2} \end{cases}$ (15)

Let us separate the (x,y) variables in well plane while z is normal to this plane:

$\Psi(x,y,z) = \varphi(x,y)\xi(z)$;

$\Delta = \nabla_\perp{}^2 + \frac{\partial^2 \xi}{\partial z^2}$, then $\left[-\frac{\hbar^2}{2m}\left(\nabla_\perp{}^2 + \frac{\partial^2}{\partial z^2}\right) + V(z)\right]\varphi\xi = (E_\perp + E_z)\varphi\xi$

Dividing this equation on product $\varphi\xi$ we obtain two equations:

(1) $-\frac{\hbar^2}{2m}\nabla^2\varphi(x,y) = E_\perp\varphi(x,y)$ - for move in (x,y) plane

(2) $-\frac{\hbar^2}{2m}\left[\frac{\partial^2}{\partial z^2} + V(z)\right]\xi(z) = E_z\xi(z)$ – for move in normal to well z direction.

The first equation gives a plane wave function and parabolic dispersion law (the E(k) dependence:

$$E_\perp = \frac{\hbar^2}{2m}\left(k_x^2 + k_y^2\right) \tag{16}$$

The second equation in well $-\frac{L_z}{2} < z < \frac{L_z}{2}$, $V_z = 0$, take the form:

$$(3)\ \frac{\partial^2}{\partial z^2}\xi_z(z) = k_z^2\xi_z(z),\ \ k_z^2 = \frac{2mE_z}{\hbar^2}$$

Its solution is:

$$\xi_z(z) = A\sin k_z z + B\cos k_z z\text{, where A and B are some constants.}$$

Boundary condition of continuity at well boundaries $\xi(L_z/2) = -\xi(L_z/2)$ give a possibility for determination of A and B constants from a normalization condition.
Due to potential symmetry the wave function may be even $\xi(-z) = \xi(z)$ or odd $\xi(-z) = -\xi(z)$.

For odd function A = 0, $\xi^+(z) = B\cos k_z^+ z = \sqrt{2/L}\cdot\cos k_z^+ z$,

where $B = \sqrt{\frac{2}{L}}$ is found from normalization condition, $k_z^+ = \frac{2\pi(n_+ - 1/2)}{L_z}$, $n_+ =$ 1,2,3... (from boundary conditions).

Then $\xi^+(z) = \sqrt{\frac{2}{L}}\cos\frac{2\pi(n_+ - 1/2)}{L_z}z$, $\quad E_z^+ = \frac{\pi^2\hbar^2}{2mL_z^2}4(n_+ - 1/2)^2$.

For even function B =0, then

$$\xi^-(z) = \sqrt{\frac{2}{L}}\sin\frac{2\pi n_-}{L_z}z \quad E_z^+ = \frac{\pi^2\hbar^2}{2mL_z^2}4n_-^2\text{, where } n_- = 0,\ 2,\ 4...$$

Comparising both relations for E_z^+ and E_z^-, one can combine them together into the single relation:

$$E_z^+ = \frac{\pi^2\hbar^2}{2mL_z^2}n^2\text{, n = 1,2,3...} \qquad (17)$$

This is the same equation obtained previously from Heisenberg relation. Note the energy is count of bottom of well, $\Delta E = E_1 = \frac{h^2}{2m^*L^2}$. For gallium arsenide GaAs $m^* = 0{,}067\,m_e$. Therefore for well of $L_z <$ 10 nm thickness, the energy $\Delta E <$ 30 meV, that is smaller then the thermal energy at room temperature, ΔE < kT. Hence the quantum confinement effects may be observed experimentally.

8.2.2. Rectangular finite potential

This is more exact model for quantum well shown in fig. 50b.

The potential looks as follows:

$$V_z = \begin{cases} 0, -\dfrac{L_z}{2} < z < \dfrac{L_z}{2} \\ V_0, |z| > \dfrac{L_z}{2} \end{cases} \tag{18}$$

Here the move of electron outside of barrier is possible, in region I and III.
The Schrodinger equation take the form:

$$\begin{aligned} &\frac{\partial^2 \xi(z)}{\partial z^2} - \overline{K}_z^2 \xi(z) = 0, \\ &\overline{K}_z^2 = \frac{2m^*}{\hbar^2}(V_0 - E_z) \end{aligned} \tag{19}$$

Let us consider the solution for bonded states, for which $E_z < V_0$ and $\overline{K}_z^2 > 0$.

For even functions $\xi(-z) = \xi(z)$ the A = 0 again while C = D. Hence the solution takes form:

$$\xi(z) = \begin{cases} B\cos k_z^+ z, for\_region\_I \\ Ce^{-i\bar{k}_z z}, for\_region\_II \\ De^{i\bar{k}_z z}, for\_region\_III \end{cases}$$

This functions and its derivatives should be matched at both boundaries between I and II, and II and III regions that gives the boundary conditions in the following form:

$$B\cos k_z \frac{L}{2} = Ce^{-\bar{k}L_z} = C'e^{-Lk_z}, (C' = C) \tag{20}$$

$$-k_z^+ B\sin k_z \frac{L}{2} = -\bar{k}_z^+ Ce^{-\bar{k}L_z} \tag{21}$$

Dividing of (21) on (20) gives: $k_z tgk_z \dfrac{L}{2} = \bar{k}_z$.

Substitute the $k_z = \dfrac{\sqrt{2mE}}{\hbar}$ and $\bar{k}_z = \dfrac{\sqrt{2m(V_0 - E)}}{\hbar}$, multiply it on L/2, and introduce the new variable $\xi = \dfrac{L}{2}k_z = \dfrac{L}{2}\dfrac{\sqrt{2mE}}{\hbar} = \sqrt{\dfrac{mEL^2}{2\hbar^2}}$.

In addition $-\dfrac{L}{2}\bar{k}_z = \dfrac{L}{2}\sqrt{\dfrac{2m}{\hbar^2}(V_0 - E)} = \sqrt{\dfrac{mL^2V_0}{2\hbar^2} - \dfrac{mL^2E}{2\hbar^2}} = \sqrt{\dfrac{mL^2V_0}{2\hbar^2} - \xi^2}$

In a result we obtain the transcendental equation:

$$\xi tg\xi = \sqrt{\frac{mL^2V_0}{2\hbar^2} - \xi^2},$$

of which solution may be determined by graphical calculation as intersection points of the left $p(\xi) = \xi \cdot tg\xi$ and right $q = \sqrt{\frac{mL^2V_0}{2\hbar^2} - \xi^2}$ functions.

The function $p(\xi)$ is the periodical one equal to:

$$p(\xi) = \begin{cases} 0, \xi = 0, \pi, 2\pi, ... \\ \infty, \xi = \frac{\pi}{2}, \frac{3\pi}{2}, ... \end{cases},$$

while the function $q(\xi)$ is the function of ring of $R = \sqrt{\frac{mL^2V_0}{2\hbar^2}}$ radius. A number of solutions depends on potential depth V_0, namely, the smaller V_0, the smaller the number of solutions. For the first solutions $\xi_1 = 1,25; E_1 = 0,1V_0$ and $\xi_2 = 3,60; E_2 = 0,8V_0$.

The solutions for odd functions may be found in the similar manner.

Analysis shows that effect of quantum confinement manifest itself more expressive under growth of barrier depth V_0. Here the exact solution of Schrodinger equation approach the qualitative energy values obtained from Heisenberg's and Bohr's relations. For example for AlGaAs/GaAs, the energy levels are $E_1 \approx 57$ meV, $E_2 \approx 31,5$ meV.

The wave functions in the case of finite potential become to be “smeared” which are shown in fig. 50b.

8.2.3. Parabolic finite potential

Parabolic potential is shown in fig. 50c described by the function

$$V_0 = k_z z^2/2 \qquad (22)$$

The energy levels and wave functions are shown ibidem to be similar to the case of the finite rectangular potential.

This potential describes approximately a model of 1D heterostructure with smeared boundaries between two layers. Such a well is obtained during a governed alloying of layers growth, for instance in case of gallium arsenide AlGaAs/GaAs. Hence this potential is sensitive and suitable for description of interphase boundaries.

Conclusion: In result of a space confinement of electrons in potential well the quantization of electronic energy arise in kind of discrete spectrum of quantum levels.

8.2.4. Rise of energy bands in periodical potential within the Kronig-Penny model

Let us consider an infinite set of the finite rectangular wells of V_0 width periodically repeating in z direction with period *a*. This may be an approximate 1D model for electron in crystal or in a periodic layered structure. This physical model is described by a mathematical model of Kronig-Penny shown in fig. 51 where the well width is L_z =b. The model is very simple but it illustrate clearly the origin of the energy bands, band gaps and dispersion law.

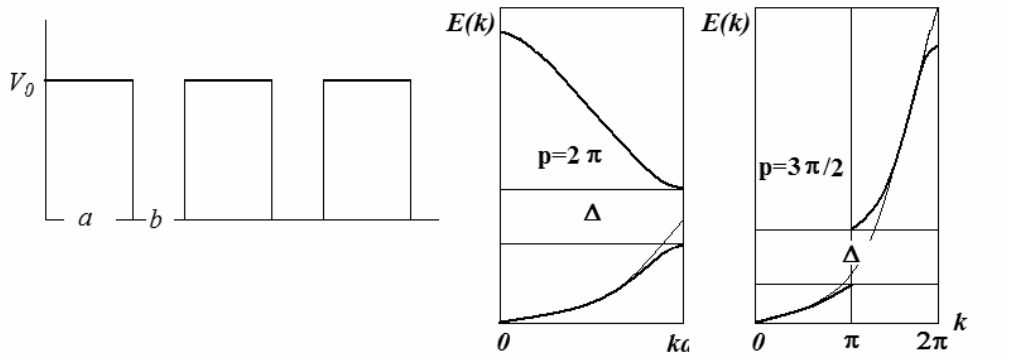

Fig. 51. Periodic finite rectangular potentials in Kronig-Penny model (a) and dispersion curves for electron energies E(k) forming the energy bands (in units $h^2/8m^*b^2$) under $p=3\pi/2$ and $p=2\pi$ (b,c). Curves for free electrons marked by dashes.

If $V_0 a \to 0$ the electrons are free, while $V_0 a \to \infty$ they are in infinite well. The plane wave modulated by lattice period a+b is the solution of the Schrodinger equation:

$$\psi(x,k) = U_k(x)e^{ikx} \tag{23}$$

where $U_k(x)$ is an periodic function with a+b period.

From the continuity conditions on the well boundaries at x=0 and x=b, which connects electron energy E with wave vector k, for free electrons ($V_0 a = const$) we obtain the equation

$$P\left(\frac{\sin\alpha b}{\alpha b} + \cos\alpha b\right) = \cos kb$$

where $\alpha = \sqrt{\frac{2mE}{\hbar^2}}$, $P = \lim_{V_0\to\infty, a\to 0} \frac{aV_0 m\alpha}{\hbar^2}$ is a barrier's transparency.

The right part of the equation is less then 1 as cosines function, while the left part may be unrestricted. Analysis shows that the k is real under $P<1$ while k is imagine under $P>1$. Physically the real numbers means the real energy levels and bands while imagine numbers means the forbidden levels and band gaps.

Note that vector k as a vector of reciprocal lattice runs the spectrum of k laying in the range $0 < k < 2\pi/b$. Such the set of wave vectors for periodic lattice is called *the Brillouin zone* and the related set of energy levels is called *the energy bands*. Hence the energy bands are seen to be originated from the potential periodicity. One electron can have wave vectors in the Brillouin zone with different energies E(k). This dependence is called as *the dispersion law*. For the filled zone this is the statistical distribution law for electron energies.

Conclusion: In result of periodicity of potential wells the quantum levels E_n transform into energy bands where electrons move in accordance with dispersion law E(k). Band structure arises including energy bands and band gaps.

8.3. Quantum well in the gallium arsenide GaAs/AlGaAs heterostructure

Above considered potentials wells serve as the model for real layered heterostructures in semiconductor physics, that we demonstrate at the example of gallium arsenide GaAs which is one of the basic semiconductor of modern microelectronics. Doping by silicon Si or germanium Ge gives the conductivity of n-type while beryllium Be of p-type.

Let us consider an ideal contact of two semiconductor layers on the example of the alumogallium arsenide/gallium arsenide AlGaAs/GaAs *heterojunction* shown in fig. 52. These two semiconductors from one side have the different but close band structures and from another side have the same lattice parameters that make them possible to form ideal junction without any stress, that is very important for their durability. At the junction a potential barriers are arisen for electrons ΔE_c in conductive band and for holes ΔE_v in valence band. The barrier for electrons one can estimate as difference between electron affinities $\Delta E_c = \chi_1 - \chi_2 = 4.07 - 3.74 = 0.33$ eV. Accounting $E_{g1} = 0.37$ eV one can estimate the barrier for holes $\Delta E_v = E_{g1} - \Delta E_c = 0.37 - 0.33 = 0.04$ eV. Therefore the potential depth for electrons and holes are equal to $V_{0e} = \Delta E_c$ and $V_{0h} = \Delta E_v$ respectivaly.

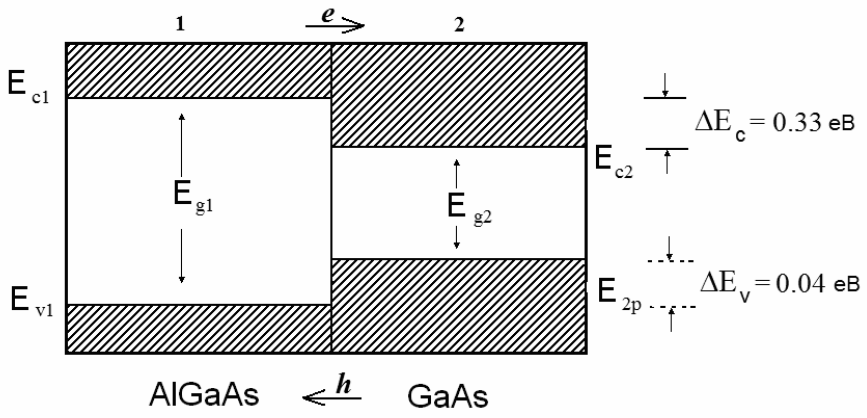

Fig. 52. Energy bands at the junction of semiconductors AlGaAs/GaAs.
E_{c1} and E_{c2} are the bottoms of conductivity bands;
E_{v1} and E_{v2} are the tops of valence bands;
$E_{g1} = E_{c1} - E_{v1}$ and $E_{g2} = E_{c2} - E_{v2}$ are the widths of band gaps;
$\Delta E_c = E_{c1} - E_{c2}$ is the depth of barrier for electrons;
$\Delta E_v = E_{v2} - E_{v1}$ is the depth of barrier for holes;
d is width of GaAs layer; Indexes 1 and 2 relate to AlGaAs and GaAs respectivaly.

If additional layer of AlGaAs to be grown from the right we obtain the heterojunction of AlGaAs/GaAs/AlGaAs in kind of potential well considered previously (see fig. 53). The potential for electrons have the width d and depth $V_{0e} = \Delta E_c$. **In result of confinement of electron in the intermediate thin nanolayer of GaAs of L~10nm width the size quantization arise of electron and hole levels considered above.**

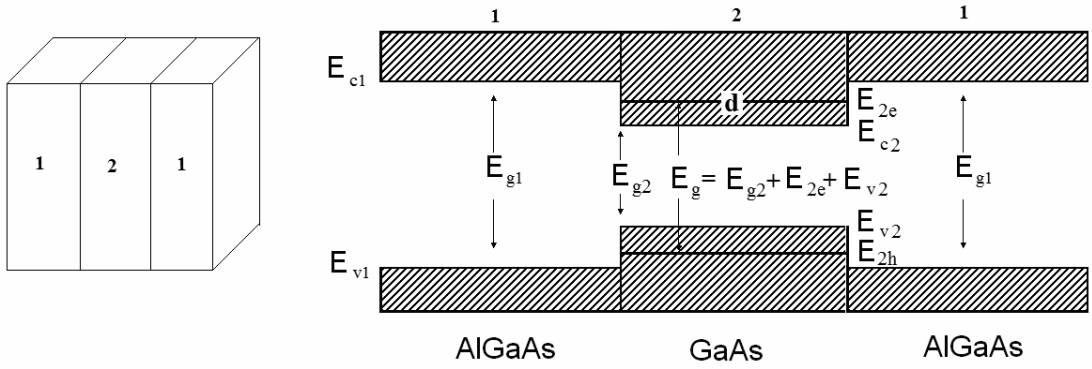

Fig. 53. Model of quantum well at the heterojunction AlGaAs/GaAs/AlGaAs as trap for electrons and holes. For notation see fig. 52.

Charge carriers (electrons and holes) are moving in the intermediate layer of GaAs. Electrons occupy the E_{2e} level while holes the E_{2v} level. The interband transition occur between these levels so the band gap is increased and becomes to be $E_g^{eh} = E_{g2} + E_{2e} + E_{2h}$.

In many-layered heterojunction with period *a* in accordance with the Kronig-Penny model a band structure arises.

Conclusion: Varying the type and width of semiconducting layers *d* and their periodicity *a* in heterostructure one can control its electron structure (E_{1e}, E_{1h}, E_g^{eh}) and govern the electronic and optical properties of the devices on this basis.

For thin layers the potential well V_0 is so deep that is able to accommodate many quantum levels E_n. For thick layers the depth of potential is smaller leading to a decrease of the numbers of layers. In extreme case of very thick semiconducting layers the potential depth becomes to be so small $V_0 < E_1$ that no confinement and no quantization occurs.

8.4. Density of electronic states for bulk 3D and low dimensional 2D, 1D, 0D systems

Density of electronic states (DOS) and their *energy distribution* $\chi(E)$ are of very important in solid state physic determining electronic and optical properties.

Let us calculate the general law for $\chi(E)$ and its dependence on dimensionality. We must calculate a total number of states with energy less then *G(E)* and then find the DOS and $\chi(E)$ by differentiation of *G(E)*.

We must consider two states as different states if they differ on the minimal value defined from Heisenberg relation in which accordance this difference is $\Delta p_x = h/\Delta x$, $\Delta p_y = h/\Delta y$, $\Delta p_z = h/\Delta z$. Hence the smallest volume per one states in impulse space is

$$V_1 = \Delta p_x \Delta p_y \Delta p_z = h^3/V \qquad (24)$$

8.4.1. General case for bulk 3D system

Let us consider the 3D body of $V=\Delta x\Delta y\Delta z$ in volume. In a reciprocal k-space it relates to the volume $k_xk_yk_z$ while in an impulse p-space to the total volume $V_p=p_xp_yp_z$. To find number of states it is requested to divide the total volume V_p on the volume of one state V_1

$$G(E)= V_p/V_1 =V_pV/h^3 \tag{25}$$

The electrons occupy the energy levels in accordance with Hund rule, i.e., from bottom to top forming therefore a Fermi sphere in impulse space

$$E(p)=(p_x^2+p_y^2+p_z^2)/2m^* = p_F^2/2m^* \tag{26}$$

with radius $p_F=(2m^*E)^{1/2}$ and volume $V_p=4\pi p_F^3/3 = 4/3\pi(2m^*E)^{3/2}$.
Substitution of these values in (26) gives

$$G_{3D}(E) = \frac{4\pi\sqrt{2mE}^3 V}{3h^3} \tag{27}$$

DOS by definition is

$$\chi(E) = \frac{2}{V}\frac{dG(E)}{dE} \tag{28}$$

where 2 accounts the Pauli principle.

Substituting and differentiating we obtain DOS for 3D crystals

$$\chi_{3D}(E) = \frac{m^*}{\pi^2\hbar^3}\left(2m^*E\right)^{1/2} \tag{29}$$

The dependence of (1/2)-power it shown in fig. 54.

8.4.2. Case for 2D-quantum well

Instead of 3D sphere for 2D well we have 2D ring in impulse space with the Fermi area

$$S_p=\pi p_F^2=\pi\ 2m^*E \tag{30}$$

Number of states in ring is

$$G_{2D}(E)=S_pS/h^2 =2\pi m^*ES/h^2$$

The DOS in ring is

$$\chi_{2D}(E) = 2/S\ dG_{2D}(E)/dE = 4\pi m^*/h^2$$

In contrast to 3D for the 2D system the energy quantization arises so the spectrum have the levels $E - E_i$.

Summation over this levels gives

$$G_{2D}(E) = \sum_i \frac{2\pi m^*}{h^2}(E - E_i)S \tag{31}$$

$$\chi_{2D}(E) = \sum_i \frac{4\pi m^*}{h^2} \tag{32}$$

The DOS within one level do not depend on energy and is constant. General DOS is of stepwise type shown in fig. 54. Note that step of quantum levels is equal to a conductivity quantum $G_0 = 2e^2/\hbar$.

8.4.3. 1D-Case for quantum wire

Number of states

$$G_{1D}(E) = \frac{P_x \cdot L_x}{h} = \frac{L\sqrt{2m(E - E_i)}}{h} \tag{33}$$

Density of one states

$$\chi^i_{1D}(E) = \frac{2}{L}\frac{dG_{1D}(E)}{dE} = \frac{2}{h\sqrt{(E - E_i)}} \tag{34}$$

DOS as sum over all levels

$$\chi_{1D}(E) = \sum_i \frac{2}{h}\frac{1}{\sqrt{E - E_i}} \tag{35}$$

The DOS do not depend on electron mass and have -1/2-power dependence shown in fig. 54.

8.4.4. 0D-Case for quantum dot

The DOS has a kind of the delta-function

$$\chi_{0D}(E) \approx \frac{dG}{dE} = \delta(E) \tag{36}$$

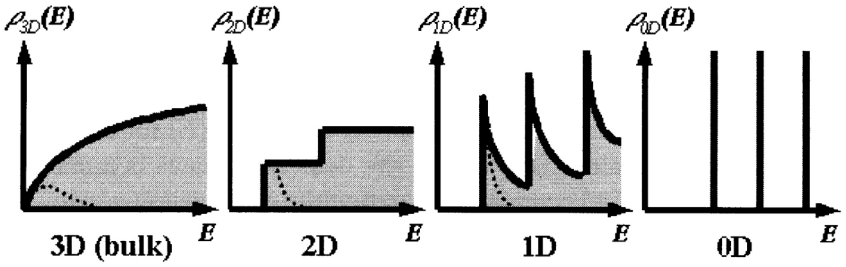

Fig. 54. Peculiar distinguish ion of electron density of states for the systems of different dimensionality.

Conclusion: DOS for 3D, 2D, 1D, and 0D system have the general dependence $\sqrt{E}, \_ stepwice \_ E_i = const, \_\_(E - E_i)^{-1/2}, \_ and \_ \delta(E - E_i)$ **respectivaly.**

This relations allow us to predict DOS using the dimensionality of nanostructures or, *vice-versa*, to predict the dimensionality of unknown nanostructure by its known experimental DOS-spectrum.

8.5. 2D-Electronic gas (2D-EG) in metal-oxide-semiconductor (MOS) structures

In 2D-case the DOS is constant and do not depend on energy. This is very important because it simplify a problem of device design.

Two-dimensional electron gas 2D-EG is formed when electrons moving is restricted in one dimension and the electrons move in plane in kind of the 2D metallic or semiconductor layers. If its width is fixed then its energy levels are also fixed. To govern the properties of 2D-EG the special MOS-structures were designed, the example is shown in fig. 55.

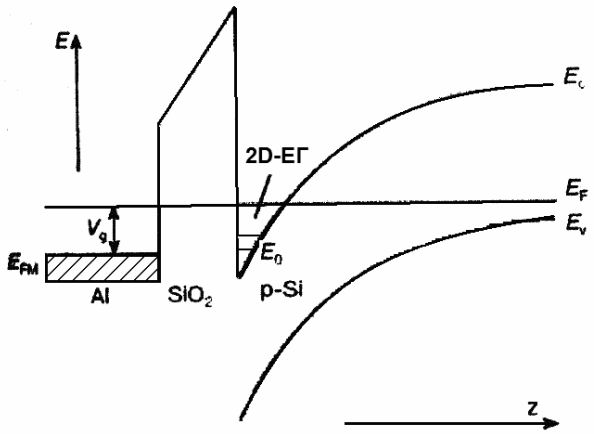

Fig. 55. Scheme of MOS-structure of Al-SiO_2-p-Si type with 2D-EG at SiO_2/p-Si boundary.

MOS structure consists of the metal layer (Al), dielectric oxide (SiO_2) and semiconductor p-Si layers. The metal play a role of gate forming an electrical field and a positive potential $V_c(z)$ in semiconductor layer playing the role of potential well for electrons. Hence the electrons in p-Si are pressed by the potential to SiO_2/p-Si boundary forming a thin layer (~ 5nm) of 2D electron gas. Its energy is quantized forming the quantum levels and bands. Varying potential at the gate one can control the depth of potential well, the related energy bands, the DOS of 2D-EG and concentration of electrons ($\sim 10^{11} - 10^{13}$ cm^{-2}).

Conclusion: MOS is metal-oxide-semiconductor structure in which 2D electron gas can be formed by applying gate voltage.

9. FULLERENES

9.1. History of fullerene discovery and Nobel Prices

Backminsterfulleren, the molecule C_{60}, consisting of 60 carbon atoms in kind of the foot ball is shown in fig. 56.3. For its discovery the Nobel Price in chemistry in 1996 was awarded in spite of the atomic clusters and molecules where known for many years ago. Why so? Because the buckyball C_{60} becomes to be the prototype and gives the impetus for synthesis of great family of the carbon C_n (n = 20–1000, and more) and noncarbon clusters, called fullerenes. In fact this is new allotropic modification of carbon, one of the fourth, pictured at the fig. 56.3.

Very illuminative is the history of its discovery. Geometric figure of C_{60} type, the icosahedron, was known even to Leonardo de Vinca (1500) and perhaps to Archimedes. On 1970 Osawa has suggested the idea of its possible existence in nature. In 1973 Bokhara and Galpern have calculated this molecule by the quantum chemistry semiempirical Huckel method showing its possible stability in reality. From that time the searches of its have been started. In 1984 Caldor in first time have observed the mass-spectrum lines with mass of 720 atomic units related to cluster C_{60} in laser ablated carbon products. In 1985 Kroto and Smalley have repeated this experiments. In 1990 Kratschmer and Huffman in first time using arc-discharge technique have synthesized C_{60} in grams quantity sufficient for experimental examination. They dissolved an obtained soot in tholuol and after evaporation have been obtained the small red crystals of which EPR spectrum was measured in first time. It was breakthrough in research. In 1990 Kroto as a member of Nature journal board and reviewer of the Kratschmer and Huffman's paper has entrusted to reproduce this experiments to his post-graduate O'Brian that was done successfully and published in 1991. Further in couple with Cerl they have resolved the structure of the red crystals, that was the icosahedral C_{60}. In 1985 Kornilov theoretically substantiated and predicted the possible existence of carbon nanotubes rolled from carbon sheets of graphite. In 1991 Iijima has synthesized them by arc-discharge technique. From that time the intensive research of carbon clusters, fullerenes and nanotubes have been triggered.

In 1996 Kroto, Cerl, and Smalley have became to be Nobel Price Winners for discovery of the novel form of carbon. But why namely they, among 11 scientists mentioned above? It should be noted that procedure of Nobel Committee decisions is based on opinions of prominent world known scientists so it is very perfect. Appear to be they were more cunning and more adroit at finish stage – they have timely reconstituted the key experiments linked with theoretical analysis of the problem, have presented and advertised skillfully own results at conferences, giving the impression of their inequality and speculating on their potential unique properties and nice geometrical form. In this way they have been crucially influenced both on the opinions of experts and decision persons as well as on the development of this research area in the whole. In fact they have wrested the victory thanks to capable management.

It is interested to reconsider the fullerene roadmap in science after 10 years. It turned out to be very perspective so a decision of Nobel Committee to awarded the novel carbon form was very prophetic and wise. However the forecast of Winners turned out to be exaggerated and speculated because of the C_{60} was found to be a “soap bubble” because of no materials truly with unique properties was created on base of the buck ball. The important lesson follows from this history, namely, to obtain the Price it is insufficient to make a brilliant scientific work but it is requested to represent it skillfully at world level.

9.2. Allotropic forms of carbon

Carbon occupy the sixth number in Periodic Table having the $1s^2 2s^2 2p^2$ configuration in a ground state. Long time ago Dmitry Mendeleev, the discover of periodic low, was stressed that "... in any of the nature elements an ability was observed for complication as in carbon...". In comparison with another elements carbon may creates different kinds of chemical bonds due to ability of its electrons to transit between s and p states, called as a hybridization of orbitals. In the result a carbon can create the single, duble, or triple covalent intercarbon bonds as in ethane C_2H_6, ethylene C_2H_4 and acetylene C_2H_2 respectivaly. In dependence of this bond type the different allotropic modifications of carbon are originated, i.e. the allotropes of different crystal structures but of the same in chemical content (fig. 56). The different structures predetermine the different properties. Four valence electrons are able to create three sp^1, sp^2, and sp^3 configurations, that leads to the formation of diverse line, plane, and bulk structures with 2, 3, 4 coordination and 180°, 120° and 109,47° interbond angels respectivaly (fig. 56). Among them it should be noted that: 1) the cubic diamond and hexagonal landslide with sp^3 bonds, the brilliant and highest superhard materials in nature, 2) the hexagonal and rhombohedra graphite, the politypes, fullerenes and nanotubes with sp^2 bonds, and 3) the amorphous carbon, soot, carbines with sp^1 bonds.

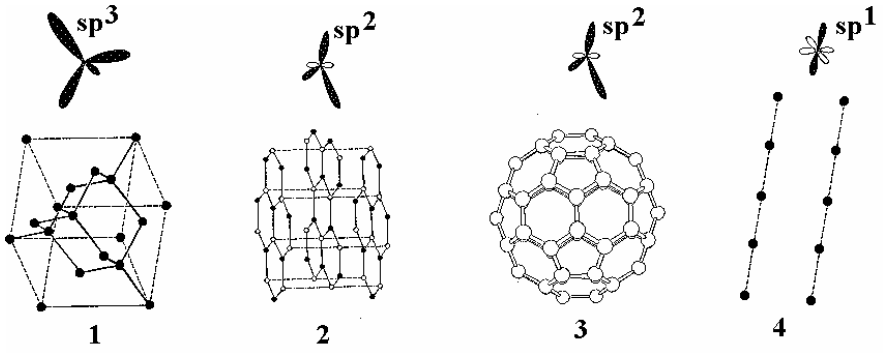

Fig. 56. Structures of main allotropic modifications of carbon:
1 – 3D cubic diamond and hexagonal lonsdelite with sp^3-bonds;
2 – 2D layered hexagonal graphite with sp^2-bonds;
3 – 1D nanotubes and 0D fullerenes like C_{60} with sp^2-bonds;
4 – amorphous carbon (soot, carbines) with sp^1-bonds.
Above are shown the related chemical orbitals.

Diamond lattice having the Fd3m or O_h^7 symmetry and the lattice parameter a=0.3567 nm originates and determines the record properties of diamond, namely, the hardness ca. 100 GPa, the bulk modulus ca. 1000 GPa, the Debay temperature θ_D = 1860 K, the density ρ= 3.515 g/cm^3. The number of related semiconducting compounds in a top right corner of Periodic Table also have the same diamond like sphalerite structure, such as the IV–IV compounds, for example SiC, the III-V compounds, for example BN, GaAs, and the II–VI compounds, for example InP, ZnO. All of them have the sphalerite (zinc-blend) lattice (analogue of the diamond) or the wurtsite lattice (analogue of the lonsdelite), in which atoms of different sort alternate each other. This compounds combine a hardness of diamond with electronic characteristics of semiconductors, that determines their wide-range application in microelectronics.

Graphite consist of hexagonal layers of honeycomb type (graphene), which may be packed in different sequences, such as ABAB, where atoms of one layer A are placed above holes of another layer B. The strong covalent bonds act in plane of any such layer, while the weak van-der-Waals bonds act between layers, that is responsible for anisotropic properties of graphite. In turbostratic graphite the layers are shifted arbitrary relative each other and packed randomly. Graphite has great cross-section of neutron scattering and used therefore as moderator of neutrons in nuclear reactors. Properties of diamond and graphite are presented in table 6.

Table 6. Physical properties of diamond and graphite.

Property	Graphite	Diamond
Lattice structure	Hexagonal	Cubic
Space group	$P6_3/mmc$ (D_{6h}^4)	Fd3m (O_h^7)
Lattice parameter (T=300K), nm	0.2462 0.6708	0.3567
Atomic density (C atom/cm^3)	$1.14 \cdot 10^{23}$	$1.77 \cdot 10^{23}$
Specific density (g/cm^3)	2.26	3.515
Heat capacity (kal/g K)	0.17	0.12
Heat conductivity (W/cm K)	30 0.06	~25
Cohesice energy (eV/C atom)	7.4	7.2
Debay temperature (K)	2500 950	1860
Bulk modulus (GPa)	286	42.2
Elastic (Young) modulus (GPa)	1060 36.5	107.6
Compressibility (cm^3/dyn)	$2.98 \cdot 10^{-12}$ ~2.63 10^5	$2.26 \cdot 10^{-13}$
Hardness in Moos scale	0.5 9	10
Band gap (eV)	-0.04	5.47
Carriers density (10^{18}/cm^3, at T=4K)	5	0
Electron mobility (cm^2/V sek)	20000 100	1800
Hole mobility (cm^2/V sec)	15000 90	1500
Specific resistivity (Ohm cm)	$50 \cdot 10^{-6}$ 1	~10^{20}
Dielectric constant (low frequencies)	3.0 5.0	5.58
Dielectric breakdown strength (V/cm)	0	10^7
Magnetic permittivity (10^{-6} cm^3/g)	–0.5 –21	–
Refractive index in visible range	–	2.4
Melting temperature (K)	4450	4500
Thermal expansion coefficient (1/K)	–10^{-6} 29 10^{-6}	~10^{-6}
Sound velocity (cm/sek)	~2.6310^5 ~10^5	~1.96 10^5
Highest Raman mode (cm^{-1})	1582 –	1332

Some another carbon forms are presented in fig. 57 showing their great diversity at atomic, micro-, mezo-, and macro-levels resulted in diverse properties. Therefore the abundance of modern carbon-based materials have been developed of the bearing, instrumental, nuclear, thermal resistance, jewellery, polymeric, rubber, etc., destination.

This abundance of carbon forms is not completed. Existence of other carbon allotropes and BN polymorphes is known in literature, such as the carbine, chaoite, metallic carbon, etc. This allotropes were synthesized and found in meteorites however

their structures was not resolved still. The discovery of fullerenes and nanotubes gives new impetus for search of novel unconventional carbon allotropes, BN polymorphes and other novel modifications. It is a large field for advanced research and discoveries.

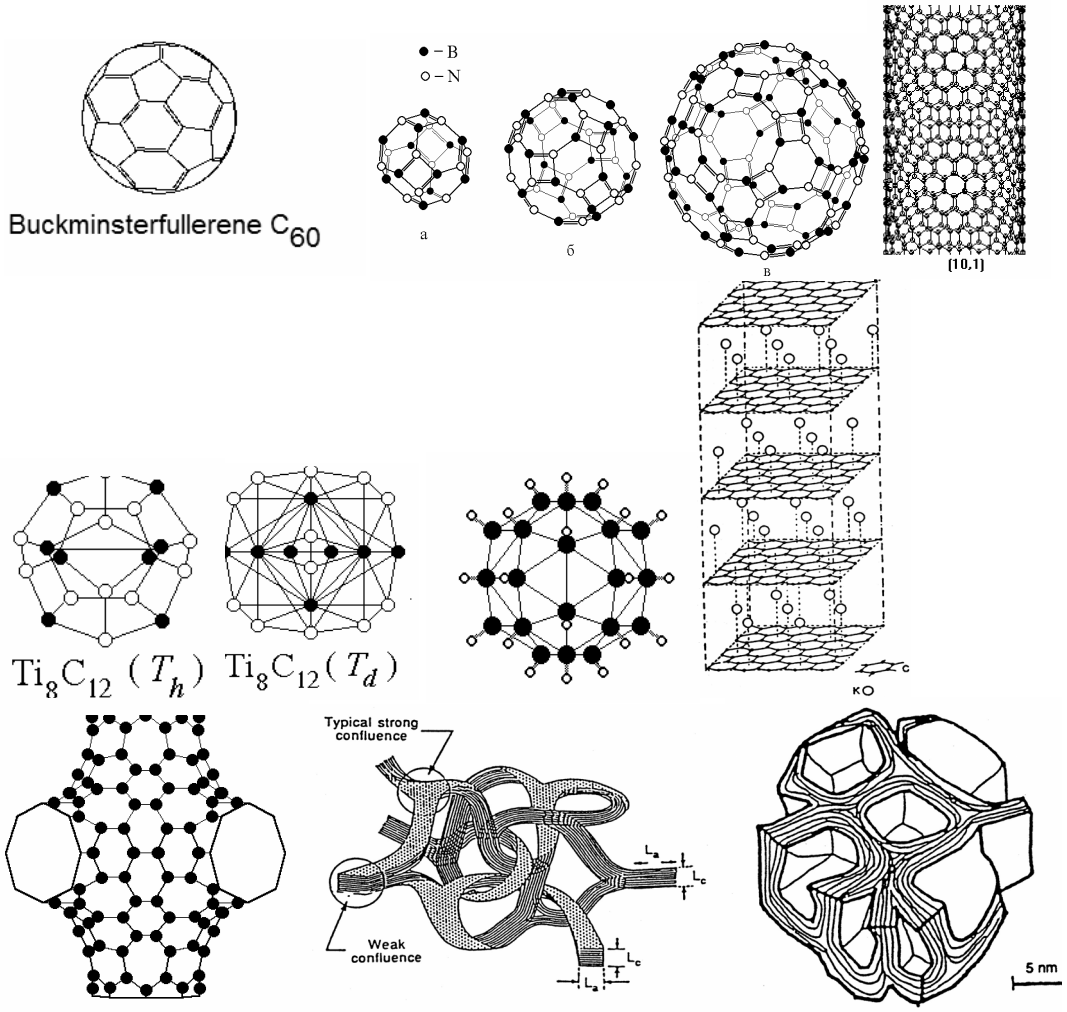

Fig. 57. Some of nanostructured forms of carbon and its analogs: the boron-nitride analogs of fullerenes, the fulborenes $B_{12}N_{12}$, $B_{24}N_{24}$, $B_{60}N_{60}$; the chiral (10,1) nanotube; metalocarben Ti_8C_{12}, the carbon cage doped with titanium; the borane $B_{32}H_{32}$, the hydrogenated boron cluster; the potassium intercalated graphite; the schwartson, the fullerene with negative curvature; the random net of carbon tapes; the packing of onions, the multilayered fullerenes.

9.3. Fullerenes – the closed carbon cages consistent of 5- and 6-membered rings

Euler relation describes the geometry of arbitrary polyhedron:

$$f+v=l+2 \qquad (37)$$

where f is a number of faces, l is a number of ledges, v is a number of vertices.

In atlas of fullerenes there are thousands of fullerenes defined as the closed carbon cages consistent only of 5-memberred (pentagons) and 6-membered rings (hexagons). For any fullerenes consisted of p pentagonal and h hexagonal faces a total number of

faces is f=p+h. Let us calculate the total number of edges, accounting that one pentagon has 5 edges, one hexagon has 6 edges, while one edge belongs to two faces l=(5p+6h)/2. Also let us calculate the total number of vertices, accounting that one vertex belong to three edges, v=(5p+6h)/3. Substituting these values in Euler relation we obtain:

$$p+h + (5p+6h)/3 = (5p+6h)/2 +2 \qquad (38)$$

The number of hexagons here is cancelled so we have p=12. This means that in all fullerenes a number of pentagon faces is equal or divisible by 12, while a number of hexagon faces may be arbitrary. When h=0 ones obtain f=12, l=30, v=20 as being dodecahedron C_{20}, while at h=20 we obtain f=32, l=90, v=60, the icosahedron, or buckminsterfullerene C_{60}.

The fullerene C_{20} consist of 12 pentagons only as being the lowest cage-type fullerene. Cluster $C_{12}Ti_8$ found in 1992 and shown in fig. 57 demonstrates the substitution fullerenes of Me_8C_{12} type, known as metallocarbohedrenes or metcarbs, where atoms of metals Me=Zr, Hf, V, Cr, Mo, Fe substitute the carbon atoms.

The buckyball molecule C_{60} have the following characteristics:
Average C-C bond length: 0.144 nm (0.146 nm in pentagons and 0.140 nm in hexagons). Average diameter is 0.71 nm, diameter of outer sphere is 1.034 nm. Binding energy per atom is 7.40 eV/atom, that is lower on 0.7 eV/atom than for graphite. Cohesive energy is 1.4 eV/atom. First ionization potential is 7.58 eV. Optical absorption edge is 1.65 eV.

9.4. Fullerites – the crystals of fullerenes

Fullerenes may be linked together by weak van-der-Waals bonds forming therefore molecular crystals. The C_{60}-fullerite under normal conditions has face-centered-cubic lattice FCC-C_{60}, every molecule in which rotates each other in random directions. Under decreasing of temperature to 260 K the rotation is frozen while fcc phase transforms into simple cubic lattice SC-C_{60}.

The fcc-C_{60} has the following characteristics: Lattice parameter is a=1.474 nm. Length between molecules C_{60}-C_{60} is 10.02 nm. Cohesive energy is 1.6 eV/atom. Density is ρ= 1.72 g/cm^3. Young modulus is Y=15.9 GPa. Melting temperature is T_{melt}=1180 C. Static dielectric constant is ε=4–4.2. Optical absorption edge is 1.7 eV. It is soft semiconductor with band gap ΔE_g=1.5–1.7 eV.

Note that in spite of a high bulk modulus a hardness of fullerite is very small so *not electronic nor optical unique properties does not marked*. It is usual conventional molecular crystal therefore any its mythical properties are falsehood.

9.5. Fullerides – doped fullerites

Fullerites lattices contain intermolecular tetrahedral or octahedral holes greater than in conventional metallic lattices. Therefore they may be very easy doped, for example, by alkali K, Rb, Li, Na atoms. The compounds of fullerites with metals were named fullerides (fig. 58). Doping is effective method to change properties so the synthesis of fullerides is perspective to obtain unusual materials. For example the alkali fulleride $RbCs_2C_{60}$ was found to be a superconductor with critical temperature T_c=117 K.

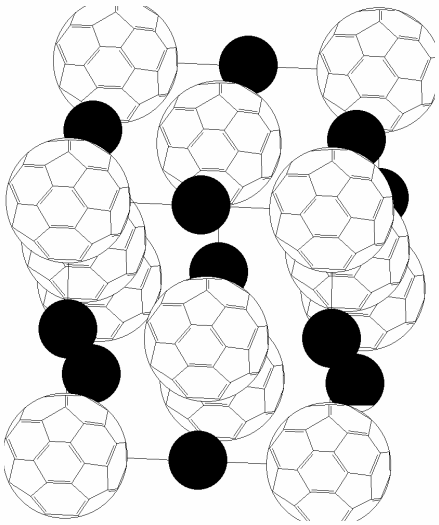

Fig. 58. Fulleride with fcc lattice doped with metal atoms.

Under heating, pressing, irradiation the fullerene molecules may be copolymerized with another ones, i.e. strong chemical inter-molecule bonds may be created. However due to icosahedral 5-order symmetry the fullerenes can not close pack all space and can't create any closed packed fcc, bcc or any other lattices. Hence from crystal chemistry point of view the fullerenes are deformed molecules. All the polymerization is able for is a formation of polymer fullerene chains.

Such supramolecular polymers were shown to be fabricated by light excitation (photopolymerization), under elevated temperatures, pressure, electron beams, et.al. Between fullerenes the 1-, 2-, 3-, 4-, 5-, and 6- time chemical bonds may be created. The structure of such polymer chains is known to be different in dependence of the vertex, edge or face acting bonds, for example, X-X-X is the monopolymer, X-У-X-У-X-У is the copolymer, XXX-УУУ-XXX-УУУ is the blocking copolymer. Such chain polymers was suggested to create branches, trees, and other skeleton structures, that may be used in tire industry.

Chemistry of fullerenes, fullerites, fullerides and their polymers has great perspectives because of their properties may be modified in wide range by this functionalization.

9.6. Synthesis of fullerenes

The first technique for fullerene synthesis proposed in 1984 by R.Smalley was the method of laser ablation (evaporation) (fig. 59) by mean of which the buckyball C_{60} was obtained and observes in first time. In 1990 Kratschmer and Huffman have been proposed the arc-discharge method (fig. 60) by mean of which the fullerene contained powder was synthesized in gram quantities that was sufficient for experimental research.

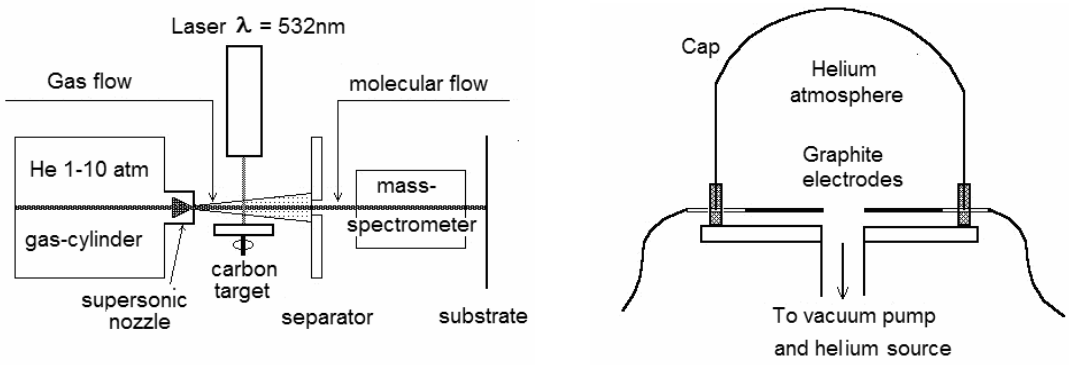

Fig. 59. Set-up of the R.Smalley laser ablation equipment for fullerene synthesis.
Fig. 60. Set-up of the Kratschmer and Huffman arc-discharge equipment for synthesis of fullerenes.

Under action of power laser irradiation (fig. 59) or arc-discharge (fig. 60) the sublimation or ablation of target graphite or graphite electrodes occurs during which carbon is evaporated in kind of atoms, dimmers C_2, benzyl rings C_6, curullenes C_{12} and other clusters C_n, n=1–100. These products are flowed away by inert gas onto a cooled substrate. In the flight a mass-spectrum is measured. The deposit (soot) on the substrate contains a mixture of different fullerenes, onions, nanotubes, and another clusters in dependence of technology parameters. Shown in fig. 61 is the example of mass spectrum of products obtained by modified arc-discharge technique demonstrating the peaks related to C_{24}, C_{28}, C_{60}, C_{70}, and set of C_{76+2n}, n=0–40 clusters.

For vaporization of target graphite the different equipments may be used, such as, the plasmotrons, ion beams, solar furnaces, et al.

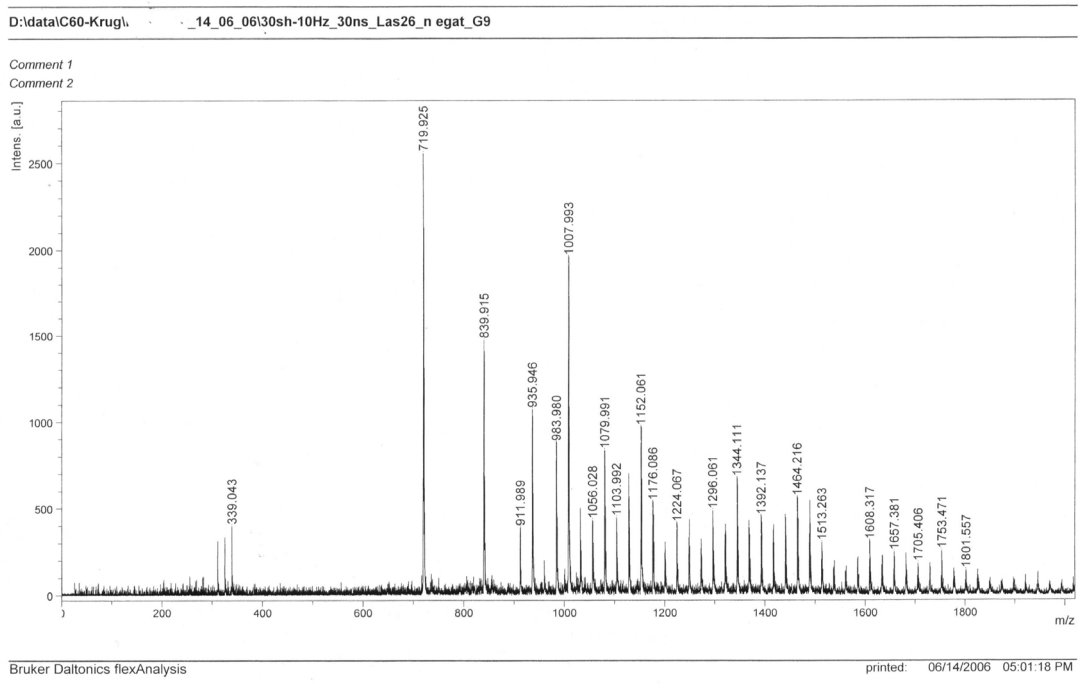

Fig. 61. Mass spectrum of fullerenes obtained by modified arc-discharge technique in IPMS NASU, Kiev. The most intensive peak with 820 a.u. relate to the cluster 820: 12 = 60 carbon atoms, i.e. buckyball C_{60}.

For chemical extraction of fullerenes from the mixture the obtained deposit is solved in the toluol, ethanol, or other solvents which further are evaporated giving the red crystals of fullerites in the vestige. Note that for each type of fullerenes the special solvent is requested.

Physical extraction techniques such as centrifugation or chromatography are used also. In the chromatography column the different clusters rearrangement in height in accordance with its weight. Then different fractions, in particular fullerenes, are extracted from different height of the column.

9.7. Spectral properties of C_{60}

Optics should know that Raman spectroscopy is most simple and informative method for studying of the molecules vibration spectra. Light excitation takes place at some frequency ν, while a scattering runs at red Stock frequency $\omega - \omega_i$, or violet anti-Stock frequency $\omega + \omega_i$, where ω_i are the natural frequencies of molecule vibrations. The molecule C_{60} has 46 natural frequencies. In accordance with group theory a decomposition of icosahedral symmetry group on irreducible representations gives the following types of vibrations

$$\Gamma_{C60} = 2A_g + 3T_{1g} + 4T_{2g} + 6G_g + 8H_g + A_u + 4T_{1u} + 5T_{2u} + 6G_u + 7H_u \qquad (39)$$

where *g* are even, *u* are odd oscillations, the number points on the order of degeneracy. Among them there are 10 Raman active modes ($2A_g$+$8H_g$) and 4 Infra-red active ($4T_{1u}$), while the rest of them are the optical silent modes. Among active modes one can emphasize three most peculiar modes, namely, the breathing A_{g1} mode, radial ω=492 cm^{-1} mode, the pentagonal tangential A_{g2} pinch mode ω=1469 cm^{-1} where pentagons are periodically compressed and stretched, and elliptical H_{g1} squash mode ω=273 $см^{-1}$, where atoms on diameter opposite sites vibrate in antiphase.

The last mode belongs to the so called gallery of whispering modes. This name originates from architecture acoustics, where the sound is propagated in colonnades or cupola at special resonant frequencies with low attenuation. The last stems from interference of ring waves propagated in opposite directions, where the integer number of half-waves keeps within the ring length, $\pi d = n\lambda/2$. In the fullerenes and nanotubes this wave lengths of whispering modes are determined by bond length, $\lambda/2 = a_{CC}$. At *n*=2 we have the elliptical squash mode.

Excitation in ultraviolet range can result not only to oscillation but to destroy of fullerenes. Actually in case of gas XeCl-laser with λ=308 nm, the quantum energy is $E=hc/\lambda$=4.1 eV, that is smaller then cohesive energy 7.4 eV, but sufficient to destroy C_{60} at two-phonon absorption.

9.8. Application of fullerenes

To day the using of fullerenes comes into starting stage of industry application. Thousands of patents have been registered in USA, Europe, Japan, et al. on the fullerene materials, methods, and devices.

In optics the fullerenes were proposed to use for the electrophotographical imaging, optical filters, photopolymer sensibilizators, nonlinear optical materials. In electronics

they are used as the molecular switchers, diodes, transistors, resistors for lithography, collar cell elements, magneto-optical recorders, photoelectronic devices. In military sphere the fullerenes used as the optical and microwave absorption coatings to prevent aircraft and missiles from radar detection.

The example is the fullerene amplifier shown in fig. 62. Under applied voltage ~ 20 mV the piezocrystal is expended, the tip is shifted at ~1 Angstrom, the fullerene is compressed at ~15%, its resistance is reduced, while the output voltage in external circuit is increased ca ~100 mV, i.e. is enhanced in ~5 time in the result.

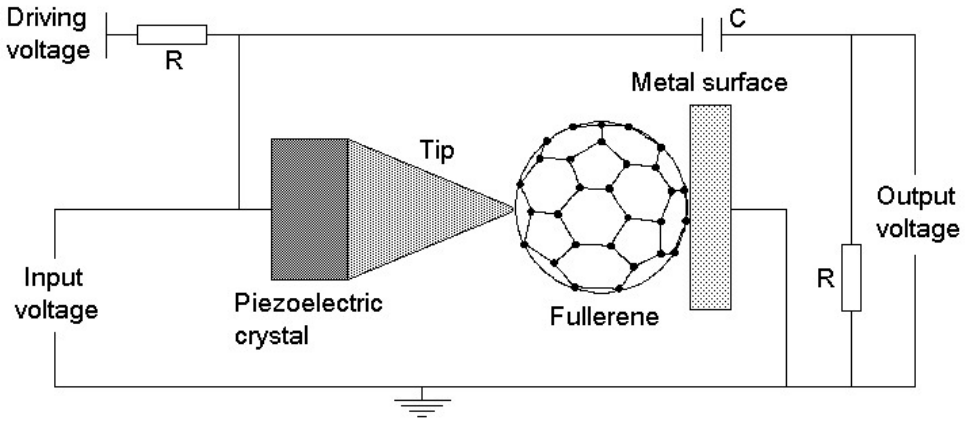

Fig. 62. Set-up of nanoamplifier on base of fullerene, developed in Zurich IBM Laboratory.

However many applications announced early does not meet a successful realization. In particular, the fullerene lubricants turn out to be very expensive, the superconducting phases and additives for missile fuel dos not gives essential advantages over conventional materials. The most perspective road for fullerenes applications appear to be the analytical chemistry and functionalization of fullerenes with application in biology, medicine and nanobiotechnology.

10. CARBON NANOTUBES (C-NT)

Nanotubes (NT) are recognized now as one of base for the future nanoelectronics. Nanotubes are the 1D quantum cylinders nanoscopic in diameter while micro/macroscopic in length so they are quantum macrocrystals possessing potential unique properties. Images of carbon nanotubes (CNT) and their arrays are shown in fig. 63.

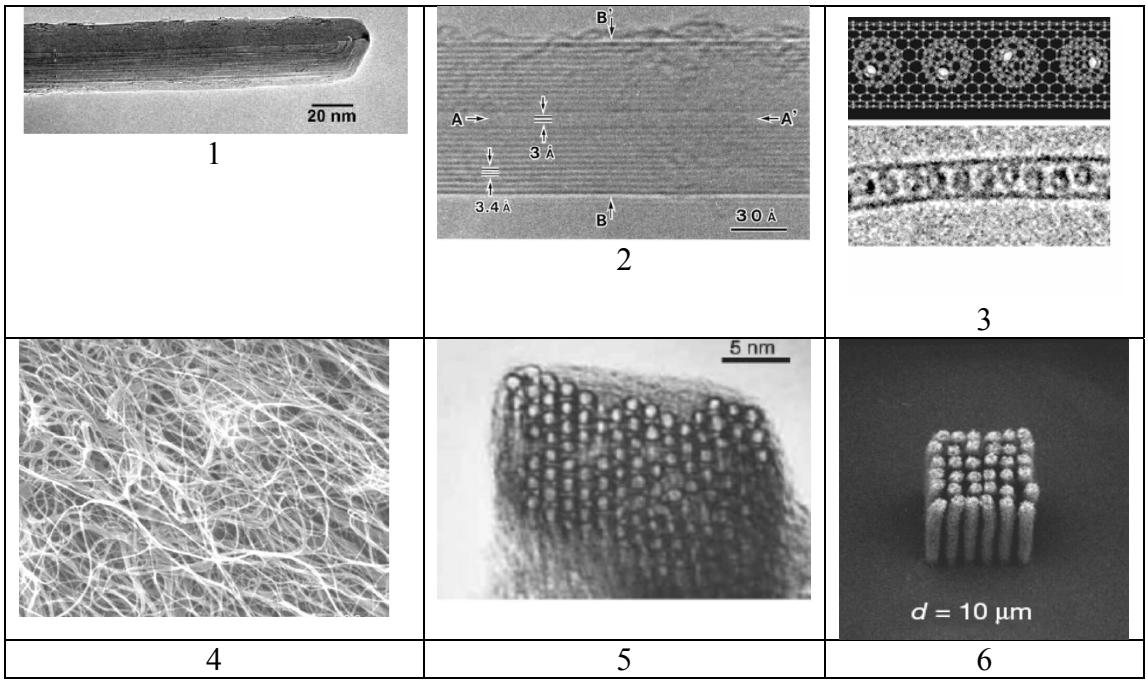

1 2 3 4 5 6

Fig. 63. Carbon nanotubes: 1 – end of NT; 2 – high resolution transmitted electron microscope image of multi-walled NT showing interlayer distance 0.34nm as in graphite (X. Zhao, et al. Phys. Rev. Lett., 92, 12, 125502 (2004)); 3 – scheme of nanotube with inserted fullerenes encapsulated by gadolinium Gd@C_{60} ; 4 – array of NTs (J.Liu, et al., Science, V.280, 1253 (1998)); 5 – bundle, cable of NTs (A.Thess, et al. Science 273**,** 483 (1996)); 6 – pillars of NTs (X. Wang, et al. In: Encyclopedia of nanoscience and nanotechnology, Ed. H. S. Nalwa, Amer. Sci. Publ., v. 1, 1–15 (2004)).

10.1. Geometrical structure

From geometric point of view NT is the graphite rolled in form of cylinder. Its geometry therefore may be expressed in terms of parameters of graphene, the single graphite-like BN sheet (fig. 64). Let us consider the hexagonal sheet in hexagonal coordinate system with center in zero point O and with unit vectors $\vec{a}_1$ and $\vec{a}_2$ (fig. 64), where any sheet site may be expressed using two integers (n,m) called as chiral numbers, so any atomic position is defined by the chiral vector:

$$\vec{C}_h = n\vec{a}_1 + m\vec{a}_2 \qquad (40)$$

where $n \geq m$ without loss of generality.

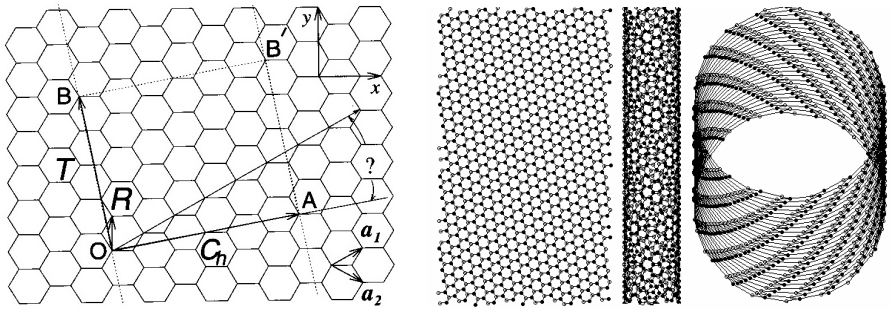

Fig. 64. Scheme of rolling of graphene sheet into the nanotube. $\mathbf{a_1}$ and $\mathbf{a_2}$ are the basic unit vectors of hexagonal sheet; $\mathbf{C}_h$ is a chiral vector; T is a translation vector; the rectangular OAB'B defines the unit cell of NT (n=4,m=2) (left) and (6,1) (right).

Rolling this sheet in such the manner when the site $C_h(n,m)$ coincides with zero O of coordinates gives the single-walled nanotube (n,m) (SWNT).

Two special high-symmetry cases arise, namely:

at n=m $C_n(n,n)$ – NT of arm-chair configuration;

at m=0 $C_n(n,0)$ – NT of zig-zag configuration;

The rest of NTs of (n,m) type are called as chiral NTs.

Nanotube may be considered as 1D crystal with translation vector $\vec{T}$ parallel with NT axis. Unit cell of NT is determined by two vectors, the chiral C_h and the translation $\vec{T}$ ones.

Diameter of NT *d* is determined by modulus of the vector $C_h = \sqrt{3}a_{cc}\sqrt{n^2+m^2+nm}$, which is the length of a circle

$$d = \frac{C_h}{\pi} = \frac{\sqrt{3}a_{cc}\sqrt{m^2+n^2+nm}}{\pi} \tag{41}$$

where a_{cc}=0.1421 nm is the nearest inter-carbon distance, that is nearly equal to interatomic distance in graphite sheet.

Number of atoms in elementary unit cell of NT is

$$N = \frac{4(n^2+m^2+nm)}{g_R} \tag{42}$$

where g_R is a least common divisor of two integers, (2n+m) and (2m+n). Number of hexagons in the unit cell is lower in twice.

Module of translation vector $\vec{T}$ is

$$T = \left|\vec{T}\right| = \frac{\sqrt{3}\left|C_h\right|}{g_R} \tag{43}$$

Angle of chirality is

$$\theta = arctn\left(\frac{\sqrt{3}m}{2n+m}\right) \tag{44}$$

In case of the arm-chair configuration (n,n) we have: the least common divisor of integers (2n+n) and (2n+n) is g_R =3n. Number of atoms is $N = 2n$. Modulus of chiral vector is $C_h = 3a_{cc}n$. Diameter is $d = \frac{3a_{cc}n}{\pi}$. Chiral angle is $\theta = 30^0$. Modulus of translation vector is $T = \sqrt{3}a_{cc}$.

In case of the zig-zag configuration (n,0) we have: the least common divisor of integers (2n+0) and (n) is g_R =n. Number of atoms is $N = 2n$. Modulus of chiral vector is $C_h = \sqrt{3}a_{cc}n$. Diameter is $d = \sqrt{3}a_{cc}n/\pi$. Chiral angle is $\theta = 0$. Modulus of translation vector is $T = 3a_{cc}$.

10.2. Symmetry

Symmetry of zig-zag (n,0) and arm-chair (n,n) NTs is the same and depend on the evenness of integer n.

1. In case of odd n the symmetry elements are:
   1. Axis of n-order symmetry C_n.
   2. Perpendicular n axes $C_{2\perp}$.
   3. Vertical n planes σ_d.

Hence symmetry group of both the zig-zag and arm-chair nanotubes with odd n is: $D_{nd} = D_n(C_n + nC_{2\perp}) + n\sigma_d$.

2. 1. In case of even n the symmetry elements are:
   1. Symmetry axis $D_{nh} = D_n(C_n + nC_{2\perp})$.
   2. Horizontal plane σ_h.
   3. Vertical n planes σ_v.

Hence symmetry group of both the zig-zag and arm-chair nanotubes with even n is:

$$D_{nh} = D_n(C_n + nC_{2\perp}) + n\sigma_v + \sigma_h .$$

Symmetry of chiral nanotubes is lower and symmetry group contains screw axis.

10.3. Unit cell and Brillouin zone

Optic absorption and Raman spectra depend on electronic band structure of nanotubes. To study of them it is necessary to introduce a reciprocal space and Brillouin zone. Only after introducing of these basic concepts we would be able to consider any dispersion law $E(\vec{k})$ and band structure.

First of all let us consider the unit cell, reciprocal lattice and Brillouin zone of graphene, the single hexagonal layer of graphite (fig. 65).

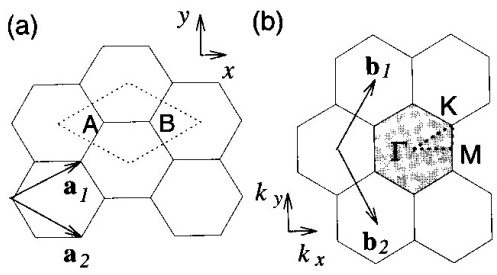

Fig. 65. Primitive unit cell (the rhomb) and Brillouin zone (the painted hexagon) of graphene. $\mathbf{b}_1$, $\mathbf{b}_2$ are the reciprocal lattice vectors; Γ, K, M are the points of highest symmetry in the center, vertex and edge of Brillouin zone respectivaly.

Unit cell vectors of graphene are:

$$\vec{a}_1 = (\frac{\sqrt{3}}{2} a_{cc}, \frac{a_{cc}}{2}),\ \vec{a}_2 = (\frac{\sqrt{3}}{2} a_{cc}, -\frac{a_{cc}}{2})$$

Parameters of unit cell are $|\vec{a}_1| = |\vec{a}_2| = \sqrt{3} a_{cc}$ =0.246 nm.

Vectors of reciprocal lattice unit cell are $\vec{b}_1 = (\frac{2\pi}{\sqrt{3} a_{cc}}, \frac{2\pi}{a_{cc}}),\ \vec{b}_2 = (\frac{2\pi}{\sqrt{3} a_{cc}}, -\frac{2\pi}{a_{cc}})$

Parameter of reciprocal lattice unit cell is $B = \frac{4\pi}{\sqrt{3} a}$.

Brillouin zone is defined as the primitive unit cell of reciprocal lattice. It is the hexagon for 2D hexagonal reciprocal lattice (fig. 65). Some points of high symmetry, the Γ, K, and M ones should be marked here, in which the dispersion law should be determined.

Let us consider a nanotube. Its unit cell in real space is determined by vectors $\vec{C}_n$ and $\vec{T}$. In reciprocal space the elementary unit cell and Brillouin zone is determined by the vectors $\vec{K}_1$ and $\vec{K}_2$ normal to the vectors $\vec{C}_n$ and $\vec{T}$. In accordance with theory of reciprocal lattice $\vec{R}_i \vec{K}_j = 2\pi\delta_{ij}$, so for nanotube

$$\vec{C}_h \vec{K}_1 = 2\pi,\ \vec{C}_h \vec{K}_2 = 0,\ \vec{T}\vec{K}_1 = 0,\ \vec{T}\vec{K}_2 = 2\pi$$

where $\vec{T} = t_1 a_1 + t_2\, a_2$.

From these conditions one can obtain the relations for the reciprocal vectors: the $\vec{K}_1 = \frac{1}{N}(-t_2\vec{b}_1 + t_1\vec{b}_2)$ is the vector along circular, where $t_1 = \frac{2m+n}{g_R}, t_2 = -\frac{2n+m}{g_R}$, $|\overline{K}_1| = \frac{2}{d}$, and the $\vec{K}_2 = \frac{1}{N}(m\vec{b}_1 + n\vec{b}_2)$ is the vector along the translation one, or NT's axes.

Hence the Brillouin zone of 1D chiral NT is a set of linear segments of $|\overline{K}_2|$ in length along NT axes $\vec{T}$ (fig. 66). Number of points in Brillouin zone for finite NT is determined by length of this segment $\frac{2\pi}{L}$, where *L* is the NT length. Number of μK_1 segments is equal to $\mu = 0,1,2 \ldots N-1$.

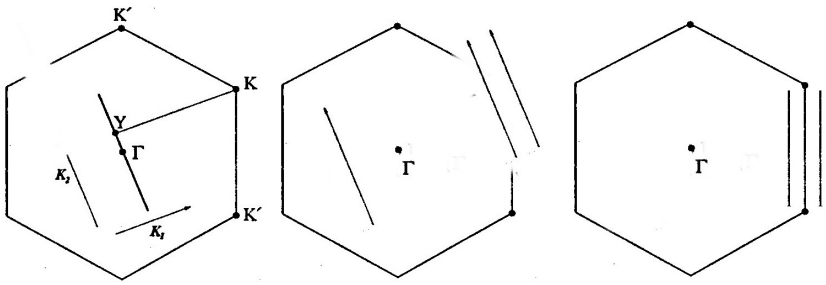

Fig. 66. Brillouin zones in kind of 1D segments for the chiral, zig-zag, and armchair nanotubes respectivaly.

10.4. Band structure

10.4.1. Band structure graphite

Band structure arises in result of structure periodicity along NT axis. If periodicity is neglected, when NT is considered as a molecule, the energy bands degenerate in molecular energy levels. Band structure predetermines the optical and Raman spectra.

Let us consider the band structure of graphite shown in fig. 67.

Two main energy dispersion curves E(k) determining the band structure after solution of eigenvectors within a tight-binding approach are as follows:

$$E_{g2D}^{\pm}(\vec{k}) = \frac{E_{2p} \pm \gamma_o \omega(k)}{1 \mp s \cdot \omega(k)} \approx (E_{2p} = 0) \pm \gamma_o \omega(k) \qquad (45)$$

where E_{2p} is the energy of 2p-orbital binding two atoms in graphite;
γ_o =2.9 eV is the matrix element of Hamiltonian between nearest neighboring orbitals p_z called an overlap integral of C-C atoms, s= 0.129 eV is a constant;

$\omega(k)$ is the function $\omega(k) = \sqrt{1 + 4\cos\frac{\sqrt{3}k_x a}{2} \cdot \cos\frac{k_y a}{2} + 4\cos^2\frac{k_y a}{2}}$.

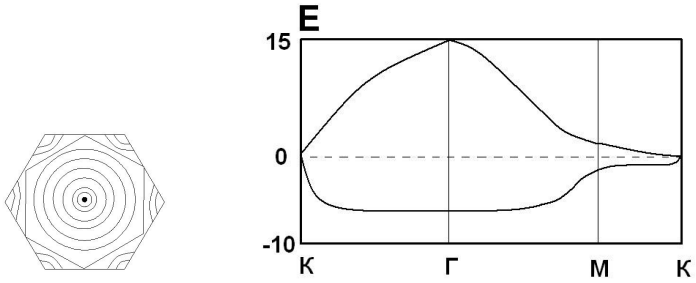

Fig. 67. Izoenergetical levels map in hexagonal Brillouin zone and scheme of the graphite band structure.

In vicinity of K-point in Brillouin zone it have the linear form $\omega(k) \approx \frac{\sqrt{3}}{2} ka\gamma_o$, then a band gap in K-point is $E_{g2D}^{\pm} \approx \pm\frac{\sqrt{3}}{2} ka\gamma_o$ = 0.04 eV. Hence graphite is a semimetal.

10.4.2. Band structure of C-NTs

Let us consider the effect of rolling of 2D-graphite into the 1D-nanotube.
The overlap integral was shown by Coster-Slatter method to change:

$$\gamma_o(d) = \gamma_o(\infty)\left[1 - \frac{1}{2}\left(\frac{a_{cc}}{d}\right)^2\right] \qquad (46)$$

Dispersion curve for 1D-NT is connected with the dispersion curve for graphite by the zone folding relation:

$$E_{\mu}(k) = E_{g2D}\left(k\frac{\vec{K}_2}{|\vec{K}_2|} + \mu\vec{K}_1 \right) \tag{47}$$

where $\mu = 0,1,2.....$ N-1, while k runs within the range $-\pi/T<k<\pi/T$.

Band structures for C-NTs were calculated as for any crystals by different methods, namely, an augmented plane waves (APW), an augmented cylindrical waves (ACW), a local density approximation (LDA), etc. It should be emphasized that the calculation of band structure is very tremendous and laborious computational problem. We consider the results right away. It was found that the band structure depends on symmetry, chiral numbers, and a type of material for the case of noncarbon NTs. Shown in fig. 68 are the dispersion relations and band structure typical for C-NTs.

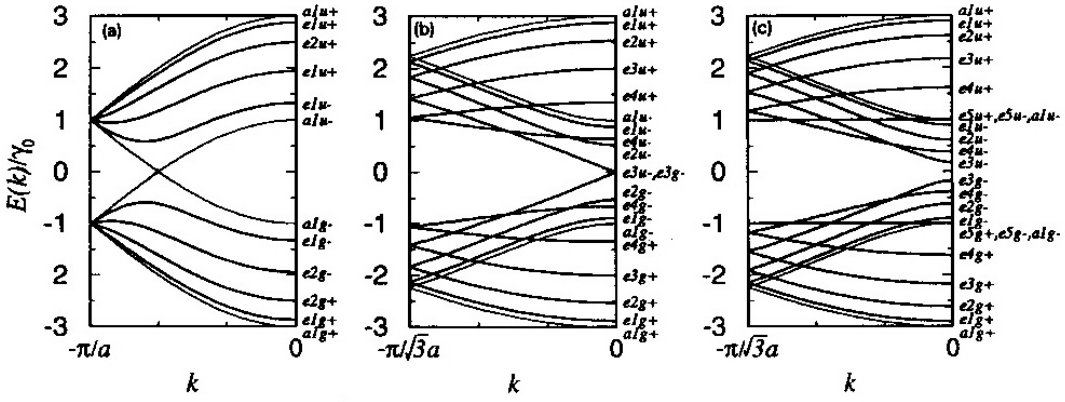

Fig. 68. Dispersion curves and band structure for typical carbon nanotubes: a) arm-chair metallic (5,5); b) zig-zag semiconducting (9,0) with odd n; c) zig-zag dielectric (10,0) with even n. Dispersion curves of *a* and *e* symmetry are undegenerated and twice degenerated respectivaly. The Fermi level is E_F=0.

It was found the following general relations for C-NTs:

1. The band structure of arm-chair (n,n) NTs, such as the (5,5) NT in fig. 68a, was found to be metallic always because of the dispersion curves cross the Fermi level always.
2. The band structure of any other NTs was found to be metallic or semiconducting in dependence of the relation between chiral numbers n and m, namely:

$$n-m=\begin{cases} 3l, l=1,2,3-metal \\ \neq 3-semiconductor \end{cases} \tag{48}$$

3. The conductivity of zig-zag (n,0) NTs was found to be different in dependence of n. If n is divisible by 3, the C-NT will be metallic or narrow-band semiconducting NTs, as for (9,0) NT in fig. 68b. If n is not multiple 3, the C-NT becomes to be dielectric, as (10,0) NT in fig. 68c.

Hence a small increase of NT's diameter leads to drastic changes in band structures and a conductivity type. This unusual important property may be utilized in special switches and transistors.

10.4.3. Electronic density of state in NT

Another important feature of electronic structure is the density of electronic state (DOES). It may be calculated via integration over energy states within each energy band and by summation of states over all occupied bands:

$$D(E) = \frac{2}{N}\sum_{\mu=1}^{N}\int \frac{1}{\left|\frac{dE_\mu(k)}{dk}\right|}\delta(E_\mu(k) - E)dE \qquad (49)$$

Important feature of DOES is seen from this equation, namely, the $D(E)$ have maxima (peaks) in the vicinity of special points where dispersion curves $E(k)$ is flat and approach to zero $\left|\frac{dE_\mu(k)}{dk}\right| \sim \sqrt{E - E_0}$.

Therefore DOES for CNTs have a typical view shown in fig. 69. The main distinguishing from graphite is seen to be the peaks of DOES called the singularities of van Hove, for which a cross section of nanotube Brillouin zone (segment) with special nodes of graphite Brillouin zone (hexagon) is responsible for.

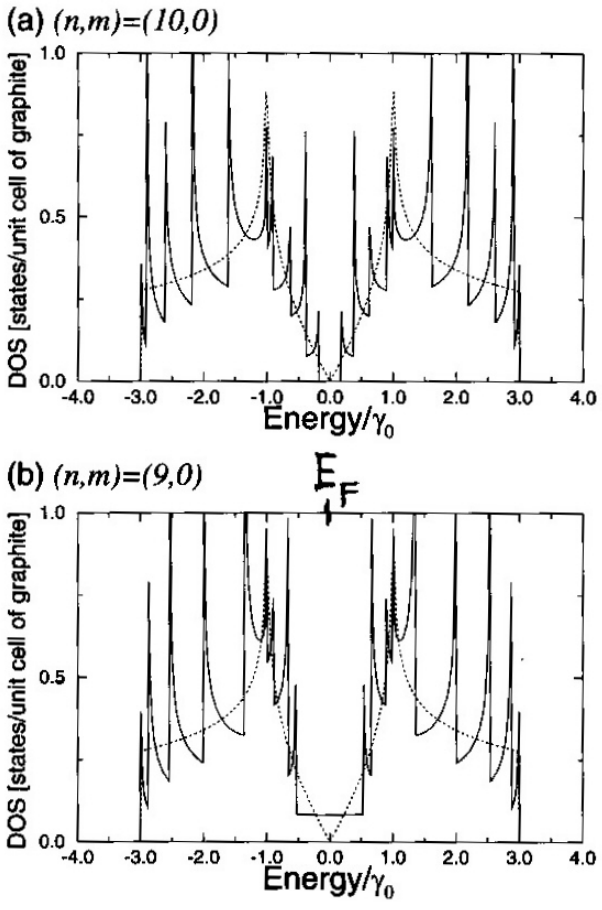

Fig. 69. Density of states (DOES) for single elementary cell of zig-zag NTs**:** a) semiconducting (10,0) NT with odd n, and b) metallic (9,0) NT with even n. By dotted line the DOES for graphene is shown emphasizing the peak structure of 1D nanotubes DOES.

One can estimate the peak location at energy scale as

$$E(k) = E_{g2D}(k) = \sqrt{3} a_{cc} \gamma_0 k \tag{50}$$

For nanotubes $k = |k_1|$, $\vec{k}_1 = \dfrac{\pi}{a(n^2 + m^2 + nm)}(\sqrt{3}(n+m), n-m)$

$k_1 = \dfrac{\pi}{a(n^2 + m^2 + nm)} \sqrt{[\sqrt{3}(n+m)]^2 + (n-m)^2} = \dfrac{\pi 2\sqrt{N}}{aN} = \dfrac{2\pi}{\sqrt{N}} = \dfrac{2}{d}$, where $a = \sqrt{3} a_{cc}$.

Substituting one can obtain the location of first DOES peaks that determine a width of energy band gap. For metallic and semiconducting NTs it is equal respectivaly to

$$E_1^M = \frac{6 a_{cc} \gamma_0}{d}, \quad E_1^H(d) = \frac{2 a_{cc} \gamma_0}{d} \tag{51}$$

Width of NT band gap depends on its diameter and have the typical hyperbolic view that approaches asymptotic meaning for graphite under $d \to \infty$, namely, a band gap increase when diameter decrease as $E_g \sim 1/d$ (fig. 70).

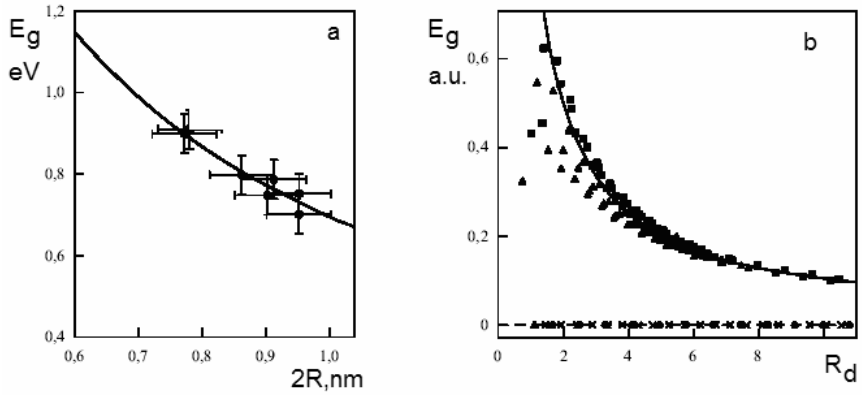

Fig. 70. Dependence of band gap width on NT relative radius R_d=R/a_0 calculated (a) and measured (b) for nanotubes with of different chirality.

For metallic nanotube at Fermi level the DOES per length unit is:

$$N(E_F) = \frac{8}{\sqrt{3} \pi a \gamma_0} \tag{52}$$

It is known that transitions from valence band into conducting band are affected by:
– absorption of photons, that is active optical or infrared modes;
– absorption of phonons, that is active resonance Raman modes.
Reversible transitions from conducting into valence band are known to result in:
– photon scattering giving the optical or infrared luminescence spectra;
– phonon scattering giving the Raman spectra.

Hence the electronic structure becomes to be apparent in experimental optical spectra demonstrating the unity between:
– electronic structure $E(k)$ with DOES $N(E)$;

– optical absorption and luminescence spectra with photon absorption and scattering respectively;
– resonance absorption Raman spectra with phonon absorption.

10.5. Phonon spectra

Shown in fig. 71 are dispersion relations and phonon spectra for graphite.

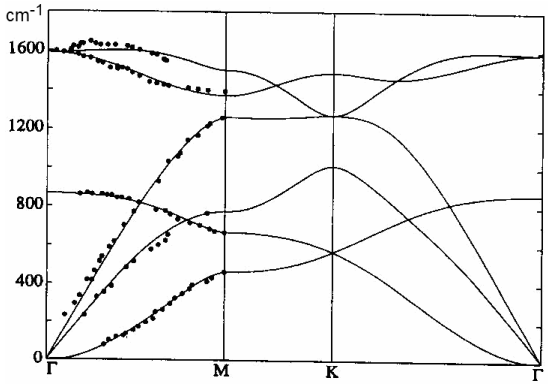

Fig. 71. Phonon dispersion curves in Brillouin zone for graphite.

From 2D phonon spectra for graphene one can obtain the phonon spectra for nanotubes via the zone folding method in the same manner as for electronic spectra:

$$\omega_{1D}^{m\mu}(k) = \omega_{2D}^{m}(k\frac{\vec{K}_2}{|\vec{K}_2|} + \mu\vec{K}_1) \qquad (53)$$

Graphically this method looks as shown in fig. 72.

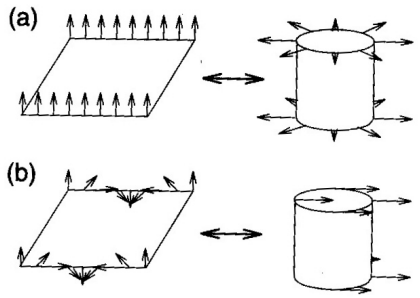

Fig. 72. Scheme illustrating the zone folding method: a) the tangential transversal acoustical (TA) mode with **k**=0 in graphene transforms into the radial breathing mode (RBM) in nanotube; b) combined transversal-longitudinal mode in graphene transforms into acoustical mode in nanotube normal to its axis.

Let us consider a typical phonon spectra of nanotubes using (10,10) C-NT as an example. Number of hexagons around the NT ring is $N(10,10) = \frac{2(n^2+n^2+n\cdot n)}{g_R} = \frac{2\cdot 3\cdot 10}{30} = 30$. Number of atoms in elementary cell is 2N=40. Number of oscillating mode equal to degree of freedom 40x3=120 among

which 66 are undegenerated and 54 are degenerated. Number of phonon states per C atom is N = 120/40=3.

In general the phonon spectra for NT resemble the same for graphite (fig. 73).

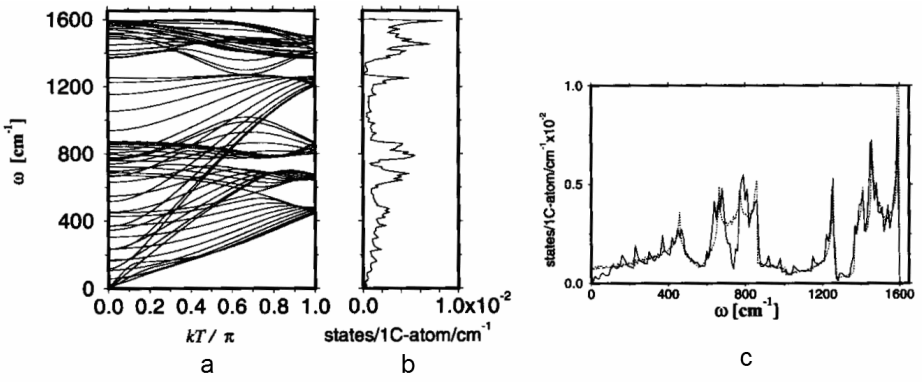

Fig. 73. Phonon dispersion curves and density of phonon states (DOPS), calculated for arm-chair (10,10) C-NT.

Intersection of dispersion curves E(k) with k=0 leads to peculiar features for DOPS of nanotubes, that manifest itself in peaks of DOPS. Consider such peculiarities in low-frequency range shown in fig. 74.

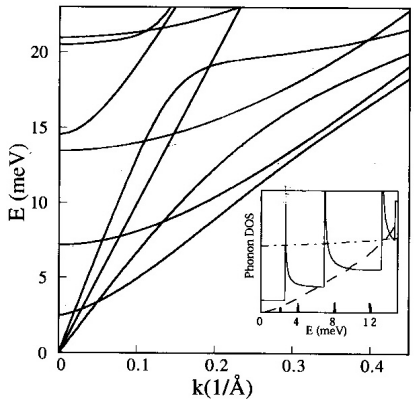

Fig. 74. Phonon dispersion curves for (10,10) C-NT with four acoustic modes. Shown in insert is DOPS for 1D NT in comparison with graphene (doted line). DOPS for NT is constant at E<2.5 meV, and then is gradually increased with van Hove singularities at the ends of subbands.

Phonon spectra contains four acoustical branches describing by general dependence: $\omega = \vartheta k$, where ϑ is a sound velocity, at that $\omega \to 0$ when $k \to 0$, and $\vartheta_{LA} = \sqrt{C_{11} / \rho}$, $\rho = 1.28 \cdot 10^3 \frac{kg}{m^3}$:

– one longitudinal acoustic (LA) mode, υ_{LA}=24 km/s;
– one torsion acoustic (TW) mode, υ_{TW} =15 km/s;
– two degenerated transverse acoustic (TA) modes, υ_{TA} 9 km/s.

In summary all acoustic modes gives a liner increased DOPS, $n(\omega) = \alpha\omega$.

Main peculiarities of NT's phonon spectra spring from their cylindrical (ring) vibration modes inherent solely for cylindrical geometry of NTs. These modes belong to the so called *gallery of whispering modes* that manifest them self in strong peaks in low- and middle-frequency range of Raman spectra. Their great intensities are caused by very low attenuation of the whispering modes due to the interference enhancement condition $\pi d = n\lambda / 2$.

Fig. 74 illustrates how the dispersion curve E(k) relating to lowest frequency E_{2g} mode transforms into a peak of DOPS $E_{2g}(\kappa)$. Such the peaks arise due to the optical type of branch which in contrast to acoustic ones behave itself as $g(\omega) \sim \frac{1}{\sqrt{\omega - \omega_0}}$ at $k \to 0$, because of $E(\kappa) \sim \kappa^2$ at $k \to 0$.

The dispersion curves are measured experimentally from inelastic scattering spectra of a penetrating radiation, especially the thermal neutrons.

Ii is shown in fig. 75 the calculated atomic displacements and frequencies of some Raman active vibration modes for (10,10) C-NT, while in table 7 all Raman and IR active modes are shown for different kinds of carbon nanotubes.

Table 7. Number and symmetry of overall Raman and IR active nodes for carbon nanotubes.

Type of nanotube	Point group	Raman active modes	IR active modes
AC(n,n), n is even	D_{nh}	$4A_{1g}+4E_{1g}+8E_{2g}$	$A_{2u}+7E_{1u}$
AC(n,n), n is odd	D_{nd}	$3A_{1g}+6E_{1g}+6E_{2g}$	$2\ A_{2u}+5\ E_{1u}$
ZZ(n,0), n is even	D_{nh}	$3A_{1g}+6E_{1g}+6E_{2g}$	$2\ A_{2u}+5\ E_{1u}$
ZZ(n,0), n is odd	D_{nd}	$3A_{1g}+6E_{1g}+6E_{2g}$	$2\ A_{2u}+5\ E_{1u}$
Chiral (n,m),n≠m≠0	C_h	$4A_{1g}+5E_{1g}+6E_{2g}$	$4\ A_{2u}+5\ E_{1u}$

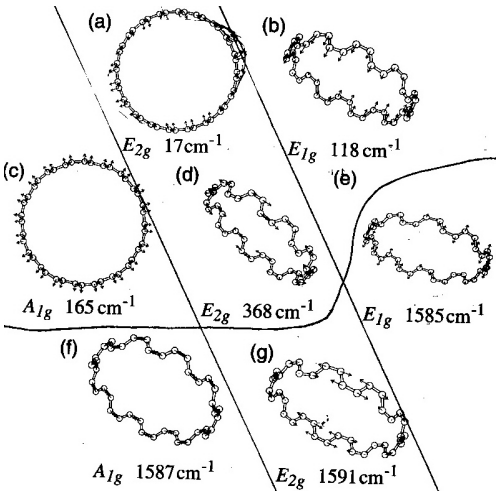

Fig. 75. Symmetry, frequency and atomic displacements of the natural characteristic normal vibrations for the (10,10) C-NT (R. Saito et al.).

Vibration frequencies one can calculate in a dynamic lattice theory from the eigenvalue matrix by solving the movement equations for atomic displacements:

$$m_i \ddot{\vec{u}}_i = \sum_{j=1}^{4} k^{ij}(\vec{u}_j - \vec{u}_i), i = 1,...N \tag{54}$$

where m_i is a mass of i-th atom, j is a type of vibration mode, $\vec{u}_i = (x_i, y_i, z_i)$ are the displacements of i-th atom, N is the number of atoms per unit cell, k^{ij}-3×3 is the tensor of force constants. Numerical values of force constants for graphite are presented in table 8. After Fourier transformation the vector $\vec{u}_i$ gives the vector $\vec{k}$ in reciprocal space while tensor $k^{ij}(r)$ transforms into dynamical matrix:

$$D^{ij}(\vec{k}) = \sum_j (k^{ij} - \omega^2(\vec{k})m_i)\delta_{ij} - \sum_j k^{ij} e^{-i\vec{k}-\Delta\vec{R}_{ij}},$$

where $\Delta\vec{R}_{ij}$ is a vector between atoms i and j.

Table 8. Values of force constants for acoustic modes of graphite (in units of 10^4 dyne/cm): r denotes the radial breathing mode, t_i denotes the tangential in-plane mode, t_o denotes the transverse out-of-plane mode.

Radial, r (tensile of bonds)	Tangential in-plane mode, t_i	Transverse mode, t_o (distortion of bonds)
ϕ^1_r= 36.50	ϕ^1_{ti}= 24.50	ϕ^1_{to}= 9.82
ϕ^2_r= 8.80	ϕ^2_{ti}= -3.23	ϕ^2_{to}= -0.40
ϕ^3_r= 3.00	ϕ^3_{ti}= -5.25	ϕ^3_{to}= 0.15
ϕ^4_r= -1.92	ϕ^4_{ti}= 2.29	ϕ^4_{to}= -0.58

Natural vibration frequencies ω^2 are extracted from the eigenvalue equation

$$\det\left|D^{ij}(\vec{k})\right| = 0 \tag{55}$$

This is scheme of solving this problems while the details are studied in solid state physics course.

Among the vibration modes in phonon spectra two special modes have to be stressed, with minimal and maximal frequency. For the (10,10) C-NT $\omega_{\min} = E_{2g} = 17cm^{-1}$.

Minimal frequency determines both the transitions between conductive and valence bands in semiconducting NTs, as well as the DOES at Fermi level for metallic C-NT:

$$N(E_F) = \frac{8}{\sqrt{3}a\gamma_0} \tag{56}$$

Maximal frequency $\omega_{\max}$ determines a Debay temperature in accordance with the relation:

$$k_B\theta_D = \hbar\omega_{\max} \tag{57}$$

Phonon spectra for the 2D bundles of NTs or the 2D crystal built from 1D nanotubes in comparison with the single NT spectra is changed due to nanotube interaction in the manner shown in fig. 76.

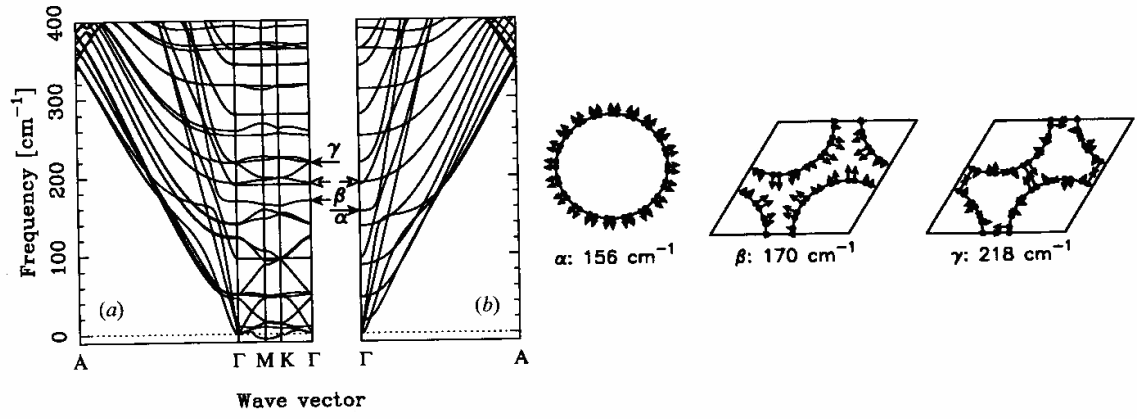

Fig. 76. Phonon dispersion curves for 3D triangular lattice of (10,10) C-NTs (Γ – A is the direction in k-space, related to axis of NT, while the another are normal points), as well as transformation of the breathing mode displacements of single NT into vibrations of 3D lattice of C-NTs.

10.6. Thermal physical properties

Average energy of thermal vibrations in harmonic oscillator model is:

$$\varepsilon(\omega,T) = \hbar\omega \cdot cth\frac{\hbar\omega}{k_B T} \tag{58}$$

Knowing the phonons spectra $g(\omega)$ one can calculate the total energy and thermal capacity of NTs:

$$E(T) = \int_{\omega_{\min}}^{\omega_{\max}} \varepsilon(\omega,T)g(\omega)d\omega = \sum_i \varepsilon(\omega_i,T)g(\omega_i) \tag{59},$$

$$C_v = \int_{\omega_{\min}}^{\omega_{\max}} \frac{\partial\varepsilon(\omega,T)}{\partial T}g(\omega)d\omega = \sum_i \frac{\partial\varepsilon(\omega_i,T)}{\partial T}g(\omega_i) \tag{60},$$

as well as another thermodynamic and thermophysic characteristics.

Calculation of phonon spectra $g(\omega)$ and solution of the related problems for carbon and noncarbon nanotubes was started not long ago. These problems are the challenges of our time so they may serve as topics of scientific research works in nearest future.

10.7. Thermal conductivity

Graphite and diamond are known to have the record extreme thermal conductivity hence the carbon nanotubes are expected also to posses the highest thermal conductivity. In free gas model or in the weakly interacted particles approximation the thermal conductivity is presented in kind of sum of thermal conductivity of electron and phonon gases:

$$\kappa = \sum c_v v l = \kappa_{ph} + \kappa_{el} \tag{61}$$

where the summation is over all phonon modes, v is the group velocity of phonons along NT axis, l is the free path length, c_v is specific thermal capacity of gas, $\kappa_{el} = L_0 \sigma T, L_0 = 2{,}45 \cdot 10^{-8} (\frac{v}{k})^2$ is Lorentz number and $\kappa_{el} << \kappa_{ph}$, $\kappa_{ph} = \frac{1}{3} c_v \langle v \rangle l_{ph} = \frac{1}{3} c_v \langle v \rangle^2 \tau_{ph} = \frac{1}{3} c_v \langle v \rangle l_p \rho$, where τ_{ph} is the relaxation time.

Dimensionality of thermal capacity is: $C_g = \frac{J}{\kappa g \cdot K}$, $C_g \cdot \rho = \frac{J}{\kappa g \cdot K} \cdot \frac{\kappa g}{m^3} = \frac{J}{m^3 \cdot K}$;

Dimensionality of thermal conductivity is: $\left[\frac{J}{m^3 \cdot K} \cdot \frac{m}{\sec} \cdot m = \frac{W}{m \cdot K} \right]$.

Thermal conductivity of carbon nanotubes at T=300 K was measured experimentally to be κ_{ph} ~6000$\frac{W}{m \cdot K}$, which in three time greater than the thermal conductivity of graphite ~2000$\frac{W}{m \cdot K}$. This is explained both by enlargement of the phonon free path due to a relatively weak scattering of all phonons in nanotubes, and by a velocity increase of new vibration modes formatted in nanotubes.

10.8. Electric conductivity

Let us consider the electric current passed through semiconducting NT. Fig. 77 illustrates the measurement scheme.

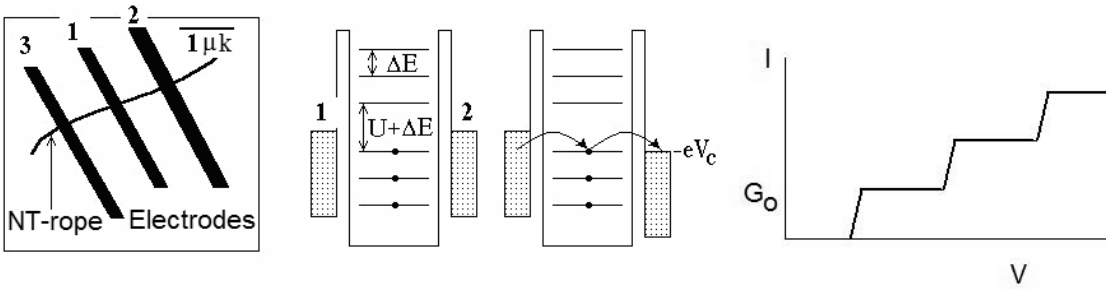

Fig. 77. Scheme of electro current measurement and passing of the current through the semiconducting C-NT. Current-voltage stepped curve is shown also.

Metallic electrodes are fabricated by lithography technique at dielectric substrate on which NT is placed by tweezers. If voltage U is applied the current is not passed, shown in fig. 77, because of NT is a quantum object, the energy levels of which in general case lies lower or higher of the energy levels of metallic electrodes 1 and 2. This is called as *Coulomb blockade*. However the position of NT energy levels may be changed applying the displacement voltage ΔE~1eV on third electrode 3. Therefore a potential of electrodes is shifted up to some quantum level of NT so the current begins to pass through this level. Changing the voltage one can shift the second, third and other levels through which a current becomes to be possible. Hence the current-voltage curve become to be of stepped type where the distance between ledges is equal to *the quantum of electroconductivity* determined as $G_0 = 2e^2 / \hbar = 7.75 \cdot 10^{-5}\, 1/ohm$. Hence the nanotube is quantum in diameter but macroscopic in length nanocylinder. It is just the reason of their unique properties.

Direction of current depends on chirality of nanotube as shown in fig. 78. In zig-zag NTs a current pass along axis, in arm-chair NTs a current pass over the ring, while in chiral NTs it twist spirally.

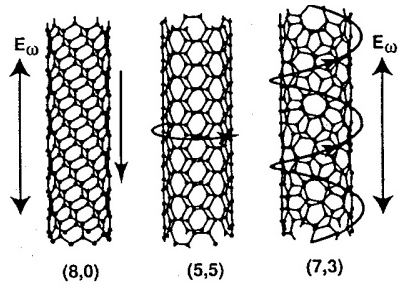

Fig. 78. Direction of the electric current, excited in nanotubes by light, polarized along NT axis.

10.9. Electron interference (Aaronov-Bohm effect)

Cylindrical geometry of NTs gives opportunity for electrons to move not only along NT axis but to circle in opposite directions too and therefore to interference. The interference of the electron circular waves known as Aaronov-Bohm effect manifests itself in experimental oscillation of electroconductivity and magnetoresistance.

Oscillations of electroconductivity caused by this quantum interference of electron waves in single-walled metallic C-NT locating between two electrodes was observed by Liang (fig. 79). Boundaries between NT and electrodes serve as mirror reflectors for electrons, while NT itself serves as the electron waves resonator of Fabry-Perrout type. Fig. 79 demonstrate the typical oscillation of electroconductivity in dependence of gate potential V_g at zero displacement voltage ($V = 0$) and low temperature T=4K.

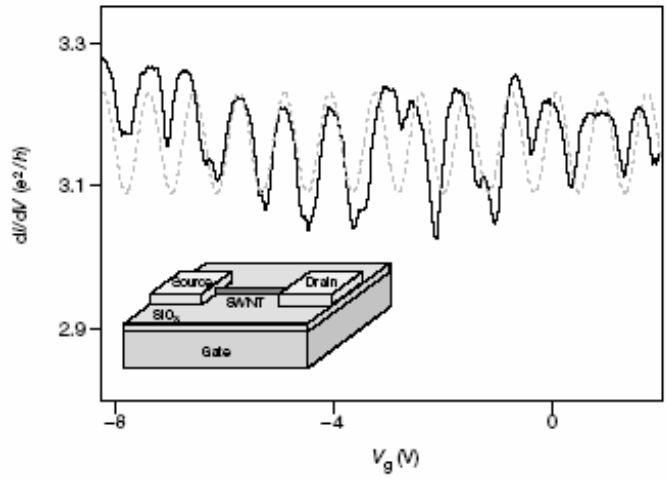

Fig. 79. Oscillations of electroconductivity for the single-walled carbon nanotube of 200 nm long in dependence of gate potential V_g that is caused by interference of the electron waves reflected from boundaries between NT and electrodes. Doted line is sinusoid. (W. Liang, et al. Nature, V.411, 665 (2001)).

The electroconductivity oscillations are observed near its average value 3.2 e^2/h with amplitude 0.1 e^2/h, where e^2/h =25.8 kohm^{-1}. Change in gate voltage shifts Fermi level and related value of electron wave vector $k = 2\pi/\lambda$, where λ is electron wave length. Therefore the oscillations caused by variation of k are similar to oscillation of light radiated from interferometer.

The oscillation of magnetoresistance in NT, the dependence of electroresistance on magnetic field induction was observed in first by Bachtold. If magnetic field is applied along NT axis then oscillations of electroconductivity one can observe in dependence of variation of magnetic induction through NT (fig. 80). This is explained by the dependence of electron wave phase on magnetic flow Φ that is the quantum-mechanical root of Aaronov-Bohm effect.

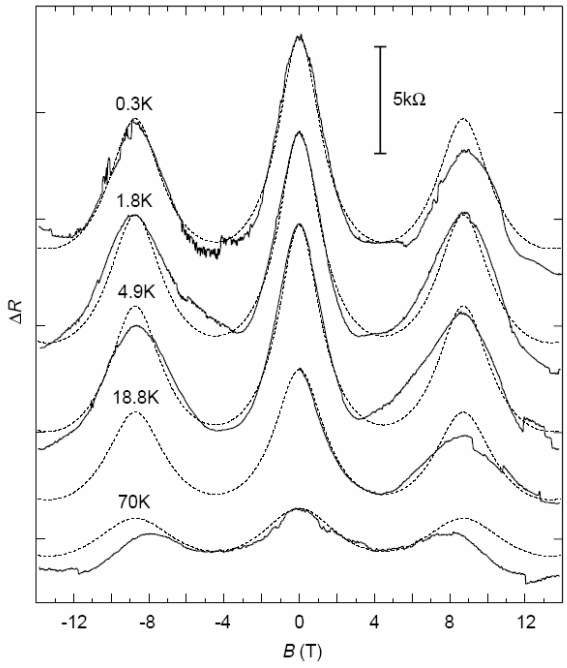

Fig. 80. Oscillations of electroresistance of multiwalled C-NT in magnetic field directed along NT axis. The full line denotes experiment while doted line show a result of calculation for cylindrical conductor of 8.6 nm in diameter and 170 nm long in the case of angle between cylinder axis and magnetic induction is 4.4^0. In absence of magnetic field the resistance is equal to 30.6, 30.1, 29.8, 25 and 21.4 κOhm at temperature from 0.3 K up to 70 K (A.Bachtold et al., Nature, V.397, 673 (1999)).

Amplitude of the resistance variation is close to *the quantum of electroresistance* $\frac{1}{G_0} = \frac{\hbar}{2e^2} = 12.9 kOhm$. Concordance between theory and experiment is achieved in assumption that current pass through one or two external walls of multiwalled NT.

In case of magnetic field is normal to NT axis the growth of electroconductivity is observed. The reason is a change of energy spectrum caused by formation of spin Landau levels in intersection point of valence and conductive bands that result in growth of DOES at Fermi level.

10.10. Nanotubular superconductivity

Superconductivity and *Cooper pairing* is known theoretically to arise when two electrons moves coherently, i.e. they have impulses equal in modulus but opposite in direction $\vec{p}_1 = -\vec{p}_2$. This case may be possible if and only when two electrons are placed at the distance equal or divisible by the half of de-Broighl wave length $\zeta_0 = x_2 - x_1 = \Delta x = \frac{h}{p_x} = \frac{\lambda}{2}$. Maximal distance is close to *the coherent length* $\xi_0 = \frac{\hbar v_F}{\Delta_0}$, where v_F is the electron velocity at Fermi level, Δ_0 is the width of superconductive gap equal to *the energy of Cooper pair*.

One can write the wave functions of two electrons as:

$$\psi_1 = A_0 \sin(k_1 x_1 + \omega_1 t_1) = A_0 \sin(\frac{p_1 x_1}{h} + \frac{E_1 t_1}{h});\ \psi_2 = A_0 \sin(\frac{p_2 x_2}{h} + \frac{E_2 t_2}{h}) \qquad (62)$$

The coherent condition $|\psi_1| = |\psi_2|$ gives: $p_1 x_1 = p_2 x_2$, $E_1 t_1 = E_2 t_2$.

The states of coherent electrons may be distinguishable only on value of quantum uncertainty that dictated by *Heisenberg relations*: $\Delta p \Delta x = h$, $\Delta E \Delta t \sim h$.

Dividing one each other reduces two Heisenberg relations into the single equation $\frac{\Delta p \Delta x}{\Delta E \Delta t} \approx 1$. Accounting $\frac{\Delta x}{\Delta t} \approx v_F$ we obtain $\Delta p = \frac{\Delta E}{\Delta v_F}$. Then the coherent length is

$$\zeta_0 = \frac{h v_F}{\Delta E} \qquad (63)$$

Typical experimental Fermi velocity by order of magnitude is $v_F = 2 \cdot 10^5 m/\sec$, the coherent length for superconductors of II order is close to $\zeta_0 = 20nm$, so the attractive energy of Cooper electrons is close to

$$\Delta E_c = \frac{h v_F}{\zeta_0} = 40meV \qquad (64)$$

Temperature caused by collision of electrons with thermal phonons changes the impulses of electrons and destroys thereby the electron coherency and superconductive state in the result. Hence the uncertainty energy of Cooper pair must be greater than energy of thermal vibrations $\Delta E_c > k_B T_c$.

The athermal nonchaoitic phonons such as the natural vibrations of crystal as assumed daringly by Frohlich are able to enhance the attractive electron interaction of Cooper pair via exchange by phonon. The energy of Cooper pair in this state may be estimated as the energy of exchange phonon $\Delta E_c = V = \hbar\omega^*$.

Within a band structure theory the Cooper pair arises in result of strong electron correlations. To be filled by correlated electrons a band becomes to be no rigid because of strongly correlated electrons change the conductive band itself – the band is bended at its edge and splitted in such a manner that the superconductive gap arises in conductive band which is equal to the energy of Cooper pair $\Delta_0 = \Delta E_c$. Maximal attractive correlation between Cooper electrons as well as a lowest destroying

interaction between Cooper pairs themselves is achieved when concentration of correlated electrons in the splitted band is equal to n_s=1/2. In this case the splitted lowest half-band is entirely filled while the highest subband is entirely empty. Just at this middle electron concentration in conductive band the greatest superconducting current was shown experimentally to arise.

In this model one can estimate the maximum superconducting critical temperature T_c. Using a simple Cooper relation $k_B T_c = \Delta E_c$ we obtain approximately $T_c \approx several 10^2 K$. This theoretical estimation may be considered as an opportunity to the room temperature superconductivity that is a world physical problem of paramount important.

This high-T_c superconductivity was suggested possible to be achieved in two kinds of materials, namely, 1) in thin superconducting or polymeric layered 2D heterostructures (idea of Ginsburg) under condition of a distance between the layers is close to correlation length $\zeta_0 = d$, or 2) in 1D filaments or wires (idea of Little and Parks), under condition of their diameter is smaller than coherent length $d < \zeta_0$. It was established in experiments that all high- and middle-temperature superconductors (YBa_2CuO_4, MgB_2, LuNiBC) have layered structure. It is not accidentally. It may be explained by the fact that interlayer empty space is the obstacle for thermal phonons interaction so the layers do not disturb each other. Therefore the interatomic interaction between layers is significantly smaller than in layers itself, so the thermal phonon interlayer vibrations influence weakly on natural in-plane phonon vibration responsible for electron-phonon interaction. Hence the breaking of Cooper pairs takes place at more higher temperatures that increases the critical superconducting temperature.

The distance between electrons in Cooper pair from one side have to be divisible by the electron half-wave at frequency $\omega^* = \frac{2\pi v_F}{\lambda^*}$, no smaller no bigger, while from another side it must be equal to interlayer distance *d*. Hence the superconductivity in 2D systems may be regarded as the quantum size effect.

As suggested by V.Pokropivny both above conditions are best satisfied in 2D crystal built from 1D nanotubes which in turns are rolled from 2D layered superconductors. This idea combine ideas of Ginsburg and Little-Parks.

This innovation is explained qualitatively as follows. In 1D nanocylinders and only in them there are natural circular cylindrical vibrations where atoms in diameter opposite side of NT oscillate in anti-phase. Therefore the localized electrons move unadiabatically with their bonded ions due to strong electron correlations (i.e. the electrons follow the whispering vibrations of ions) and oscillate also in anti-phase. Hence the impulses of these two electrons at diameter opposite side have impulses equal modulo but opposite in sign $\vec{p}_1 = -\vec{p}_2$. *Just this is the Cooper pair* by definition. Note for wires this condition is valid only particularly as being the reason of wire superconductivity. However in contrast to the solid cylindrical wires in the hole cylindrical nanotubes these circular cylindrical vibrations form the gallery of whispering modes, the peculiar feature of which is their low attenuation and enhancement due to interference condition for waves moving along ring in opposite directions, $\pi d = n\frac{\lambda^*}{2}$.

In addition it must be stressed that whispering modes are the collective vibrations in which all atoms of NT and variety of electron pairs are involved. Therefore everything of these pairs vibrate in antiphase forming thereby *the Bose-Einstein condensate of Cooper pairs*. Hence a nanotube looks as *ideal superconductor* but under three special conditions:

$\pi d = n\frac{\lambda_{el}^*}{2}$, (65), *the enhancement condition* of *electron waves interference*;

$\pi d = n\frac{\lambda_\phi *}{2}$, (66), *the enhancement condition* of *natural phonon vibrations* in nanocylinder;

$\zeta_0 = \frac{h v_F}{\Delta E}$, (67), *the compatibility condition* of the length of Cooper pair (correlation length) with Heisenberg relations.

From the first two equations leads $\lambda_{el} * = \lambda_\phi *$, that in fact is *the condition of the parametric resonance* of electronic and acoustical waves. Equating with correlation length gives $\lambda_{el} * = \lambda_\phi * = \zeta_0 = \frac{h v_F}{\Delta E} = \frac{h v_F}{h \nu *} = \frac{v_F}{\nu *} \approx \frac{2 \cdot 10^5 m/s}{118 cm^{-1}} \approx \frac{2000 m/s}{30 \cdot 10^9 Hz} = 56 nm$ where the typical frequency 118 cm^{-1} was taken for phonon E_{1g}-mode of (10,10) C-NT. Therefore the diameter of this nanotube in superconducting state must be equal to $d = \lambda * / 2\pi \approx 9 nm$, that is close to real diameter of (10,10) C-NT $d = \frac{\sqrt{3} a_{CC}}{\pi} \sqrt{10^2 + 10^2 + 10^2} \approx 13.8 nm$.

Let's estimate the critical superconducting temperature from Bardeen-Cooper-Schrieffer (BCS) theory within the framework of the phonon mechanism of superconductivity

$$T_c = \theta_D \exp^{-\frac{1}{N(0)V}} \tag{68}$$

where $N(0) = N(E_F) = \frac{8}{\sqrt{3}\pi a \gamma_0}$ is the density of electronic state at Fermi level per NT length unit, $V \approx E_{2g} d$ is the energy of electron-phonon interaction. Assuming d=10 nm, a=0.3 nm, E_{2g}=1600 cm^{-1}, we obtain

$N(0)V = 1.47 \frac{d \cdot E_{1g}}{a \cdot \gamma} \approx 1.5 \frac{10 \cdot 118 cm^{-1}}{0.3 \cdot 2.9 eV} = \frac{2034.5}{8.0668} 10^{-3} = 0.25$, $T_c \approx 2000 \exp^{-\frac{1}{0.25}} \approx 10^2$.

Hence theoretically one can possible to obtain the high-T_c or even *room-T_c superconductivity on the whispering mode in nanotubes*. Of cource these qualitative considerations needs confirmation within a strong theory of nanotubular superconductivity which have to be developed as yet.

Shown in fig. 81 are the schemes of two types of nanotubular superconductors in kind of the brush of nanowires covered by superconducting layered sheets forming nanotubes, as well as in kind of the superconducting nanotubes covered inner surface of cylindrical nanoporous membrane or zeolite.

To day the little of experimental research is known concerning the nanotubular superconductivity. Kasumov with co-workers from CNRS, France, has shown the carbon multi-walled nanotubes becomes to be superconductive with critical temperature T_c~0.5K in microwave field. The idea was proposed by V.Pokropivny that rolling of sheet into tube give rise the increment, enhancement of critical temperature on the ΔT_c value, which depends on the number of parameters, namely, type of NT material, its size and structure, parameter of NT lattice, etc. Rolling of layered superconductor of YBa_2CuO_4 type with high critical temperature T_c(bulk)~100K was assumed to increase this increment essentially

$$T_c(\text{NT}) = T_c(\text{bulk}) + \Delta T_c$$

down to room temperature.

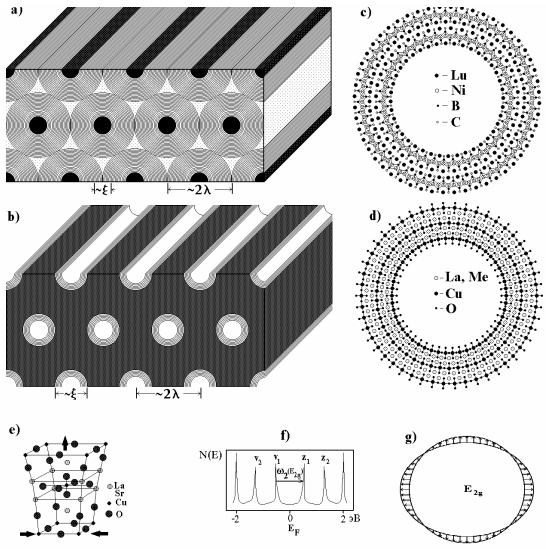

Fig. 81. Project of high-Tc superconductors on base of noncarbon superconducting nanotubes.
a) Lattice of metallic nanowires on the external surface of which the sheets in kind of nanotubes are deposited on base of the superconductors of LuNiBC(c), LaSrCuO (d) type; b) Nanoporous membrane on inner cylindrical surface of which the sheets in kind of nanotubes are deposited on base of the superconductors of LaCuO type; e) Deformation of LaSrCuO cause the growth of critical temperature, that take place in nanotubes; f) Typical density of phonon states in nanotubes; – густина фононних станів нанотрубки; g) Low attenuated whispering E_{2g}-mode in nanotube, responsible for enhancement of electron-phonon interaction.

For experimental observation of nanotubular superconductivity the route was also proposed as being the artificial fabrication of the crystals built from the noncarbon nanotubes based on superconductors. To day such the composites have been synthesized from carbon nanotubes but have not from noncarbon NT yet. This is the challenge of our time. From the above theoretical consideration this problem is expected to be solved in reality in near future.

10.11. Mechanical properties

Young modulus by definition is:

$$Y = \frac{1}{V_o}\left(\frac{\partial^2 E}{\partial \varepsilon^2}\right)_{\varepsilon=0} = \frac{1}{S_o \delta R}\left(\frac{\partial^2 E}{\partial \varepsilon^2}\right)_{\varepsilon=0} \qquad (69)$$

where E is a total energy, ε is a stress, V_o is an equilibrium volume, S_o is a square of cross-section of NT, $\delta R=h$ is a thickness of NT wall.

In set of superhard materials their Young modula vary in the following order:

$$\text{C (~1200 GPa)} \rightarrow \text{BC}_3 \text{ (~900 GPa)} \rightarrow \text{BN (~800 GPa)} \rightarrow \text{C}_3\text{N}_4 \text{ (~600 GPa)} \rightarrow \text{P (~280 GPa).}$$

It is evident that rolling of graphite-like sheet in cylindrical nanotube result in mechanical stress counteracted against the rolling.

The energy of rolling deformation per atom is equal:

$$\frac{E_s}{N} = \frac{1}{6} h^3 Y \frac{S_A}{d} \sim \frac{1}{d^2} \qquad (70)$$

where h is the cylinder width, which for SWNT may be considered as van-der-Waals distance between layers, Y is the Young modulus, d is the diameter of NT.

For carbon nanotubes approximately: Y=1130 GPa, h=0,335/2 nm, d=1 nm, a=0,246 nm, S=0,0524$\cdot 10^{-18}$ m^2. Then $\frac{E_s}{N}$=0.29 eV/atom. The general view is shown in fig. 82.

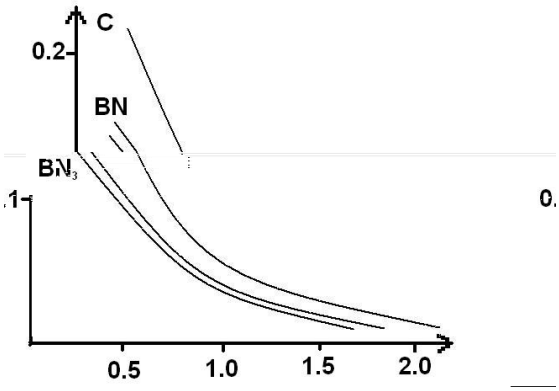

Fig. 82. Hyperbolic dependence of deformation twist rolling energy per atom on NT diameter.

Shown in the fig. 82 is the rolling energy estimated theoretically for noncarbon nanotubes which in the case of BN and BC_3 nanotubes is even smaller than for carbon nanotubes. It means that theoretically not only graphite but *any other layered materials can be rolled in nanotubes*. Therefore one can conclude the existence of noncarbon nanotubes considered further.

Due to cylindrical form the nanotubes posses low rolling friction coefficient that is known to be smaller than coefficient of sliding friction. This property make them possible to be utilized as the lubricant in future nano- and micro-electromechanical systems (MEMS), nanoengine and nanorobots.

Consider mechanical properties of single NTs by the example of carbon arm-chair (7,7) C-NT of 1 nm in diameter calculated by MD-method using Tersoff potential.

Observation and molecular dynamic simulation of NT *squeezing* show the high non-axial flexibility of nanotubes. Axial squeezing deformation of SWCNT causes a shape waviness, kinking and symmetry lowering as follows $D_{nh} \rightarrow S_4 \rightarrow D_{2h} \rightarrow C_{2h} \rightarrow C_1$. Neck is formed at ε_1=0.05 deformation, the double neck at ε_2=0.076, the loop at ε_3=0.09, and squash is occur at ε_4=0.13 (fig. 83.1).

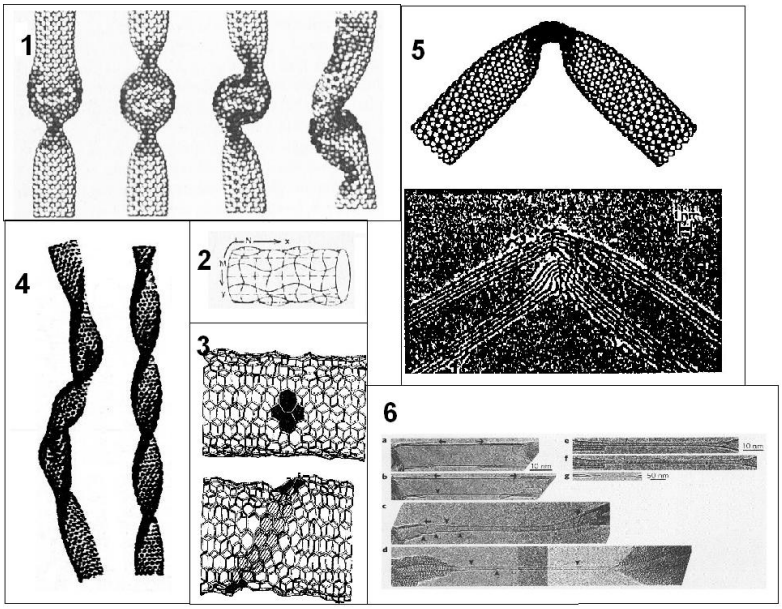

Fig. 83. Deformation of the single-walled carbon nanotube under the axial squeezing (1), stretching (2,3), twisting (4), bending (5) calculated by molecular dynamics method, and the superplasticity (6) observed experimentally by Dresselhaus et al.

Under *axial stretching* of nanotube the static deformation standing waves was shown to occur in accordance with Fourier harmonics, the N longitudinal and M transverse waves (fig. 83.2). For short nanotube when its length is smaller than standing wave length $L << \lambda$ the simple necking and buckling is occurs. It is interesting to note that at M=2 a deformation energy is lowers. This deformation resembles in shape the whispering modes pointing again at their peculiarity.

Under *torsion twisting* the axial-symmetry helicoids in kind of spiral ribbons, belts and then bending loops are formed (fig. 83. 4).

Under *bending* the SWCNT is elastically bent up to 110^0 angle and restore its shape under unloading (fig. 83.5). If the bending angle becomes greater > 120^o then the hexagonal net of NT sheets is destroyed and further kinks are formed.

It should be noted that the results of the atomistic molecular dynamic simulations are in good accordance with the continued deformation theory.

Under high deformations ε~ 5% – 6 % of axial stretching type the processes of plastic deformations and brittle fracture have occurs.

These results one can present in kind of *the map of ductile-brittle behavior* of NT (fig. 84), which determines the brittleness of C-NTs in dependence of their chirality.

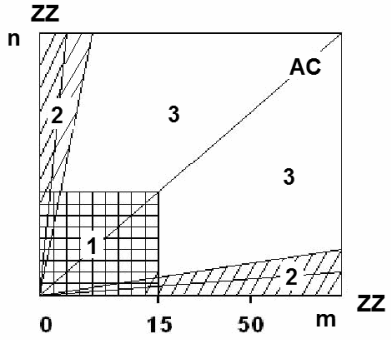

Fig. 84. Map of ductile and brittle nanotubes in dependence of their chirality (n,m).

Fig. 84 show that thin NTs (n<15, *d*~13 nm) independent of their chirality are ductile. More thicker nanotubes behaves in different manner, namely, the zig-zag nanotubes becomes to be brittle, the arm-chair are ductile, while chiral are ductile-brittle. Such distinction is explained by structural transformations in fracture process.

Arm-chair NTs behaves in ductile manner because of deformation energy is dissipated in the Stone-Weile defect formation (fig. 85). At further elongation these defects are splitted in the result of which the arm-chair NT transforms stepwise into chiral NTs and further into zig-zag NT in finish, as follows: $(n,n) \to (n,n-1) \to (n,n-2) \to ...(n,0)$.

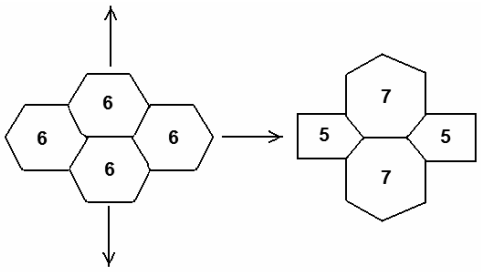

Fig. 85. Transformation of hexagonal (6,6)-net into (5,7)-net under stretching (Stone – Weile defect).

Zig-zag NTs behaves in brittle manner because of axial load direction lie in direction of C-C bonds which are simply elongated and then are broken forming 8-, 9-, and more rings –holes. Further redistribution of load leads to the next step of this brittle breaking.

Superplasticity was discovered recently by Dresselhaus et al. in carbon NTs. At high temperature T~1500 C the MWNT demonstrate the 10 time elongation (fig. 83.6) the narrowing of which is provided by a fracture of external wall and a formation of ledges at the external surface of multiwalled NT.

Bundles of NTs are very anisotropic, namely, in axial direction they are very rigid (C_{33}~1.1 TPa) while in basic plane are relatively soft and flexible (C_{11}~0.1 TPa). Bulk module of NTs bundle (B~0.02 TPa) is on order of magnitude smaller than for single SWNT, i.e. they are easily compressed and packed overpassing a weak van der Waals forces between NTs. Young module (Y ~0.4 – 0.7 TPa) only twice smaller than for diamond and it is reversible decreased with increase of NT diameter. However accounting relatively low density of NT (ρ~1.3 g/cm^3 < $\rho_{diamond}$~3.5 g/cm^3) the specific bulk module of NTs bundles is evident to be greater than for diamond.

Bundles of NTs posses a high elasticity. Single NTs can easily rotate and slide relative each other. Compression of 2D NT bundle at P=20 kbar=2 GPa was shown by computer experiments to change the ring shape of every NT cross section in hexagonal shape forming the honeycomb cross-section of the bundles. The faces of the hexagons are connected by van der Waals forces as in graphite forming the molecular nanotubular crystal. When unloading the bundle recovers completely its structure and volume demonstrating the NTs bundles as being very elastic material up to 29 kbar that may be employed as dissipative damping materials.

One can conclude that NT bundles posses extremely high specific rigidity that make them an ideal reinforced material for development of the light, strong and rigid composite nanomaterials.

The mechanical properties of the single MWNTs may them possible to use in MEMS and NEMS in kind of the nanorotors, where coaxial SWNTs rotates each other, the nanobearings, nanogears, telescopic nanoantenna, nanosprings, etc.

10.12. Vibrations of C-NTs

Nanotubes vibrate as any other beams, wires and strings. In continuum theory the oscillation spectra are known to be extracted from a solution of wave equations. For example, according to the well-known Bernoulli-Euler beam model, the equation describing transverse or flexural vibrations of continuous, homogeneous, isotropic, linear elastic beam may be expressed as

$$EI\frac{\partial^4 u}{\partial x^4}+\rho S\frac{\partial^2 u}{\partial t^2}=0$$

where E is the Young modulus of beam material, I is the moment of inertia, S is cross-section area, ρ is the mass density, x the distance along beam, $u(x,t)$ the transverse displacement of beam and t is the time.

Frequencies of flexural n-th vibration modes for any wire are

$$v_n=\frac{(k_nL)^2}{2\pi L^2}\sqrt{\frac{EI}{\rho S}}$$

where L is a length of beam, n is the mode number, k_nL is the eigenvalue for n-th mode.

For the cylindrical tube with outside diameter d_o and inside diameter d_i, the geometrical ratio I/S is such that the previous equation becomes to be

$$v_n=\frac{(k_nL)^2}{8\pi L^2}\sqrt{\frac{E}{\rho}(d_o^2+d_i^2)}$$

For coaxial N-walled NTs a van der Waals intertube interaction have to be taken into account leading to N coupled equations. For MWNT embedded in an elastic medium such as a polymer matrix a distributed elastic reaction forces must be applied.

Note that continuum models do not account the discrete atomistic structure of the walls. For the atomistic calculation more accurate methods are widely employed such as the *ab-initio*, semi-empirical tight-binding, molecular dynamics, hybrid atomistic/continuum models, etc.

Shown in fig. 86 are the mode shapes for SWNT calculated by a molecular structural mechanics approach that for the case of cantilevered (one clamped) and bridged (two clamped) ends gives the frequencies felled in the range 10 GHz – 1 THz.

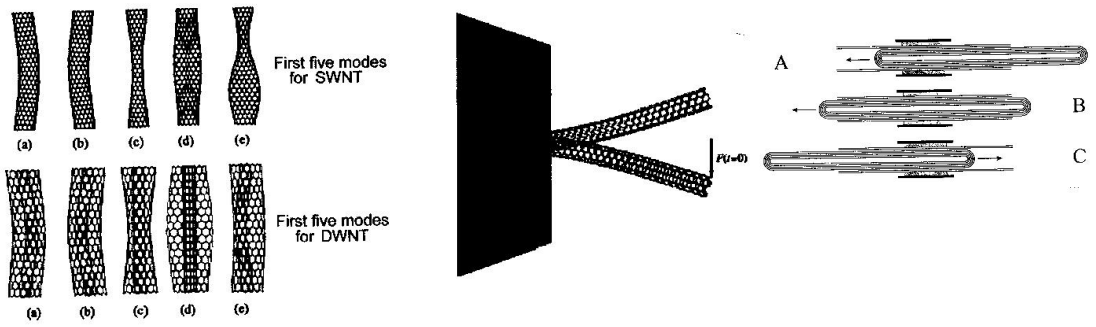

Fig. 86. First five vibration modes for SWNT and double walled NT; Vibration of the one clamped cantilevered NT; Oscillator on base of MWNT.

However the most peculiar feature of NT vibrations are believed to be *the gallery of the very intensive and low attenuated whispering modes* mentioned above. The gigahertz frequencies of such acoustical vibrations correspond to gigahertz electromagnetic microwaves. When the frequency of the natural acoustic NT vibration are equal to the radio frequency of the external microwave the resonant interaction due to Coulomb forces between electric field of the microwave and the electric charge on the CNT becomes to be possible. Strong absorption of 2.45 GHz microwaves has been observed by Imholt et al. in unpurified SWNT to cause ignition, burning, outgassing, intense mechanical motion, and volume expanding. One can think of resonant interaction is responsible for these phenomena in spite of there have been no systematic attempts to find optimum resonant frequencies.

To day variety of nanodevises have been developed on base of the nanotubular resonator, such as the micro-electro-mechanical resonance systems, actuators, nano-cantilever, nanobalances, molecular chemical sensors, field-effect transistor sensors, etc.

10.13. Nanothors from carbon nanotubes

Kornilov from Kiev National University was the first who have been predicted the existence of nanorings or nanothores constructed from NTs by jointing their open ends (fig. 87). Hereafter they have been synthesized (fig. 87). This new shape give a new properties, for instance, a possibility of cyclotron resonance in magnetic field, that was supposed to be used for development of electron nanoasselerators or for creating of powerful local magnetic fields.

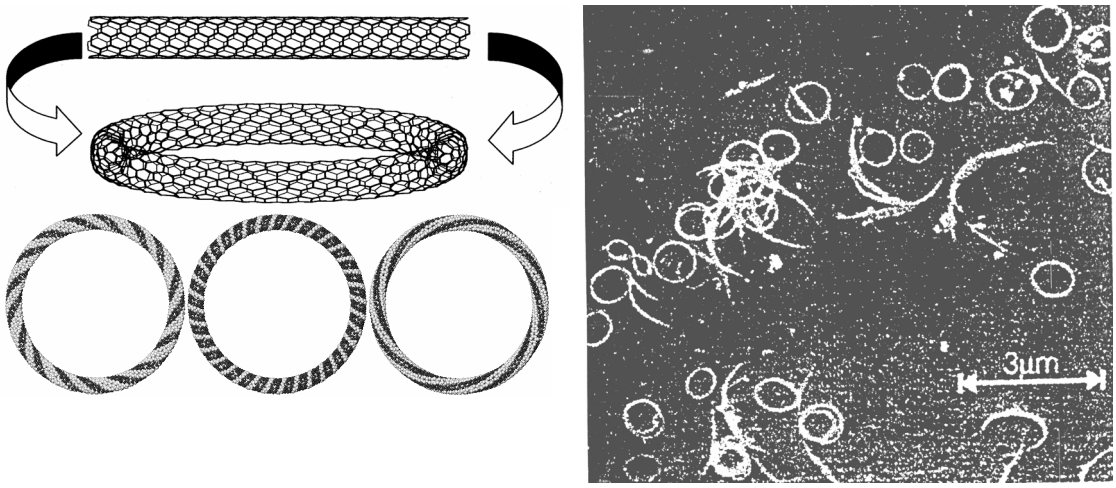

Fig. 87. Carbon nanorings or nanothors predicted theoretically by Kornilov (Kornilov M., Isaev C. Pulsar (in Russian) № 1, p.14 (1998)) and synthesized experimentally (Martel R. et al. Nature. Vol. 398, P. 299 (1999)).

11. NONCARBON NANOSTRUCTURES AND NANOTUBEs

Low screw deformation energy ($E_S / N < 0.2$ eV/atom) serves as the criterion of NT formation. Hence only layered 2D structures with relatively weak interaction between layers can serve as the building material for nanotubes formation. There are variety of such materials, in particular, the boron nitride, chalcogenides, dichalcogenides, oxides, phosphides, molecular structures, etc.

11.1. Fulborenes and fulborenites, the BN analogues of fullerenes and fullerites

Boron nitride is a full isomorphic analogue of carbon having all polymorphic modifications as for the carbon allotropes, namely:
– sphalerite (c-BN) is the analogue of the cubic diamond (C),
– wurtzite (w-BN) is the analogue of the hexagonal lonsdelite (C),
– graphitelike h-BN is the analogue of the graphite (C).
Hence one can easily predict the existence of BN-fullerenes, BN-nanotubes and BN-fullerites as carbon analogues.

What structure have BN-fullerenes?

Energy gain appear to be the first criterion of their stability. From thermodynamics standard formation enthalpies it is known that interatomic bond energy of B-N bonds (4.00 eV) is greater than for B-B (2.32 eV) and N-N (2.11 eV) bonds. From this follows the formation rule No 1: Deviation of atomic content from stoichiometric relationship (1:1) have to be minimum. In other words this means that the stable fulborenes must do not contain pentagons and other odd rings peculiar for fullerenes but have to be built from 4-, 6-, 8-, 10- and other even ring faces. This rule have been confirmed later by electron energy loss spectra (EELS) of synthesized fulborenes.

Table 9. Geometrical parameters of fulborenes. N_a, N_b, N_4, N_6, N_8, N_{10} are the number of atoms, bonds, squares, hexagons, octagons, and decagons respectivaly; d_4, d_6 are the diameters of molecules in angstrom along square and hexagon respectivaly; a and c are lattice parameters in angstroms, ρ is a density in g/cm^3.

ful-boren	N_a	N_b	N_4	d_4 nm	N_6	d_6 nm	N_8	N_{10}	lattice	a	c	ρ
$B_{12}N_{12}$	24	36	6	4.4	8	3.5			SC	5.35–6.00		2.91–2.30
									BCC	5.76–6,23		5.18–4.08
									Sph.	11.52–12.47		2.59–2.04
									W.	8.14–8.82	13.29–	2.24–1.71
$B_{24}N_{24}$	48	72	12	6.4	8	6.0	6		SC	6.98–7.56	14.30	2.91–2.29
									BCC	8.65–9.36		3.06–2.41
									FCC	11.07–11.98		2.92–2.30
$B_{60}N_{60}$	120	180	30	1.08	20	1.06		12	vdW	20.26		1.19

The rule of isolated pentagons C_5 where every pentagon is surrounded by five hexagons is known to serve as the second stability criterion of buckminsterfullerene C_{60} because of the valence of all carbon atoms will be 4. In this case pentagonal C_6 ring is of Kekule structure type with alternating single B-N and double B=N bonds. From this analogy follows the second stability rule No 2: the rule of isolated squares C_4 or other isolated even rings ensuring valence 4 for all molecule atoms. Among the spheroid-like convex Archimedes polyhedra there are small set of such polyhedra meeting these two rules. Three smallest of them are shown in fig. 88, namely, the $B_{12}N_{12}$, $B_{48}N_{48}$, and $B_{60}N_{60}$. In table 9 their parameters are presented.

Fulborene molecule $B_{60}N_{60}$ is a full analogue of C_{60}, because it have:
- icosahedral I-symmetry;
- spherical form with a smallest deviation from of angles sum from 360^0;
- 12 isolated decagons instead of 12 isolated pentagons;
- lowest cohesive energy (~5.63 eV per atom);
- highest HOMO-LUMO gap (8.73 eV).

In the table 9 the covalent crystals are also shown which are possible theoretically to build from this molecules providing the covalent bonds between molecule faces. This gives the simple crystallographic rule No 3 governing the copolymerization of molecules, namely, the number of double covalent bonds between both junction faces must be equal to the number of alternating single covalent bonds.

Note the fulborenite BCC $B_{12}N_{12}$ have the density (5.18 g/cm^3) greater than diamond (3.5 g/cm^3). It may be called as superdense diamond.

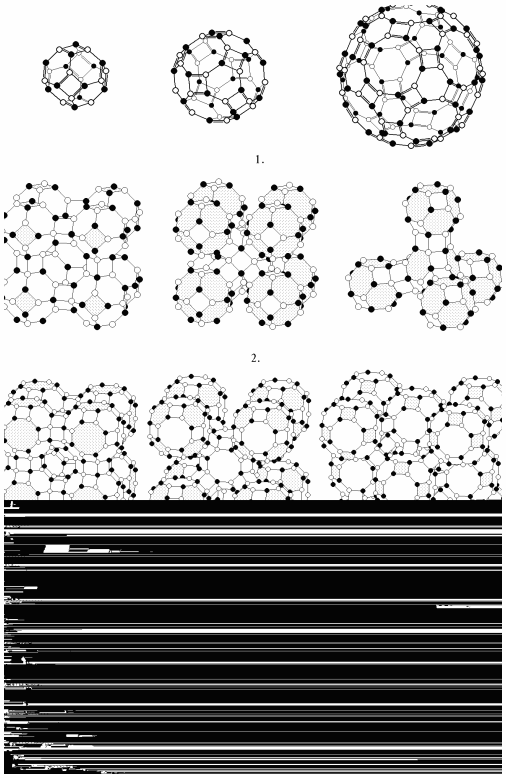

Fig. 88. 1 – Fulborenes $B_{12}N_{12}$, $B_{24}N_{24}$, and $B_{60}N_{60}$, the boron nitride analogues of carbon fullerenes; 2 – fulborenites with simple cubic, BCC and diamond lattice, in vertices of which the molecules $B_{12}N_{12}$ are placed; 3 – with simple cubic, FCC and BCC lattice, in vertices of which the molecules $B_{24}N_{24}$ are placed; 4 – molecular crystal and polymeric chain built from fulborenes $B_{60}N_{60}$.

Wurtzite $B_{12}N_{12}$ have the hexagonal diamond lattice (lonsdelite), in vertices of which the molecules $B_{12}N_{12}$ are placed. This is hyperdiamond, the density of which (2.24 g/cm^3) is smaller than for graphite-like h-BN (2.29 g/cm^3).

Fulborenite have the hollow channels as being the molecular sieve, the new class of zeolite on base of boron nitride.

11.2. Boron-nitride nanotubes

BN-NTs in first time have been discovered in USA by Shopra et al. in 1995 by laser ablation of h-BN. Then madam Loiseau et al. from France in 1996 have synthesized BN-NTs by arc-discharge technique. Since BN is dielectric and do not conduct current it was pressed into holes specially drilled in metallic tungsten electrodes. Then in 1997 BN-NTs, fulborenes and onions were obtained by Golberg et al. in Japan.

Ii is interest to note that in Ukraine this jobs where unknown due to undeveloped fullerene science in that 1997 time. However V.Pokropivny have predicted independently the existence of BN-NTs and have proposed for chemists to synthesize them. It turned out, that fullerene-like nanostructures including BN-NTs have been synthesized in IPMS in early 1984 but in that time they have been dumped in refuse because of only superhard BN modifications where interested. Later looking closely at the samples leading in table 15 years from that time Oleinik have been found the BN-NTs. They were obtained by carbothermal technique by following substitution reactions:

$$B_2 0_3 + 3B_4C + 7N_2 = 14BN(HT) + 3CO_2 \text{ (in solid phase)}$$
$$B_2O_3 + 3CO + N_2 = 2BN(HT) + 3CO_2 \text{ (in gas phase)}$$
$$xB_2O_3 + 3xC(HT) = 2BxC(HT) + 3xCO \text{ (uncompleted substitution reaction).}$$

The blend of carbon with boron oxide was annealed in furnace at T=1200 C – 1800 C in nitrogen N_2 flow. At T = 1500^{0}K the mixed B_xC_{1-x}-NTs were created, at 1623^{0}K – $B_xC_{1-x-y}N_y$-NTs, and at 1700^{0}K – BN-NTs. At greater temperatures a thurbostratic t-BN and rhombohedral r-BN were formed in couple with blend of BN fullerene-like particles, platelet filaments and nanotubes. This results have been published only in 1998–1999 and we becomes to be the forth who synthesized BN-NTs. This is instructive history that experimentalists must cooperate closely with theorists.

Boron nitride nanotubes consist of graphite-like hexagonal BN-layers. Moreover the similar B-N-layers or sheets may consist of not only net of hexagonal B_3N_3-rings but of net of square B_2N_2-rings mixed with octagon B_4N_4 -rings, shown in fig. 89, or another net of $B_4N_4/B_6N_6/B_{10}N_{10}$-rings and so on.

In contrast to C-NTs the BN-NTs are the dielectrics always with band gap near 5.8 eV. This gives an opportunity to employ them in combination with conducting C-NTs for development of coaxial cylindrical heterostructures.

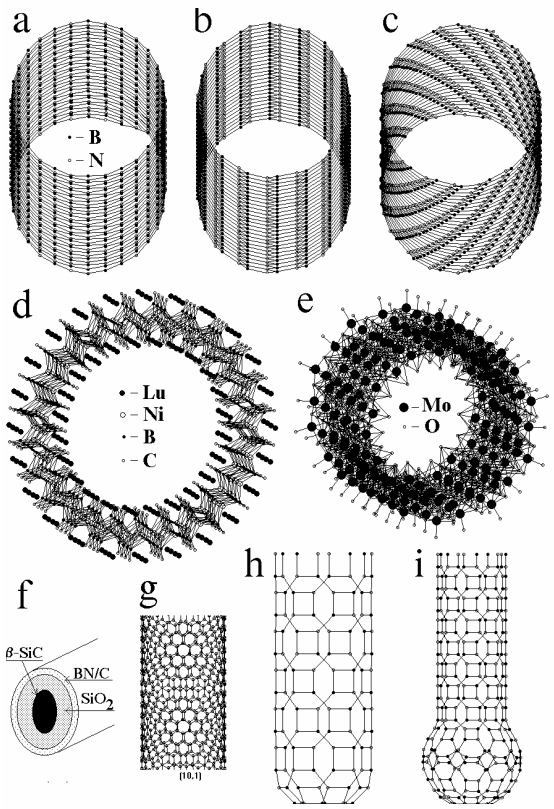

Fig. 89. Some kinds of noncarbon nanotubes: a, b, c are zig-zag, arm-chair, and chiral BN-NTs; g is chiral (10,1) BN-NTs; h, i are BN-NTs, rolled from sheets of 4- and 8-rings; d is LuNiBC-nanotube; e is oxide MoO-nanotube.

Again BN is piezoelectric material that may be used in development of piezoelectric transducer of electric oscillations into acoustical vibrations and *vice-versa* in extremely high frequency hypersonic range. Hence a generator of phonons, i.e. phonon laser (phaser), may think possible to be developed on this base, shown in fig. 90.

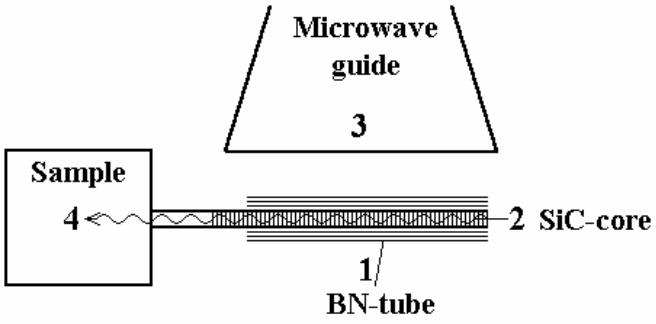

Fig. 90. Set-up of the hypersonic generator.

11.3. Dichalcogenide NTs

Dichalcogenides are determined as compounds of general formula MeX_2, where Me = Mo, W, Nb, Ta; X = S, Se, Te, which have the layered hexagonal structure (fig. 91).

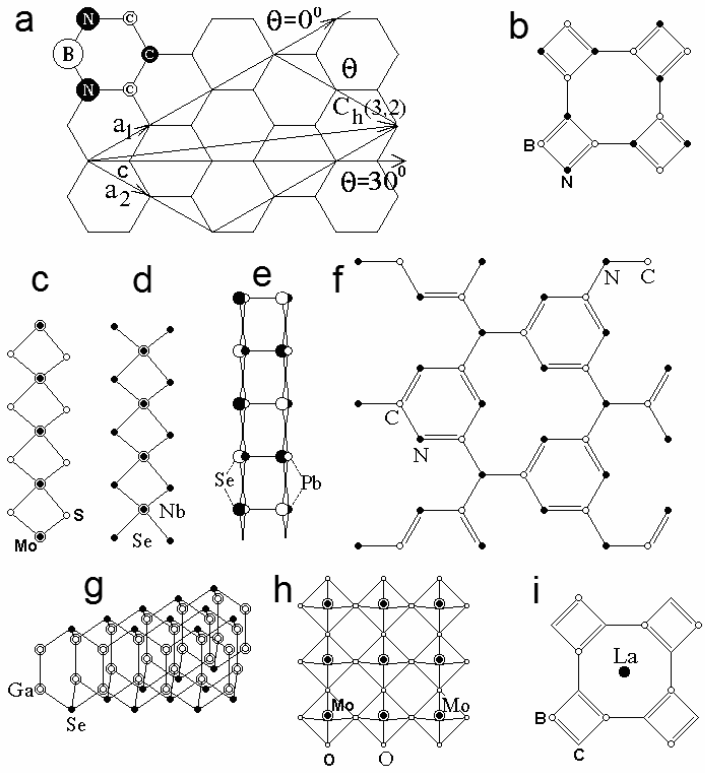

Fig. 91. Different kinds of sheets to be rolled in different kinds of noncarbon nanotubes: a) (6,6) BN; b) (4,8) BN; c,d,e) dichalcogenides; g) chalcogenides; f) vacancy (6,6) CN sheet; h) MoO_6; i) (4,8) LaBC.

The sheets themselves are goffered while interlayer van der Waals interaction forces are so weak that interlayer distance ~ 6–7 angstrom is significantly greater than in other layered compounds. It means that into interlayer holes all kinds of impurity elements from hydrogen up to heavy metals called intercalates may be intercalated. Such the compounds were named as intercalated dichalcogenides. Their properties may be easily varied in wide range by varying the content and concentration of intercalates.

It is evident theoretically that dichalcogenide sheets may be easily rolled in MeX_2-nanotubes. Variety of such nanotubes have been synthesized some years ago after discovery of carbon nanotubes. R.Tenne from Weizmann Institute, Israel, was the first who have been obtained MoS_2-nanotubes in ovens in accordance with following chemical reactions:

$$MoO_3(solid) + xH_2(gaz) \rightarrow MoO_{3-x}(gaz) + xH_2O(gaz)$$

$$MoO_{3-x}(gaz) + (1-x)H_2(gaz) + 2H_2S(gaz) \rightarrow MoS_2(solid) + (3-x)H_2O(gaz)$$

In process of the synthesis the MeX_2-NTs were observed to self assemble often in bundles of nanotubes in kind of forest or ropes forming the 2D ordered arrays, crystals built of 1D nanotubes.

Dichalcogenide MeX_2-NTs may be utilized as hydrogen-stored materials, as nano-labricants, etc. Interested effect was shown by Remskar group from Slovenia, the tungsten selenide WS_2, which in bulk state do not form any compounds with gold, in kind of nanotubes was found to form the WS_2-Au compounds unknown previously.

11.4. Oxide NTs

Oxide on base of refractory metals, for instance molybdenum, consist of elementary octahedrons MoO_6 or tetrahedrons MoO_4 which may be linked by the vertices, edges and faces thereby packing in different kinds of compounds. In particular bonding by edges the octahedra may form layers and double sheets in (010) plane shown in fig. 92, giving the compound of MoO_3 structure. This formula follows due to: 1) two top atoms of octahedron do not bond with any other octahedrons (2 = 2); 2) four plane atoms of octahedron square are bonded by edges with four nearest octahedrons giving 1 atom (4/4=1) in formula. Weak van der Waals and ionic interaction acts between layers, while strong covalent-ionic bonds act in plane between octahedrons.

The MoO_3-NTs have been synthesized by evaporation of Mo-wires by power electric current in air oxygen via the oxidation reaction ($Mo + O \rightarrow MoO_3$). Particles of white smoke are collected on a substrate. Structure of the MoO_3 – NTs are shown in fig. 92.

The vanadium oxide V_2O_5-NTs were synthesized by laser ablation and arc-discharge of vanadium in air by the same oxidation reactions.

To day variety of oxide nanotubes on base of TiO_2, SiO_2, ZnO, MgO, helicoids of SiO_2, SiO_2 – NTs inside of membrane template were synthesized. In particular, TiO_2 – microtubes have been synthesized by sol-gel technique in Tartu University by Maeorg, Redo and Jarvekulg.

Properties of oxide nanotubes were pure studied yet. Transparent oxide to be rolled in nanotubes should *a priory* evident to exhibit the unique combination of properties, the non transparent bulk oxide may be transparent in nanotubular form, etc.

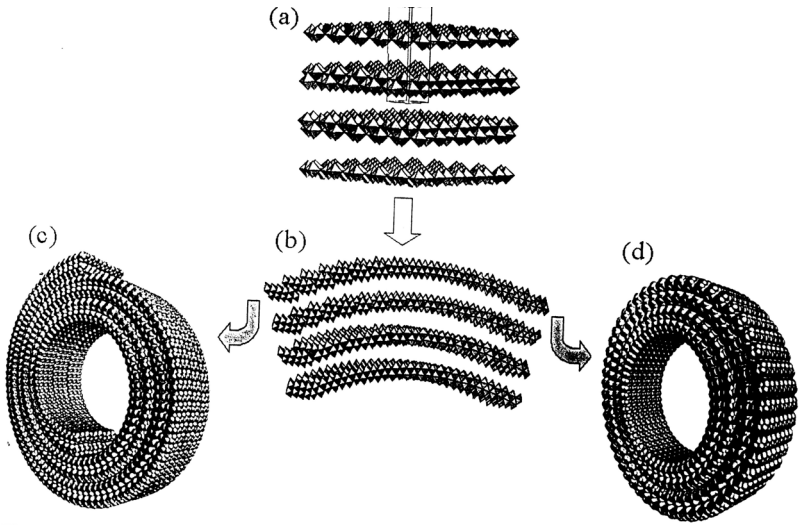

Fig. 92. Scheme of rolling oxide sheets (a), consisting of chemical bonded octahedrons MeO_6 into the roll (c) and tube (d).

11.5. Other kinds of noncarbon nanotubes

Family of noncarbon nanotubes in recent time is sharply grown, in particular, the nanotubes on base of molecular polymers, carbides, etc., have been synthesized. Even nonlayered semiconductors such as GaAs were obtained in form of nanotubes within membrane template using nanolithography technique.

Intrigue problem is the existence of nanotubes on base of silicon carbide as being the basic wide band gap semiconductor for future tera-hertz nanoelectronics. In accordance with theoretical calculations performed by quantum chemistry RHF/6–31G method (restricted Harthree-Fock on base of 6–31G molecular orbitals) it was shown that the single-wall SiC-NTs may to be stable but the usual layered SiC nanotubes like C-NTs have not observed experimentally. However metastable several-layer SiC-NTs, the poly-nano-grained nanotubes were obtained as well as nanotubular fibers by chemical vapour deposition from methylthreechlorsilane in the temperature range 800–1000^{0}C. To avoid the inconsistencies all SiC nanotubes in dependence of their wall structure was suggested by author of the book to classify under three kinds shown in fig. 93–95: 1) the layered usual NTs with rolled layers shown in fig. 93; 2) the polynanocrystalline NTs the walls of which consist of linked nanograins shown in fig. 94; 3) the monocrystalline NTs with perfect crystalline walls, shown in fig. 95.

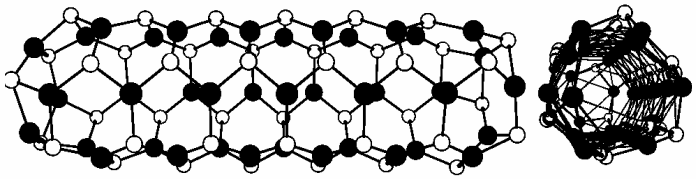

Fig. 93. Usual single-wall SiC nanotube of first 1-st order calculated by ab-initio DFT/3–21 method (Pokropivny V., Silenko P. Exp.Theor.Chem. №1, (2006)).

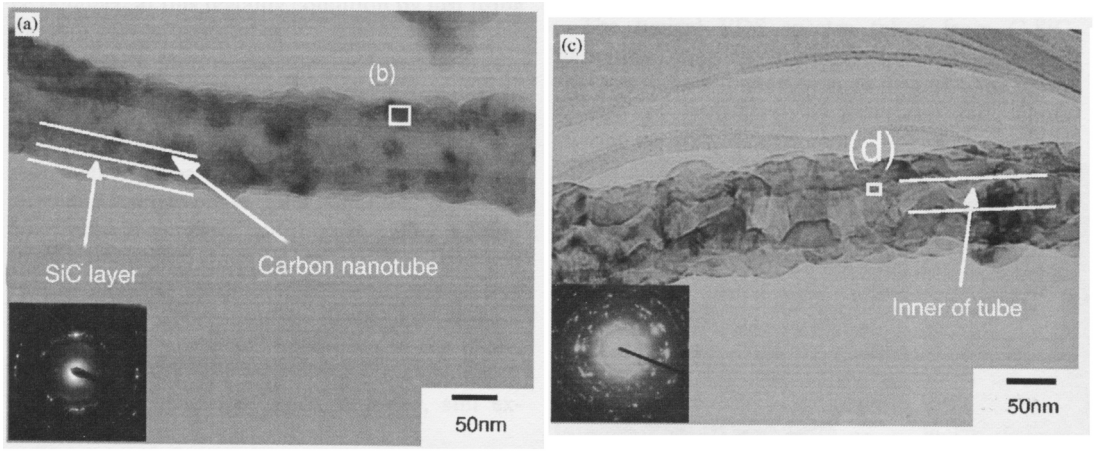

Fig. 94. Carbon nanotube covered by SiC layer (a) and nanograine SiC nanotube of second 2-nd order, the walls of which consist of nanograins SiC (c) (Taguchi T., Igawa N., Yamamoto H., Shamoto S., Jitsukava S. // Physica E. (2005)).

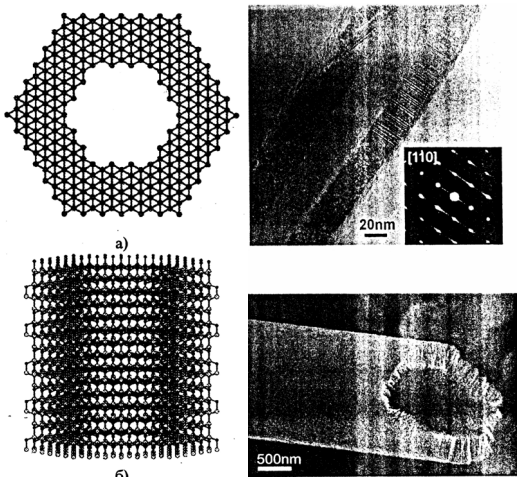

Fig. 95. Monocrystalline no curved no rolled nanotube of third 3-th order, the (111) walls of which are normal to the tube axis**:** theoretical structure of SiC-NT [Pokropivny V., Silenko P. Exp.Theor.Chem. №1, (2006)] and experimentally obtained Si-NT [Hu J., Bando Y. NIMS Now International. **3**, 2 (2005)].

For to day it was concluded that: 1) the usual SiC-NTs of 1-st kind are unstable except for one- or -two-layer NTs; 2) the stable SiC-NTs of 1-th kind and SiC-NTs of 3-th kind were not found so far; 3) only the monocrystalline NTs and nanotubular fibers of 2-th kind were synthesized unambiguously.

12. APPLICATIONS OF NANOTUBES

12.1. Field Emitting Transistor (FET) based on C-NTs

Transistor (triode) is the electronic device the current in which between two electrodes under bias voltage V_{bias} depends strongly on gate voltage V_{gate} on third gate electrode. Tans was the first who fabricated the transistor on base of semiconducting carbon nanotube, shown in fig. 96.

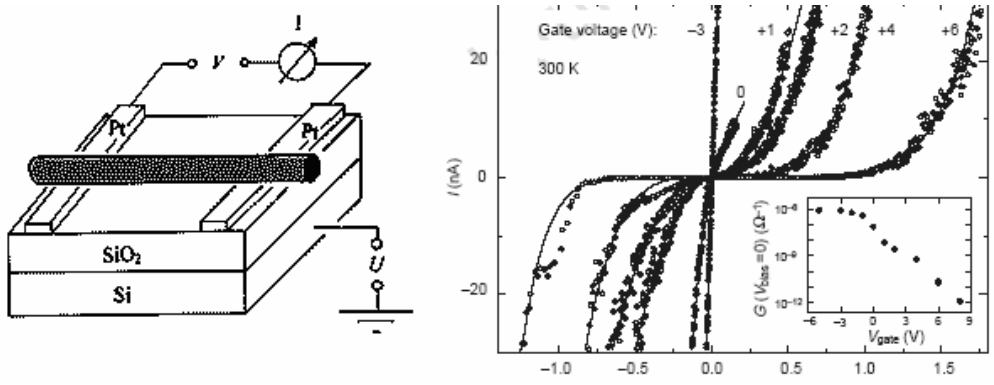

Fig. 96. Set-up of the first field emitting transistor on base of C-NT and it current-voltage curve, the I–V_{bias} dependence on V_{gate} ~ –3–8 V. Nanotube lie between two platinum nanoelectrodes on nonconducting quartz substrate. Silicon layer plays the role of gate electrode. Under positive V_{gate} the current drops while under negative it is increased. (S. J. Tans, et al. Nature V.393, 49–51 (1998)).

Semiconducting C-NT in general have the strong resistance at V_{bias} due to existence of band gap. However applied gate voltage V_{gate} induces an electric field in C-NT which bends energetic bands that in turns changes the current. Negative potential leads to increase while positive to decrease of the current through C-NT. It is evident of the hole conductivity as being the main charge carriers in the C-NT transistor. Concentration of holes in C-NT is estimated to be one per 250 carbon atoms, that in order of magnitude greater than in graphite (one hole per 10^4 carbon atoms).

12.2. Logical circuits

Modern electronic circuits are based on the transistor switchers processing in the ON/OUT mode. Their work is described by lows of Bullet algebra. This gives the opportunity of using a digital information processing which in turn overcomes an analogous processing in posting/reading information quality. For its electronic realization a calculus scale on 2 base is ideally suitable in which ON and OUT correspond to 0 or 1 of binary integers, that relate in turn to logical 1 (TRUE) or 0 (FALSE). Three main logical functions have been designed called as OR, AND, NOT on base of these elementary functions. These three logical functions are known all requested to built digital circuits and in turn computers, since in essence every processor is well known to present complex branchy combination of these 3 functions.

12.2.1. Voltage inverter

Voltage inverter change a sign of input voltage V_{in} into output reversible sign $V_{out} = - V_{in}$. If in logical circuit its positive value will adopted as logical 1 while negative as 0 then the inverter becomes to be logical NOT. Such inverter on base of C-NTs have become to be the first example of logical nanocircuit on single molecule.

Derycle has developed an inverter on base of semiconducting NT of 1.4 nm in diameter with band gap 0.6 eV. Nanotube is replaced on dielectric silicon (Si) substrate covered by thin silica (SiO_2) layer in contact with three gold electrodes. The inverter consist of two kinds of field emitting transistors, namely, with electron (*n*-FET) and hole (*p*-FET) conductivity (fig. 97). Usually the C-NT have the hole type of conductivity but it is changed on electron conductivity when doped by potassium. If one half of *p*-type NT will be doped by potassium with intermediate layer of PMMA than *p*-*n* transition is formed.

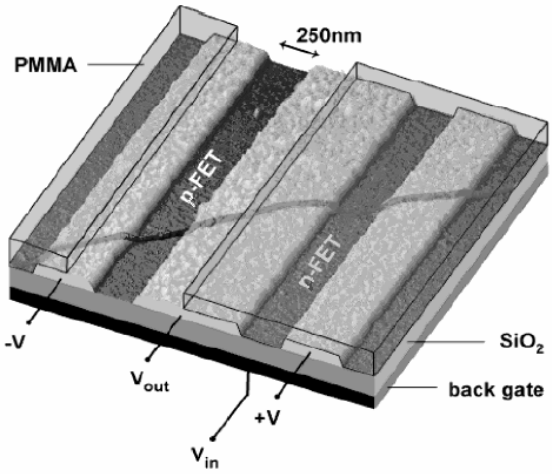

Fig. 97. Voltage inverter on base of single C-NT with conductivity of *p*-type (left half) and *n*-type (right half) replaced on three electrodes (A. Derycke, et al. Nano Lett. 1, 453 (2001)

In such inverter the voltage V_{in} is applied at outer gate electrode while the potential V_{out} is killed out of middle electrode. Left and right electrodes are used to apply bias voltage V. Positive gate V_g voltage promotes current through n-type NT due to growth of free electron concentration in n-FET and suppress current in p-type NT due to increase of free hole concentration in P-FET. Negative voltage acts in opposite manner.

12.2.2. Chips with logical elements

To enhance the affectivity of electronic circuits on base of FETs, they have to be packed at substrate as dense as possible. Bachtold takes a first step in the way of the logical elements integration, fabricating a smallest chip on base of C-NTs arranged on alumina Al_2O_3 film with aluminums gate below. Fig. 98 show one of this chip FET.

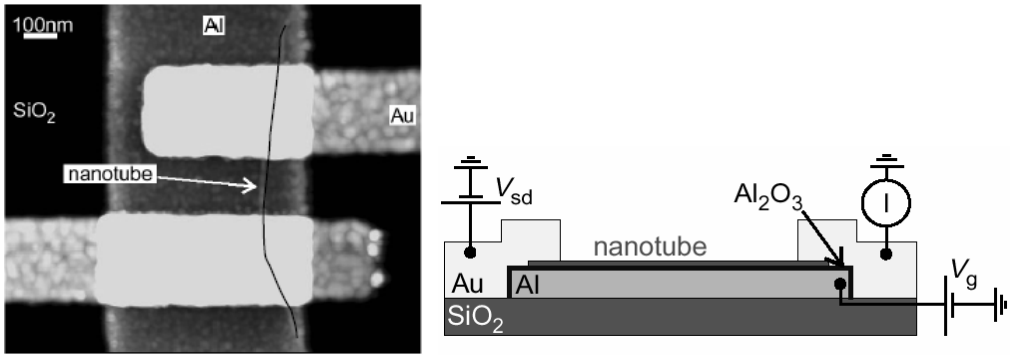

Fig. 98. Field transistor based on C-NT as one element of smallest chip (A. Bachtold, et al. Science, V.294, 1317 (2001)).

Fig. 99 demonstrate the example of logical elements circuits.

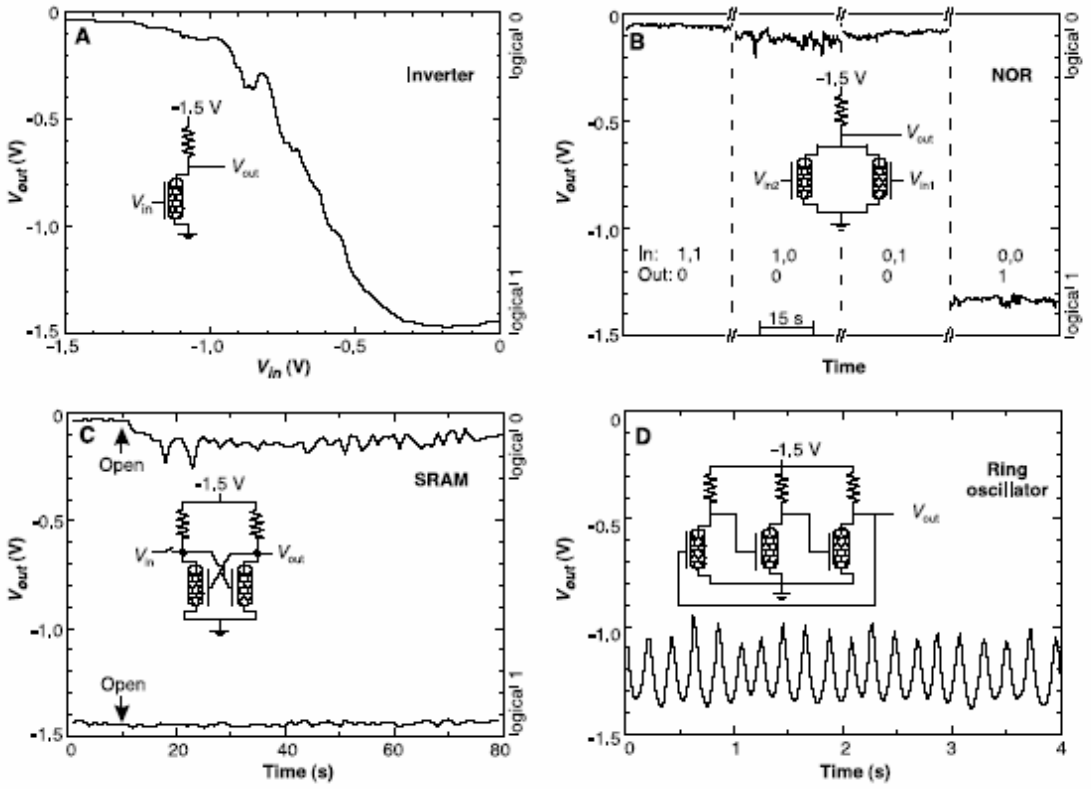

Fig. 99. Electrical characteristics of one-, two-, and three-transistor circuits on base of C-NTs. A) One-transistor inverter and its dependence of output voltage V_{out} on input V_{in} . B) Two-transistors logical unit NOT-OR (NOR)and its dependence of output voltage V_{out} on possible input states (0,0), (0,1), (1,0) and (1,1). C) Static random access memory (SRAM) on base of two-transistor trigger. D) Three-transistors circuit ring oscillator on base of semiconducting C-NTs [A. Bachtold, P. Hadley, T. Nakanishi, C. Dekker, Logic circuits with carbon nanotube transistors, Science, 294, 1317 (2001)].

Shown in fig. 99,B is the two-transistor circuit with two inputs V_{in1} and V_{in2}, obtained by change of one inverter on two ones linked in parallel. If one or both transistors are in state of logical unity then one NT at least is in conductive state and V_{out} = 0 (logical zero). If both NTs are in nonconductive state then a logical unity is in output. Thus for

these two-transistor logical circuit $Y(0,0) = 1$, $Y(1,0) = 0$, $Y(0,1) = 0$, $Y(1,1) = 0$, that correspond to the logical function $Y = \overline{A + B}$, that is logical summation with following logical negator NOT, denoted as OR-NOT or NOR. Nonconjunction element NOT-AND or NAND linked with element NOT gives element OR.

Consider the circuit built of two inverter (fig. 99,C), where output of one inverter is connected with input of another one. Trigger is obtained in the result known as the flip-flop circuit that is the elementary cell of the static random access memory (SRAM) in computers. In such trigger two stable state are possible, the (1,0) and (0,1), corresponding to a current only left or only through right nanotube. This pair of states is used for design of logical unity 1 or zero. If input voltage is applied on gate of right transistor $V_{in} = 0$, then no current in right nanotube exists and the voltage on left gate become to be $V_{out} = -1.5$ V inspiring the current in left nanotube. If here input V_{in} contact is broken than the system comes in this (1,0) state during long time (70 sec on fig. 99C). If than gate voltage $V_{in} = -1.5$ V is applied to right transistor, then a resistance of right NT will drop while voltage on left gate will increase to $V_{out} = 0$ that correspond to the state (0,1) of the system. In the result the trigger "remember" the last voltage V_{in} so the information may be read measuring output V_{out} voltage.

12.3. Indicators and flat displays

Thin carbon NTs have ideal geometry for electron emission due to their smallest atomistic tip radius that result in turn to a high electric field strength, in order of magnitude greater than a work function of electrons. Moreover C-NTs are known to exhibit the high strength, melting temperature, resistance to aggressive media as graphite, and are able to work in technical vacuum. Cold emitter on base of C-NTs was proposed to be a key element for the future flat panel TV set as being the alternative for hot emitters on base of electron-beam tube, that make possible to avoid high dangerous asseverated 20–30 kV voltages. At ambient temperature the C-NT are able to emit electrons and current of the same density as the standard tungsten cathode operating at high temperatures and voltages. Set-up of light panel display on base of C-NTs clamped at cathode and oriented in the anode direction is shown in fig. 100.

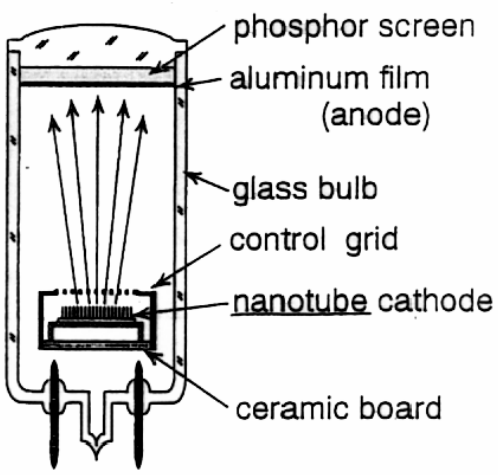

Fig. 100. Set-up of the light panel display on base of autoelectron emission of carbon nanotubes (de Heer).

To obtain the image a phosphor is covered at aluminum anode. Electron shock excites phosphor's molecules which phosphorescence the light photons under transition into ground state. For instance the phosphor on base of zinc sulphide with copper and aluminum doping shines in green range while silver doped in the blue range. Red light gives phosphor on base of yttrium oxide Y_2O_3 doped by europium.

Obviously to fabricate such the panels the high ordered arrays of nanotubes on large area are requested. They can be grown by CVD template technique. In kind of template the zeolite like alumina Al_2O_3 or silica SiO_2 are used often because they contain ordered arrays of cylindrical nanoporous. The arrays of pores of typical diameter 40 nm and interpore distance 100 nm are grown by electrochemical etching of aluminum in acids. Preliminary cobalt is deposited at the pores bottom that serves as catalysist for growth of nanotubes. They growth inside pores under pyrolysis of acetylene in nitrogen atmosphere at 700°C. Average density of nanotubes is $\sim 10^{10} cm^{-2}$, a wall thickness is near 10 graphene layers, an substrate area may be of several square meters.

To day such high-bright light source on base of C-NTs have been fabricated (fig. 101). It consist if cathode, grid and anode inside glass tube of 32 mm in diameter. At it inner surface the doped phosphors giving the blue, green and red lights are deposited. At it external surface the lenses are clamped which focuses light in center of glass tube. Electronic circuits are clamped at the lamp-cap.

This lamp with cold cathode is very efficient, the light of which is visible at very large distances under 70^o view angle.

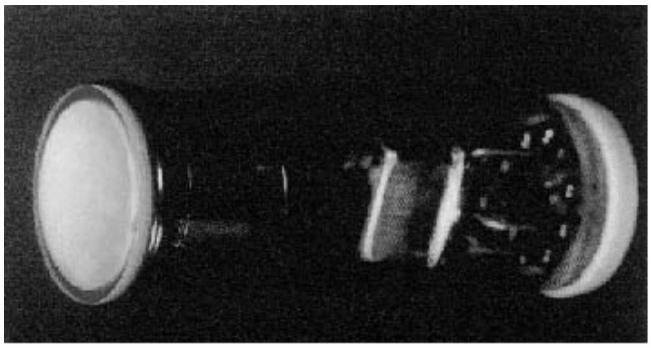

Fig. 101. Power bright mini-lamp with cold cathode on base of CNT (NS027A, *Noritake*).

12.4. Thermometer

The least thermometer have been fabricated on base MgO nanotube playing the role of capillary shown in fig. 102.

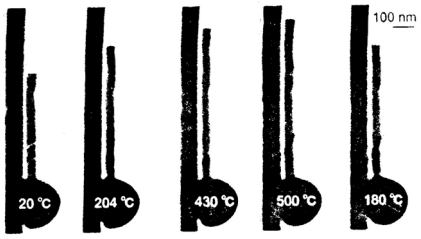

Fig. 102. Thermometer on base of MgO nanotube, fabricated in NIMS, Japan.

13. PHOTONIC CRYSTALS

13.1. Physical ideas for light control via Bragg diffraction

Tendency for miniaturization of integrated circuits (IC) meets with the physical restrictions on size of semiconducting elements. Density of elementary units in to-day IC
(~10 million/cm^2) reaches its culminate level. These limitations have lead to the concept of photonics in which accordance the photons instead of electrons serve as information carriers.

The light quantum have the number of advantages over the electrons, namely:

1. Light velocity is in 3 order of magnitude greater than velocity of electron excitations ($\approx 10^5$ m/s), therefore the photons are able to carry and transmit more greater information per second than electrons.
2. Interaction between photons is absent, hence the transmitted band for optical fibers (≈ 1 THz) is significantly broader than for electronic transmission links in the usual telephone communication (≈ 1 MHz).
3. Resistance loss are significantly smaller.

However on the route of development of completely optical integrated circuits the number of problems have been arisen of the development of optical logical elements, such as optical switchers, diodes and other optical devices as being their electronic analogues. For the purpose a new class of optical materials, the photonic crystals (PC), have been suggested and developed.

Fundamental concept of PC is based on idea of Yablonovitch, namely, to govern the radiation properties of light, and Jone's idea, namely, to drive the light localization in special PC in the manner similar to driving of electrons in conventional semiconductors. Let's remind that electrons as the quantum particles and de Broighl waves are propagated in periodic crystalline atomic lattice, the parameters of which tune the energy bands. Governing of the structure and content of the semiconductor lattice lies in the base of fabrication of electronic materials and devices. Electromagnetic waves and optical light in particular have the wave length (400–800nm) in two order of magnitude greater than for the electronic waves (~5 nm). The idea was arisen to form the periodic lattice for photons similar to atomic crystalline lattice for electrons. Since the interaction of photons or electromagnetic waves with a matter is determined by a dielectric permittivity function $\varepsilon(q,\omega)$ it is requested for this aim to build some periodic lattice consisted of particles or/and wires or/and layers distinguished by their dielectric permittivity. Hence to realize the concept of PC the heterogeneous composite materials are requested with a dielectric permittivity periodic in one, or/and two, or/and three directions. It follows the aim of photonics, namely, to govern the photons in PC similar to electrons in semiconductors tuning the structure of PC and material of such periodic dielectric $\varepsilon(q,\omega,x,y,z)$-lattice.

Hence the photonic crystals (PC) looks as the periodical lattices consisted of zero-, one-, or two-dimensional structures with the periodically alternated dielectric permittivity $\varepsilon(q,\omega,x,y,z)$ or/and magnetic permeability $\mu(q,\omega,x,y,z)$.

Photonics is a complex fundamental and engineering science at the junction of materials science, optics, and electronics focused on research of interaction of the designed PC with external electromagnetic waves aimed for development of PC and devices tuning the periodic dielectric function $\varepsilon(q,\omega,x,y,z)$, D=$\varepsilon$E. Similarly the

spintronics was raised as the science at the junction of materials science, magnetooptics, and electronics, focused on research of interaction of periodic spin structures with electromagnetic waves aimed for development of magnetic crystals and devices tuning the periodic magnetic function $\mu(q,\omega,x,y,z)$, B= μ H.

In contrast to fiber optics, where a light is propagated in accordance with a total internal reflection low, in the PC a light is propagated in accordance with the Bragg diffraction and reflection lows as electrons in semiconductors.

For photons in PC as for electrons in semiconductors the photonic bands arise as being the analogue of energy electronic bands, in particular the photonic band gap arise as the analogue of band gap in semiconductors.

In analogy with the impurity and structure defects in semiconductors, in the photonic crystals the manifold of the impurity and structure defects as being the defects in periodic dielectric lattice was shown to be possible, as being the analogues of points defects, dislocations, stacking faults, grain boundaries, etc. For example, the vacancy in PC is the absence of one dielectric particle, the interstitial is additional particle, the dislocation is absence of one-half of close-packed plane in particles lattice, the stacking fault is the fault in packing sequence of the particle planes, etc. Such the defects may result in formation of localized photonic states inside photonic band gap.

Opals, membranes, zeolites present the examples of natural PCs. However most of PCs were developed in kind of the artificial architectures, such as 3D lattice of nanoparticles, nanowires, nanolayers and their combinations.

The size effects play the key role in formation of properties of PC. For instance, in field of infra-red electronics (devices of night vision, etc.) a lattice parameter should be comparable with a wave length, typically λ ~a ~ 1 μk, that is in ~3000 time greater then lattice constant of conventional crystals, but in 100 time smaller then diameter of human hair.

From theoretical point of view the advantages of PCs lies in the following.

1. Solution of Maxwell equations for periodic dielectric nanostructured media may be obtained exactly in contrast to Schrodinger equation for strongly interacting electrons in crystals the solution of which is in order of magnitude complicated.
2. Scaling exists for the electromagnetic waves because of no fundamental restrictions exist for them in kind of a Planck constant or a free path length for electronic waves. Hence, the properties of PC for centimeter, micrometer or nanometer waves range seems to be the same that allow us to imitate and simulate the PC and photonic phenomena at distinct scale levels. Therefore a computer design of PC structures and modeling of PC properties becomes to be the powerful tool for PC investigation.

13.2. Methods for fabrication of photonic crystals and membranes

Variety of methods was developed, namely, the electrochemical anodization of Al_2O_3 and SiO_2, the lithography methods (electronic, ionic, photo, holography), the ionic bombardment of polymers to obtain membranes, the colloidal methods to obtain 3D-opals, etc. Fig. 103 illustrates some of these typical methods.

Previously we have considered the method of the NTs deposition at plane substrates, where NTs where grown normal to the surface. The NTs were ordered in kind of the bundles, the ropes, the arrays, the forest but with a number of undesirable growth defects.

To obtain a perfect ordered 2D lattice of NTs it was suggested to deposit NTs at the special membrane substrates playing the role of template predetermining the requested structure of lattice. Membrane is the plate with cylindrical channels forming the 2D

lattice. The membranes are characterized by the diameter of channel, the type of 2D lattice (triangular, square, hexagonal), the parameter of the lattice, the length of NTs, etc.

Under chemical or physical deposition of vapor on membranes inside the channels both the hollow nanotubes or solid wires may be obtained in dependence of the temperature, processes duration, and other kinetic parameters tuning of which gives an opportunity to fabricate the varieties of nanostructures requested.

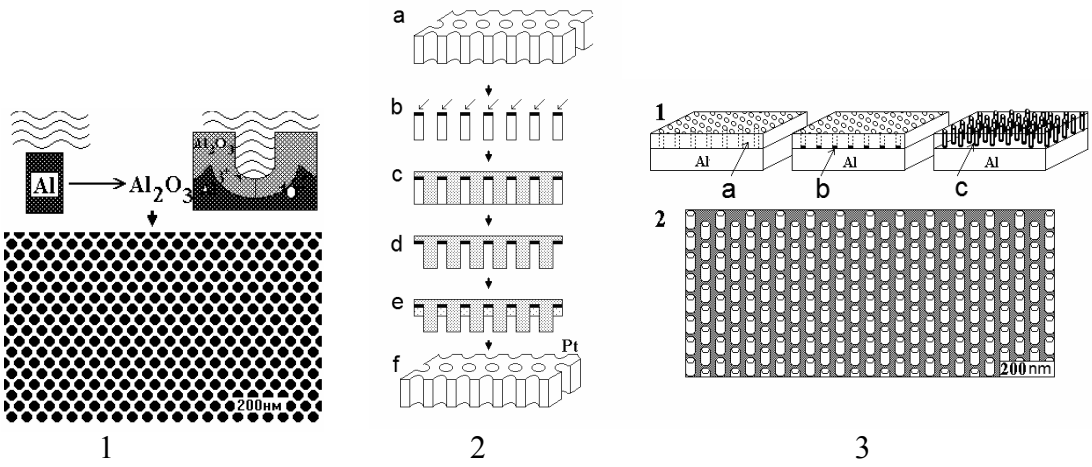

Fig. 103.
1 – Electrochemical method of alumosilicate Al_2O_3 and SiO_2 anodization. In some acids the close packed triangular lattice of nanoporous channels are etched.
2 – Photolithography method: a) is the alumosilica membrane, b) is the catalyst deposition, c) is the deposition of given compound or metal, d) is the deposition of resist mask, e) is the etching of resist, f) is the metallic (platinum) membrane, which inherits the shape of starting alumina membrane.
3 – Template synthesis of 2D crystal of C-NTs: a) is the porous membrane; b) is the metallic catalyst deposited at the bottom of nanochannels acting as anchor for growing nanotubes; c) is the deposition of carbon on the walls of nanochannels; the following is the "forest" of nanotubes on the substrate after etching of Al_2O_3 membrane.

13.3. Phenomenon of photon-trapping by defects in PC

Susumu Noda, professor of Kioto University, has discovered the photon-trapping by PC's defects phenomenon in 2000. In the triangular channel lattice of alumina 2D PC the line of channels was "cited of" forming the linear defect in the PC that acts as light-guide. Near this 1D slab two isolated substitution defects were introduced in kind of the same channels but of greater diameters. Shown in fig. 104 is such the photonic crystal with linear defect acting as waveguide for light and with two isolated point defects acting as the localizer of photons.

Laser light with wave length $\lambda \sim 1.55$ μk and relative frequency $f = 0{,}2710\dfrac{c}{a}$, where c is light velocity, traps through optofiber into light guide shown by arrow. Light was observed to trap in the vacancy defects and then irradiates in vertical direction that was registered by IR-camera. At these conditions one defect shines the light at

$f_1 = 0{,}2718\dfrac{c}{a}$ frequency, while another one at $f_2 = 0{,}2682\dfrac{c}{a}$ frequency. Hence the defects act as traps for photons in which the strong light localization is occurs in very small volume V~λ^3.

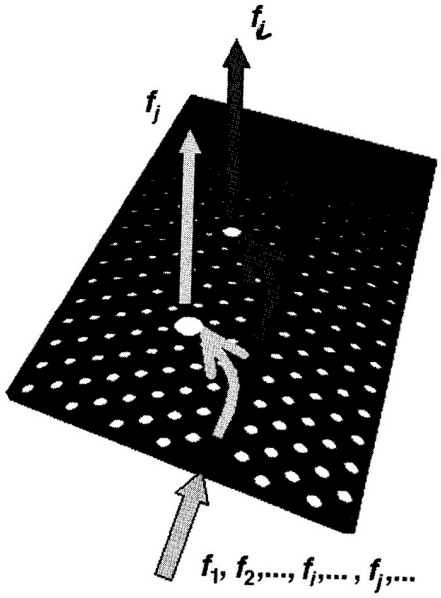

Fig. 104. Schematic illustration of a 2D photonic-crystal slab with lattice parameter a=0.42 nm and with a line-shaped defect (the absence of number of channels) and with two isolated 0D defects (channels of other diameters).

The irradiated frequency is strongly fixed and depends on the defect diameter. The quality factor of such PC is very high Q=400–500. This phenomenon gives an opportunity to obtain spectra of the frequencies which are possible to summate and subtract thereby forming the optical summator.

13.4. Photonic band structure

In analogy with an electronic band structure in conventional atomic crystals the photonic band structure arises in PC crystals. One of the main method for calculation of photonic and electronic band structure is the augmented plane wave (APW) method. Electromagnetic wave is expanded in the Fourier series upon vectors g, as being the vectors of a reciprocal lattice of PC:

$$E(r,\omega) = \sum_g A(g,k)e^{i(k+g)r} \qquad (70)$$

Consider 2D-PC in kind of some lattice of 1D wires on which a light incidents with vector $E(r,\omega)$ parallel to wire axis. Knowing the structure of PC one can write the function of dielectric permittivity in dependence of coordinates $\varepsilon(r)$. Substituting this periodic function and the expansion (70) in the completed Maxwell relation

$$(\nabla \frac{1}{\mu(r,\omega)} \nabla) E(r) = \frac{\omega^2}{c^2} \varepsilon(r,\omega) E(r) \tag{71}$$

one can obtain eigenvalue equation:

$$\sum_{g'} (k+g')^2 \kappa(g-g') A(g'k) = \frac{\omega^2}{c^2} A(g,k) \tag{72}$$

where $\kappa(g-g') = \int \frac{1}{\varepsilon(r,\omega)} e^{i(g-g')r} dr$ is a Fourier coefficient of expansion of a reverse dielectric function $\frac{1}{\varepsilon(r,\omega)}$ in points of Brillouin zone, the number of which is determined by solution accuracy requested. Solution of this equation gives the dispersion relation $\omega(k)$ and photonic band structure for electric field, called the E-mode, and for magnetic field, called the H-mode.

In contrast to the electronic band structure here polarization of light must be accounted and the more plane waves must be given in expansion series because the periodic dielectric function $\varepsilon(r)$ is sharp in contrast to smooth pseudopotential for electrons.

In the analogy substituting Fourier expansion of magnetic field and periodic function of magnetic permeability in completed Maxwell equation for magnetic field

$$(\nabla \frac{1}{\varepsilon(r,\omega)} \nabla) H(r) = \frac{\omega^2}{c^2} \mu(\omega,r) H(r) \tag{73}$$

one can obtain the dispersion relation $\omega(k)$ and photonic band structure for magnetic field, M-modes.

Shown in fig. 105 are the examples of typical lattices of PC, their Brillouin zones, and photonic band structure where for simplicity the dielectric permittivity function of 2D wire lattice was taken to be constant $\varepsilon = const$, without dispersion of $\varepsilon(q,\omega)$.
Photonic band gap is a frequencies range where light can not propagate through PC entirely or strongly attenuates.

To determine the space localization of light the simple *empirical rule* exists, namely: **for TM-mode the photonic band gap is localized in isolated high-dielectric lattice, while for TE-band gap in binding matrix lattice.** In fig. 105 the binding lattice serves as a high dielectric media hence both TM- and TE-band gaps are situated in the media while electromagnetic field is concentrated in air channels.

For calculation of the dispersion relations and photonic band structure the computer code have been developed in Massachusetts Institute of Technologies. It is free of charge package called MIT Photonic-Bands available on web-site (http://ab-initio.mit.edu/mpb/doc/installation.html).

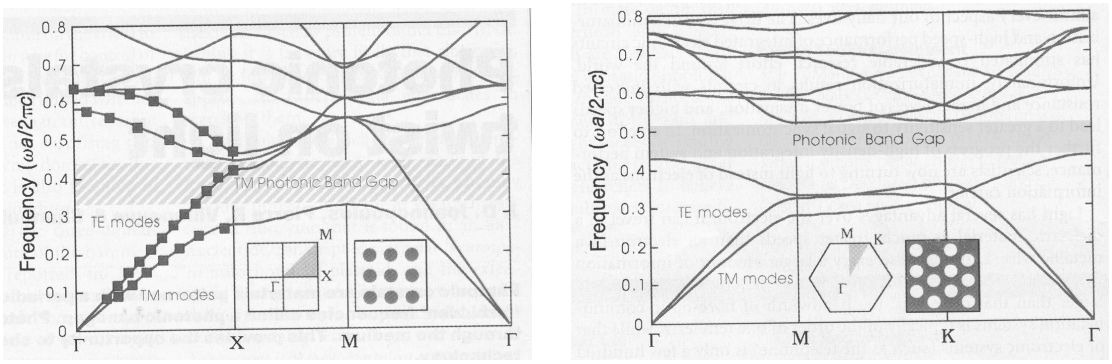

Fig. 105. Photonic spectra and photonic band gap for:
– (top) TM-mode in Brillouin zone for square 2D lattice of dielectric 1D alumina wires (ε=8.9) of 0.2a in radius in air, where a is PC lattice parameter.
– (bottom) TM- and TE-modes in Brillouin zone for triangular lattice of air hole cylinders of 0.48a in radius in dielectric matrix (ε=13).

The calculation of PC properties is very promising problem for theorists. In this field one can search new effects of negative double refraction, unusual nonlinear effects, etc.

13.5. Application

13.5.1. Waveguide

Consider again 2D lattice of dielectric wires in air. TM mode have photonic band gap in wires, while light propagates in air. If the linear defect have to be created such as a set of "cutted" wires in the PC crystal, then in photonic band gap a defect TM-mode is appeared (see fig. 106c). The light trapped in this defect can not penetrate in 2D PC due to band gap there so it forced to propagate by means of Bragg reflection in the linear defect only. It is the waveguide by definition.

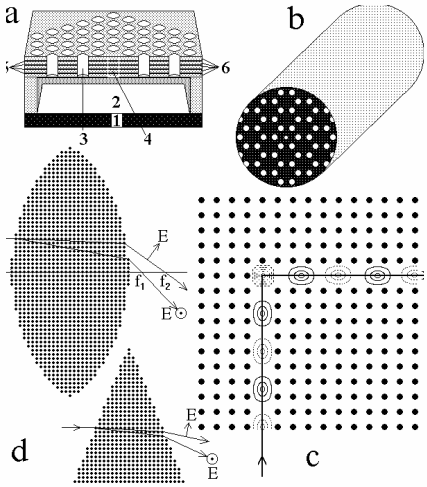

Fig. 106. Optical elements on base of PCs: a is the defect (4) in PC as element of laser on defect mode; б is the fiber PC with linear defect inside, in which the light propagates by means of Bragg reflection; c is the Bragg waveguide on base of rectangular linear defect in PC made of periodic wires lattice in air; d is the lens and prism on base of PC.

The peculiar feature of this waveguide is the light propagation via a Bragg reflection instead of a total internal reflection as in a conventional optic fiber. The Bragg reflection occurs when the Bragg diffraction condition is fulfilled $2a\sin\theta = n\lambda$. It is important to note that light can be reflected at 90º angle, as shown in fig. 106c, that is impossible in conventional optic fibers.

13.5.2. Hollow concentrators of light

Single wire "cutted" from 2D wire PC as well as single dielectric sphere "cutted" from 3D PC may be regarded as hollow channel or vacancy respectivaly. These hollows were shown in first time by E.Parsell may to enhance or weaken a *spontaneous emission of atoms (SEA)* replaced in such the hollow.
Two factors influence on the SEA:

1. Interaction between photon and electron in atom;
2. Density of electromagnetic waves in point of photon emission.

Vector-potential of electromagnetic wave in PC may be varied in dependence of geometry and structure of the defect. This can result in change of "selective rules" – permitted transitions can become forbidden ones and *vice-versa*. The last, i.e. the cancel of forbiddances, is possible in case of a resonance between wave length of electron and photon. The hollow serving as a resonator of $\sim\lambda^3$ in size, may increase the density of light inside the resonator and therefore enhance the probability of emission and irradiation.

In the hollow the emission speed is proportional to the density of free photon states per a volume unit

$$D_f \approx \frac{1}{\omega}\frac{1}{\lambda^3} \tag{74}$$

In the resonant hollow of PC the density of photon states may be increased appreciably

$$\frac{D_r}{D_f} = \frac{\omega\lambda^3}{\Delta\omega\Omega} = \frac{Q}{\Omega/\lambda^3} \tag{75}$$

where $Q = \omega/\Delta\omega$ is a quality factor of the resonant hollow, Ω is the hollow volume. Hence a probability of a spontaneous light emission in such the hollow may be enhanced in hundreds of times.

13.5.3. Filters

Parker from Southampton University has fabricated the PC on base of 2D lattice of channels in Si_3N_4-substrate with air resonator. The PC has a photonic band gap in infrared range. If light propagates in plane of hollows when vector E is parallel to the channel axis, then the wave length of TE-mode lie in range of 725 nm < λ < 825 nm so PC completely blocks up the light, while at λ > 825 nm the light usually runs through PC. Just this is the optic filter (fig. 107).

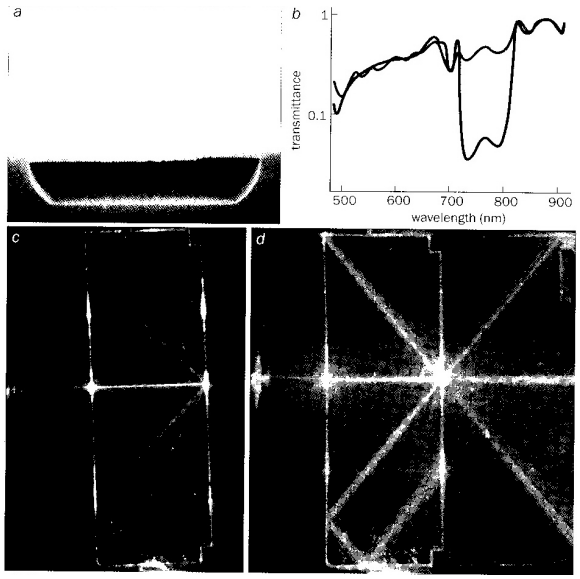

Fig. 107. Optic filter on base of photonic crystal: a) triangular 2D lattice of hollow channels in Si_3N_4-substrate with air resonator; b) transmission spectrum showing band gap in the range 725 nm < λ < 825 nm; c, d) top view on PC when c) the λ fall in the band gap is blocked out; and when d) the λ lie beyond the band gap and light pass through PC (G. Parker, M. Charlton. Physics Word,V. 13, No 8, p. 29 (2000)).

13.5.4. Fibers

Fiber photonic crystal built of packed wires, for instance silicon wires, with defect in center in kind of "cutted" wire, may serves as waveguide at resonant frequency. The light at this frequency is localized inside the defect and transmitted through PC (fig. 106б). This is the photonic optic fiber in which the light is propagated due to a Bragg diffraction mechanism instead of a total internal reflection as in conventional fibers. In contrast to the usual optical fibers in the photonic optical fibers a light dispersion $\omega(k)$ is absent.

Omnidirectional mirror was fabricated by Thomas from Massachusetts Institute of Technology. It consist of coaxial tellurian cylinders of 1 μk width alternated with polystyrene cylindrical padding. In IR range, 1.0 μk < λ < 1.5 μk, the light is reflected by Bragg manner from the tellurian cylinders and pass through the fiber without losses. Such the tubular PC fiber is flexible optic fiber.

13.5.5. Prisms, lenses, interferometers

In fig. 106d the lens and prism on base of PC were shown. Interferometer on base of PC is shown in fig. 108. Path-length difference is tuned easily by the length of splitted waveguides.

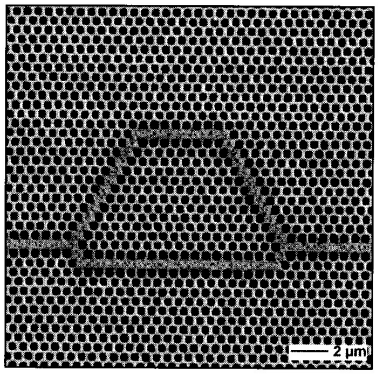

Fig. 108. Mach-Zener interferometer on base of photonic crystal.

14. SEMICONDUCTOR MICROLASERS ON BASE OF NANOSTRUCTURES

14.1. Introduction to injection lasers

Every laser has two main units, the active gain media and resonator. The former have the property under excitation by light, current, chemical reaction, synchrotron irradiation to eliminate a light at some frequency depended of electronic structure of material, namely, $\nu_g = \frac{E_i - E_j}{h}$, where E_i is a level with inverse population, E_j is a stable level. The last enhances oscillations at the special frequencies depended of its sizes, for instance, in simplest parallel-sided Fabry-Perrout resonator of L length $\nu_n = n\frac{c}{2L}$, where n is an integer number of half-waves denoted the overtone frequencies.

Lasing or the light generation is possible under condition $\nu_g = \nu_n$. The first lasers with long resonator were operating at high overtones. Apparently the maximum light density and the highest resonator quality may be obtained at the first main mode n=1. Because of wave length of lasing mode λ_g have a nanoscale size one can conclude that the effective quality resonator must be also of nanoscale size.

This idea was resulted in development of *microlasers* based on the low dimensional structure units illuminating the new route in nanoelectronics and nanophotonics. In the low dimensional heterostructures such as the quantum 2D layers-walls, 1D wires, 0D dots, the size quantum confinement is known to arise radically changing the properties of low dimensional semiconductors. In quantum layers the charge carriers are restricted in one direction, hence they may be freely move in two other directions of plane layer; in the quantum wires electrons are restricted in two directions moving freely only in one direction; while in quantum dots they are restricted in three-directions. In periodic lattices of the quantum layers, wires and dots the energy band structure is known to arise as in usual 3D crystals. However the band structure of low-dimensional nanostructures posses some peculiarities, in particular, in the 0D quantum dots the bands are very narrow and discrete as in molecules, so they called supramolecules. They have size ranging from several nanometers to several tens of nanometers containing ca. tens of thousands of atoms.

Semiconductors (SC) on base of IV–IV, III–V, II–VI compounds were shown to be the most suitable materials for development of microlasers because of the recombination emission is possible to arise under condition of inverse population $\varepsilon_{fc} - \varepsilon_{fv} > h\nu$, where ε_{fc} and ε_{fv} are the Fermi levels of the electrons in conductive band and the holes on valence band respectivaly. Shown in fig. 109.1 is the SC with inverse population produced artificially. The excited electrons from conductive band fall down back into valence band recombining with holes there and emitting the coherent photons in the result. Hence if the inverse population to create in the SC then the laser lasing is possible that was observed actually in first time in 1962.

Most suitable method for the inverse pumping of SC-lasers is a displacement voltage applied to a p-n junction as diode. In active SCs a concentration of acceptors and donors is so large (~10^{18} atom/cm^3) that Fermi level of holes E_{Fp} in p-region falls in range near top of valence band, while E_{Fn} of electrons in n-region lies near the bottom of conductive band. In absence of the displacement voltage this levels are imagined at the same horizontal line as shown in fig. 109.2. If the voltage is applied then this levels are

displaced splitting by gap ΔE as shown in fig. 109.3. Under this displacement the injection of electrons into p-SC and holes into n-SC is occurs. In the region of p-n transition the inverse population of electrons and holes is arisen acting as the gain media of $d = \sqrt{D\tau}$ in width, where D is a diffusion coefficient of electrons, and τ is an average life time of electrons before a recombination. For example in GaAs D=10 cm^2/s, τ~1 ns, hence $d \sim 1$ μk and the displacement voltage is $V = \Delta E / e = E_g / e$=1.5 V. Such the SC lasers with pumping by direct voltage through p-n junction affecting both the electron injection into valence band and the hole injection into conduction band, where their recombination occurs, are called as *injection lasers*.

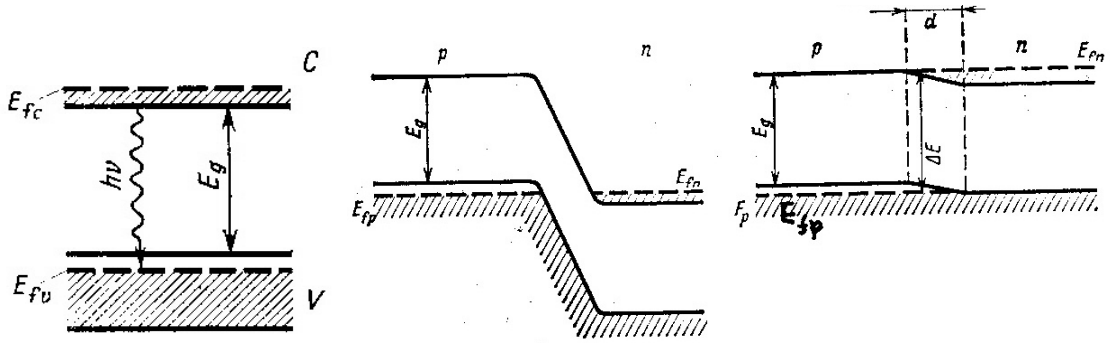

Fig. 109. Principle of action of semiconductor laser: 1 is the scheme of recombination elimination; 2 is the p-n junction in absence of displacement voltage, and 3 is the p-n junction under voltage displacement ΔE. In the region of p-n junction the active gain media of d-width is shown.

The first SC injection laser on base of the p-n junction also named as light-emission diode (LED), was developed in 1962 by Nick Golonyak from General Electric.

Jores Alferov from Ioffe Institute in 1963 have discovered that the gallium arsenide GaAs doped with impurities possess optimal performance that make it most suitable and convenient gain media for fabrication of inverse population and SC lasers. Doped with donor impurities (Si, Ge, etc.) it takes conductivity of n-type while doped with acceptor (Be, etc.) it becomes p-type SC. Moreover the GaAs was shown to be easy-technological in growth of quantum heterostructures of different form and size. In 1971 Alferov also has shown the key role of the heterostructure AlGaAs/GaAs, in which reduction in dimensionality of gain media significantly decreases the threshold current of emission. The size quantum confinement was shown to be able to decrease the threshold lasing, weaker the temperature dependence of threshold current, offer the temperature stability and significantly improve all other laser characteristics. Moreover the using of nanostructures offers wide possibilities to tune the lasing frequencies or emission color, the range of lasing spectra, and a *quality factor Q* that is a key characteristics of laser resonators as being the relation of the total energy of all standing waves arisen in resonator divided to the loss light energy lost in resonator. Shown in fig. 110 is the comparison of the quality factors on base of different low-dimensional structures demonstrating their preference over bulk 3D structures.

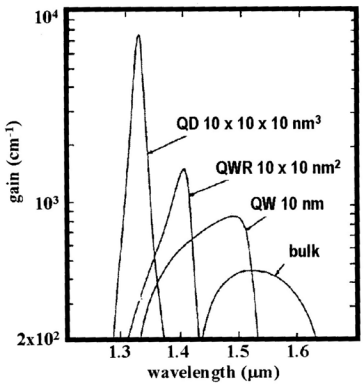

Fig. 110. Quality factors of the quantum dots (QD), quantum wires (QWR) and quantum walls (QW) in comparison with conventional (bulk) resonators.

14.2. Laser on base of double heterojunction

Single p-n junction is well while two or more is better. J.Alferov created the first laser using a double heterojunction GaAs(n)/AlGaAs(n)/AlGaAs(p)/GaAs(p) (fig. 111), for development of which he was awarded Nobel Price in physics in 2003. The width of single GaAs (λ_g=0.85 μk) layer for a first lasing mode was equal to L=n λ_g /2n_{ef}=(n=1, n_{ef}=3.6)=0.118 μk and its divisible. From this relation it follows the demand of smallest roughness of the face ends of resonator that is responsible for the broadening of laser mode by value $\Delta\lambda=\lambda_0^2/2n_{ef}L$ ~ 10 nm (fig. 111).

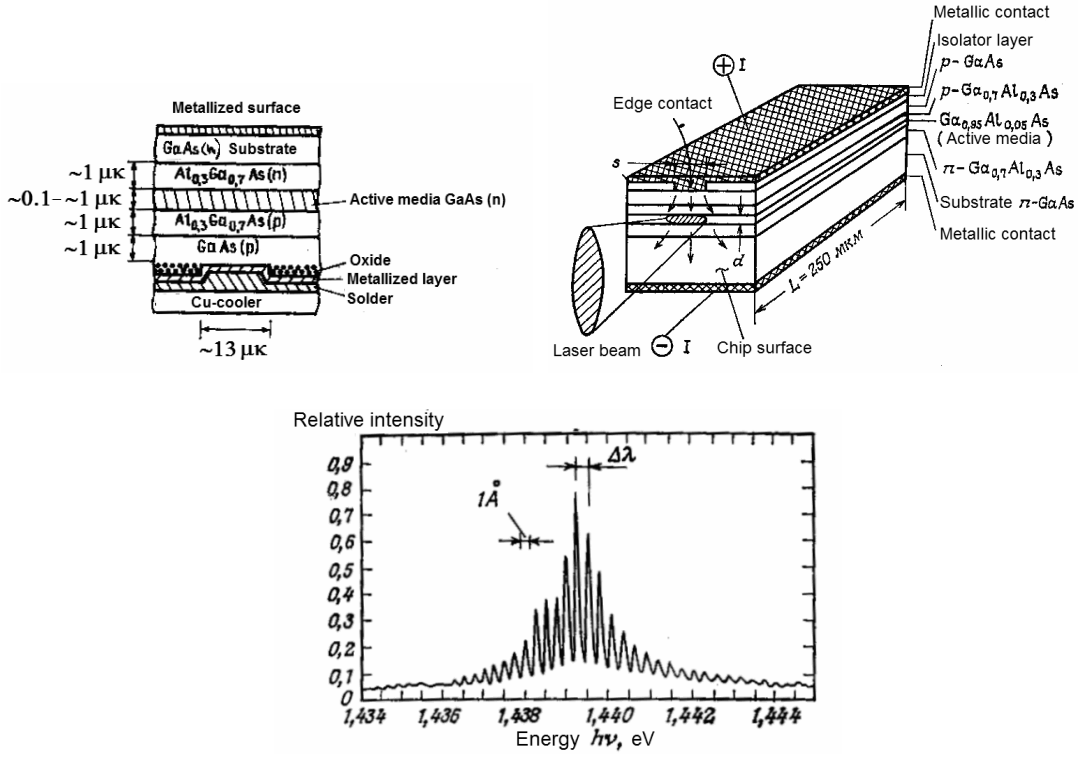

Fig. 111. The double heterojunction and scheme of SC-laser on its base. Also the typical illumination spectrum of such Fabry-Perrout resonator is shown.

14.3. Cascade multi-layered laser

Shown in fig. 112 is the cascade laser consisted of periodical packed set of quantum walls, typically 25 ones. Quantum confinement in such lattice of 2D walls leads to splitting of bands and creating of set of the conduction narrow (~100 meV) mini subbands equal to number of walls isolated by band gaps. Quantum of light is generated under transition of electron from the lowest main level of first subband E_2 onto the highest level of lower second subband E_1. Then the electron quickly relaxes from the top to the bottom E_0 level of the second band scattering a phonon. Again it transits from the bottom of second subband E_0 onto the top of the lower third subband emitting the second photon. Such the process is repeated at the next walls until electron do not transmits through all the subbands. During this cascade process the number of photons is generated equal to number of the walls. Inverse population is kept due to very small relaxation time which is smaller then lifetime of the inversion levels. By principal distinguishing feature of the cascade laser is that the width of band gaps are determined by the width of active heterolayers and parameter of periodical cascade lattice. Hence adjusting the structure of the lattice in couple with a type of material one can possible to control the performance of lasers (the frequency, quality factor, power, etc.).

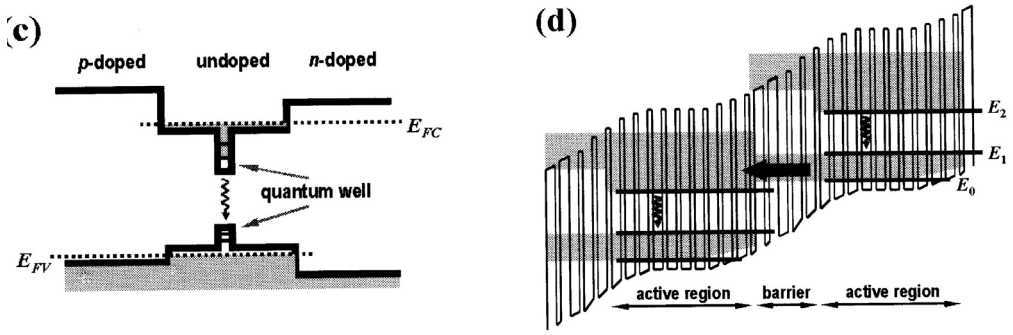

Fig. 112. Scheme of cascade laser based on set of quantum walls.

The active media of first SC-lasers were consisted of the set of the plane p-n-p plates the edges of which serve as Fabry-Perrout resonator. This type of laser has been called as *the edge-emitting laser* (fig. 113a). Due to relatively long $L \approx 100\lambda_g$ resonator the laser operates in multi-mode regime at highest overtones (fig. 111). The quality factor of such resonators was relatively small because of technology difficult to fabricate the parallel unroughned edge surfaces with high accuracy.

Progress in growth of heterostructures makes laser resonators possible to fabricate of another forms, in particular, the microdisk laser (fig. 113c), microwire laser (fig. 114), and quantum dots laser (fig. 119).

14.4. Microdisc laser

Microdisc laser have resonator in form of a disc fabricated of a semiconductor with high refractive index n_{ef} (fig. 113c). In such a resonator a total internal reflection is occur resulted to excitation and amplification only circular ring modes belonging to so called *a gallery of whispering modes*. These modes are the natural standing vibrations when an integer number of half-waves are arranged along circular length. The peculiar feature of this whispering modes is low attenuation due to interference of incident and reflected

waves circulated in opposite directions along ring. Because of small incident angles the coefficient of total internal reflection is great while losses of the whispering modes are small resulted in very high quality factor in ~1000 time overcomes the Fabry-Perrout resonator. Disadvantage of such laser is a leakage of light in all directions influenced by light scattering caused by surface defects.

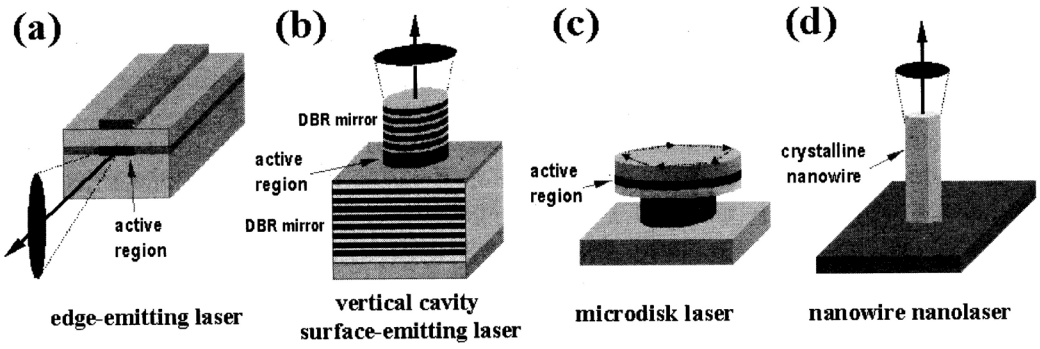

Fig. 113. Different kinds of SC-laser resonators: a is the edge emitting laser; b is the vertical-edge emitting laser; c is the microdisc laser; d is the wire laser.

14.5. Nanowire laser

Wire laser (fig. 113d, 114) consists of the 2D lattice of nanowires on a substrate, for example, ZnO-wires of ~ 5 μk in length and 70–100 nm in diameter on a sapphire substrate (fig. 114). The wires play a double role both as the optical resonator when the wire length is divisible on the integer number of half-waves and the active media. Under irradiation of Nd:YAG-laser (λ=266 nm, impulse duration is 3 ps) a spontaneous emission arises when current power overcome some lasing barrier (~40 kW/cm^2). It is caused by recombination of excitons in process of exciton-exciton scattering. Such nanowire ZnO-laser possess relatively small lasing threshold owing to ZnO parameters and operate in single-mode regime due to the low length of wires.

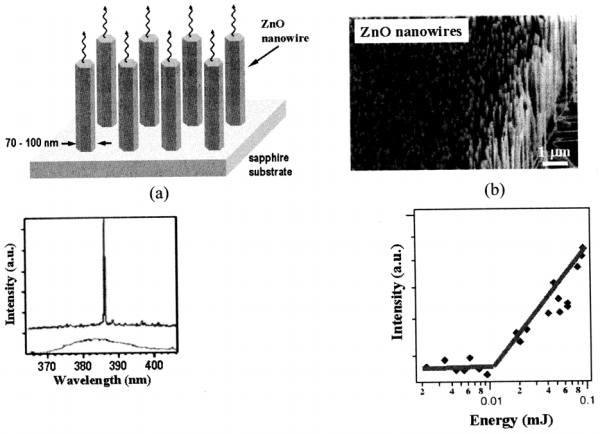

Fig. 114. Microwire laser on base of ZnO-nanowires, and their emission spectrum below and above lasing threshold.

14.6. Zeolite-dye laser

Zeolite-dye laser (fig. 115) is the smallest among wire lasers. Zeolites are the natural or artificial minerals consisting of very small cylindrical nanopores of several nanometers in diameter. The pores may be easy impregnated by any liquid active dye obtaining thereby active gain media in kind of fibers inside of cylindrical nanopores which in turn play also the role of resonator. In such the manner the laser on base of $AlPO_4$-zeolite with Pyridine-2 wires (λ=685 nm) of 0.74 nm in diameter. Up to 2005 year it was record tiny laser in the world of smallest size ~8 μk with superfine wires.

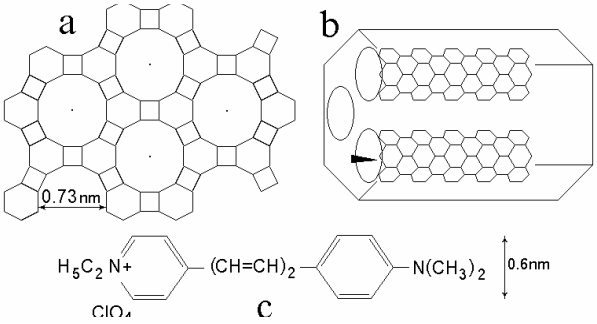

Fig. 115. Active media of laser on base Pyridine-2 dye wires inside the cylindrical pores of $AlPO_4$-zeolite.

14.7. Laser with distributed feedback (DFB)

Laser with distributed feedback (DFB) was developed with aim to enhance a total internal reflection and a quality factor in the result (fig. 116). At the boundary of active media a special crimped layer is grown resembling a diffracting screen with a step length equal to half-wave length of the active media $\Delta L = \lambda_0/2n_{ef}$. The distributed reflection arises under Bragg reflection of laser beam when refractive index is changed at the crimped layer which acts as distributed phase-locked antenna.

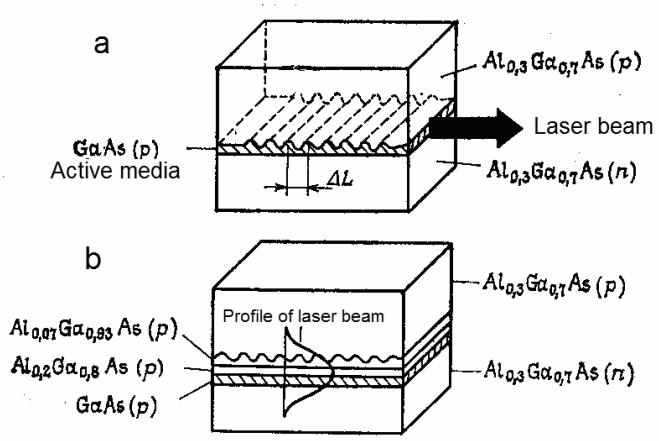

Fig. 116. Scheme of SC-laser with the distributed feedback in which the crimped structure is grown a) at one surface of the active GaAs layer, or b) at additional AlGaAs layer near the active media.

14.8. Vertical cavity surface emitting laser – VCSEL

Vertical cavity surface emitting laser (VCSEL, fig. 113b) was in first demonstrated in 1979 as being the first laser with Bragg resonator the size of which is of order of wave length of emitting light. Multi-layered heterostructure where a layer width is equal or divisible to half-wave length of light serves as Bragg mirror of the resonator where a light possess a multiple reflection at this alternated multiple layers. Such a mirror was named as distributed Bragg reflector.

14.9. Surface-emitting 2D photonic-crystal laser with multidirectional distributed-feedback

Photonic crystals (PC) are periodical lattices consisted of the zero-, one-, or two-dimensional structures which have periodically alternated layers with different dielectric or/and magnetic sucseptibility than for matrix. For example it may be lattice of holes in layered heterostructure. Consider here the laser on base of such PC.

Noda from Japan has developed this type of laser, the surface-emitting 2D photonic-crystal laser with the multidirectional distributed-feedback (fig. 117). In contrast to conventional lasers in the PC-lasers the Bragg reflection is used instead of total internal reflection. This laser consists of two juncted waffles. Waffle A is the active gain media, λ=1,285 μm. Waffle B is the triangular photonic crystal acting as the distributed feedback because of its lattice period in Γ –X direction is equal to wave length of active media. Bragg condition in this triangular PC $2a\sin(\pm 60,\pm 20) = n\lambda$ is obeyed for 6 angles in plane shown in fig. 117b.

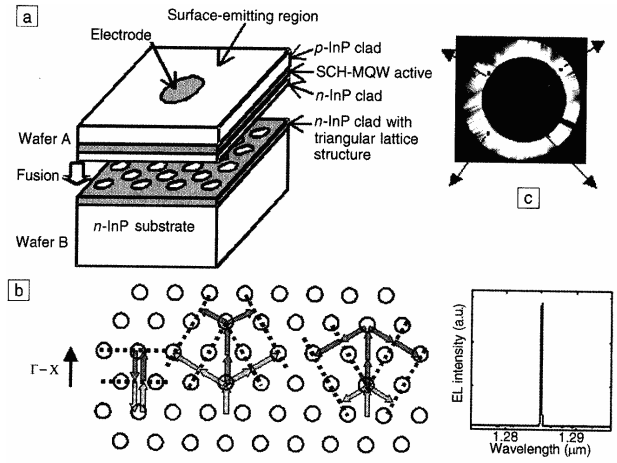

Fig. 117. (a) Scheme of surface-emitting 2D photonic-crystal laser with multidirectional distributed-feedback, SCH-MQW is the layered heterostructure from quantum walls; (b) scheme of multidirectional amplification and emission spectra; (c) top view of laser emitting in all directions.

Therefore a coherent amplification due to interference in three equivalent Γ – X directions cause a light emission in this 6 directions in the plane of active media.

14.10. Laser on defect mode of photonic crystal

Defects in photonic crystals are the localisators of photons in the same manner as crystalline defects in semiconductors are localisators of electrons or holes. The absent holes or the holes of another diameter in the hollow PC may serve as example of the defect.

Painter from Caltech in 1999 has fabricated the first laser on the defect mode of photonic crystal (fig. 118). Layered heterostructure is active media while the triangular lattice of holes forms the photonic crystal where the layers with common cavity serve as resonator. In this PC the photonic band gap arises of 1.32 μm in width. Shown in fig. 118, right, is the defect in the hollow PC in kind of absent single hollow and two nearest hollows of another diameter. This defect is a place where light is localized with wave length λ=1.504 μm under pumping at λ=830 nm. Light is localized in very small volume of this defect $\sim\left(\frac{\lambda}{n}\right)^3$ =0.03 μm^3 and then is emitted in vertical normal direction. The quality factor of such resonator may be very high Q ~ 200–1500 depending of the parameters of PC.

This type of lasers have number of advantages and record performance, namely, the low noise level, the low lasing threshold, the easy opportunity to tune the frequency of gain mode.

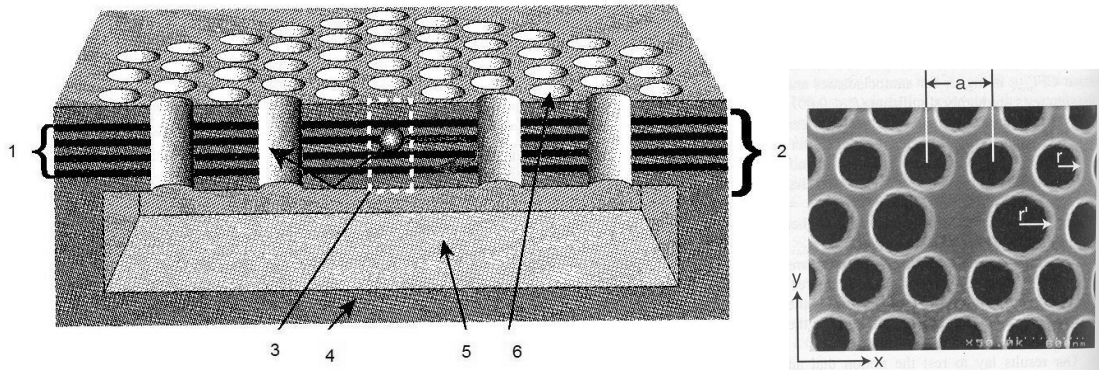

Fig. 118. 1 – is the active media of 4 quantum walls of gallium antimonite and phosphorous arsenide InGa/AsP each of 9 nm in width and refractive index n=3.4; 2 – is the Bragg λ/2–layered resonator of light in vertical direction; 3 – is the defect in PC shown right; 4 – is the InP substrate (n=3.2); 5 – is the cavity resonator (n=1); 6 – is the air holes of PC (n=1).

14.11. Quantum dots laser

Shown in fig. 119 is the quantum dots laser consisted of lattice of quantum dots (QDs) serving as active media surrounded by cladding semiconducting layers serving as resonator. The light is generated in QDs by means of recombination of electrons with holes at the frequency $\hbar\omega_0 = E_g + \varepsilon_n + \varepsilon_p$ under transition between energy levels ε_n and ε_p arisen in QDs due to confinement. Density of this states is known to be very sharp in 0D QDs leading to delta-like emission spectrum that is peculiar advantage of such QDs-lasers.

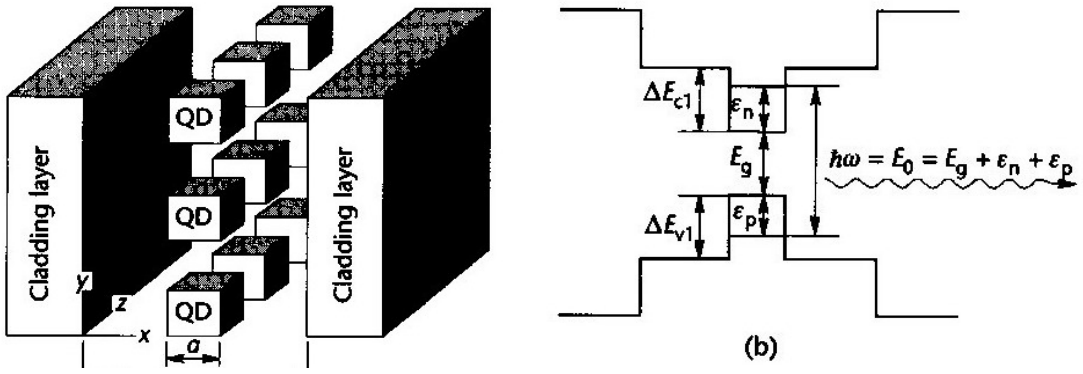

Fig. 119. Scheme of structure (a) and energy levels (b) in the laser based on quantum dots.

However for realization of these advantages all the QDs have to be very similar and homogeneous. This is very difficult technology problem so the real as-present QDs differs in size, form and local deformation. This unhomogenity cause a widening of δ-like emitting spectrum and a worsening of other laser characteristics. Another disadvantage of QDs-laser is a temperature shift of lasing mode arisen in result of temperature excitation of electrons and holes $\hbar\omega = \hbar\omega_0 + kT$.

To prevent this parasitic recombination the idea of *the tunnel injection* of current carriers have been proposed, namely, the QDs have to be covered by thin sheet through which the carriers do not transit but tunnel through the layer. In this case the threshold of tunnel injection is determined by a height and permittivity of the tunnel cover dependent slowly of temperature. Scheme of such *quantum dots laser with tunnel injection* of current carriers is shown in fig. 120.

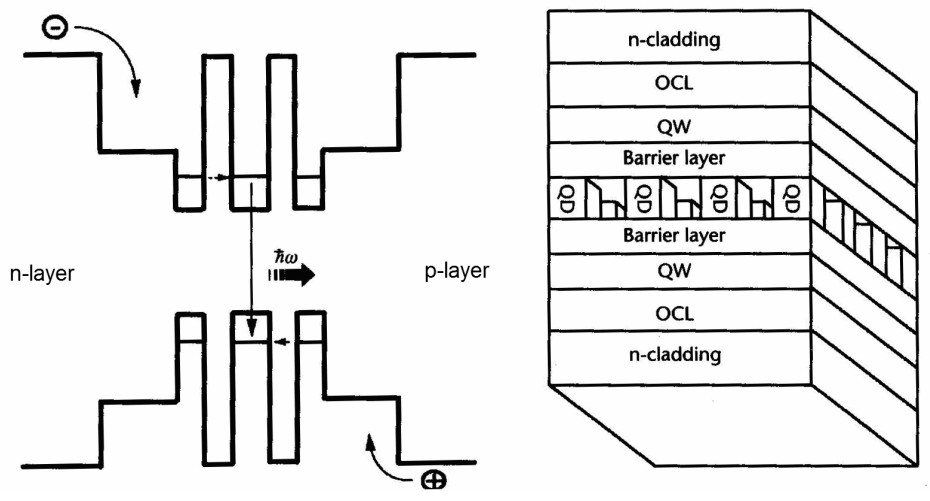

Fig. 120. Structure scheme (a) of quantum dots laser with tunnel injection of current carriers, and scheme of its energy levels (б).

n-cladding is the $Al_{0.55}Ga_{0.45}As$ layer of 1.5 μm thick; OQL is the optical quantum GaAs layer of 65 nm thick; QW is the quantum $In_{0.25}Ga_{0.75}As$ wall of 9.5 nm thick; Barrier layer is the $Al_{0.55}Ga_{0.45}As$ layer of 2 nm thick; QD is quantum $In_{0.4}Ga_{0.6}As$ dot.

14.12. Laser light diode on base of nanotube

Misewich at al. has developed the first injection light emitting diode (LED) on base of a semiconducting carbon nanotube in ambipolar transistor (fig. 121).

Carbon semiconducting nanotube of 1.4 nm in diameter is arranged at the titanium electrodes grown at the silicon layer based on silica substrate of 150 nm thick. Metallic substrate under SiO_2 layer plays the role of third gate electrode as the greed in a valve triode.

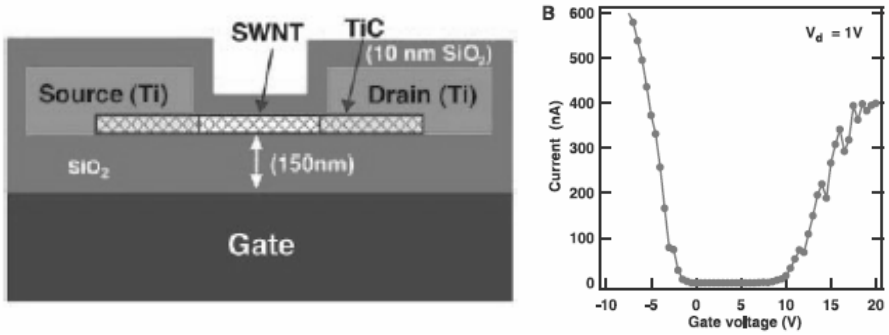

Fig. 121. Scheme of ambipolar transistor on base of single-wall semiconducting carbon nanotube and the current-voltage dependence through C-NT under displacement voltage V_d =1 V. (J. A. Misewich et al. Science, 300, 783 (2003)).

The current-voltage curve have the ambipolar nature, namely, under negative voltage the electrons serves as current carriers while at positive voltage the holes are carriers. This is explained by the quantum dependence of electroconductivity of NTs. At interface of NT with metallic electrode the Schottky barrier arises in result of their different work functions. This result in appearance of the surface quantum levels through which electrons are tunneled. Magnitude of this levels depends on a sign and value of a displacement voltage. This offers a possibility to drive a conductivity type through Schottky barrier, i.e. to switch on/off tunneling of electrons and holes.

To form active media it is necessary to synchronize the injection of electrons and holes into NT for their recombination. The injection is achieved in the case of a displacement voltage overcomes a gate voltage. For example, if the voltage is applied 10 V to discharge electrode and 5 V to gate electrode at grounding source electrode, then the difference of potentials between electrodes should be the same, 5 V in magnitude but opposite in sign, to gate voltage on the contacts. The field at source electrode should stimulate electron injection while the field at discharge electrode should stimulate the hole injection. In result the conductivity of n- and p-type arises in vicinity of the source and the discharge region respectivaly that may be determined as p-n transition.

At conditions of simultaneous injection of electrons and holes under their transition through such p-n junction the recombination of electrons is evident to occur resulted in photon generation inside nanotube. Scheme of this laser emitting diode on base of nanotube is shown in fig. 122.

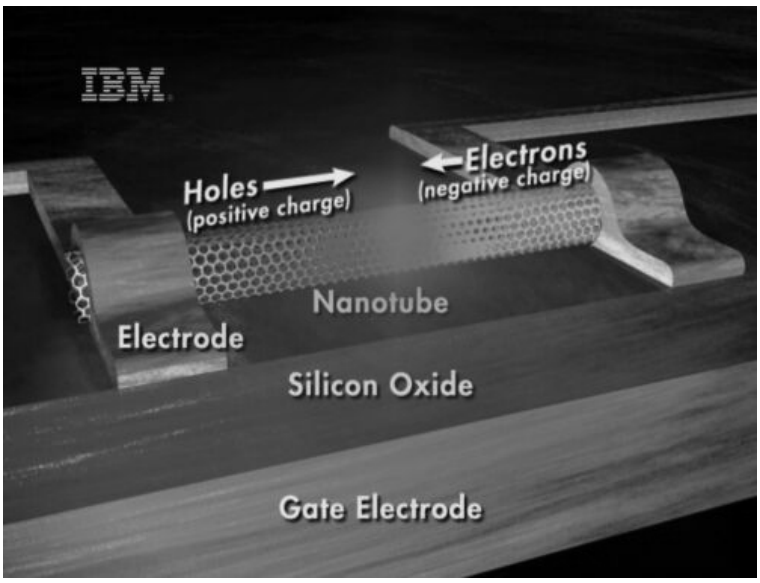

Fig. 122. Scheme of laser emitting diode on base of carbon nanotube (J. A. Misewich et al. Science, 300, 783 (2003))

The emitting wave length is determined by width of band gap, that in the case shown in figure is λ=1650 nm under E_g=0.75 eV. Because of the last depend on nanotube diameter it is possible to tune the frequency of emitting light. The light emitting by nanotube was shown to be linear polarized.

15. ELECTRODYNAMICS OF "LEFT-HANDED" METAMATERIALS WITH $\varepsilon < 0$ AND $\mu < 0$

15.1. General remarks and determinations

Let's consider an interest peculiarity of the general dispersion law connecting the dielectric permittivity $\varepsilon(\omega)$ with the magnetic permeability $\mu(\omega)$.

Write the Maxwell equations for any media without any charges and currents:

$$\overline{D} = \varepsilon\overline{E}\,,\ div\overline{D} = 0\,,\ rot\overline{E} = -\frac{1}{c}\frac{\partial\overline{B}}{\partial t} \tag{76a}$$

$$\overline{B} = \mu\overline{H}\,,\ div\overline{B} = 0\,,\ rot\overline{H} = \frac{1}{c}\frac{\partial\overline{E}}{\partial t} \tag{76b}$$

For plane monochromatic wave:

$$\overline{E} = E_0 e^{i\bar{k}\bar{r}-i\omega t}\,,\ \overline{H} = H_0 e^{i\bar{k}\bar{r}-i\omega t} \tag{77}$$

the time derivatives are:

$$rot\overline{E} = -\frac{1}{c}\mu(-i\omega)\overline{H} = \frac{i\omega\mu}{c}\overline{H} \tag{78a}$$

$$rot\overline{H} = \frac{1}{c}\varepsilon(-i\omega)\overline{E} = -\frac{i\omega\varepsilon}{c}\overline{E} \tag{78b}$$

and spatial derivatives are:

$$rot\overline{E} = i[\bar{k}\overline{E}];\quad rot\overline{H} = i[\bar{k}\overline{H}] \tag{79}$$

Hence:

$$i[\bar{k}\overline{E}] = i\frac{\omega\mu}{c}\overline{H}\,, \qquad c[\bar{k}\overline{E}] = \omega\mu\overline{H} \tag{80a}$$

$$i[\bar{k}\overline{H}] = -i\frac{1}{c}\omega\varepsilon\overline{E}\,, \qquad c[\bar{k}\overline{H}] = -\omega\varepsilon\overline{E} \tag{80b}$$

Exclude $\overline{H}$ from (80a) and substitute in (80b):

$$c[\bar{k}[\frac{c}{\omega\mu}[\bar{k}\overline{E}]]] = -\omega\varepsilon E\,,\quad \frac{c^2}{\omega^2\mu\varepsilon}[\bar{k}[\bar{k}\overline{E}]] = -E\,,\ [\bar{k}[\bar{k}\overline{E}]] = (k(kE)) - Ekk = -k^2E$$

from which after algebraic manipulations we obtain *the general dispersion relation*:

$$k^2 = \varepsilon(\omega)\mu(\omega)\frac{\omega^2}{c^2} \tag{81}$$

that is absolutely valid for all media, from which a refractive index is determined as:

$$n^2 = \varepsilon\mu \qquad (82)$$

Glance at this dispersion law from another point of view. Note that equation (82) is obeyed not only at $\varepsilon > 0$ and $\mu > 0$, but also at their negative meanings: $\varepsilon < 0$ and $\mu < 0$.

It is logically valid and do not contradicts nature's laws including the Maxwell equations.

What the case of $\varepsilon < 0$ and $\mu < 0$ means?

1. Perhaps the properties of matter do not depend on simultaneous change in their signs ε and μ? The answer is no, because logically it should not be the case due to the physical properties of matter with $\varepsilon < 0$ and $\mu < 0$ should be different from the properties of matter with $\varepsilon > 0$ and $\mu > 0$.

2. Perhaps there is some fundamental restriction for existence of such the matter? The answer is no, because there are no visible physical restrictions, limitations or forbiddances.

Hence the matter with $\varepsilon < 0$ and $\mu < 0$ theoretically must exist.

However to resent time there were no such the materials unless in 2000 Jone Pendry and David Smith from San-Diego University in first time have been made the material with negative both dielectric permittivity $\varepsilon < 0$ and magnetic permeability $\mu < 0$ on base of photonic crystals. It was recognized at the American Physical Society Meeting as the unique discovery in physics in 2000 year.

Interest to note that existence of such substance with $\varepsilon < 0$ and $\mu < 0$ have been predicted by L. Mandelstam, while the theory have been developed in early 1967 by Victor Veselago, professor of Moscow Physico-Technical Institute, called him as left-handed materials. It evenly shows a high level of fundamental sciences in former Soviet Union that was the second after USA, in spite of the funding was in the order of magnitude smaller than in USA. Why? Reason of such high level at this poorness funding was a jocosity, wit, inventiveness, resourcefulness of mind in couple with practical importance on demand of government rather then money. This is very instructive lesson.

15.2. Veselago theory of left-handed matter

It is clear from equation (81), that at $\varepsilon > 0$ and $\mu > 0$ the vectors $\vec{E}, \vec{H}, \vec{k}$ constitute the right triple of vectors (for the conventional right matter) while at $\varepsilon < 0$ and $\mu < 0$ the same vectors $\vec{E}, \vec{H}, \vec{k}$ constitute the left triple. Therefore such matter was named as *the left-handed matter or metamaterials*.

Fundamentally the Pointing vector $\vec{S} = \frac{c}{4\pi}[\vec{E}\vec{H}]$, determining the energy flow of wave, constitute only the right triple vectors with *E* and *H* always.

Hence for conventional right-handed matter the vectors $\vec{S}$ and $\vec{k}$ are directed in same direction, while for left-handed matter – in opposite directions (fig. 123).

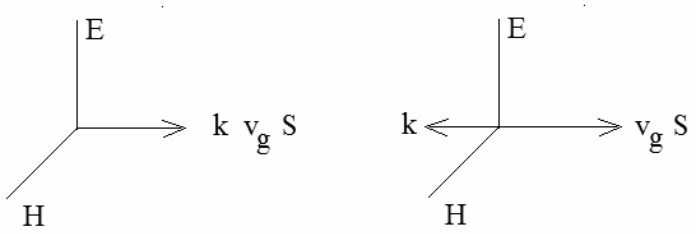

Fig. 123. Directions of field vectors for the right-handed and left-handed matter.

Vectors of the phase velocity $\vec{\upsilon} = \frac{\omega}{\vec{k}}$ coincide always with direction $\vec{k}$ while the direction of vector of the group velocity

$$\vec{\upsilon}_g = \frac{d\omega(\vec{k})}{d\vec{k}} = \frac{\vec{k}}{k}\frac{d\omega(k)}{dk} \tag{83}$$

depend on the sign of derivative of dispersion law $\frac{d\omega(k)}{dk}$, so it may be negative when $\frac{d\omega(k)}{dk} < 0$. It means that left-handed matter is the matter with negative group velocity $\upsilon_g < 0$. It is hard to imagine himself but valid logically.

Consider the sequences of $\upsilon_g < 0$. Let's introduce for triple vectors $(\vec{E},\vec{H},\vec{k})$ a matrix of directed cosines, the determinant of which

$$p = \det\begin{pmatrix} \alpha_1 & \alpha_2 & \alpha_3 \\ \beta_1 & \beta_2 & \beta_3 \\ \gamma_1 & \gamma_2 & \gamma_3 \end{pmatrix} \tag{84}$$

is equal to p=+1 for right-handed and p=–1 for left handed materials.

15.3. Inverse Doppler effect

Doppler effect is a change of frequency of electromagnetic or acoustic waves in dependence of velocity of moving source relative to receiver. It is described by general relation valid for both the right- and left-handed matter

$$\omega = \omega_0(1 + p\frac{\upsilon}{c}\cos\theta) \tag{85}$$

This relation depends on sigh of coefficient p.

For right-handed matter p =1 and $\theta = 0$, that gives $\omega = \omega_0(1+\frac{\upsilon}{c})$, i.e. the frequency is increased under approach and decreased under removing of source, that called as blue shift.

For left-handed matter p =-1 and $\theta = 0$, that gives $\omega = \omega_0 (1 - \frac{\upsilon}{c})$, i.e. the red shift is occurs instead of blue shift (fig. 124).

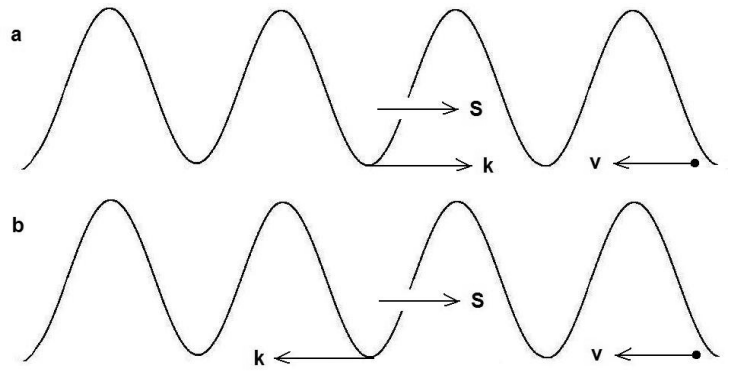

Fig. 124. Scheme of Doppler effect in the right and left-handed substances.

15.4. Inverse Cherenkov effect

Cherenkov effect is the irradiation of electromagnetic waves by particle moving in media with velocity exceeding the velocity of light in this media $\frac{c}{n} < v < c$. The eliminating particle drops its energy surplus and brakes to the normal velocity c/n.

In right-handed media the vectors of velocity $\vec{\upsilon}$ and energy flux $\vec{S}$ are directed in the same side under sharp angle θ, dependent on velocity (fig. 125). The wave vector have the components $k_z = k\cos\theta$, $k_r = \sqrt{k^2 - k_z^2}$ and due to angle θ between k_z and $\vec{S}$ is sharp, the Pointing vector is directed in the direction of wave propagation k_z. Hence the cone of irradiation is forward directed.

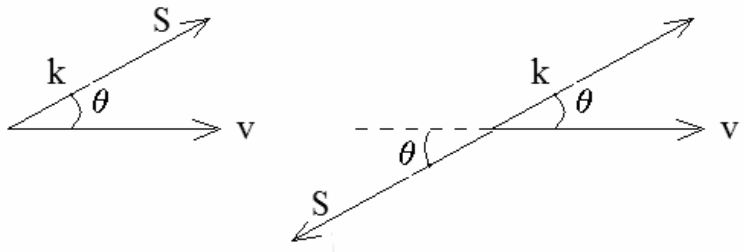

Fig. 125. Scheme of Cherenkov irradiation for the right-handed and left-handed matter.

For left-handed matter the vectors $\vec{k}$ and $\vec{S}$ are directed in opposite sides, so the angle θ between k_z and $\vec{S}$ is obtuse, and irradiation cone is directed back.

In general case for right- and left-handed matter the irradiation angle is described by

$$\cos\theta = p\frac{c}{\upsilon n} \tag{86}$$

15.5. Inverse Snell law or negative refractive index

The boundary conditions under transition of light beam from one media to another must be obeyed independent of their handed for both the right- and left-handed media:

$$E_{t1} = E_{t2},\ H_{t1} = H_{t2} \tag{87}$$

$$\varepsilon_1 E_{n1} = \varepsilon_2 E_{n2},\ \mu_1 H_{n1} = \mu_2 H_{n2} \tag{88}$$

It follows from (87) that tangential x,y-components of $\vec{E}$ and $\vec{H}$ conserve their direction for both the right- and left-handed media while z–component for left-handed media alternate its sign. It means that under transition into a media with another handed the vectors $\vec{E}$ and $\vec{H}$ change not only its value in accordance with ε and μ but also reflect relatively to the boundary between these media. The same concerns the vector $\vec{k}$, i.e. simultaneous reflection of all three vectors relates to change of sign of $\det|G| = p$. The beam path is shown in fig. 126. All beams are symmetrical relative to incident axis.

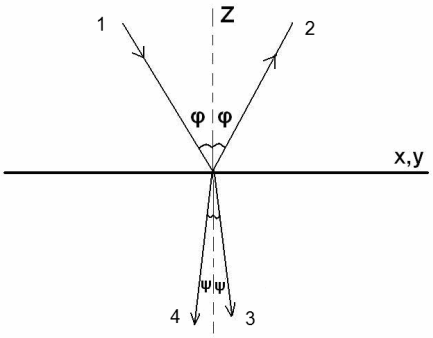

Fig. 126. Scheme of refraction under transition of light beam from right into left handed media: 1 – is the incident beam, 2 – is the reflected beam, 4 – is the refracted beam (right media), 3 – is the refracted beam (left media).

The Snell law have to be updated with account of the media handed and takes the general view:

$$\frac{\sin\varphi}{\sin\psi} = n_{1,2} = \frac{p_2}{p_1}\sqrt{\frac{\varepsilon_2\mu_2}{\varepsilon_1\mu_1}} \tag{89}$$

Here calculating the amplitudes of refracted and reflected beams using Fresnel formula, the values $\varepsilon, \mu, n, \varphi$ and ψ must be taken in its absolute value.

Apparently the refractive index may be negative also at transition through media of different types. In particular the refractive index of left media relative vacuum is negative.

Reflected beam is directed always in the same side for both the right- and left-media. But for refracted beam under transition from right into left handed media $\sin\psi < 0$, and the refracted angle is obtuse $\psi > 90^0$. This means that in left media the beam alternate its refracted direction relative incident axis, as shown in fig. 126.

15.6. Optical units from left-handed media

Plane-parallel plate with negative refractive index $n = -1$ is able to focus a light when its thickness overcome a focus length $d > l$, i.e. the plate acts as the lens (fig. 127) .

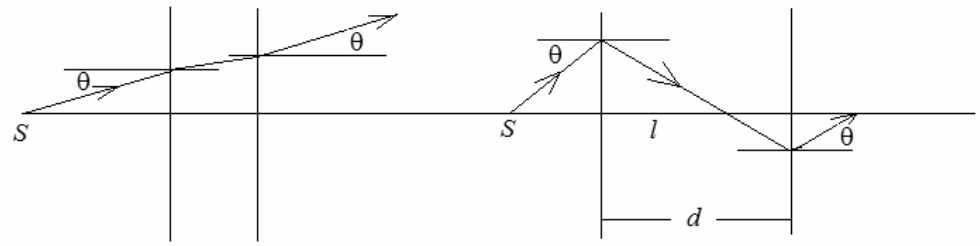

Fig. 127. Light beam path in plane-parallel plate with positive (left) and negative (right) refractive index when its thickness overcome focus length $d > l$.

Convex and concave lenses on base of the negative refractive material alternate by roles, i.e. the convex lens becomes to be the scattered lens, while the concave lens becomes to be collective lens (fig. 128).

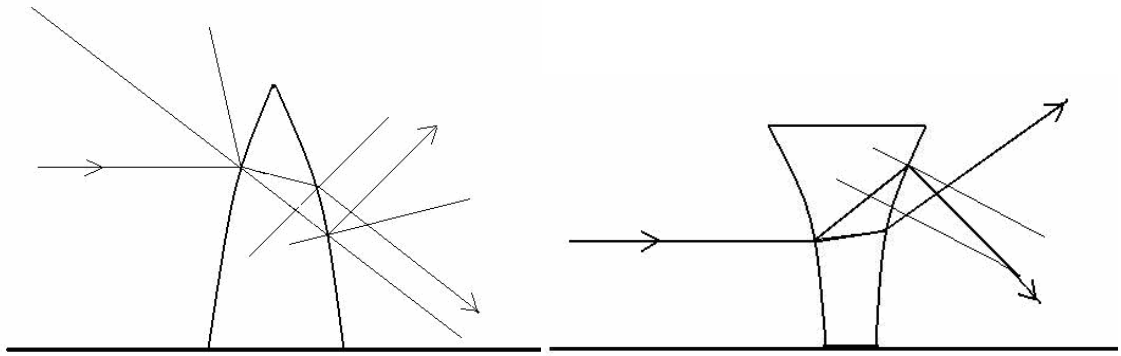

Fig. 128. Light path in lenses with negative refractive index: 1 – in concave lens, 2 –in convex lens.

15.7. Light pressure from left-handed media

Light pressure from left-handed material disappears and becomes to be light attraction, because of light impulse of photon $\vec{p} = 2n\hbar\vec{k}$ changes its sign due to negative refractive index $\vec{p} = -2n\hbar\vec{k}$, so the reflected light impulse is directed backward out of the source light (fig. 129).

Fig. 129. Direction of incident and reflected light impulse for the right-handed (left) and left-handed (right) materials.

15.8. Superprizm phenomenon

Kosiaka from Japan discovered "superprizm" phenomenon, that was turn out a reversible Snell law in the photonic crystal, demonstrating the PC in kind of the left media. The photonic 3D crystal looks as the hexagonal graphite-like lattice built from microdisks Si and SiO_2 with the refractive indexes n=3.24 and n=1.46 respectively (fig. 130). Lattice parameter is a=0.40 μm, for which an adduced normalized frequency is $\Omega = \frac{a}{\lambda} = \nu\frac{a}{c} = 0,42$. Polarized light with $\lambda = 0{,}956$ μm from laser incidents on the PC under sharp angle.

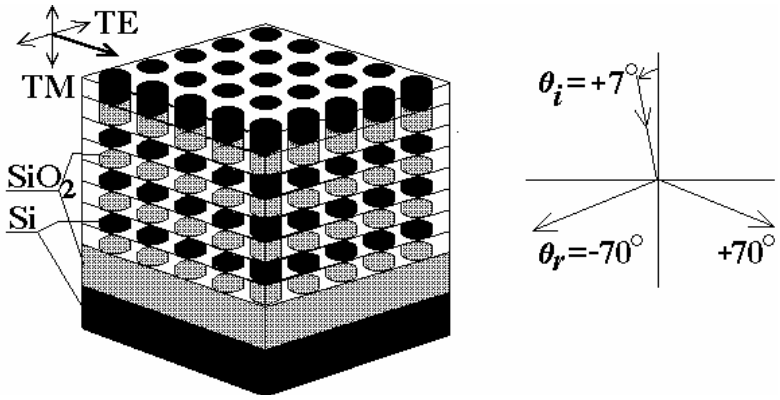

Fig. 130. Scheme of photonic crystal acting as the left-handed material in which superprizm phenomenon have been observed as being the negative refraction (Kosiaka et al.)

Variation of incident angle in range of $-7° < \varphi < 7°$ was shown experimentally to change the refraction angle in range of –70° до 70° (fig. 130). Therefore in accordance with Snell law the refractive index of such the PC is negative

Phenomenon of negative refraction as shown by Mandelstam is the general property for waves of different nature with negative group velocity. So we may expect that the acoustic, electronic, and spin waves also may posses the negative refraction.

15.8. General $\varepsilon - \mu$-diagram

Design and search of novel left-handed materials to-day is very promising research topic. All physical laws in vacuum have been discovered for to day. Hence to find new phenomena it is requested to design new media in which such the new predicted phenomenon may exist and realized.

It is interest to compare all kinds of matters using the $\varepsilon - \mu$ - diagram me (fig. 131).

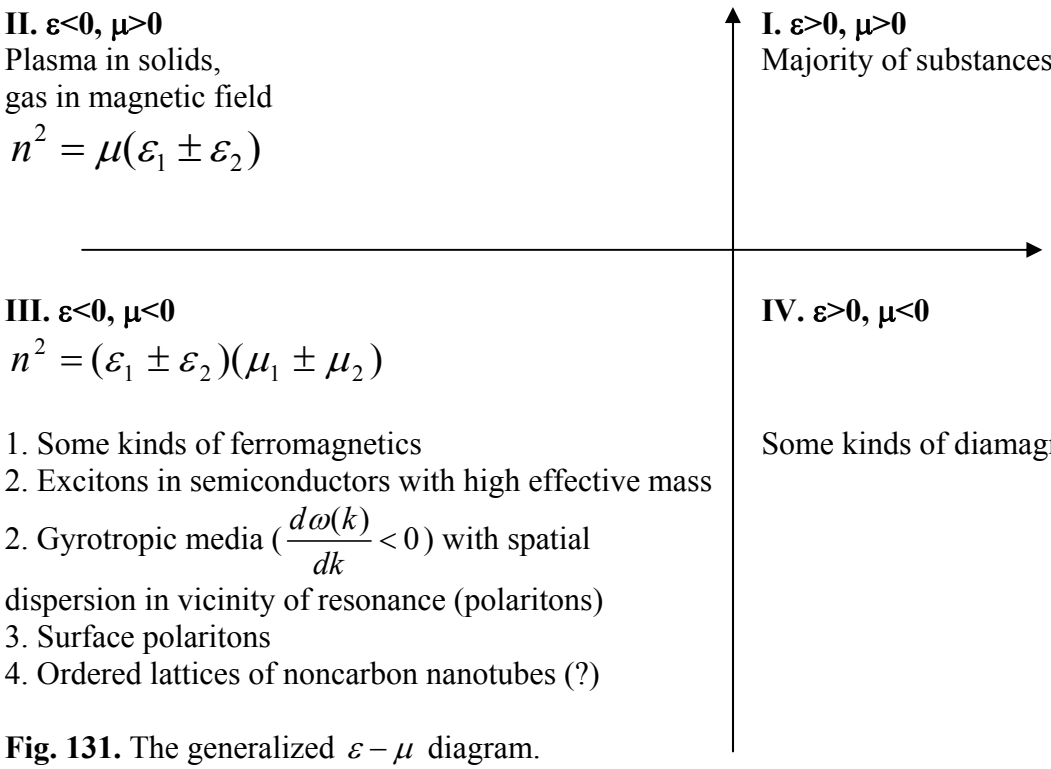

Fig. 131. The generalized $\varepsilon - \mu$ diagram.

The left-handed materials in general was predicted early to search among the gyrotropic media with negative group velocity ($\frac{d\omega(k)}{dk} < 0$), in which permittivity have a tensor nature. To day it is clear that metamaterials should be created artificially on base of heteronanostructures, for example of 2D320 type. V.Pokropivny has suggested that nanotubes are natural left handed metamaterials because: 1) some of them possess the helicoidal type of symmetry, that is peculiar for hyrotropic media with negative group velocity; 2) all nanotubes are 1D nanostructures rolled from 2D multilayers, so the excitation of surface plasmo-polaritons is possible to occur in noncarbon nanotubes. The left handed effect can be achieved at some electromagnetic frequencies in metamaterials consisting of 2D arrays of 1D metallic wires having $\varepsilon < 0$ below effective plasma frequency combined with 2D layers of 0D double split ring resonators having $\mu < 0$. Such the very complex nanocomposites are in fact the nanodevises some of them are shown in fig. 132.

Characterized by set of parameters these metamaterials give us the possibilities to drive and control their properties, in particular the frequency range where they becomes to be left-handed. On this base one can produce novel super-high-frequency tera-hertz nanoelectronics. To day the design of such artificial nanostructured materials is sharply developed, so we may expect a discovery of novel phenomena and achievements in this

field. It is the most interest and perspective field of fundamental research in modern physics and materials science.

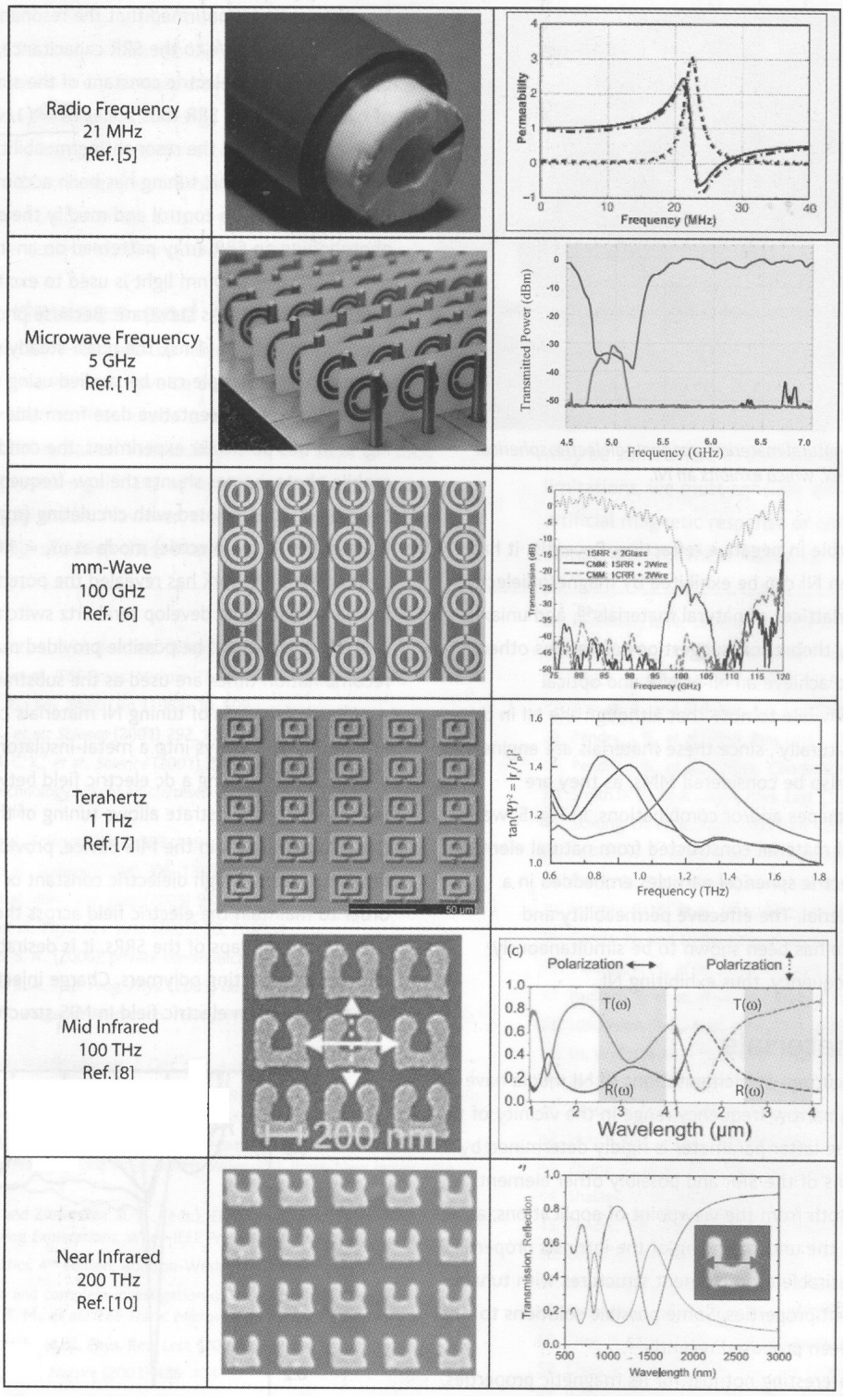

Fig. 132. Types of metamaterials in different wave-length ranges. Shown in the left column is a frequency range, in the middle column is a structure, and in rights column is the physical characteristics. Shown in the top row is the cable metamaterial to control a magnetic flow (M.C. Wiltshire et al. Science **292**, 77 (2001)); Shown in the second row is the metamaterials developed in first time by D.R.Smith et al. (Phys.Rev.Lett. 84, 4184 (2000));

16. SCANNING PROBE MICROSCOPY

16.1. Introduction – from Hooke to Binnig

The first instrument named "microscope" is believed to be built in the 17th century by Robert Hooke. This simple apparatus, being the system of lenses and rather called "light microscope", has made a real revolution in natural science. However, its maximum resolution is limited by the wavelength of visible light (~0.5 μm) and cannot satisfy all the demands of modern science.

Next serious scientific breakthrough was made only in 1930s when electron microscope was developed, in which an electron beam is used instead of photons to obtain much better image magnification. But still scientists were looking for more powerful tools, wishing not only to see, but to "feel" and even to manipulate the matter on the nano and atomic scale.

In the year 1981 fundamentally new instrument – Scanning Tunneling Microscope (STM) – was invented by G. Binnig and H. Rohrer (Nobel Prize 1986). This invention has raised the surface science on the new level by surpassing all experimental results obtained so far by other techniques. Several years later even more powerful tool, the Atomic Force Microscope (AFM), was developed. A lot of other surface-science techniques based on the similar principles have been developed since that time. All these techniques subsumed under the name of Scanning Probe Microscopy (SPM).

16.2. Basics of SPM

As appears from the name, the central part of all Scanning Probe Microscopes is a special probe. The probe is equipped with small extra sharp tip, which works as a very sensitive sensor. The choice of the probe type, as well as material and geometry of the tip, depends on particular application.

The general principle of SPM operation is simplistically illustrated in fig. 133. The sample is scanned with appropriate probe and the local interaction between the tip apex and the surface is detected at very high (in certain cases down to atomic level) spatial resolution. At that, the resolution depends dramatically on the geometry and curvature radius of the tip – the sharper the tip, the better the resolution. Ideally, the tip is ended with single atom.

The probe is moved along the line first in forward, and then in reverse direction, then passes to the next line (similar to electron beam in TV). The movement is performed by means of piezoscanner, which, depending on the model of microscope, can be placed either under the sample or above the probe. In the SPM piezoscanner, piezoelements are placed in such a way, that by applying the voltage it is possible to bend and to lengthen or reduce the scanner, allowing scanning in X, Y plane and changing the distance between the tip and the sample.

For precise control of the tip-sample distance, the feedback system is used. Changes in tip-sample distance during the scanning due to the surface relief cause the changes in registered signal. Feedback system tries to keep constant the value of signal by moving the sample (or probe) in vertical direction. In modern probe microscopes the distance can be controlled with accuracy up to 10^{-3} nm.

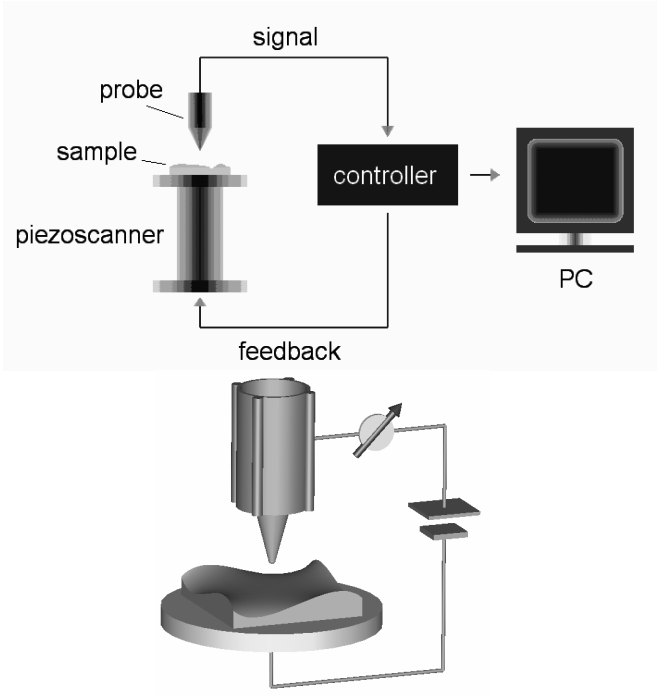

Fig. 133. Principle of SPM and STM operation

Measured signal goes to the controller and transmits to the computer, where the tip-sample interaction is recorded as a function of position. Information then processed to be stored in the desirable form. In such a way, pictorial images of surface topography or any other surface properties can be achieved. The type of registered interaction depends on the probe type, operating mode, and particular type of SPM. It means that the image can represent not only the surface topography, but e.g. electronic structure, electric or magnetic fields, thermal or any other local properties. Visualization of the scanning data is done by computer graphics and can be represented either as 2D brightness images or 3D images. In 2D images the relative brightness of details on the surface corresponds to the magnitude of the measured signal (in particular, the height of the surface structures) (fig. 134a). 3D image of the surface can be plotted in an axonometric view (fig. 134b). The other way of representing the data in 3D form is simulating the surface illumination by a point source located in some point of space above the surface (fig. 134c).

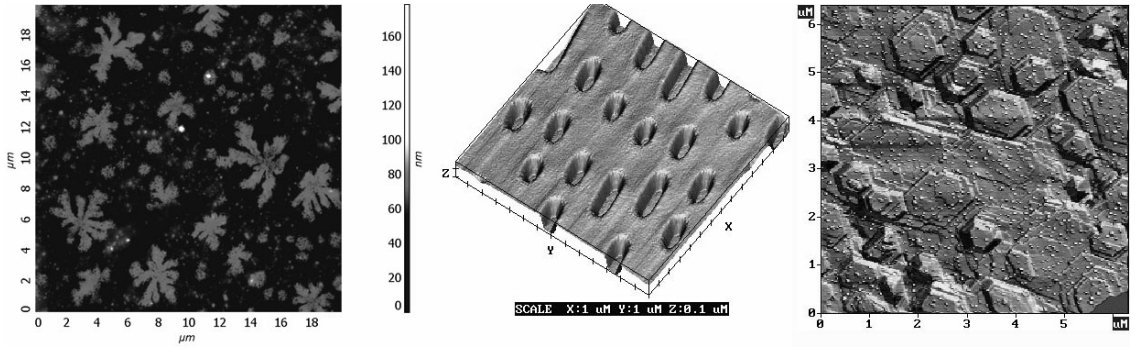

a) b) c)

Fig. 134. Visualization of certain surface properties of different samples represented in 2D brightness image mode (a) and two types of 3D image mode (b, c).

16.3. SPM techniques

There are lot of different SPM types and methods, but only the most common models will be considered here starting with Scanning Tunneling Microscope, as it opened the Scanning Probe Microscope era.

16.3.1. Scanning tunneling microscopy

The principle of operation of *Scanning Tunneling Microscope* is based on marvelous quantum phenomenon known as the tunnel effect. The bias voltage (usually < 1 V) is applied between the tip and the sample. The air gap is considered as energy barrier for electrons. At certain separation the tunnel current arises. Its magnitude (I) depends exponentially on the distance (d), so the sensitivity to vertical deflections is very high. The typical operating value of tunnel current is ~1 nA and distance is several angstroms. The value of the current and separation can be registered continuously during the scanning with high accuracy and provide information about surface topography. STM correlates the geometric positions of atoms with their resulting electronic structure.

The formation of the STM images depends on the operating mode. The basics modes are *constant current mode* and *constant height mode*.

In *Constant Current Mode (CCM)* tunneling current is kept constant by feedback circuit during the scanning process. This is achieved by moving the tip up and down accordingly to the surface topography, so that the current is constant during the whole scanning process. In this case, vertical displacement of the scanner (feedback signal) reflects surface topography (fig. 135). The scanning speed in constant current mode is lower than that in constant height mode, but in CCM it is possible to investigate the samples with developed relief.

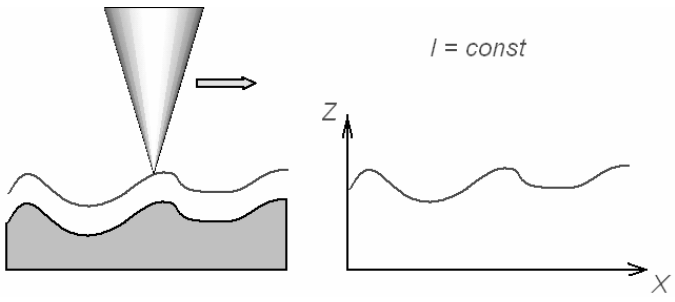

Fig. 135. Constant current mode

In Constant Height Mode (CHM) the tip movement is implemented only in X-Y plane and the vertical (Z) position is kept constant, so the current changes according to the surface topography (fig. 136). It allows to increase the speed of scanning, but only provided that the surface is very flat. Otherwise the tip will be damaged.

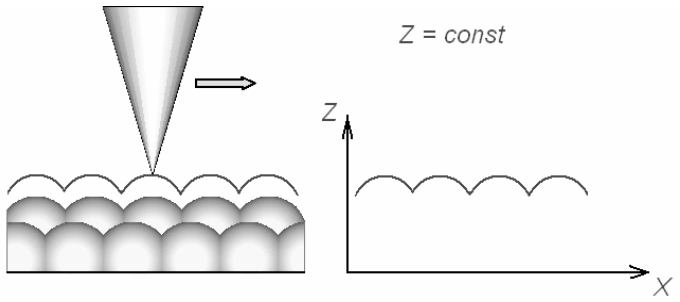

Fig. 136. Constant height mode

Other important modes include Local Barrier High (LBH) imaging, Local Density of States (LDOS), I(z) Spectroscopy and I(V) Spectroscopy (or Current Imaging Tunneling Spectroscopy).

Application field of STM is quite wide. In addition to mentioned above, the STM can be used to study charge transport mechanisms in molecules or other small structures. The other important application of STM is the investigations of crystal growth. Furthermore, STM can be used as a tool for the surface modification. It can be done by indenting the surface with the tip or by the electron emission. At low temperatures it is even possible to move single atoms with high accuracy using STM tip.

Due to exponential dependence of the tunnel current on the distance, the resolution of STM in the direction normal to the surface is very high and reaches fractions of Angstrom even at ambient conditions. The lateral resolution strongly depends on the atomic geometry of the tip apex. The best STM tips have a single atom or small cluster of atoms on their apex, so the tunnel current flows just between these atoms on the apex and particular surface atoms. In this case, provided that tip is clean, the atomic resolution can be achieved.

Despite an excellent resolution, STM technique has a serious disadvantage – the choice of material for investigation with STM is limited by the requirement for them to be conducting.

Another important thing is the surface condition, primarily its cleanliness. Any insulator particle on the investigated surface will cause the tunnel current to decrease and, as a result, will look on the STM image the same as cavity. For the same reason the surface areas with low conductivity (nonconductive impurities) also make the interpretation of STM image more difficult. For high-resolution of metals and semiconductors, the STM is usually operated in ultrahigh vacuum to avoid contamination or oxidation of the surface.

16.3.2. Atomic-force microscopy (AFM)

In *Atomic Force Microscopy* (fig. 137) the surface is scanned with a probe made of an elastic microscopic cantilever provided with a small sharp tip (fig. 138). The most common materials for the probes are Si, SiO_2 and Si_3N_4.

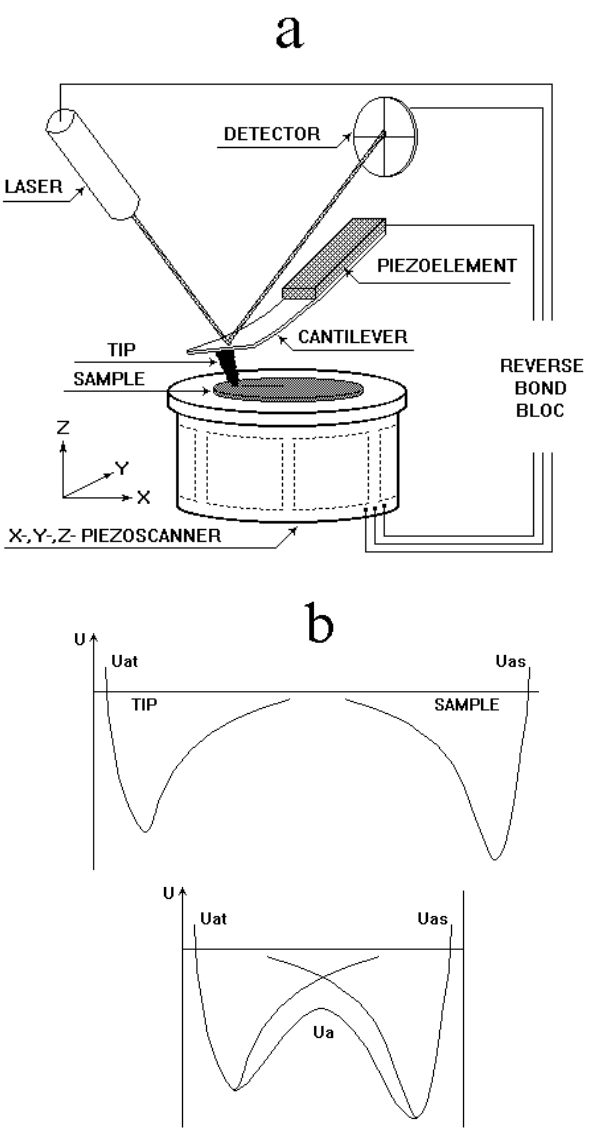

Fig. 137. Scheme of atomic force microscope (a) and potential of interatomic interactions between tip and sample (b).

Atomic forces between the tip apex and the surface atoms (fig. 137) are sufficient enough to bend the cantilever (fig. 138). By measuring the rate of bending, the tip-sample interaction is evaluated.

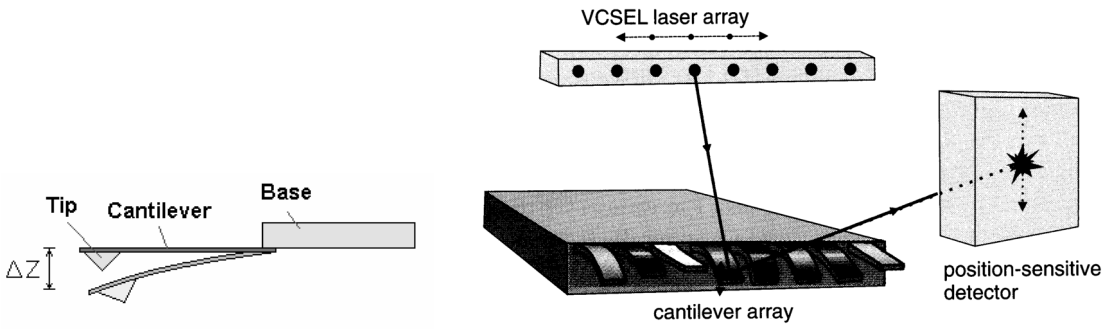

Fig. 138. Scheme of the probe and optical detecting system of Atomic Force Microscope.

The bending can be measured in different ways. Currently the most common is optical method (*beam-bounce*). The laser beam is focused on the cantilever, which is coated with reflecting film. When the cantilever is in rest position, the reflected beam is directed exactly to the center of segmented photodetector. When cantilever approaches the surface it bends under the action of interatomic forces and the reflected beam is deflected. The deflection is registered by photodetector, which construction enables registering both vertical and lateral deflection of the beam, and, consequently, calculating vertical and lateral components of the forces.

In other aspects the working principle of AFM is similar to STM. The movement of the probe or the sample is implemented by means of piezoscanner. For precise control of the tip-sample separation the feedback system is used. Signal is transmitted to the computer where it is stored and processed.

There are lot of different types of interaction between the tip and the sample. The most important are elastic, Van der Waals and capillary forces. Elastic interaction (repulsive forces) dominates in contact mode. Van der Waals forces are the major forces at tip-sample separation of the order of several nanometers. Capillary (or meniscus) forces arise when water layer is adsorbed on the surface of the object exposed to the open air. To measure any other forces, the meniscus force must be eliminated by working in low humidity environment or by dipping both sample and tip in a liquid environment.

There are three general AFM operation modes – *contact mode*, *non-contact mode*, and "*semi-contact" mode* (also called "*intermitted-contact mode*" or "*tapping mode*").

In contact mode the tip is in direct contact with the surface, and the cantilever deflection under scanning reflects repulsive force and is used to imagine the sample surface profile. Contact mode is used only in the case of sufficiently smooth and hard samples. Otherwise the tip or sample can be damaged.

In non-contact mode the contact between the tip and the sample is avoided, providing highest scanning speed and longest tip life. But, at the same time, non-contact mode has the lowest sensitivity and resolution.

In semi-contact mode cantilever oscillates on its resonant frequency. Interaction with surface causes changes in phase and amplitude of oscillations. These changes are used to obtain the surface topography.

Moreover, above-mentioned measurements can be carried out either at *constant force* or at *constant average distance (*or *constant height)*. Each mode has its advantage and disadvantage.

At constant force the value of cantilever bend is kept constant by feedback system. Constant force mode enables to measure with high resolution simultaneously with topogra-phy some other characteristics like e.g. friction forces, spreading resistance etc. However, speed of scanning is restricted by the response time of feedback system. Constant height mode provides high scanning speeds, but probability of tip or sample damage is high.

Using special probes and modes of operation, not only topography, but also other surface properties can be visualized with AFM. Moreover, AFM enables to perform nanolithography with high resolution.

Most important and perspective applications of SPM and AFM developed recently are the manipulation of nanostructures and surface modification shown in fig. 139.

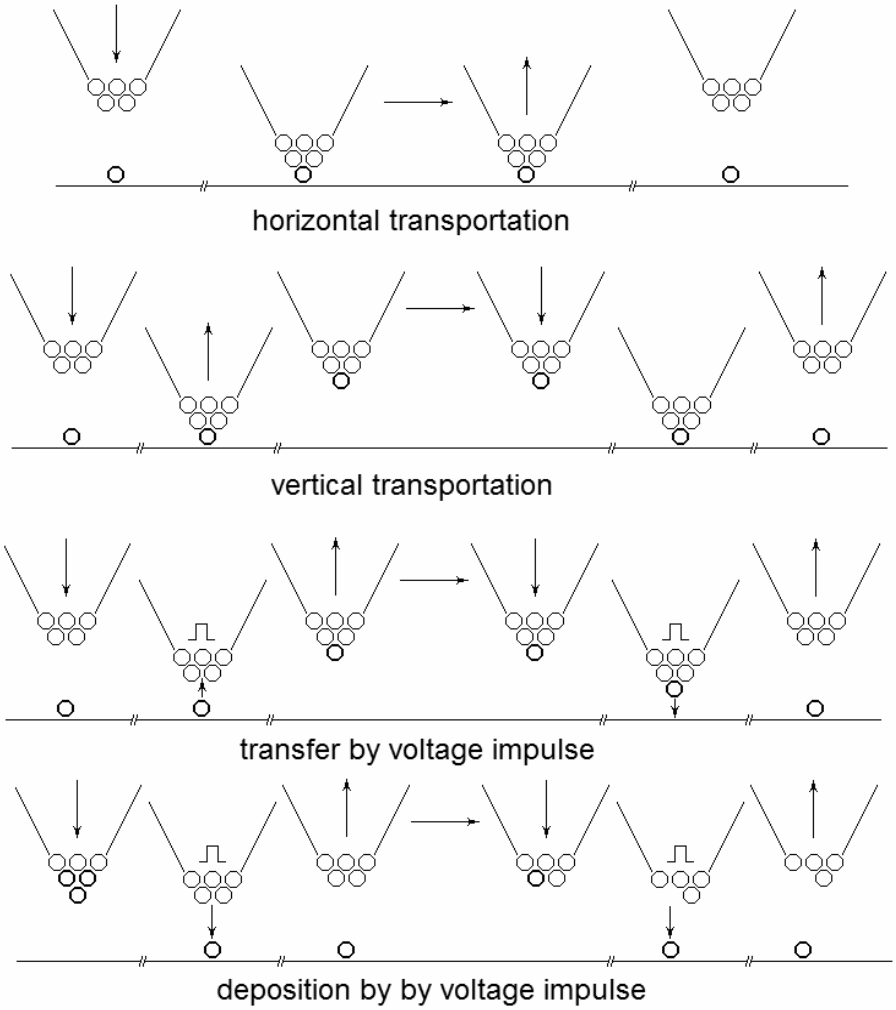

Fig. 139. Methods for manipulations and modification of surface nanostructures by SPM (T. Tsong. Mater. ChemPhys. V.33, p.1 (1993)).

17. MEMS and NEMS

17.1. Introduction

The term MEMS (Micro Electro-Mechanical Systems) first started being used in the 1980's and was applied to a broad set of technologies with the goal of miniaturizing electro-mechanical systems. Recently, with development of nanotechnologies, it became possible to decrease the size of such systems down to nano-scale and the term NEMS (Nano Electro-Mechanical Systems) came into use. Today MEMS and NEMS is a rapidly growing field dealing with creation of micro and nano-scale devices generally on a silicon substrate through microfabrication technology. Unlike conventional integrated circuits, these devices can have many different functions. Even the complete systems-on-a-chip is possible. And just like microelectronics once did, MEMS and NEMS technologies will permeate our everyday live in the nearest future.

17.2. Fabrication of MEMS and NEMS

There are many ways to fabricate MEMS and NEMS. The most common MEMS fabrication technologies are *Surface Micromachining* and *Bulk Micromachining*, and the most common substrate is silicon. Its strength-to-weight ratio is higher than many other engineering materials.

NEMS can be fabricated either in a *top-down* or *bottom-up* approach. The top-down approach consists of scaling down the existing MEMS technology into the nm range. In the bottom-up approach devices a made from nanostructures like nanotubes or nano-wires. Below is a brief overview of the typical MEMS and NEMS fabrication processes.

17.2.1. Surface micromachining

Silicon *surface micromachining* uses the same equipment and processes as the electronics semiconductor industry and was first demonstrated already in 1967. Thus, a serious experience, appropriate equipment and skilled operators were available for applying the surface micromachining technologies for MEMS and NEMS fabrication. And first micromechanical devices made with surface micromachining were presented in 1987.

Surface micromachining technology consists in deposition of layers of sacrificial and structural material on the surface of substrate followed by patterning of sacrificial material by photolithographic imaging and ended by etching of the films selectively to the mask. When the sacrificial material is removed, completely formed and assembled mechanical devices are left.

17.2.2. Bulk Micromachining

Bulk Micromachining is a method of making structures by selectively etching directly inside a substrate (silicon wafer). Anisotropic properties of silicon are used to etch different structures. Bulk Micromachining makes also extensive use of wafer bonding, where different silicon wafers are joined together. Two most common bonding techni-

ques are anodic bonding and silicon fusing bonding. When several bulk micromachined wafers are bonded together, a wide range and complexity of mechanical structures can be made.

17.2.3. Fabrication stages

17.2.3.1. Deposition

Deposition of sacrificial and structural material on the substrate is the first stage in surface micromachining and it can be done either by chemical processes like CVD (Chemical Vapor Deposition), Electrodeposition, VPE (Vapor Phase Epitaxy) and Thermal oxidation or by physical processes like PVD (Physical Vapor Deposition) and Casting.

In CVD, a substrate is placed inside a reactor to which a number of gases are supplied and heated to relatively high temperatures (at least 300°C). The fundamental principle of the process is that a chemical reaction takes place between the source gases. The product of that reaction is a solid material with condenses on all surfaces inside the reactor. CVD result in thin films with good coverage. A variety of materials can be deposited with this technology.

Another chemical process is *electrodeposition* and is typically restricted to electrically conductive materials and therefore is well suited to make films of metals such as copper, gold and nickel. There are basically two technologies for electrodeposition – *electroplating* and *electroless* plating. In the electroplating the substrate is placed in electrolyte solution and electrical potential is applied between substrate and a counter electrode. Redox process takes place resulting in the formation of a layer of material on the substrate. In the electroless plating process a more complex chemical solution is used, in which deposition happens spontaneously on any surface which forms a sufficiently high electrochemical potential with the solution. This process does not require any external electrical potential and contact to the substrate during processing. However, it is also more difficult to control.

Next process, *Vapor Phase Epitaxy*, is quite similar to CVD – a number of gases are introduced in a reactor where, in contrast to CVD, only the substrate is heated. If the substrate is an ordered semiconductor crystal, it acts as a seed for the deposition and it is possible to continue building on the substrate with the same crystallographic orientation. In the case of amorphous/polycrystalline substrate surface, the film will also be amorphous or poly-crystalline. VPE allows the high growth rate and is primarily used for deposition of silicon.

Thermal oxidation is the classical technology used to form silicon dioxide on a silicon substrate. Process itself is simply oxidation of the substrate surface in oxygen atmosphere at 800° C-1100° C and it only form films that are oxides of that material. Thermal oxidation is typically used to form films that are used for electrical insulation.

Physical Vapor Deposition (PVD) is a deposition technology in which material is released from a source and transferred to the substrate by *evaporation* or *sputtering*. For metals, PVD is far more common process than CVD, since it can be performed cheaper and at lower process risk. However, the quality of the films is lower than in CVD.

In *evaporation* the substrate and source of the material are placed inside a vacuum chamber. The source material is evaporated by heating with electron beam (fig. 140) or electrically with high current. Evaporated material condenses on all surfaces.

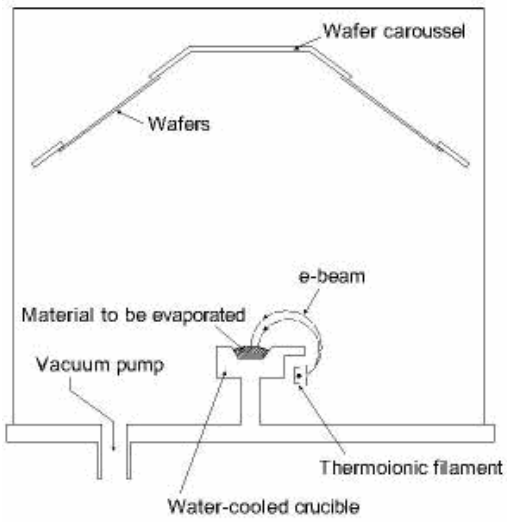

Fig. 140. A schematic diagram of a typical system for e-beam evaporation (What is MEMS? http://www.memsnet.org/mems/what-is.html).

Sputtering is a technology in which the material is released from the source at much lower temperature than evaporation. The substrate and the source material (target) are placed in some inert gas atmosphere at low pressure. The gas is then ionized by RF power source and the ions are accelerated towards the target at high speed so that atoms are dislodged from the surface and condensed on all surfaces including the substrate (fig. 141).

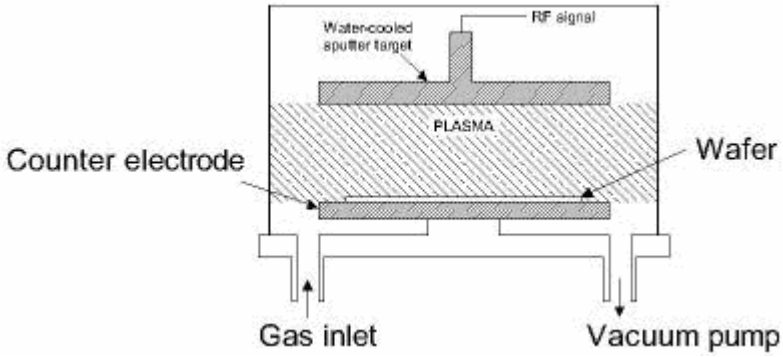

Fig. 141. Typical RF sputtering system (What is MEMS? http://www.memsnet.org/mems/what-is.html).

Casting. In this process the material to be deposited is dissolved in a solvent and applied to the substrate by spraying or spinning (fig. 142). After evaporation of solvent, a thin film of the material remains on the substrate. The thicknesses of the layer range from a single monolayer of molecules to tens of micrometers. Casting can be used for a variety of materials (mostly polymers and it is an integral part of photolithography.

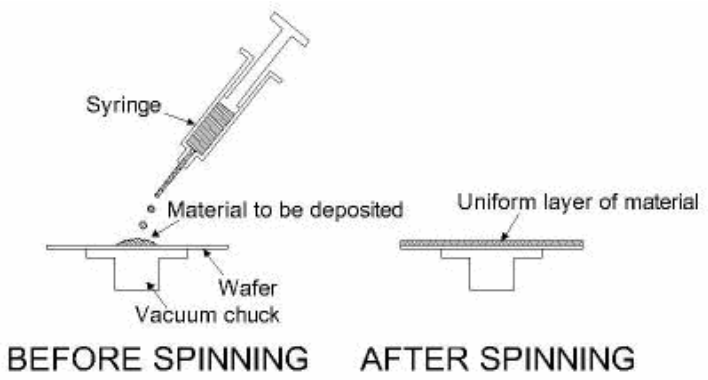

Fig. 142. The spin casting process as used for photoresist in photolithography (What is MEMS? http://www.memsnet.org/mems/what-is.html)

17.2.3.2. Patterning

Patterning is the next important stage in surface micromachining. It is done by lithography, that is typically the transfer of a pattern to a photosensitive material by selective exposure it (through the mask) to a radiation, so that the properties of the exposed and unexposed regions a different. After the exposure it is possible to etch away either only exposed or only unexposed region of the photosensitive material (fig. 143).

If the exposed material is etched away by the developer and the unexposed region is resilient, the material is considered to be a positive resist. If the exposed material is resilient to the developer and the unexposed region is etched away, it is considered to be a negative resist.

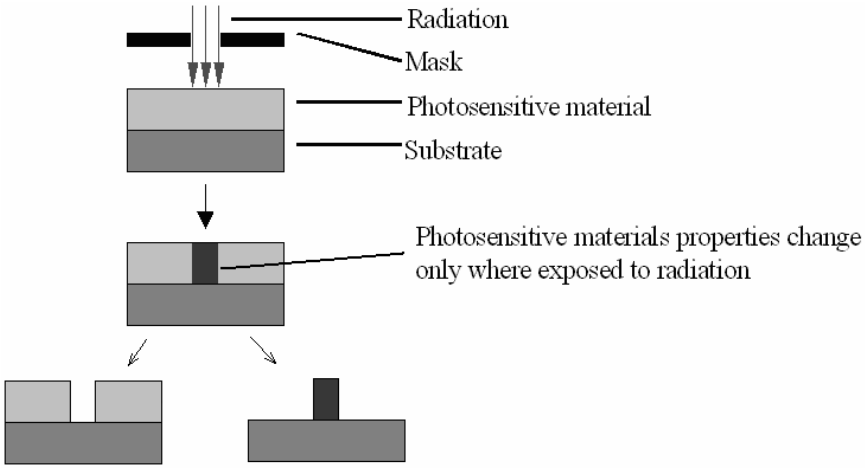

Fig. 143. Transfer of a pattern to a photosensitive material and selective etching.

Unfortunately, photosensitive compounds, which are usually organic, do not cover the whole spectrum of needed properties for micro and nano devices. However, a photosensitive layer is often used as a temporary mask when etching an underlying layer, so that the pattern may be transferred to the underlying layer (fig. 144). Photoresist may also be used as a template for patterning material deposited after lithography (fig. 144). The resist is subsequently etched away, and the material deposited on the resist is “lifted off".

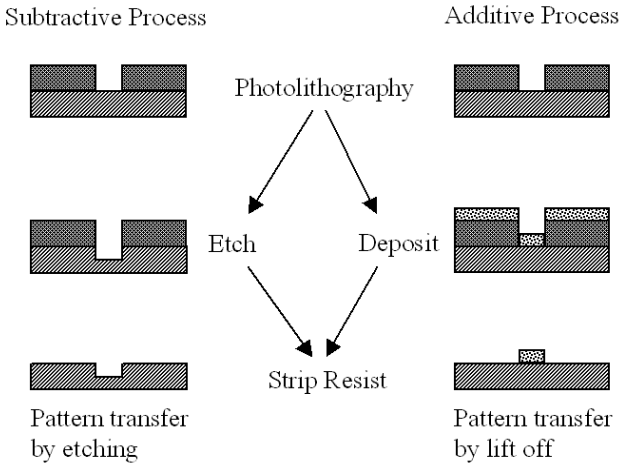

Fig. 144. a) Pattern transfer from patterned photoresist to underlying layer by etching, b) Pattern transfer from patterned photoresist to overlying layer by lift-off (*MEMS & NEMS Micro/Nano-Electro-Mechanical Systems, Silicon Valley Technical Institute, www.svtii.com)*

17.2.3.3. Etching

To form a functional structure on a substrate, it is necessary to etch thin films previously deposited or to etch the substrate itself. In general, there are two classes of etching processes: wet etching where the material is dissolved when immersed in a chemical solution, and dry etching where the material is sputtered or dissolved using reactive ions or a vapor phase etchant.

Wet etching is the simplest and cheapest etching technology. It requires only a vessel with liquid etchant. However, wet etching has a feature, that in some cases might be undesirable – the shape of etched whole will depend on the etchant type and substrate material. In the case of some crystalline material like silicon the shape of the whole will depend on the crystallographic orientation. This phenomenon is known as *anisotropic etching* and it is the most common silicon etching technology. Typically alkali etchants like KOH are used to etch different crystallographic directions at different rates, with some orientations dissolving up to 1000 times faster than others. Crystallographic planes that etched extremely slowly are called *stop planes*. A surprising number of structures can be made using the etch stop planes in crystalline silicon. Anisotropic etching usually produces V-shaped grooves, pyramids, and channels into the surface of the silicon wafer (fig. 145). If the etch is carried out correctly the surface of these grooves can be atomically smooth. *Isotropic etching*, in contrast, etches all directions with nearly the same rate, and produces rounded depressions on the surface of the wafer that usually resemble hemispheres and cylinders (fig. 145).

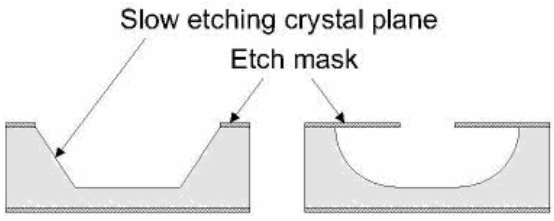

Fig. 145. Example of anisotropic (left) and isotropic (right) etching.

Dry etching is much more expensive, but it allows etching almost straight down without undercutting, which provides much higher resolution. The dry etching technology can be divided in three separate classes called *reactive ion etching* (RIE), *sputter etching*, and *vapor phase etching*.

In RIE, the substrate is placed inside a reactor with gas mixture. Gas mixture is ionized by RF power source. The ions are then accelerated towards the surface of substrate and can either react and form another gaseous material (chemical part) or, if ions have sufficient energy, they can knock atoms out of the material (physical part). First process is isotropic and the second one is highly anisotropic. By adjusting the balance between two processes it is possible to form sidewalls that have shapes from rounded to vertical.

A popular subclass of RIE is deep RIE (DRIE). In this process, etch depths of hundreds of microns can be achieved with almost vertical sidewalls. The technology is based on the so-called “Bosch process", where two different gas compositions are alternated in the reactor. The first gas composition creates a polymer on the surface of the substrate, and the second gas composition etches the substrate. The horizontal surfaces of polymer are sputtered away by the physical part of the etching. The sidewalls are left unaffected. Since the polymer only dissolves very slowly in the chemical part of the etching, it builds up on the sidewalls and protects them from etching. As a result, etching aspect ratios of 50 to 1 can be achieved. The process can easily be used to etch completely through a silicon substrate, and etch rates are 3–4 times higher than wet etching.

Sputter etching is essentially RIE without reactive ions. The difference is that substrate is now subjected to the ion bombardment instead of the material target used in sputter deposition.

Vapor phase etching is another dry etching method, which can be done with simpler equipment than what RIE requires. In this process the wafer to be etched is placed inside a chamber, in which one or more gases are introduced. The material to be etched is dissolved at the surface in a chemical reaction with the gas molecules. The two most common vapor phase etching technologies are silicon dioxide etching using HF and silicon etching using XeF_2, both of which are isotropic in nature.

17.3. Examples

Actuators are the MEMS that transform mechanical force, work and move into electric current or voltage and *vice-verse* using the electrostatic, piezoelectric, thermoelectro-mechanical, electromagnetic and other mechanisms of energy conversation.

The simplest actuator is the electrostatic capacitor. In response of applied voltage V between charged plates an electrostatic force arise $F = \frac{\varepsilon S}{2(d-z)^2} V^2$, where ε is the dielectric constant of interplate material, S is the plate area, d is the distance between plates, z is the plate deflection caused by the voltage.

In contrast to a conventional capacitor in the actuator one plate may be moved relative another one, or deflected in kind of a cantilever in AFM. Under applied voltage the cantilever is attracted to surface at distance of z that is used to drive a clearance, for example, in switcher.

In the comb actuator presented in fig. 146, the interaction force is constant, therefore the upper comb my hanging over the lower comb (the levitation).

Piezoactuator shown in fig. 146 causes a deformation deflection at angle φ or displacement of piezoelectric plate under applied voltage V due to piezoeffect in piezomaterials, such as $BaTiO_3$, ZnO, AlN, PZT, etc.

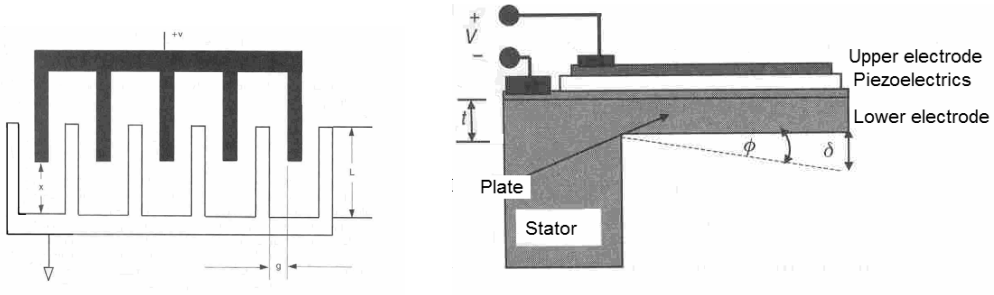

Fig. 146. Schemes of the comb electrostatic (left) and piezoelectric (right) actuators.

MEMS have a lot of different application like e.g. sensing, communication, actuation, and are widely used in aerospace, automotive, biotechnology, instrumentation, robotics, manufacturing and other fields. For example, high frequency circuits benefit considerably from the MEMS technology. Electrical components such as inductors and tunable capacitors can be improved significantly compared to their integrated counterparts. The performance of communication circuits can be improved, while the total circuit area, power consumption and cost are reduced. The micro- and nano-mechanical switches have quality factors much higher than anything previously available. Electrically-driven motors smaller than the diameter of a human hair are already possible. MEMS accelerometers are quickly replacing conventional accelero-meters for crash air-bag deployment systems in automobiles. They are much smaller, more functional, lighter, more reliable, and are produced for a fraction of the cost of the conventional macroscale accelerometer elements.

Examples of MEMS are shown in figs. 147–150.

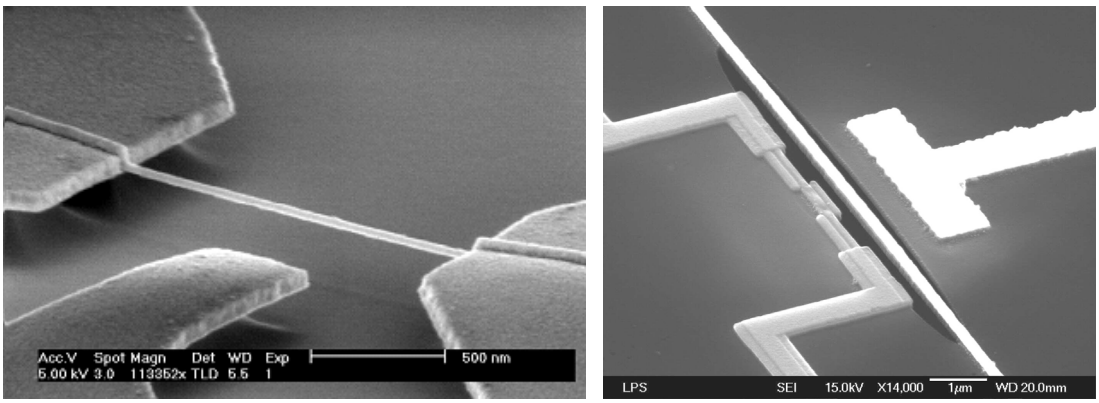

Fig. 147. Nanotube placed between two gate electrodes (Physics of Nanoelectro-mechanical Systems: Introduction, http://www.nottingham.ac.uk/~ppxada/research.html)

Fig. 148. Nanomechanical single electron transistor (Physics of Nanoelectromechanical Systems: Introduction, http://www.nottingham.ac.uk/~ppxada/research.html)

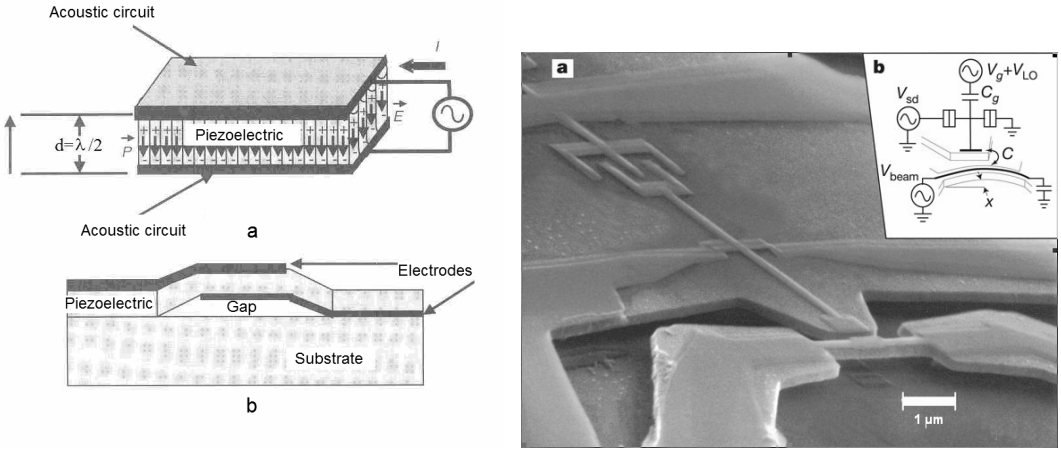

Fig. 149. Principle of layer acoustic resonator (a) and scheme of membrane-type resonator (b).

Fig. 150. Nanometre-scale displacement sensing using a single electron transistor. Doubly clamped GaAs beam and the aluminum electrodes (colored) forming the single electron transistor and beam electrode. The $Al/AlO_x/Al$ tunnel junctions have approximately 50 x 50 nm^2 overlap (**a**). A schematic of the mechanical and electrical operation of the device (**b**) (Nanometre-scale displacement sensing using a single electron transistor, http://www.nature.com/nature/journal/v424/n6946/fig_tab/nature01773_F1.html).

NEMS is intensively developing field which don't have as much applications yet as MEMS have. However, a numerous researches have shown that NEMS can be successfully used as nano-transistors, as extremely sensitive sensors for the force and mass detection down to the single molecule level, as high-frequency resonators up to the GHz range, as ultra-fast, low-power switches, and more. It is clear, that the number of applications for the NEMS will increase very fast with further development of nanotechnologies.

TEST QUESTIONS

1. Adduce and explain a formula for classification of nanostructures by dimensionality.
2. Quote Gleiter's definition of size effects. What are intrinsic and extrinsic size effects? Give an example.
3. What is confinement?
4. Write a formula for energy levels in infinite potential well of L width. What is the difference for case of finite potential V_0?
5. Draw and describe a quantum well for heterojunction AlGaAs/GaAs/AlGaAs.
6. Write a formula for band gap in second semiconductor.
7. Picture a MOS structure and explain a creation of 2D-electron gas.
8. Draw a $\chi(E)$ dependence of density of electronic states for 3D, 2D, 1D, 0D nanostructures.
9. Explain the intrinsic classic (IC) size effects, a(d), $T_m(d)$, $D_{dif}(d)$, K(d), $\sigma(d)$.
10. Define an extrinsic classic (EC) size effects and give the example for wire polarization.
11. Define the intrinsic quantum (IQ) size effects and give an example.
12. Define the extrinsic quantum size effects and give an example.
13. What is a peculiar feature of nano-structures distinguished them from micro- and macro-structures? Types of size effects. Types of grain boundaries.
14. Pair potential method. Estimate free surface energy of crystal.
15. Explain blue shift in ZnO and transformation of energy spectrum from atom through cluster to solid.
16. Adduce external quantum (EQ) size effects in semimetallic bismuth.
17. Define and classify methods for synthesis of nanostructured materials.
18. Describe the principles and processes in chemical and physical vapor deposition (CVD and PVD) methods for synthesis of NSM.
19. Describe the principles and processes in plasma assisted methods for synthesis of NSM.
20. Describe the principles and processes in molecular beam epitaxy (MBE) method for synthesis of NSM.
21. Describe the principles and processes in flame pyrolysis method for synthesis of NSM.
22. Describe the principles and processes in liquid-phase methods for synthesis of NSM.
23. Describe the principles and processes in sol-gel method for synthesis of NSM.
24. Describe the principles and processes in mechanical milling and attriction for synthesis of NSM.
25. Describe the principles and processes in severe plastic deformation method for synthesis of NSM.
26. Describe the principles and processes for consolidation of nanopowders.
27. Describe the principles and processes for sintering of nanopowders.
28. Describe the peculiar mechanical properties of NSM.
29. Describe the peculiar electric and optical properties of NSM.
30. How the hardness and strength of NSM depend on their grain-size?
31. What are the peculiar properties of mesoporous materials and MCM41 in particular?
32. What are the peculiar properties of zeolites?
33. Describe the structure of fullerenes, fullerites and fullerides.

34. Describe the principles and processes of arc-discharge and laser-ablation methods for synthesis of fullerenes.
35. Describe the principles and processes of laser-ablation methods for synthesis of nanotubes.
36. Geometrical description of chiral, armchair and zigzag carbon nanotubes.
37. Chiral numbers, chiral angles, and diameter of carbon nanotubes.
39. Unit cells and Brillouin zones of carbon nanotubes.
39. Band structure of arm-chair and zig-zag carbon nanotubes.
40. Typical density of electronic states of carbon nanotubes.
41. How conductivity of carbon nanotubes depend on chiral numbers?
42. Band gap of metallic and semiconducting carbon nanotubes and how it depends on diameter?
43. Dispersion curves for acoustical and optical modes of carbon nanotubes vibrations.
44. Typical phonon spectra for metallic and semiconducting carbon nanotubes.
45. Breathing and whispering modes of carbon nanotube vibrations.
46. Thermal conductivity of carbon nanotubes.
47. Coulomb blockade and current-voltage curve in carbon nanotubes.
48. Nature and observation of Aaronov-Bohm effect in carbon nanotubes.
49. Nature of superconductivity in nanotubes and formula for Tc in BCS-theory.
50. Strain deformation rolling energy for C and BN nanotubes and how it depend on diameter.
51. Map of ductile and brittle nanotubes and why zigzag nanotube is brittle while arm-chair is ductile.
52. Principles of photonic crystals (Bragg diffraction, Yablonovich idea, Jone idea).
53. Phenomenon of photon trapping be defects in photonic crystals.
54. Photonic band structure and band gap in photonic crystals.
55. Principle of waveguide and light localization on base of defects in photonic crystals.
56. Principle of photonic crystals. Filter, fiber and interferometer on its base.
57. Principles of injection semiconducting laser (LED).
58. Types of lasers on base of low-dimensional structures and their comparison.
59. Principle and scheme of semiconducting laser on base a double heterojunction.
60. Principle and scheme of semiconducting cascade multi-layered laser.
61. Principle and scheme of vertical cavity surface emitting laser (VCSEL).
62. Principle and scheme of semiconducting nanowire laser.
63. Principle and scheme of semiconducting zeolite-dye laser.
64. Principle and scheme of surface-emitting 2D photonic-crystal laser with multi-directional distributed-feedback.
65. Principle and scheme of laser on defect mode in photonic crystal.
66. Principle and scheme of laser on base of quantum dots.
67. Define the left-handed metamaterials and inverse Snell low.
68. Types and principles scanning probe microscopes.
69. Principle and scheme of scanning probe microscope.
70. Principle and scheme of atomic force microscope.
71. Describe the principles and methods for fabrication of MEMS.
72. What are MEMS and NEMS?

LITERATURE

1. P. J. Harris. Carbon nanotubes and related structures. Cambridge University Press, 1999.
2. Handbook of nanophase and nanostructured materials. Ed. by Zhong Lin Wang, Yi Liu, Ze Zhang. V.1. Synthesis; V.2. Characterization; V.3. Materials systems and applications I; V.4. Materials systems and applications II. Kluwer Academic/ Plenum Publishers, 2003.
3. Guozhong Cao. Nanostructures & Nanomaterials. Synthesis, properties & applications. Imperial College Press, 2004.
4. Nanoscale Science and Technology. Ed. by R.W. Kelsall, I.W. Hamley, M. Geoghegan. John Wiley & Sons, Ltd., 2005.
5. P. Harrison. Quantum wells, wires and dots. John Wiley & Sons. Ltd., 2005.
6. Nanomaterials Handbook. Ed. by Yu.Gogotsi. Taylor & Francis Group, LLC, 2006.
7. M. S. Dresselhaus, P.C.Eklund. Phonons in carbon nanotubes// Advances in physics. – 2000. – V.49, N6. – P. 705–814.
8. H.Gleiter. Nanostructured materials: basic concepts and microstructures// Acta Metallurgica. – 2000. – 48, N1. – P. 1–29.
9. J.D.Joannopoulos, P.R.Villeneuve, S.Fan. Photonic crystals: putting a new twist on light// Nature. – 1997. – 386. – P. 143–149.
10. V.V. Pokropivny. Noncarbon nanotubes. Review// Powder Metallurgy and Metal Ceramics. I. Methods of synthesis V.40, Issue 9/10, p. 485–496 (2001).
    II. Types and structures V. 40, Issue 11/12, p. 582–594 (2001).
    III. Properties and promising applications V. 41, Issue 3/4, p. 123–135 (2002).
11. V.V. Pokropivny. Two-dimensional nanocomposites. Review// Powder Metallurgy and Metal Ceramics. I. Types and fabrication V. 41, Issue 5/6, p. 264–272 (2002)
    II. Properties and applications V. 41, Issue 7/8, p. 369–381 (2002)